

# **Poly(lactic acid) Nanocomposites: Water Barrier Properties and Electrospinning**

by  
**Bowen Tan**

A doctoral thesis to be inserted

Submitted in partial fulfillment of the requirements for the award of degree  
of Doctor of Philosophy of Loughborough University

Supervisor: Dr N. L. Thomas

8<sup>th</sup> December 2016

© by Bowen Tan (2016)

## **Acknowledgment**

I would like to express my appreciation and thanks to my supervisor Dr Noreen Thomas, you have not only been a guide in my research career but also a tremendous mentor for me. I would like to thank you for the continuous encouragement and valuable advice during my PhD study. You helped me take every obstacle in the research experiment and the thesis writing. You make me feel lucky of being one of you PhD students. I could not have imagined having a better supervisor and mentor for my PhD study.

A very special thanks to my family. Words cannot express how grateful I am to my parents during the past four years, for your unconditional love and support. Also, a grateful thanks to my husband. Thanks for always being at my side. I could not finish my PhD without you.

My sincere thanks also goes to the LMCC staffs and the technicians in the department of materials who gave me access to the laboratory and training of the facilities. Without your precious support and patience I would not be able to conduct the experiment successfully.

## **Abstract**

The PhD thesis investigated poly(lactic acid) nanocomposite in terms of water barrier properties and electrospinning. The thesis addresses two different but related topics. The first topic is improvement of the water vapour barrier properties of PLA films. The effect of montmorillonite clay and its alignment on water vapour permeability and the effect of crystallinity (introduced by annealing) on nanoclay alignment and barrier properties were investigated (Chapter 4). PLA nanocomposites containing 0 to 5 wt.% montmorillonite layered silicate were prepared. Both amorphous and semi-crystalline PLA nanocomposite films were obtained by compression moulding. Thermal properties of the samples were measured by DSC. The nanoclay dispersion was measured using TEM and WAXD. Water vapour transmission rates through the films were measured at 38°C and at a relative humidity of 90%. A new tortuous path model was developed to quantify the effect of crystallinity, nanoclay concentration and nanoclay alignment on water vapour permeability and showed a good fit with the experimental data from the annealed PLA nanocomposites.

A further development of this topic was to use mechanical stretching to introduce orientation and molecular alignment to the PLA nanocomposite films. The effect of mechanical stretching on PLA nanocomposite in terms of nanoclay structure and water barrier properties were investigated (Chapter 5). Uniaxial stretching was applied to amorphous PLA nanocomposite sheets at 60 °C and a draw ratio of 3. Thermal properties of the stretched films were measured by DSC. T<sub>g</sub> of the stretched films significantly increased with clay concentration due to the presence of nanoclay that reduced the mobility of the polymer chains and hence increased chain relaxation time. The nanoclay dispersion was measured using TEM and WAXD. Better delamination of the clay layers was obtained due to the drawing of the intercalated clay tactoids by uniaxial stretching. The stretched PLA nanocomposite films showed better water vapour permeability than the quenched PLA nanocomposite films.

The second topic is to produce PLA nanocomposite fibres by a novel technique of electrospinning (Chapter 6). The aim is to investigate how nano-sized particles (i.e., montmorillonite clay and zinc oxide nanoparticles) affect PLA nanofibres in

terms of the morphology and properties. Two grades of PLA (4060D and 4032D) nanofibres containing 1, 3, and 5 wt.% montmorillonite clay were produced using electrospinning. The morphology of the nanofibres was investigated using SEM and the nanoclay structure in the nanofibres was measured using TEM. Continuous nanofibres with the existence of a few beads were obtained in both grades of PLA nanocomposite fibres. Thermal properties of the nanofibres were investigated using DSC. Both PLA grades showed a reduction in T<sub>g</sub> with the addition of nanoclay. The crystallisable PLA / clay nanofibres showed the degree of crystallinity increased from 21% to 31% with clay content increasing from 0 to 5 wt.%. The mechanical properties of PLA nanofibre mats were analysed by tensile tests. PLA nanofibres exhibited worse mechanical properties with the addition of nanoclay.

The second part investigates the effect of ZnO nanoparticles on PLA nanofibres. PLA 4060D nanocomposite nanofibres containing 1, 3, 5, 7 and 9 wt.% ZnO were produced using electrospinning. The morphology of the nanofibres was investigated using SEM and the ZnO particle structure was measured using TEM. A good distribution of the ZnO particles was obtained with some nanoparticle agglomerates. Thermal properties of the nanofibres were investigated using DSC. The incorporation of ZnO enhanced the enthalpy relaxation of the polymer chains at the glass transition. The wetting properties of the nanofibre mats were evaluated by water contact angle measurement. Antimicrobial properties of the PLA / ZnO nanofibres were evaluated against E.coli bacterial at 37°C. Zone inhibition was observed when ZnO content was above 5 wt.%.

## Contents

List of Abbreviations .....	8
List of Figures .....	10
List of Tables .....	17
1 Introduction.....	19
1.1 Background .....	19
1.2 Aims of the project.....	21
1.3 List of publication.....	23
2 Literature review .....	24
2.1 Poly(lactic acid).....	24
2.1.1 Structure of PLA .....	24
2.1.2 Polymerisation of PLA .....	26
2.1.3 Properties of PLA .....	28
2.2 Polymer/clay nanocomposites.....	40
2.2.1 Structure and composition of montmorillonite clay.....	40
2.2.2 Properties of montmorillonite clay.....	41
2.2.3 Montmorillonite clay reinforced polymer nanocomposites .....	42
2.2.4 Preparation of polymer/clay nanocomposites .....	43
2.3 Barrier properties.....	45
2.3.1 Barrier properties of polymer .....	45
2.3.2 Barrier properties of polymer nanocomposites .....	49
2.4 PLA nanocomposites .....	56
2.4.1 Preparation of PLA nanocomposites .....	56
2.4.2 Morphology.....	57
2.4.3 Oxygen and water vapour barrier properties.....	61
2.4.4 Effect of uniaxial and biaxial stretching on PLA and PLA nanocomposites..	63
2.5 Orientation of polymers.....	66
2.6 Electrospinning of PLA.....	69
2.6.1 Introduction to electrospinning.....	69
2.6.2 Effect of various parameters on electrospinning.....	71
2.6.3 Electrospinning of PLA based nanofibres .....	73
2.6.4 Electrospinning of nanoclay composite fibres .....	77
2.6.5 Electrospinning of zinc oxide composite fibres .....	80
3 Experimental .....	84
3.1 Raw materials.....	84
3.2 Sample preparation.....	85
3.2.1 Pre-drying of PLA.....	85
3.2.2 Compounding (Haake Rheomix OS).....	85

3.2.3	Compression moulding.....	87
3.2.4	Uniaxial stretching.....	88
3.2.5	Electrospinning of PLA nanocomposite solution.....	89
3.3	Characterisation.....	92
3.3.1	Differential scanning calorimetry (DSC).....	92
3.3.2	Water vapour transmission rate test.....	92
3.3.3	Wide angle X-ray diffraction (WAXD).....	94
3.3.4	Birefringence.....	95
3.3.5	Transmission electron microscopy (TEM).....	97
3.3.6	Scanning electron microscopy (SEM).....	98
3.3.7	Tensile testing of electrospun mats.....	98
3.3.8	Antibacterial testing of electrospun mats.....	99
4	Effect of clay on the water barrier property of PLA nanocomposites.....	100
4.1	Effect of clay concentration on quenched PLA nanocomposites.....	100
4.1.1	DSC of quenched PLA nanocomposites.....	100
4.1.2	TEM of quenched PLA nanocomposites.....	101
4.1.3	WAXD of quenched PLA nanocomposites.....	105
4.1.4	Water vapour permeability results.....	106
4.2	Effect of annealing on PLA nanocomposites.....	110
4.2.1	DSC of annealed PLA nanocomposites.....	110
4.2.2	Optical microscopy results of annealed PLA nanocomposites.....	114
4.2.3	XRD results of annealed PLA nanocomposites.....	116
4.2.4	TEM results of annealed PLA nanocomposites.....	116
4.2.5	Water vapour permeability results.....	120
4.3	Summary.....	126
5	Uniaxial stretching of PLA nanocomposites.....	127
5.1	Uniaxial stretching of neat PLA sheets.....	127
5.1.1	Birefringence test on uniaxially stretched PLA films.....	129
5.1.2	DSC results of uniaxially stretched PLA films.....	131
5.1.4	XRD of uniaxially stretched PLA films.....	134
5.1.5	Water vapour permeability results.....	135
5.2	Effect of mechanical stretching on PLA nanocomposites.....	138
5.2.1	DSC of uniaxially stretched PLA nanocomposites.....	138
5.2.2	TEM of uniaxially stretched PLA nanocomposites.....	140
5.2.3	XRD of uniaxially stretched PLA nanocomposites.....	144
5.2.4	Water vapour permeability results.....	145
5.3	Summary.....	148
6	Electrospinning of PLA based nanofibres.....	150
6.1	Electrospinning of PLA - Selecting the optimum solvent system.....	150

6.2 Electrospinning of PLA / clay nanofibres.....	153
6.2.1 Morphology of PLA / clay nanofibres (SEM and diameter distribution).....	153
6.2.2 TEM of PLA / clay nanofibres .....	159
6.2.3 DSC results of PLA / clay nanofibres .....	161
6.2.4 Mechanical properties of PLA / clay nanofibres.....	164
6.2.5 Summary of PLA / clay nanofibres.....	169
6.3 Electrospun PLA / ZnO nanofibres.....	171
6.3.1 Preparation and morphology of PLA / ZnO nanofibres.....	171
6.3.2 TEM of PLA / ZnO nanofibres.....	177
6.3.3 DSC result of PLA / ZnO nanofibres.....	178
6.3.4 Wettability of PLA / ZnO nanofibres.....	179
6.3.5 Antimicrobial properties of PLA / ZnO nanofibres.....	180
6.3.6 Summary of PLA/ZnO nanofibres .....	182
7 Conclusions.....	183
8 Further work.....	187
References .....	188

## List of Abbreviations

PLA	Poly(lactic acid)
PLLA	Poly(L-lactic acid)
PDLA	Poly(D-lactic acid)
PCL	Poly( $\epsilon$ -caprolactone)
PBS	Poly(butylene succinate)
PVA	Poly(vinyl alcohol)
PEO	Poly(ethylene oxide)
PVAc	Poly(vinyl acetate)
PS	Polystyrene
PET	Polyethylene terephthalate
PI	Polyimide
PA	Polyamide
PVDF	Polyvinylidene fluoride
CAB	Cocamidopropylbetaine
MMT	Montmorillonite clay
HNT	Halloysite nanotubes
ZnO	Zinc oxide
SA	Sodium alginate
AC	Acetone
DMF	Dimethylformamide
CHL	Chloroform
DMAc	Dimethylacetamide
T <sub>g</sub>	Glass transition temperature
T <sub>c</sub>	Crystallisation temperature
T <sub>m</sub>	Melting temperature
X <sub>c</sub>	Degree of crystallinity

OP	Optical purity
DSC	Differential scanning calorimetry
$\Delta H$	Enthalpy
$M_w$	Weight molecular weight of polymer
$M_n$	Number molecular weight of polymer
ISBM	Injection stretch blow moulding
P	Permeability coefficient
D	Diffusion coefficient
S	Solubility coefficient
Q	Transmission rate
$\xi$	Immobility factor
WVTR	Water vapour transmission rate
TEM	Transmission electron microscopy
SEM	Scanning transmission electron microscopy
XRD	X-ray diffraction
WAXD	Wide-angle X-ray diffraction
TD	Transverse direction in biaxial stretching
MD	Machine direction in biaxial stretching
ND	Normal direction of a sample in biaxial stretching
UCW	Uniaxial Constant Width
SB	Simultaneous Biaxial
SEQ	Sequential Biaxial
$\lambda$	Draw ratio of stretching
$\Delta n$	Birefringence
vol. %	Volume percentage
wt. %	Mass percentage

## List of Figures

Figure 2.1 Chemical structure of L- (left) and D-(right) lactic acid

Figure 2.2 Chemical structures of LL-, DD- and meso-lactide (from left to right, respectively)

Figure 2.3 Three configurations of PLA

Figure 2.4 Methods of synthesis of PLA from lactic acids

Figure 2.5 Current production process of ring-opening polymerisation of PLA

Figure 2.6 T<sub>g</sub> for PLA samples of different L/D ratios as a function of molecular weight

Figure 2.7 Effect of aging temperature and time on thermal properties of PLA samples: (A) DSC scans of PLA aged at room temperature for different periods of time; (B) DSC scans of PLA aged at different temperatures for 24 hours

Figure 2.8 DSC scans of melt crystallised PLLA sheet obtained by water-quenching; air-annealing (cooled from 220 °C to room temperature in 5 min) and full-annealing (cooled from 220 °C to room temperature in 105 min)

Figure 2.9 A typical DSC trace for semi-crystalline polymers

Figure 2.10 A schematic of PLA hydrolysis reaction [1]

Figure 2.11 Crystal structure of montmorillonite clay [2]

Figure 2.12 Schematic diagrams of three morphologies of polymer/clay nanocomposites

Figure 2.13 Water vapour permeability of oriented PET films versus film density (film thickness = 1 mil)

Figure 2.14 Model for the path of a diffusing molecule through a polymer filled with circular or square plate fillers

Figure 2.15 WAXD patterns and corresponding TEM images of three different morphologies of PLA nanocomposite

Figure 2.16 a. WAXD patterns for different compositions of neat PLLA and Cloisite 15A; b. TEM image of PLLA nanocomposite sample with 10wt% Cloisite 15A

Figure 2.17 a. WAXD patterns for different compositions of neat PLLA and Cloisite 25A; b. TEM image of PLLA nanocomposite sample with 10wt% Cloisite 25A

Figure 2.18 a. WAXD patterns for different compositions of neat PLLA and Cloisite 30B; b. TEM image of PLLA nanocomposite sample with 10wt% Cloisite 30B

Figure 2.19 Oxygen permeability of PLA / montmorillonite nanocomposites (right), and PLA / synthetic mica nanocomposites (left)

Figure 2.20 Crystallinity of simultaneous biaxial (left) and uniaxial (right) oriented PLA films as a function of draw ratio

Figure 2.21 Crystallinity of sequential biaxial stretched PLA films as a function of draw ratio

Figure 2.22 XRD patterns of uniaxially and biaxially oriented PLA and its nanocomposite films

Figure 2.23 Schematic diagram of the orientation of clay tactoids with respect to the film axes, for (a) uniaxially and (b) biaxially stretched PLA nanocomposite films

Figure 2.24 Schematic of stretching modes (MD=machine direction; TD=transversal direction)

Figure 2.25 Schematic diagrams of set up of electrospinning apparatus (a) typical vertical set up and (b) horizontal set up of electrospinning apparatus

Figure 2.26 SEM images of PLLA and PLLA/PDLA (1:1) blend fibres that were electrospun at applied voltages of -12 and -25 kV

Figure 2.27 Effect of single solvent systems on nanofibre morphology: scanning electron micrographs of PLA nanofibres from solutions of 10% (w/v) of PLA in: (a) acetone with nanofibre diameter distribution, (b) 1,4-dioxane, (c) tetrahydrofuran, (d) dichloromethane, (e) chloroform, (f) dimethylformamide and (g) dimethylacetamide

Figure 2.28 Effect of binary-solvent systems on nanofibre morphology: scanning electron micrographs of PLA nanofibres with nanofibre diameter distribution from solutions of 10% (w/ v) of PLA in (a) acetone / 1,4-dioxane, (b)acetone /

tetrahydrofuran, (c)acetone / dichloromethane, (d)acetone/chloroform, (e)acetone / dime-thylformamide and (f)acetone / dimethylacetamide

Figure 2.29 TEM images of paracetamol (PCM)-loaded PLA and PCM-loaded PLA nanocomposite with 2wt.% clay content

Figure 2.30 TEM images of exfoliated PLA nanocomposite containing (a) 15.3 wt.% and (b) 25 wt.% clay

Figure 2.31 SEM image of PCL and PCL nanocomposite membrane with different ZnO nanoparticles

Figure 2.32 Plates showing the antibacterial activity of the fabricated PCL membranes with different concentrations of ZnO nanoparticles against *E. coli* (plate (a)) and *S. aureus* (plate (b)). In both plates are 2 wt.%(a), 3 wt.% (b), 4 wt.% (c), 5 wt.% (d), and 6wt.%(e) ZnO nanoparticles, and PCL membrane alone (f)

Figure 2.33 SEM images (left) and elemental mapping (right) of electrospun mats obtained by electrospinning of a PLA solution and electro spraying of nano-ZnO dispersed in MeOH at a 1, b 3, and c 5 wt% with respect to PLA

Figure 2.34 morphology of the ZnO-on-PLA nanofibres: (A) SEM images (C) TEM images; and the ZnO-in-PLA nanofibres: (B) SEM images (D) TEM images

Figure 3.1 Parts of Haake Rheomix OS

Figure 3.2 Compression moulding sample setup and hot press machine

Figure 3.3 Dimensions of the moulds

Figure 3.4 Main parts of biaxial stretching machine

Figure 3.5 The spraybase electro spray instrument

Figure 3.6 Main parts of sample insertion system of MOCON

Figure 3.7 Parts of cold stage microtome and a sample being cut on it.

Figure 3.8 Cutting of TEM samples

Figure 3.9 PLA nanofibre mats peeled off

Figure 4.1 DSC curves of pure PLA4060D and its nanocomposites containing 1-5 wt.% clay contents

Figure 4.2 TEM images of PLA nanocomposites containing 1, 2, 3 wt. % clay at 40k, 100k and 200k magnifications

Figure 4.3 Transmission electron micrograph of PLA nanocomposite with 3 wt.% clay at 200K magnification

Figure 4.4 Transmission electron micrograph of PLA nanocomposite with 1 wt.% clay at 200K magnification

Figure 4.5 Transmission electron micrograph of PLA nanocomposite with 1 wt.% clay at 400K magnification

Figure 4.6 Transmission electron micrograph of PLA nanocomposite with 3 wt. % clay at 400K magnification

Figure 4.7 WAXD traces of organoclay, PLA and PLA nanocomposite

Figure 4.8 Water vapour permeabilities of neat PLA and PLA nanocomposites

Figure 4.9 Water vapour permeabilities of PLA and PLA nanocomposites in comparison with Nielsen theoretical values

Figure 4.10 DSC heating scan for the annealed PLA 4032D

Figure 4.11 DSC heating scan for the annealed PLA 4032D nanocomposite with 1 wt.% nanoclay

Figure 4.12 DSC heating scan for the annealed PLA 4032D nanocomposite with 3 wt.% nanoclay

Figure 4.13 DSC heating scan for the annealed PLA 4032D nanocomposite with 5 wt.% nanoclay

Figure 4.14 Annealed PLA 4032D viewed in hot stage polarised optical microscope when heated at 115 °C and 168 °C and 170 °C

Figure 4.15 WAXD traces of quenched and annealed PLA nanocomposites with 3 wt.% nanoclay

Figure 4.16 TEM images of quenched and annealed PLA nanocomposites containing 1 wt. % clay at 60k , 100k and 200k magnifications

Figure 4.17 TEM images of annealed PLA nanocomposite with 1 wt.% clay at 400k magnifications

Figure 4.18 TEM images of annealed PLA nanocomposite with 1 wt.% clay at

400k magnifications

Figure 4.19 Water vapour permeabilities of annealed PLA and PLA nanocomposites in comparison with Nielsen theoretical values

Figure 4.20 Water vapour permeabilities of annealed PLA and PLA nanocomposites in comparison with theoretical values predicted from the Bharadwaj model

Figure 4.21 Water vapour permeabilities of annealed PLA nanocomposites in comparison with theoretical value predicted from the new model, equation (4.9)

Figure 5.1 Photos of an unstretched PLA sheet and two uniaxially stretched PLA sheets

Figure 5.2 Force versus displacement curve for 60 °C and 75 °C uniaxially stretching on PLA sheets

Figure 5.3 A diagram of the dimensions of a stretched sheet (MD=machine direction; TD=transversal direction; ND= normal direction of the sample)

Figure 5.4 Birefringence of PLA sheets stretched at different temperatures

Figure 5.5 DSC heating scans for normal PLA and four stretched PLA samples at various drawing temperatures

Figure 5.6 Tg of the stretched PLA samples as a function of drawing temperature

Figure 5.7 WAXD traces for normal PLA and stretched PLA at various drawing temperatures

Figure 5.8 WVTR data for stretched PLA versus drawing temperature

Figure 5.9 DSC curves of 3x1 stretched PLA4060D and its nanocomposites at 60 °C

Figure 5.10 Tg trend of PLA nanocomposite against clay content for both stretched samples and normal quenched samples

Figure 5.11 TEM images of quenched and stretched PLA nanocomposites containing 1 wt. % clay at 25k, 100k and 200k magnifications

Figure 5.12 Schematic diagram of how intercalated clay tactoids is drew during uniaxially stretching

Figure 5.13 TEM images of a stretched PLA nanocomposites containing 1 wt. %

clay at 200k magnification

Figure 5.14 WAXD traces of quenched and uniaxially stretched PLA nanocomposites with 3 wt.% nanoclay

Figure 5.15 Water vapour permeabilities of uniaxially stretched PLA nanocomposites in comparison with quenched PLA nanocomposites

Figure 5.16 Water vapour permeabilities of quenched and uniaxially stretched PLA nanocomposites in comparison with Nielsen theoretical values (when  $L/D=48$ )

Figure 6.1 SEM images of PLA nanofibres from solutions of 12.5% (w/v) amorphous PLA (grade 4060D) in acetone, chloroform, and acetone/chloroform and crystallisable PLA (grade 4032D) in chloroform, and acetone/chloroform solvent systems

Figure 6.2 SEM images of PLA 4060D/clay nanofibres containing (a) 0 wt.%, (b) 1 wt.%, (c) 3 wt.% and (d) 5 wt.% nanoclay

Figure 6.3 SEM images of PLA 4032D/clay nanofibres containing (a) 0 wt.%, (b) 1 wt.%, (c) 3 wt.% and (d) 5 wt.% nanoclay

Figure 6.4 Average diameters of PLA/clay nanofibres as a function of clay concentration

Figure 6.5 TEM images of PLA4060D / MMT nanofibres with different clay contents

Figure 6.6 DSC scans of amorphous PLA and PLA/MMT nanofibres containing 1, 3, and 5 wt.% MMT

Figure 6.7 DSC scans of semi-crystalline PLA and PLA / clay nanofibres containing 1, 3, and 5 wt.% clay

Figure 6.8 Strain - stress curves of PLA 4060D and its nanocomposite mats

Figure 6.9 Strain - stress curves of PLA 4032D / 3wt.% clay nanocomposite mats

Figure 6.10 Tensile properties of amorphous PLA/clay nanofibre mats as a function of clay concentration (a) tensile strength (b) Young's modulus (c) Elongation at break

Figure 6.11 SEM images of (a) PLA and PLA/ZnO nanofibres containing (b) 1

wt.%, (c) 3 wt.%, (d) 5 wt.%, (e) 7 wt.%, (f) 9 wt.% ZnO

Figure 6.12 SEM images of PLA/ZnO nanofibres containing 5 wt.% ZnO at different magnifications using backscattered electrons

Figure 6.13 Average diameters of PLA/ZnO nanofibres as a function of ZnO concentration

Figure 6.14 TEM images of PLA/ZnO nanofibres containing 1, 3, 5 wt.% ZnO

Figure 6.15 DSC scans of PLA / ZnO nanofibres containing 1 to 9 wt.% ZnO

Figure 6.16 Water droplet contact angle on the surface of PLA fibrous mats containing 0, 5, and 9 wt.% ZnO nanoparticles

Figure 6.17 Antimicrobial test of electrospun PLA fibrous mats containing (a) 0 wt.% and (b) 9 wt.% ZnO nanoparticles

Figure 6.18 Image of bacterial zone inhibition of PLA/ZnO fibrous mats against E.coli

## **List of Tables**

Table 2.1 Effects of stereochemistry and crystallinity on the mechanical properties of PLA

Table 2.2 Processing temperature profile for biaxial orientation PLA films (screw speed: 20-100rpm)

Table 2.3 Summaries of electrospinning parameters and their effect of the fibre morphology

Table 3.1 Information of PLA 4060D and PLA 4032D

Table 3.2 Masterbatch formulation

Table 3.3 Sample formulations

Table 3.4 Stretching parameters of PLA nanocomposites

Table 3.5 process parameter of electrospinning

Table 3.6 MOCON WVTR test setup parameters

Table 4.1 DSC data for all samples

Table 4.2 Water vapour transmission rate of quenched PLA nanocomposites

Table 4.3 Weight fraction to volume fraction conversion

Table 4.4 DSC data for all samples

Table 4.5 Results of water vapour transmission rate of annealed and quenched PLA nanocomposites

Table 5.1 Birefringence for drawn PLA at different temperatures

Table 5.2 Tg values of the stretched PLA sheets

Table 5.3 WVTR data for stretched PLA

Table 5.4 WVTR of stretched PLA in different thickness compared with the quenched PLA

Table 5.5 DSC results of stretched PLA 4060D nanocomposites in comparison with unstretched PLA 4060D nanocomposites

Table 6.1 Composition of two grades of PLA solutions with different solvent systems

Table 6.2 Nanofibre diameter of PLA and PLA/clay nanocomposite fibres

Table 6.3 DSC result for electrospun PLA and PLA / clay nanofibres

Table 6.4 Mechanical properties of PLA and PLA/clay nanofibre mats obtained from electrospinning

Table 6.5 Nanofibre diameter of PLA/ZnO nanocomposite mats

Table 6.6 DSC result of electrospun PLA / ZnO nanofibres

Table 6.7 Diameter of bacterial zone inhibition

# 1 Introduction

## 1.1 Background

Over the past decades, the development of synthetic petroleum-based polymers has brought economic development and great benefits to human lives. An increasing number of plastics are produced each year. Back in 1950, the annual production of plastics worldwide was only 1.5 million tons. Whilst this amount increased to 200 million tons in 2002 and 322 million tons in 2015 [3]. It is estimated that approximately 8% of the annual oil production is consumed in the plastics industry.

Synthetic plastics are extensively used as packaging materials due to their low cost, good processability and good mechanical properties. Approximately 30% of the plastics are used for packaging applications, which is still expanding at a high rate of 12% per annum [4]. However, many plastic packaging products, e.g. for food, pharmaceuticals, cosmetics, detergents and chemicals, have a short service life [5]. After a limited time of use, plastic packaging has to be disposed. Only a limited amount of plastic waste can be recycled and reused. The majority of plastic waste is disposed of through landfill, which creates big issues for the environment since plastics are persistence in the environment. Nowadays, most commodity plastics used are conventional plastics that take decades to degrade.

The environmental impact of plastic waste is increasing the need for alternative materials for short-term packaging and disposal applications. Therefore, bio-based polymers are being developed as a replacement for petroleum based packaging plastics. Bio-based polymers are derived from renewable resources, e.g. corn, cane sugar and starch. They can be divided into two categories: 1) One is 'biopolymers', which are polymers produced by the metabolic process of the living cells. This type includes some carbohydrates (e.g. cellulose and starch) and some proteins (e.g. keratin); 2) The other category includes the polymers that are synthesised from biomass monomers, for example poly(lactic acid) (PLA).

Most bio-based polymers are biodegradable, which means they can be hydrolysed followed by bacterial breakdown in the natural environment. Some synthetic plastics that are derived from petroleum are also biodegradable, such as polycaprolactone (PCL) and polyesteramide. But some bio-based polymers

like bio-derived polyethylene cannot be biodegraded.

Poly(lactic acid) is one of the most commercially successful bio-plastics due to its good mechanical and barrier properties. Its monomer, lactic acid, is derived from renewable sources, such as starch or maize sugar, through fermentation [6]. PLA is not only a biodegradable polymer, but also has good biocompatibility with the human body. Therefore, it has been extensively used in medical applications, such as wound healing, tissue engineering and drug delivery.

PLA has good mechanical properties and transparency compared with other bio-based polymers. Hence, it has been widely used for short life-time packaging products, such as food packaging and disposal items for catering. However, as a compostable polymer, PLA has poor water barrier properties compared with conventional thermoplastics. This is because PLA is a polar polymer and therefore has high water vapour solubility and hence high permeability. One way of addressing this problem is through the development of polymer / clay nanocomposites, which have been very successful in improving barrier properties [7].

In this thesis, the water vapour barrier property of PLA / clay nanocomposite used for package applications was investigated. Meanwhile, electrospun PLA nanocomposite fibres used for medical applications and water filtration membranes have also been investigated.

## 1.2 Aims of the project

This thesis addresses two different but related topics. The first topic is improvement of the water vapour barrier properties of PLA films. It is investigated how incorporation of montmorillonite clay and its alignment affect water vapour permeability (Chapter 4) and furthermore how crystallinity (introduced by annealing) affects nanoclay alignment and barrier properties. A new tortuous path model was developed to quantify the effect of crystallinity, nanoclay concentration and nanoclay alignment on water vapour permeability.

A further development of this topic was to use mechanical stretching to introduce orientation and molecular alignment to the PLA nanocomposite films. The effect of mechanical stretching on PLA nanocomposite films in terms of nanoclay structure and water vapour barrier properties were further investigated (Chapter 5). There are three objectives for this topic:

1. Incorporate montmorillonite clay in PLA to improve the water barrier properties of PLA films.
2. Investigate the combined effect of crystallinity and nanoclay in PLA films in terms of water barrier properties by annealing of PLA nanocomposite films.
3. Investigate the effect of orientation of polymer chains and nanoclay alignment on water barrier properties of PLA nanocomposite sheets by using mechanical stretching.

The second topic is to produce PLA nanocomposite fibres by a novel technique of electrospinning (Chapter 6). In this case, the aim is to investigate how nano-sized particles (i.e., montmorillonite clay and zinc oxide nanoparticles) affect the morphology, thermal properties, water contact angle, antimicrobial properties and mechanical properties of PLA nanofibres. Three objectives of this topic are listed below:

1. Select the optimum solvent system for PLA solution that is electrospinnable and accessible to continuous and uniform fibre morphology.
2. Investigate the effect of incorporating montmorillonite clay in PLA nanofibres, in terms of fibre morphology, thermal behaviour and

mechanical properties.

3. Investigate the effect of incorporating ZnO nanoparticles in PLA nanofibres, in terms of fibre morphology, thermal behaviour, antimicrobial properties and wettability.

### 1.3 List of publication

1. B.Tan and N.L.Thomas, A review of the water barrier properties of polymer/clay and polymer/graphene nanocomposites. *Journal of membrane science* (2016), 514, 595-612

Abstract:

This paper reviews the literature on moisture barrier properties of polymer/clay and polymer/graphene-based nanocomposites. The various models proposed to predict the effects of nanofillers in reducing water vapour permeability through polymers are outlined. These models are based on a range of different factors such as; tortuosity, geometry, platelet stacking, orientation, polymer chain confinement and plasticisation. Published experimental studies of water vapour permeability in both polymer/clay and polymer/graphene nanocomposites are then reviewed. The extent to which the models are validated by the results of these studies is discussed, together with the degree to which the potential for water barrier improvement in polymer nanocomposites has been realised.

2. B.Tan and N.L.Thomas, Tortuosity model to predict the combined effects of crystallinity and nanoclay on the water vapour permeability of polylactic acid, *Applied Clay Science* (2017), 141, 46-54

Abstract:

The combined effects of crystallinity and nanoclay fillers on the water vapour barrier properties of poly(lactic acid) (PLA) nanocomposites are investigated. Both amorphous and semi-crystalline PLA nanocomposites containing 0 to 5 wt.% montmorillonite layered silicate are prepared by melt compounding followed by compression moulding with two different thermal treatments: quenching and annealing. Thermal properties and morphology are investigated using differential scanning calorimetry (DSC), polarised light microscopy, transmission electron microscopy (TEM) and wide-angle X-ray diffraction (WAXD). It is confirmed that the nanocomposite structures are intercalated and the clay aspect ratio is measured to be 40 in both quenched and annealed samples. Water vapour transmission rates (WVTR) through the film samples are measured. A new tortuous path model is developed that fits the WVTR data and accounts for the effects of crystallinity as well as nanoclay aspect ratio, concentration and orientation.

## 2 Literature review

### 2.1 Poly(lactic acid)

#### 2.1.1 Structure of PLA

The monomer of PLA, lactic acid, is derived from a renewable source, such as starch and maize sugar, through dextrose fermentation [8]. Since lactic acid has an asymmetric carbon atom, it has two optically active configurations as shown in Figure 2.1. Commercial PLA is produced by ring-opening polymerisation of lactide, which is a cyclic dimer composed of two lactic acid units. Lactide has three optically isomeric forms: L-lactide (a dimer of L-lactic acid); D-lactide (a dimer of D-lactic acid) and meso-lactide (a dimer of L- and D-lactic acid), as shown in Figure 2.2.

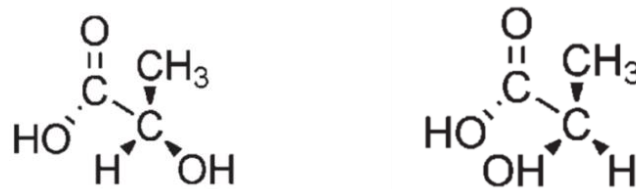


Figure 2.1 Chemical structure of L- (left) and D-(right) lactic acid [9]

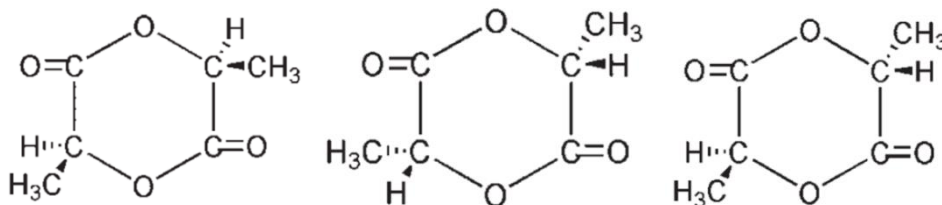


Figure 2.2 Chemical structures of LL-, DD- and meso-lactide (from left to right, respectively) [8]

PLA is a crystallisable polymer. The crystallisability of PLA is dependent on the ratio of L-, D- and meso- lactide in the polymer backbone: higher crystallinities are obtained with more optically pure polymers with higher chain symmetry [5]. PLA has three configurations, i.e. poly(L-lactic acid), poly(D-lactic acid) and poly(L/D-lactic acid) (see Figure 2.3), in which PLLA and PDLA are crystalline polymers, whereas PDLLA is an amorphous polymer.

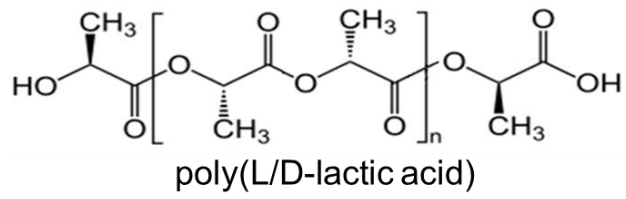
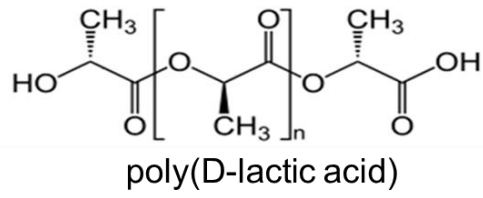
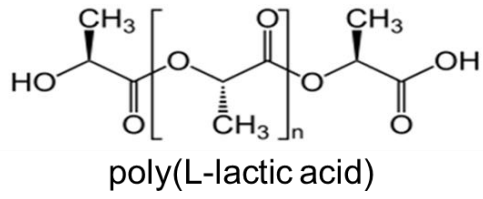


Figure 2.3 Three configurations of PLA [9]

## 2.1.2 Polymerisation of PLA

There are three polymerisation methods that can be used to produce commercial high-molecular-weight PLA, as shown in Figure 2.4. They are 1) direct condensation from lactic acid, 2) ring-opening polymerisation of lactide and 3) azeotropic condensation polymerisation [6], [8], [9].

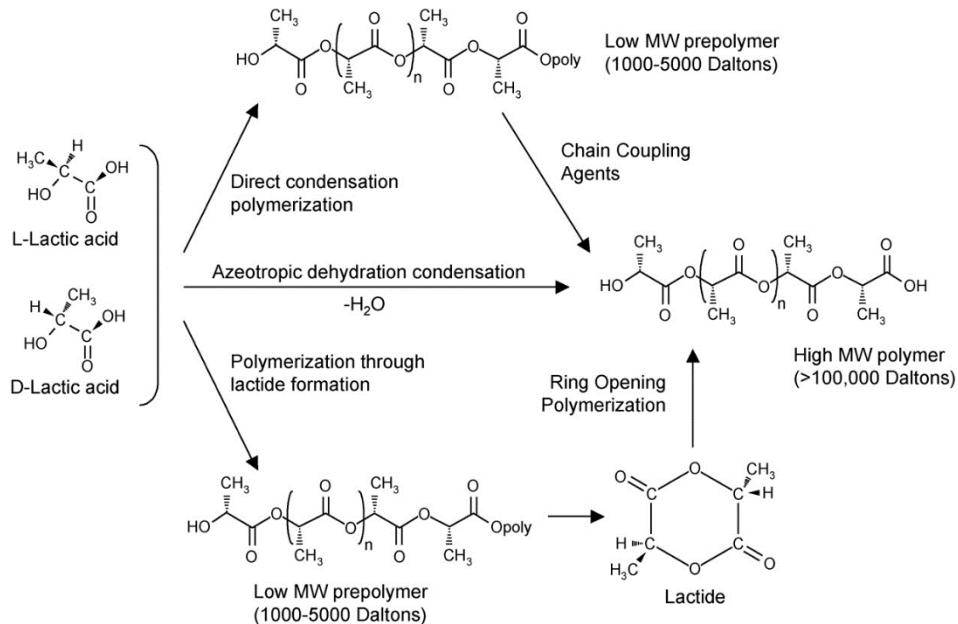


Figure 2.4 Methods of synthesis of PLA from lactic acids [8]

Direct condensation of lactic acid is the cheapest polymerisation route. However, it is difficult to obtain high molecular weight PLA through direct condensation. Therefore, PLA produced by direct condensation polymerisation usually exhibits brittle and glassy properties, which are unsuitable for most commodity applications. Various esterification promoting additives and chain-extending agents, such as bis(trichloromethyl) carbonate, dicyclohexylcarbodiimide and carbonyl diimidazole, are used to increase the molecular weight of the final PLA product. The by-products derived from the esterification promoting additives must be neutralised or removed at the end of the polymerisation to obtain a highly purified final product. Since the esterification promoting additives are relatively expensive, some cheaper chain-extending agents may be used instead, even though the PLA produced with chain-extending agents is not as pure as that produced with esterification promoting additives [6].

Ring-opening polymerisation is the most popular method to produce commercial PLA. It was first applied to produce high-molecular-weight PLA in 1954 by

DuPont [6]. A synthesis procedure currently used for commercial PLA is shown in Figure 2.5. Lactic acid (either D-, L- or meso-) is first produced by dextrose fermentation and then being extracted and pre-polymerised into an intermediate low molecular weight pre-polymer. The pre-polymer is then catalytically depolymerised under low pressure forming lactide, which is the cyclic dimer of lactic acid. High molecular weight PLA is polymerised through ring-opening polymerisation of lactide [9].

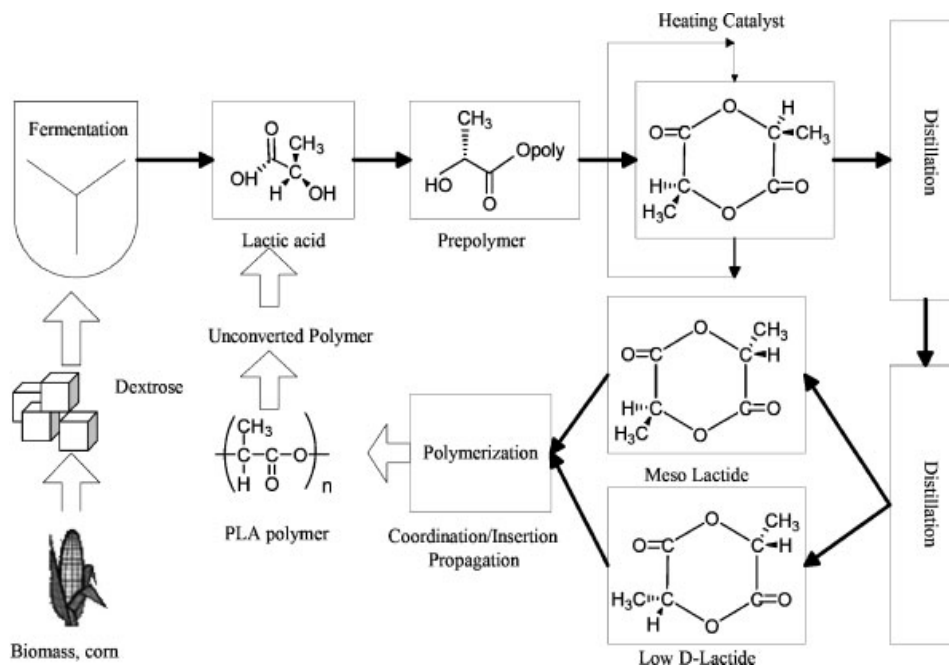


Figure 2.5 Current production process of ring-opening polymerisation of PLA [9]

Azeotropic condensation polymerisation is used to produce high-molecular-weight polymer without adding chain extending agents or additives. The general procedure of this method is as follow: firstly the lactic acid is distilled at reduced pressure for 2-3 hours at 130°C to remove the majority of condensation water. Then catalyst and diphenyl ether are added and a tube packed with 3-Å molecular sieves is attached to the reaction vessel. The refluxing solvent returns to the vessel by way of the molecular sieves for an additional 30-40 hours at 130°C [10]. The polymer can be isolated for further purification. Although this polymerisation technique provide high-molecular-weight PLA, it is high-cost and results in considerable catalyst impurities, which will cause several problems, e.g. degradation, uncontrolled hydrolysis rates and catalyst toxicity, during further processing [9]. Therefore, this is not preferred by the majority of PLA manufactures.

## 2.1.3 Properties of PLA

### 2.1.3.1 Thermal properties

Thermal properties of PLA are dependent on factors such as molecular weight, chain regularity and processing history of the polymer [5]. The glass transition temperature ( $T_g$ ) of PLA is mainly influenced by its molecular weight and chain regularity [8]. The relationship between  $T_g$  and molecular weight is represented by the Flory-Fox equation:

$$T_g = T_g^\infty - \frac{K}{\overline{M}_n} \dots\dots\dots (2.1)$$

where  $T_g^\infty$  is the  $T_g$  at the infinite molecular weight;  $K$  is a constant representing the excess free volume of the end groups for the polymer chains;  $\overline{M}_n$  is the number average molecular weight.

The  $T_g^\infty$  and  $K$  values for PLLA and PDLLA are around 57-58°C and 55000-73000, respectively [11]. The  $T_g$  value of PLA increases with the molecular weight and the chain regularity, i.e. PLA containing higher L-lactide shows higher  $T_g$  values (see Figure 2.6) [12].

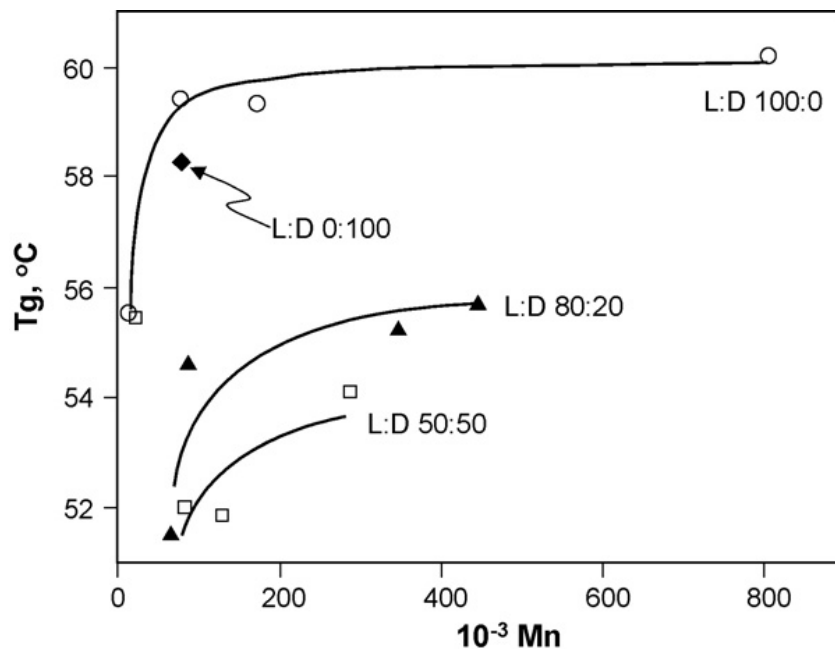


Figure 2.6  $T_g$  for PLA samples of different L/D ratios as a function of molecular weight [12]

The glass transition behaviour of PLA is also influenced by the thermal history of the polymer. For example, PLA that has been quenched from the melting state

showed a tendency to undergo aging at ambient conditions for a couple of days [13], [14]. This phenomenon is known as 'physical aging'. As a result, the polymer becomes more and more rigid when being stored below  $T_g$ , which causes embrittlement of the polymer.

Cai et al. [15] investigated the effect of 'physical aging' on PLA by using DSC analysis. An endothermic peak was observed just above the glass transition temperature, which was associated with relaxation of non-equilibrium structure. The area of the endothermic peak was found to increase with the aging time, as shown in Figure 2.7 (A). This is because the chain relaxation tends toward the equilibrium state after being aged. They also showed the rate of 'physical aging' increased with the increase of aging temperature when it was in the range between room temperature and  $T_g$ . However, when the aging temperature was above  $T_g$ , the endothermic peak disappeared indicating that 'physical aging' did not occur when the temperature was higher than  $T_g$  (see Figure 2.7 (B)).

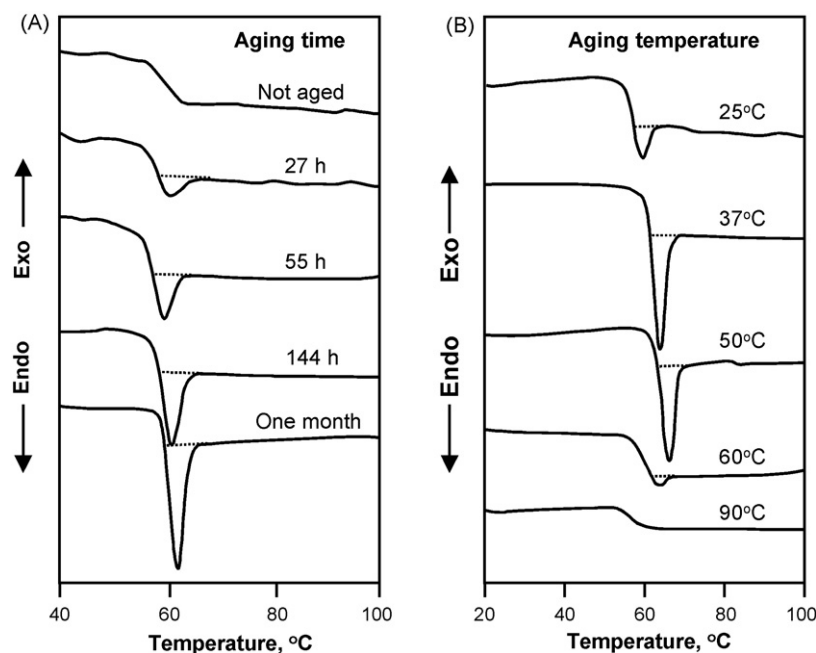


Figure 2.7 Effect of aging temperature and time on thermal properties of PLA samples: (A) DSC scans of PLA aged at room temperature for different periods of time; (B) DSC scans of PLA aged at different temperatures for 24 hours [15]

The 'physical aging' effect of PLLA is dependent not only on the aging temperature, but also on the molecular weight [13]. The extent of aging increases with the decrease of the molecular weight, since the increased chain ends can possess higher motional freedom than the internal chain segments.

### 2.1.3.2 Crystallisation behaviour

#### 2.1.3.2.1 Effect of optical purity on crystallinity

PLA can be either amorphous or semi-crystalline depending on the stereochemistry of the polymer and its thermal history. The effect of chain stereoregularity on the crystallinity of PLA was investigated by Tsuji and Ikada [16], who observed that the crystallinity of the PLA increased with the increasing of its optical purity. When the optical purity became lower than 76%, the polymer could no longer crystallise. Sarasua et al. [17] also observed similar results and reported that PLA with an optical purity below 43% did not have crystallisability.

Optical purity (OP) is a comparison of the optical rotation of a pure sample of unknown stereochemistry versus the optical rotation of a sample of pure enantiomer. It is proportional to the stereo-regularity of a polymer. OP can be calculated by means of the rotatory power  $[\alpha_L^{25}]$  from the following equation:

$$OP = \frac{[\alpha_L^{25}]}{[\alpha_L^{25}]_0} \times 100\% \dots\dots\dots (2.2)$$

where  $[\alpha_L^{25}]_0$  is the rotatory power of the 100% optical pure PLLA [17].

Different thermal treatments of semi-crystalline PLA samples result in different crystallisation behaviours. As shown in Figure 2.8, the DSC curves of PLLA that had been water-quenched or air-cooled shows a clear exothermic cold crystalline peak at about 110 °C. Whereas, PLLA that had been annealed at longer time did not exhibit a crystallisation peak in DSC, since the long-time annealed sample had a very high degree of crystallinity [18].

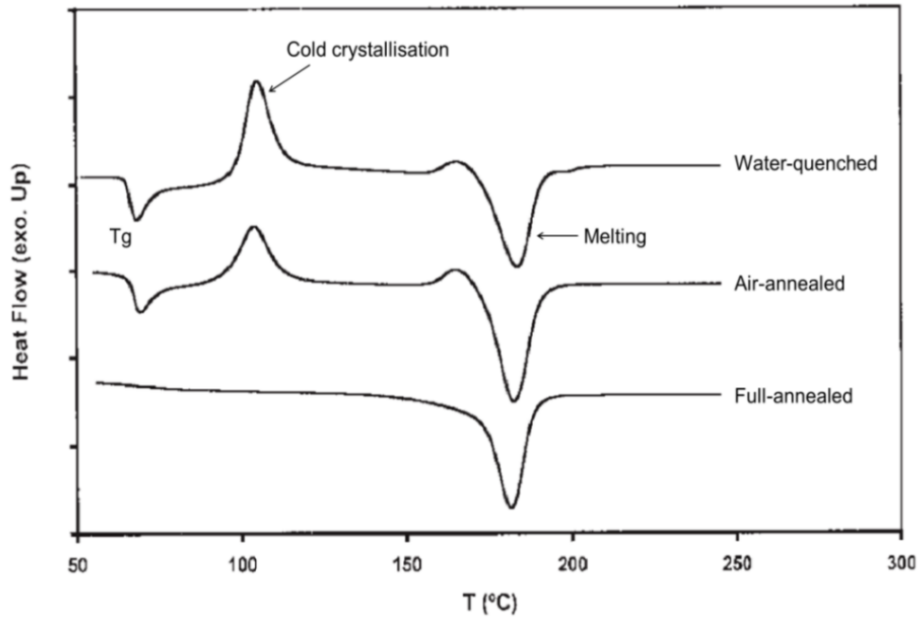


Figure 2.8 DSC scans of melt crystallised PLLA sheet obtained by water-quenching; air-annealing (cooled from 220°C to room temperature in 5 min) and full-annealing (cooled from 220°C to room temperature in 105 min) [18]

Cooling rate of the annealing process has a significant effect on the size and morphology of the spherulite crystals, i.e. slow cooling results in large spherulite sizes and fast cooling results in small sized spherulites [8], [9], [19].

### 2.1.3.2.2 Measurement of crystallinity by DSC

The most common way to measure the degree of crystallinity is by using differential scanning calorimetry (DSC). Figure 2.9 shows a typical DSC scan of semi-crystalline polymers.

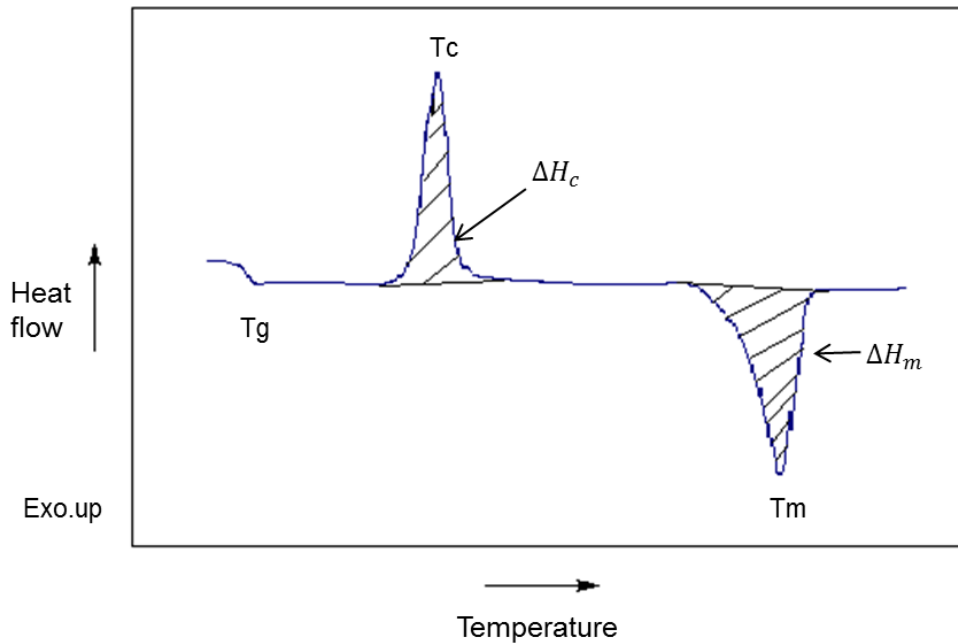


Figure 2.9 A typical DSC trace for semi-crystalline polymers

The degree of crystallinity can be calculated from the heat of fusion ( $\Delta H_m$ , the area of the melting peak) and heat of crystallisation ( $\Delta H_c$ , the area under the cold crystallisation peak):

$$\text{Crystallinity (\%)} = \frac{\Delta H_m - \Delta H_c}{93.1 \text{ J/g}} \times 100 \dots\dots\dots (2.3)$$

where 93.1 J/g is the heat of fusion for PLA with 100% crystallinity [20].

### 2.1.3.2.3 Crystallisation forms

PLA has three forms of crystals ( $\alpha$ ,  $\beta$ ,  $\gamma$  crystals) based on different crystallisation conditions. The most stable crystal modification is the  $\alpha$ -crystal, which can be formed from melt, solution, or cold crystallisation of PLA under normal conditions. The structure of  $\alpha$ -crystals is pseudo-orthorhombic with the chains in a  $10_3$  helical conformation, in which two chains interact in an orthorhombic unit cell [21].  $\beta$ -crystal modification was firstly found by Eling et al. [22] from melt-spun and solution-spun PLA fibres. The structure of the  $\beta$ -form crystal has a left-handed  $3_1$  helical conformation [23], [24], which can be formed by stretching of  $\alpha$ -crystals at high temperature and high drawing ratio [25], [26]. The  $\gamma$ -crystal is the most recently observed structure, which has two antiparallel helices packed in an orthorhombic unit-cell as firstly observed by Cartier et al. [27].

Recently, a new crystal modification,  $\alpha'$ -form, was proposed by Zhang et al. [23], who produced crystalline PLLA at a relatively low crystallisation temperature (80°C).  $\alpha'$ -crystal has a  $10_3$  helical chain conformation, like the  $\alpha$  crystal, but has relatively loose lateral packing of the helical chains. It is found that the thermal stability of  $\alpha'$ -crystal was not as good as that of  $\alpha$ -crystal due to the larger lattice dimension and weaker interchain interaction [23], [28]. Pan et al. [29], [30] investigated the effect of the annealing period and temperature on the crystalline phase transition in PLLA and found that  $\alpha'$ -crystals can transform into  $\alpha$ -crystals via annealing process. During the phase transition, the molecular chain conformation readjusted and the unit cell packing changed to a more energetically favourable state.

The melting temperature ( $T_m$ ) of PLA is related to the crystal forms of the polymer. An occurrence of a double melting peak has been observed in PLLA in many studies [25], [26], [29]–[31]. The mechanism proposed to explain double melting is melt-recrystallisation. It suggests that the appearance of low-temperature and high-temperature endotherm peaks are attributed to the melting of the  $\alpha$ -crystals that was formed at  $T_c$  and some crystals formed through the melt-recrystallisation, respectively. The main melting peak is the high-temperature peak (in the range of 173–178°C), which corresponds to the melting of  $\alpha$ -crystals in PLLA. In addition, the melting behaviour is also related to the stereo-regularity of the polymer. Lim et al. [8] reported that the maximum practical obtainable  $T_m$  for stereochemically

pure PLA (either L or D) is around 180°C with an enthalpy of 40-50 J/g. While the typical  $T_m$  values for PLLA is in the range of 173-178°C [5].

### 2.1.3.3 Rheological properties

The rheological properties of PLA have a profound effect on its melt processing. PLA melts behave as pseudoplastic (shear thinning) fluid, i.e. the melt viscosity decreases significantly as the shear rate increases. The melt viscosity of PLA is dependent on the average molecular weight, crystallinity, the amount of plasticiser, shear rate, and processing temperature. The relation is commonly described by the power law model [32], as expressed below:

$$\eta = m\dot{\gamma}^{n-1} \dots\dots\dots (2.4)$$

where  $m$  is the consistency factor;  $\dot{\gamma}$  is shear rate;  $n$  is power law index ( $n > 1$  dilatant;  $n = 1$  Newtonian;  $n < 1$  pseudoplastic).

The melt viscosities of both amorphous and semi-crystalline PLA have been studied by Fang and Hanna [32], who reported that semi-crystalline PLA exhibited higher shear viscosity than the amorphous PLA due to the difference in stereo-regularity of the molecular structure. For both types of PLA, the shear viscosities reduced with increasing processing temperature and shear rate.

It has been reported that high molecular weight PLA ( $M_w \approx 100,000 - 300,000$  Da) had melt viscosities between 500 and 1000 Pas, at shear rates of 10-50  $s^{-1}$  [6]. Cooper-White and Mackay [33] reported that low molecular weight PLA ( $M_w \approx 40,000$  Da) showed Newtonian fluid behaviour at typical shear rates of extrusion. They also proposed that the zero-shear viscosity ( $\eta_0$ ) of PLA melt was dependent on the molecular weight ( $M_w$ ) to the power law exponent ( $\alpha$ ) of 4.0 instead of the theoretical value of 3.4, which exists for most polymer melts in the Mark-Houwink equation, as shown below:

$$\eta = K(M_w)^\alpha \dots\dots\dots(2.5)$$

where  $\eta$  is viscosity,  $K$  is a constant depending on polymer type,  $M_w$  is molecular weight,  $\alpha$  is the power law exponent.

Dorgan and Williams [34] reported that  $\eta_0$  of linear PLLA was dependent on  $M_w$

to  $\alpha$  of 4.6, which is also higher than the theoretical value of 3.4. This is probably due to the steric hindrance effect, as a result of excessive coil expansion produced by possible chemical shift difference within and between isotactic PLLA polymer chains [33].

#### **2.1.3.4 Processing of PLA**

The main conversion method for PLA is based on melt processing. PLA is a highly versatile thermoplastic, which can be made into different grades for a comprehensive range of applications. The processability of PLA is greatly influenced by various polymer properties, such as thermal stability, melting and crystallisation behaviour of the polymer [35].

PLA can be melt processed in many ways depending on the specific demands on the final products. Conversion methods for processing PLA products include injection moulding, stretch blow moulding, film and sheet casting, thermoforming, and fibre spinning. Lim et al. [8] reviewed various processing technologies for PLA in detail. It is reported that the processing conditions, such as processing temperature, shear rate, residence time, and moisture content in the polymers and atmosphere, are crucial to the quality of the final end products in melt processing [35]. In addition, before processing PLA must be dried sufficiently to prevent excessive hydrolysis during melt processing since the polymer can absorb moisture during storage.

Injection moulding is commonly used for the manufacture of articles, which are complex in shape and require high dimensional precision. However, injection moulded PLA articles are relatively brittle due to the rapid physical aging of the polymer [8]. Accordingly, increasing the crystallinity of the polymer can reduce the aging effect, since the 'crosslinking' effect of the crystalline domains can retard polymer chain mobility. In addition, process parameters, such as mould temperature, packing pressure, cooling rate and post-mould cooling treatment, have significant effect on the aging behaviour of PLA subsequent to injection moulding. Injection moulded amorphous PLA articles are usually intended for further processing, such as stretch blow moulding.

The injection stretch blow moulding (ISBM) technique provides biaxial oriented products with much improved physical and barrier properties compared with the injection moulding process. The molecular orientation induced during the ISBM process decreases the effect of aging by stabilising the polymer free volume. In addition, the crystallites produced during strain-induced crystallisation also reduce the aging effect, and thereby prevent brittleness of the product due to the crosslinking effect of the crystallites [8].

Cast film extrusion has been widely used to produce PLA sheets and films. The difference between a sheet and a film is in their stiffness and flexibility, which is dependent on the thicknesses (e.g. films are typically  $< 0.076$  mm in thickness, while sheets are 0.25 mm or even thicker). In this technique, PLA melts are extruded through a die and quenched on cool polished chrome rollers, which is usually a three-roll stack. A horizontal roll stack configuration is preferred for PLA due to its low melt strength. The roller temperature is usually between 25°C and 50°C in order to avoid the condensation of lactide monomers and the slippage of the web on the rollers [36].

Thermoforming is commonly used to produce PLA containers, such as disposable cups, single-use food trays and blister packaging. During the process, extruded PLA sheet is heated below its melting point and forced against the mould to form the shape into the final product. Then the product is removed off the mould before cooling. Before thermoforming, the extruded PLA sheets are relatively brittle at room temperature. However, orientation takes place during the thermoforming process, which can bring enhanced toughness to the final products.

Commercial PLA fibres are produced by spinning from the melt or solution. Since the disposal of solvent is an environmental issue, the solution spinning technique is only really suitable for lab scale, whereas melt spinning technique is used for industrial scale-up. In the first stage of melt spinning, PLA is heated above its melting point and then extruded through the spinneret before cooling in air. In the second stage, the fibres undergo hot drawing. The filament is pulled down by a take-up roll to provide orientation, which is able to increase the tenacity and stiffness of the fibres. During the hot draw process, the degree of crystallinity of the fibres increases with spinning velocity.

It should be noticed that PLA can be thermally degraded during its melting processing. Thermal degradation of PLA is mainly caused by: (a) hydrolysis by trace amounts of water; (b) zipper-like depolymerisation; (c) oxidative, random main-chain scission; (d) intermolecular transesterification to monomer and oligomeric esters and (e) intramolecular transesterification resulting in the formation of monomer and oligomer lactides of low Mw [35]. Therefore, the temperature of the melting processing has to be strictly controlled. It is reported that when the temperature is above 200°C, PLA could be degraded through intra and intermolecular ester exchange, cis-elimination, radical and concerted non-radical reactions [37].

#### **2.1.3.5 Mechanical properties**

Mechanical properties of PLA are dependent on the molecular weight, the degree of crystallinity, and the stereochemical composition of the polymer [9].

It is reported that the impact strength and Vicat softening temperature of PLA increased with increasing molecular weight and crystallinity. Modulus and tensile strength of PLA reach the greatest values when the viscosity-average molecular weight of the polymer was higher than 55,000 g/mol [6]. Many researchers have studied the effects of stereochemistry and crystallinity on the mechanical properties of PLA [6], [9], [38]. Table 2.1 shows the mechanical properties of different types of PLA. It is observed that annealed PLLA had higher tensile strength than quenched PLLA due to the high stereo-regularity of the polymer chains. The annealed PLLA also exhibited a remarkable increase in impact resistance because of the crosslinking effects on the crystalline domains formed during annealing [6]. PDLLA, a fully amorphous polymer, exhibited the lowest values in tensile strength, modulus and impact resistance compared with PLLA samples, indicating that the stereo-regularity had significant effects on the mechanical properties of PLA [38].

Table 2.1 Effects of stereochemistry and crystallinity on the mechanical properties of PLA [6], [9], [38]

	<b>Quenched PLLA (Mw=66000)</b>	<b>Annealed PLLA (Mw=66000)</b>	<b>PDLLA (Mw=114000)</b>
Tensile strength (MPa)	59	66	44
Elongation at break (%)	7.0	4.0	5.4
Modulus of elasticity (MPa)	3750	4150	3900
Yield strength (MPa)	70	70	53
Flexural strength (MPa)	106	119	88
Notched impact strength (J/m)	26	66	18
Unnotched impact strength (J/m)	195	350	150
Rockwell hardness	88	88	76
Heat deflection temperature (°C)	55	61	50
Vicat penetration (°C)	59	165	52

Tensile strength and elastic modulus of poly(98%L-lactide) and poly(94%L-lactide) films was determined by Auras et al. [9], who found that PLA with higher L-lactide content exhibited higher tensile strength. The tensile strength value for these PLA films was found to be similar to polystyrene (PS), but lower than polyethylene terephthalate (PET) under the same testing conditions as reported in the literature.



## 2.2 Polymer/clay nanocomposites

### 2.2.1 Structure and composition of montmorillonite clay

Montmorillonite (MMT) is a layered silicate clay, which belongs to the 2:1 layered phyllosilicate family. Its crystal structure consists of an aluminium or magnesium hydroxide octahedral sheet, which is sandwiched between two silicon oxide tetrahedral sheets, as shown in Figure 2.11. The layer thickness of each platelet is nearly 1 nm and the space between two layers is less than 1 nm. The lateral dimension of these layers varies from 30 nm to several microns depending on the particular layered silicate [41], [42].

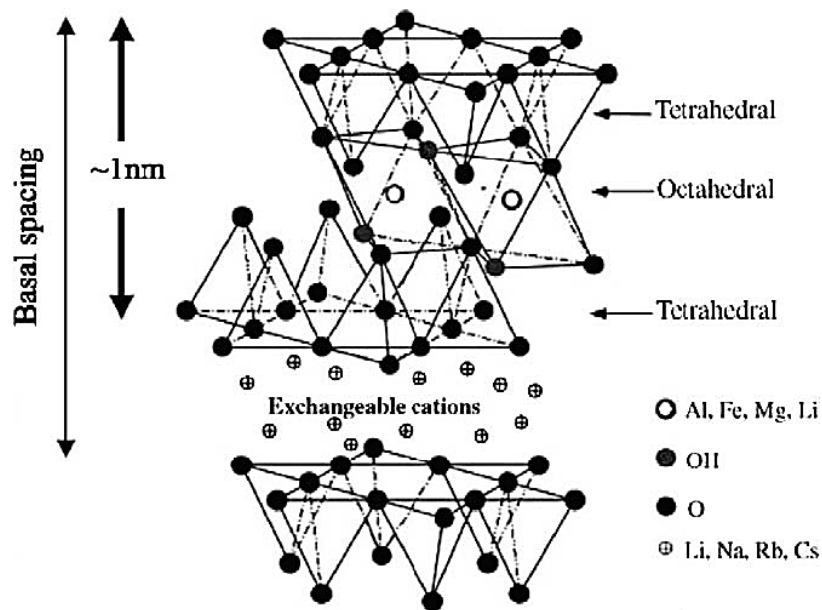


Figure 2.11 Crystal structure of montmorillonite clay [2]

The stacking of the silicate layers causes a regular van der Waals gap between the layers, known as 'interlayers' or 'galleries'. Isomorphic substitution of the tetrahedral or octahedral cation (e.g. the substitution of  $\text{Al}^{3+}$  with  $\text{Mg}^{2+}$  or  $\text{Fe}^{2+}$  with  $\text{Li}^+$ ) yields negative charges that are counterbalanced by alkali and alkaline-earth cations situated inside of the galleries. The negative charges created by tetrahedral substitution are located on the surface of the silicate layers, which is more interactive with the polymer chains in comparison with octahedral substitution [2].

### 2.2.2 Properties of montmorillonite clay

Montmorillonite has been used as reinforcement for many polymers. There are two important characteristics for the clay: 1) the ability of the clay galleries to delaminate and 2) the possibility to modify their surface chemistry with organic and inorganic cations [2], [42]. These two characteristics are inter-related and influence the miscibility of layered silicate with the polymer matrix.

The layered silicate contains hydrated  $\text{Na}^+$  and  $\text{K}^+$  ions, which are only compatible with hydrophilic polymers, for example poly(vinyl alcohol) and poly(ethylene oxide). To make the layered silicate miscible with other polymers, the hydrophilic silicate surface must be modified to organophilic, i.e. so-called organically modified layered silicate. This can be produced by ion exchange reactions with cationic surfactants that include primary, secondary, tertiary and quaternary alkylammonium or alkylphosphonium cations. The presence of alkylammonium or alkylphosphonium cations in the organosilicates can lower the surface energy of the inorganic reinforcement and improve the wetting characteristics of the polymer matrix, thus resulting in larger interlayer spacing between silicate layers. In addition, the functional groups of the alkylammonium or alkylphosphonium cations can react with the polymer matrix and strengthen the interface between the clay and the polymer matrix [42]–[44].

Different commercial grades of organically modified montmorillonite have different surfactant coatings and hence different interplanar spacings. Cloisite 20A is modified by dimethyl dehydrogenated tallow quaternary ammonium chloride at a loading of 95 meq/100 g and has a d-spacing of 2.42 nm. Whereas, Cloisite 25A is modified by dimethyl dehydrogenated tallow 2-ethylhexyl quaternary ammonium at a level of 95 meq/100 g, and its d-spacing is 1.86 nm. Cloisite 30B is modified by methyl tallow bis-2-hydroxyethyl quaternary ammonium chloride at a loading of 90 meq/100 g, and has d-spacing, 1.85 nm. Finally, Cloisite 93A is modified by methyl dehydrogenated tallow ammonium at 90 meq/100 g loading, and has a d-spacing of 2.36 nm. The choice of grade has been found to affect permeability results [7].

### **2.2.3 Montmorillonite clay reinforced polymer nanocomposites**

Polymer/clay nanocomposites are two phase systems, which consist of a polymeric matrix and nano-fillers dispersed in the matrix. The most frequently used inorganic fillers in polymer nanocomposites belong to a family of 2:1 phyllosilicates, which have a sheet silicate structure. Montmorillonite, hectorite and vermiculite are amongst the most commonly used fillers in polymer-clay nanocomposites [42].

The preparation of a nanocomposite requires good dispersion of the layered silicate in the polymer matrix at the nano-meter scale. The excellent performance of montmorillonite clay as a reinforcement in the matrix is determined by its high aspect ratio and the large surface area of the clay particles. Coating with surfactant, such as quaternary ammonium salts, helps to improve compatibility and hence provide a strong interfacial interaction between the clay and polymer chains, thus contributing to good reinforcement and good barrier properties [41], [45]–[51].

There are three types of morphologies for nanocomposites based on the degree of the clay dispersion: aggregated, intercalated and exfoliated (see Figure 2.12). In the aggregated structure, the clay tactoids are well distributed in the polymer matrix, but the single clay layers are not delaminated. In the intercalated structure, the clay tactoids are delaminated to some extent but remain ordered: thus polymer chains can diffuse into the galleries between them. In the exfoliated structure, the clay tactoids are completely broken apart into single layered platelets, which are homogeneously dispersed in the matrix. The exfoliated structure is often the most desirable state as it can provide excellent thermal and mechanical properties at very low clay contents [42]. However, most polymer nanocomposites are in a state between intercalated and exfoliated [2]. Due to the unique structure, polymer nanocomposites have been found to have advantages compared with the neat polymer matrix, such as improved mechanical properties and barrier properties. The development of polymer nanocomposites has become of great interest in packaging applications.

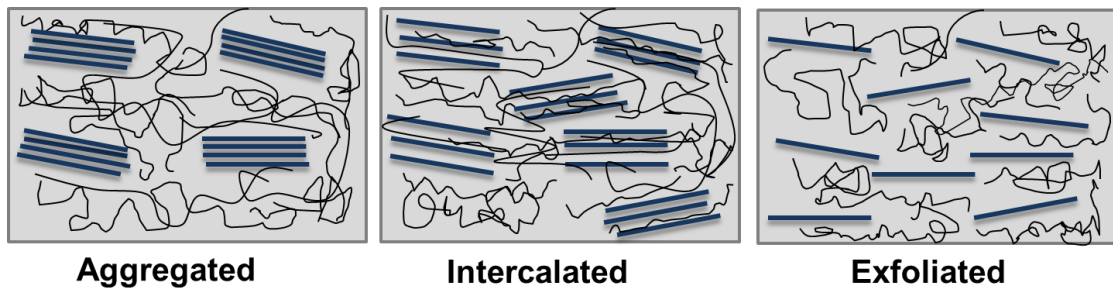


Figure 2.12 Schematic diagrams of three morphologies of polymer/clay nanocomposites

#### 2.2.4 Preparation of polymer/clay nanocomposites

The main preparation methods for making films or sheets of polymer/clay nanocomposites are melt processing and solution casting. Melt processing is arguably the more practical and realistic process because it is the process suitable for commercial production of thermoplastic nanocomposites. The drawbacks of this technique are its dependence on the processing parameters (temperature, screw speed, etc.) and the necessity for favourable interactions between the clay and polymer. Also, many studies have shown that exfoliated nanocomposites are only achieved with MMT additions up to 5 wt.% [52]. The shear stress exerted during melt processing is advantageous in dispersing the clay tactoids but may be detrimental in breaking up the larger clay particles and thus reducing their aspect ratio.

Solution casting is suitable in the laboratory when using small quantities of materials. However, it is challenging for industrial scale-up due to environmental pollution and cost issues associated with the handling and disposal of solvents. It also has the drawback of requiring a specific solvent to achieve intercalation or exfoliation. For example, Giannakas et al. [53] produced PS nanocomposites by a solution casting method using different solvents ( $\text{CCl}_4$  and  $\text{CHCl}_3$ ). They reported that samples prepared with  $\text{CHCl}_3$  showed an intercalated nanocomposite structure, whereas samples prepared with  $\text{CCl}_4$  were exfoliated. This was reflected in the barrier properties of the materials. At a clay content of 10 wt.%, samples prepared from  $\text{CCl}_4$  showed a decrease in water vapour

permeability of 54%, whereas samples prepared from  $\text{CHCl}_3$  exhibited a reduction of 44% compared with pure PS samples.

In a review paper by Tan and Thomas [7] it was found that on comparing the relative reductions in water permeability through polymer / clay nanocomposites prepared by the two different methods (melt processing and solution casting), it transpires that neither method gives significantly better results than the other one.

A third preparation method is in-situ polymerisation. The layered silicate is swollen within the monomer liquid or a monomer solution before polymerisation is initiated. The onset of the reaction can cause polymer chains to grow within the clay gallery and therefore force intercalation or exfoliation to take place [42]. However, this process suffers from the disadvantage that a suitable monomer is not always available [54]. Only one study by Chien and Lin [55] used in-situ polymerisation to prepare poly(vinyl acetate) / MMT nanocomposite film. In this case emulsion polymerisation followed by solution casting was used and resulted in a 90% reduction in permeability, albeit at a 10 wt.% clay addition level. The filler particles in this nanocomposite were found to have a very high aspect ratio.

Some good results using in-situ polymerisation have also been reported in a recent review on gas barrier properties of polymer/clay nanocomposites [54]. Dai et al. [56] prepared epoxy resin / MMT  $\text{Na}^+$  nanocomposites by in-situ thermal ring-opening polymerisation and reported that the oxygen permeability reduced by 86% at a clay loading of 7 wt.%. Also, the  $\text{CO}_2$  permeability of PCL / Cloisite 30B nanocomposites produced from in-situ polymerisation showed a reduction of 68.5% at a clay loading of only 3 wt.% [57].

## 2.3 Barrier properties

### 2.3.1 Barrier properties of polymer

#### 2.3.1.1 Theory, Definitions and units

The fundamental principles describing the permeation of gases or vapours through polymer films have been discussed in numerous publications [58]–[64]. Permeation across a polymer film or coating involves both solubilisation of the penetrant molecule into the polymer matrix and diffusion through it [58], [59].

Fick's first and second laws describe diffusion in many polymer systems. They are given in equations (2.5) and (2.6) below:

$$J = -D(c) \frac{dc}{dx} \dots\dots\dots(2.5)$$

$$\frac{dc}{dt} = \frac{d}{dx} \left[ D(c) \frac{dc}{dx} \right] \dots\dots\dots(2.6)$$

Here, J represents the amount of penetrant moving through unit area per unit time (i.e. the flux), c is concentration, x is the direction of diffusion and D is the diffusion coefficient [58].

The flux can be described by equation (2.7), if there is a linear concentration gradient under steady state conditions.

$$J = D \frac{(c_1 - c_2)}{l} \dots\dots\dots(2.7)$$

Here, l is the thickness of the film, and c<sub>1</sub> and c<sub>2</sub> represent the penetrant concentrations at the two film surfaces. However, rather than measuring concentration in the surfaces of the film, it is usually easier to measure the partial pressures of the vapour or gas on either side of the film. Hence flux is more often represented by equation (2.8).

$$J = P \frac{(p_1 - p_2)}{l} \dots\dots\dots(2.8)$$

Here, p<sub>1</sub> and p<sub>2</sub>, are the vapour pressures on either side of the polymer film. P is the permeability coefficient, which is the rate per unit area at which gas or vapour moves through unit thickness of the film under a single unit of pressure difference [58], [59].

The concentration of gas or vapour in the polymer film surface is related to its vapour pressure in the gaseous state by means of the solubility coefficient (S),

as given in equation (2.9).

$$c = S.p \dots \dots \dots (2.9)$$

A relationship is derived between the permeability coefficient (P), diffusion coefficient (D) and the solubility coefficient (S) by combining equations (2.7), (2.8) and (2.9):

$$P = D.S \dots \dots \dots (2.10)$$

This simple and well known equation shows that permeability is the product of diffusivity and solubility [58]–[60]. Equation (2.10) provides a good basis for a conceptual understanding of the basic principles of permeability through polymer films. Once the penetrant molecule has adsorbed onto the surface of the polymer, it must dissolve in the polymer matrix and then diffuse down a concentration gradient through the film, before desorbing from the opposite surface. Either the diffusivity, D, or the solubility, S, may be the rate controlling process. Meares [60] first reported that the permeation of gases, such as CO<sub>2</sub> and O<sub>2</sub>, through polymer films is usually dominated by the diffusion coefficient. However, it is found that the water permeability through polymer films is likely to be controlled by the solubility of water in the polymer [59]. Hence, highly polar polymers have poor water barrier properties because of the high solubility of water in these polymers. On the other hand, non-polar polymers, like polyethylene, have very good water barrier properties because water has a low solubility in hydrophobic polymers.

The units of permeability require some consideration. As defined in equation (2.8), permeability has the following dimensions:

$$P = \frac{(amount\ of\ permeant) \times (film\ thickness)}{(area) \times (time) \times (pressure\ drop\ across\ film)}$$

This applies to the transport of most gases through most polymer films. However, for organic vapours and water, permeability can vary with both pressure drop and the thickness of the film. Hence, in these cases, data are usually expressed in terms of a transmission rate, Q, which has the dimensions:

$$Q = \frac{(amount\ of\ permeant) \times (film\ thickness)}{(area) \times (time)}$$

It is important to quote both the test temperature and the vapour pressure applied [61].

### 2.3.1.2 Factors affecting PLA barrier properties

Polymer structures have significant effect on the barrier property of the polymer. As discussed in the previous section, non-polar polymers tend to have good barrier to water but poor gas barriers, whereas, polar polymers usually have excellent gas barrier but very sensitive to water [59].

It is generally agreed that the barrier properties of polymer membranes are related to crystallinity, as the impermeable crystallites act as barriers to the permeation path of gases and water vapour molecules [65]–[67]. One of the earliest papers on this was by Michaels et al. [68], who studied diffusion of various gases in glassy and rubbery polyethylene terephthalate in the temperature range 25 to 130 °C. They found that below the glass transition temperature ( $T_g$ ), diffusion was impeded by the presence of crystallites to an extent dependent on the reciprocal of the amorphous volume fraction. The effects of crystallisation polymorphism and crystallinity on the water vapour permeability for PLLA has been studied by Cocca et al. [28], who reported that the water vapour permeability changed slightly at low degrees of crystallinity but suddenly dropped dramatically when the crystallinity reached a certain range between 39% and 40%. This rapid decrease in water vapour permeability was attributed to the change of crystal conformation from  $\alpha'$  crystal to  $\alpha$  crystal.

Tsuji and Tsuruno [69] studied the effect of crystallinity on the barrier property of PLLA and reported that the water vapour permeability of PLLA films decreased rapidly by 43% with increasing the degree of crystallisation from 0 to 20 %. In another study of Tsuji et al. [66], the water vapour transmission rate (WVTR) of PLLA films was found monotonically decreased with the increase of crystallinity from 1-20%, and then became equilibrium as the crystallinity was above 30%. The dependence of WVTR on crystallinity was attributed to the restricted amorphous regions (corresponding to high crystallinity films), which provided higher resistance to water vapour comparing with the amorphous regions in low crystallinity films. Duan and Thomas [19] have modified the Nielsen equation to predict the water vapour permeability of semi-crystalline PLA films by assuming that the spherulites are impermeable spherical particles. In their study, a series of semi-crystalline PLA samples with crystallinity ranging from 0 to 50% was tested and the experimental results of water vapour permeability were found to

fit well with the modified Nielsen model in equation (2.11) (see Section 2.4.3).

In addition, orientation of polymers has been reported to improve their barrier properties. Orientation of polymers by mechanical drawing can promote the chain organisation of both crystalline and amorphous phases and hence prevent the transport of permeant molecules through the polymer [70]. Lasoski and Cobbs [71] studied the role of orientation in water permeability of crystalline polyethylene terephthalate (PET) and reported that the crystalline PET decreased water vapour permeability after being uniaxially and biaxially stretched. Figure 2.13 shows the water permeability of orientated PET films versus film densities. The film density is dependent on the crystallinity of the PET samples. It is found that the differences between the permeabilities of oriented and unoriented samples at the same film densities are greatest at low degrees of crystallinity (10-15%, density of 1.33-1.35) and become gradually less as the degree of crystallinity increases. Until at 40-50% crystallinity (density of 1.38-1.40), no significant differences in permeability value are observed between the orientated and unorientated samples. This indicates that orientation has effect on permeability only for polymers at low crystallinity.

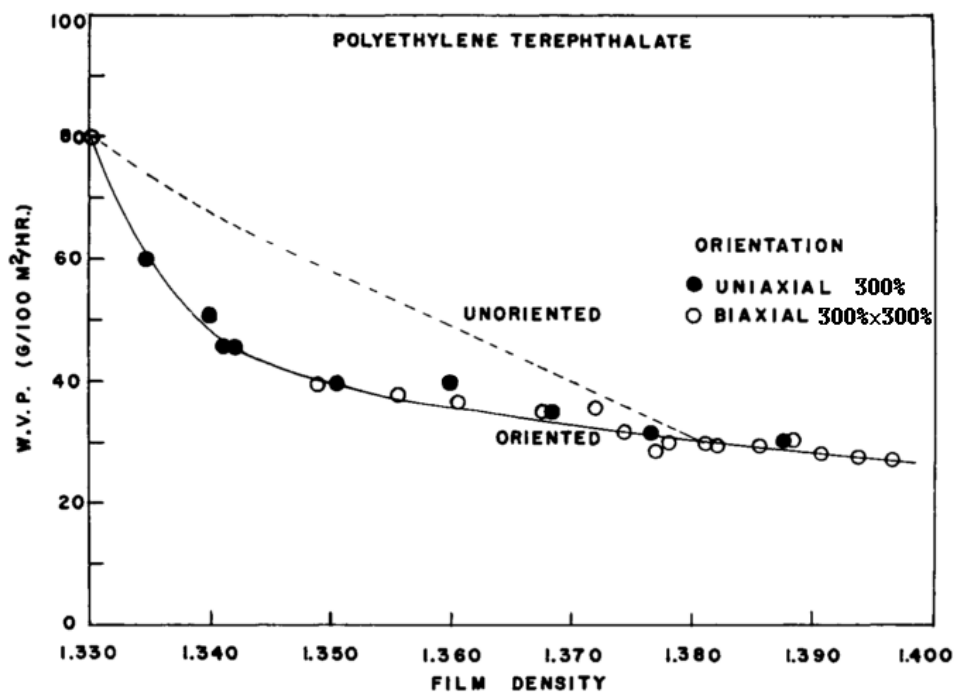


Figure 2.13 Water vapour permeability of oriented PET films versus film density (film thickness = 1 mil)

## 2.3.2 Barrier properties of polymer nanocomposites

### 2.3.2.1 Modelling of Polymer Nanocomposite Permeability

An important success of polymer / clay nanocomposites is the improvement in barrier properties that can be generated. At relatively low additions of nanoclay, it is possible to achieve quite dramatic reductions in permeability to both gases and water vapour. For example, in a study on polyimide-clay nanocomposites, Yano et al. [72] reported a decrease of 90% in water vapour permeability in a polyimide-mica composite with only 2 wt.% of added mica. These researchers demonstrated that the larger diameter of the filler particle, the better the improvement in permeability.

Nielsen [73] first proposed a model for the permeability of filled polymer systems. The model is based on the premise that penetrant molecules have an increased diffusion path because of the presence of impermeable filler particles. Therefore this model is often referred to as the 'tortuous path' model, as shown in Figure 2.14. The assumption is that the filler particles are rectangular platelets that are orientated perpendicular to the direction of diffusion. The Nielsen model is given in equation (2.11), in which  $P$  represents the permeability of the polymer composite,  $P_0$  represents the permeability of the unfilled polymer,  $L/D$  is the aspect ratio (length/thickness) of the filler particles and  $\phi$  is the volume fraction of the filler.

$$\frac{P}{P_0} = \frac{1-\phi}{1+\left(\frac{L}{2D}\right)\phi} \dots\dots\dots(2.11)$$

Despite its simplicity, the Nielsen equation is remarkably successful in predicting the permeability reduction found in polymer / clay nanocomposite systems. For example, it gave accurate predictions of the effect of montmorillonite concentration on the water permeability in polyimide nanocomposites [74]. In a recent study, Duan et al. [75] showed that water vapour transmissions rates through films of poly(lactic acid) / montmorillonite nanocomposites fitted predictions from the Nielsen model. The Nielsen equation has also been used to model the effect of crystallinity on the water vapour permeability of poly(lactic acid) [19].

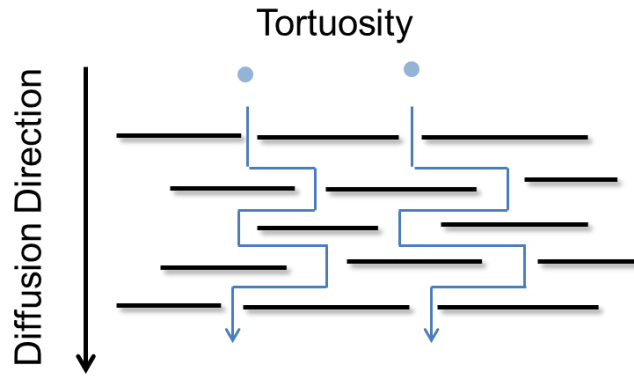


Figure 2.14 Model for the path of a diffusing molecule through a polymer filled with circular or square plate fillers

A review of the various models that have been proposed to predict the permeability of polymer-clay nanocomposites has been published by Choudalakis and Gotsis [2]. They also reviewed some experimental data on gaseous permeability in polymer nanoclay systems and the extent to which the models had been validated. A common factor of most of the models was that relative permeability depended on the aspect ratio, volume fraction and orientation of the filler particles. It was also noted that relative permeability was not dependent on the type of polymer or gas. The authors concluded that the Nielsen model is good at predicting permeability if the geometric parameters of the polymer-clay nanocomposites are known.

In their review, Choudalakis and Gotsis [2] discussed a number of alternatives to the Nielsen model. Equation (2.12) is the model due to Cussler et al. [76], who considered the filler particles (described as flakes) to be arranged in discrete layers with narrow slits separating the particles within each layer.

$$\frac{P}{P_0} = \left(1 + \frac{\alpha^2 \phi^2}{1 - \phi}\right)^{-1} \dots\dots\dots(2.12)$$

In their paper, Cussler et al. [76] define  $\alpha$  as the flake aspect ratio ( $d/a$ ), where  $d$  is half the flake width and ' $a$ ' is the flake thickness. Hence  $\alpha$  is half the aspect ratio ( $L/D$ ) of the Nielsen model (note in the paper by Choudalakis and Gotsis [2], the term  $\alpha$  is sometimes used for the aspect ratio  $L/D$  and sometimes for the half aspect ratio  $d/a$ , which may be a source of confusion).

Another model is that due to Fredrickson and Bicerano [77]. The notation in this

this paper is similar to that of Cussler et al. [76] in that the aspect ratio,  $\alpha$ , is defined as half the platelet width (which in this case is the platelet radius) divided by thickness. The Fredrickson-Bicerano model is given in equation (2.13), where  $k = \pi / \ln \alpha$ , and  $a_1 = (2 - \sqrt{2})/4$  and  $a_2 = (2 + \sqrt{2})/4$ .

$$\frac{P}{P_0} = \frac{1}{4} \left( \frac{1}{1+a_1 k \alpha \phi} + \frac{1}{1+a_2 k \alpha \phi} \right)^2 \dots\dots\dots (2.13)$$

A different approach was taken by Gusev and Lusti [78], who used a finite-element based methodology to derive the model shown in equation (2.14).

$$\frac{P}{P_0} = \exp \left[ - \left( \frac{x}{x_0} \right)^\beta \right] \dots\dots\dots (2.14)$$

In equation (2.14),  $x = \left(\frac{L}{D}\right)\phi$  and  $x_0$  and  $\beta$  are constants that can be fitted to the experimental data.

The models described above all assume that the filler particles are aligned at right angles to the diffusion direction. However, Bharadwaj [79] has described what would happen if the filler particles were oriented in different ways with respect to the diffusion direction. To do this, an order parameter,  $S$ , was inserted into the model. The order parameter is shown in equation (2.15), where  $\theta$  is the angle between the diffusion direction and the normal to the filler particles.

$$S = \frac{1}{2} \langle 3 \cos^2 \theta - 1 \rangle \dots\dots\dots (2.15)$$

It is seen from equation (2.15) that when the filler particles are orientated perpendicular to the direction of diffusion (i.e.  $\theta=0$ ) then  $S=1$ , whereas if the filler particles are orientated parallel to the direction of diffusion (i.e.  $\theta=\pi/2$ ) then  $S=-1/2$ . When there is random orientation, then  $S=0$ .

The order parameter is inserted into the Nielsen equation to allow for orientation, as shown in equation (2.16).

$$\frac{P}{P_0} = \frac{1-\phi}{1+\frac{L\phi}{2D} \left(\frac{2}{3}\right) \left(S+\frac{1}{2}\right)} \dots\dots\dots (2.16)$$

Bharadwaj [79] also considered the state of delamination of the filler particles. In considering the permeability of polymer/clay nanocomposites, it is usually assumed that the nanoclay particles are completely exfoliated. However, this may not be the case and under these circumstances, where aggregation of the

clay platelets occurs due to intercalation without complete exfoliation, then the tortuous path is correspondingly reduced. Nazarenko et al. [80] incorporated the effect of stacking into the Nielsen model, assuming that the stacked layers were aligned perpendicular to the diffusion direction.

In their paper, Choudalakis and Gotsis [2] included a modified Nielsen equation to allow for stacking, as shown in equation (2.17), where N corresponds to the number of clay layers in the stack.

$$\frac{P}{P_0} = \frac{1-\phi}{1+\frac{L\phi}{2DN}} \dots\dots\dots(2.17)$$

When the aggregates are randomly orientated equation (2.17) is converted to:

$$\frac{P}{P_0} = \frac{1-\phi}{1+\frac{1}{3}\frac{L\phi}{2DN}} \dots\dots\dots(2.18)$$

Combining equations (2.16) and (2.17) it is possible to come up with an expression that considers the effects of platelet stacking and orientation in addition to the aspect ratio and volume fraction [2]. That expression is given in equation (2.19).

$$\frac{P}{P_0} = \frac{1-\phi}{1+\frac{L\phi}{3DN}\left(S+\frac{1}{2}\right)} \dots\dots\dots(2.19)$$

Another development of the Nielsen equation is that due to Xu et al. [81], who investigated the effects of clay layers and polymer chain immobility on the barrier properties of polymer nanocomposites. In their model, there is a chain-segment immobility factor ( $\xi$ ) to allow for the effect of polymer chain confinement on barrier properties. This model is given in equation (2.20), where H is the separation gap between adjacent clay platelets. This model predicts a lower relative permeability at clay aspect ratios between 10 and 300 than predicted by other models [73], [77], [78], [82].

$$\frac{P}{P_0} = \frac{(1-\phi)/\xi}{1+\frac{L}{2}\left(\frac{D}{\phi}\right)^{1/2} (D+H)^{-3/2}} \dots\dots\dots(2.20)$$

A further development of the Cussler-Aris model [76] is that due to Lape, Nuxoll and Cussler [83]. In the Cussler-Lape model, the particles are randomly dispersed with infinite length. The flake thickness D is constant and there is a discrete distribution of values of the flake width, w. The relative permeability is given by equation (2.21):

$$\frac{P}{P_0} = \frac{1-\phi}{[1+(\frac{2}{3}(\phi/D \sum_i n_i w_i) \sum_i n_i w_i^2)]^2} \dots\dots\dots(2.21)$$

where  $n_i$  is the number of flakes in a particular width category and  $w_i$  is one-half of the intermediate flake width.

Lu and Mai [84] have proposed a model to estimate the critical volume fraction of clay for minimum permeability in exfoliated nanocomposites. They suggested that in exfoliated nanocomposites the pathway of gas and liquid molecules is a self-avoiding random walk, due to the disordered distribution of exfoliated silicate platelets. The probability ( $p$ ) of a cell acting as a barrier to diffusion was determined via a ‘Kadanoff cell’ simulation. The critical volume fraction ( $\phi_c$ ) of nanoclay for minimum permeability was obtained as a function of the probability ( $p$ ) and the geometric parameters of the clay, as given in equation (2.22), where  $S$  is the orientation parameter of nanoclay platelets as in the Bharadwaj model [79]. Values of  $p$  were taken as 0.38 and 0.72 in two- and three-dimensional models respectively.

$$\phi_c = \frac{3}{2S+1} (L/D)^{-1} p \dots\dots\dots(2.22)$$

The prediction of the critical volume fraction was shown to fit with experimental data of some typical clays (e.g. hectorite, saponite, montmorillonite and mica) from the literature [74], [81], [85], [86].

A different geometric model was developed by Sorrentino et al. [87]. This model is given in equation (2.23), where  $D_c$  and  $D_o$  are the diffusion coefficients of polymer nanocomposite and neat polymer respectively; and  $\beta = \frac{V_s D_s}{\phi D_o} - \frac{V_s + \phi}{\phi}$ , where  $D_s$  and  $V_s$  are the diffusion coefficient and volume fraction of the interface respectively.  $\phi$ ,  $L$ ,  $D$  and  $\theta$  are as previously defined.

$$\frac{D_c}{D_o} = \frac{(1+\beta\phi)}{[(1-\phi)+\phi(\frac{L+2D}{L \sin \theta + 2D \cos \theta})^2]} \dots\dots\dots(2.23)$$

When compared with effective diffusivity generated using random walk simulations, fair agreement was found between predictions from the model and results of numerical simulations. In addition, there was good agreement between the model and experimental data of relative diffusivity of water vapour in exfoliated PCL nanocomposites [88], [89]. Compared with other models, this

model was claimed to be more suitable for describing diffusion behaviour in polymer nanocomposites with high aspect ratio fillers.

Alexandre et al. [90] developed a model for water permeability through certain polymers in which water has appreciable solubility. They considered plasticisation effects of water as well as the possibility of adsorption of water vapour at the polymer/filler interface. This was shown to be relevant for the transport of water through polyamide12 – based nanocomposite films, where it was found that at higher clay contents water permeability no longer decreased but started increasing [90].

These authors modified the tortuosity models of Nielsen [73] and Bharadwaj [79] to take into account not only tortuosity effects (i.e. aspect ratio, crystallinity, immobility factor, recovery parameter) but also a solubility factor and a plasticisation factor. Additionally, the model allows for a change in aspect ratio as a function of volume fraction. The model is expressed by equation (2.24).

$$\frac{P}{P_o} = \frac{1-\beta\phi_i}{\xi_{(\phi)}[1+\phi_i(1+\frac{L(\phi)}{3D})(\frac{V_m}{V_i})^{-1}]} \left[\frac{1-X_c^n}{1-X_c^o}\right]^2 \left[\frac{\gamma'_n}{\gamma'_m}\right]^\varepsilon \dots\dots\dots(2.24)$$

In this equation  $\beta$  is the solubility factor;  $\xi_{(\phi)}$  is the polymer chain-segment immobility;  $V_m$  and  $V_i$  are the velocity of the diffusing molecules in the polymer matrix and that in the interface zone respectively;  $\gamma'_n$  and  $\gamma'_m$  represent the plasticising effect on filled and unfilled polymer;  $\varepsilon$  is the adjustable parameter for the plasticising effect;  $X_c^n$  and  $X_c^m$  are the crystallinity of filled and unfilled polymer.

### **2.3.2.2 Factors affect the barrier properties of polymer nanocomposites**

As discussed in Section 2.3, water has a high solubility in polar polymers and so these polymers have poor water barrier properties, whereas non-polar polymers have good water barrier properties because of the low solubility of water in hydrophobic polymers. However, as discussed in a review paper by Tan and Thomas [7], the reduction in water permeability caused by the addition of clay nanofillers is largely independent of the polymer type: instead it depends mainly on the filler type, concentration and aspect ratio (exceptions to this are polymers, such as PA6 and PA12, which are susceptible to plasticisation effects by water [90]). A similar result has been reported by Choudalakis and Gotsis [2]. In their review of gaseous permeability through polymer nanoclay systems. They concluded that the reduction in permeability 'seems to be independent of the nature of the polymer matrix and the gas species', but depends on aspect ratio, volume fraction and orientation of the filler particles.

Yano et al. [72] synthesized polyimide (PI) / clay nanocomposites from four clay minerals (montmorillonite, saponite, synthetic mica and hectorite). They observed that the improvement in water barrier properties depended on the diameter of the filler particles. Among all the clay minerals, mica was found to be the most effective clay: the water vapour permeability coefficient reduced by 90% with the addition of only 2 wt.% mica in polyimide nanocomposites. In a study on PA6-montmorillonite membranes prepared by melt blending, Picard et al. [91] carried out a detailed analysis of the clay dispersion using both TEM (transmission electron microscopy) and STEM (scanning transmission electron microscopy). They measured the average aspect ratio to be 20. From experimental results on water permeability, they then calculated the theoretical mean aspect ratio from the various models that gave the best fit to their data. The Nielsen model gave a value of 25.5, whereas a somewhat closer value of 17.2 was predicted from the Cussler-Lape model.

In terms of filler concentration, numerous studies have found that the optimum nanoclay content is around 5 wt.% or below. It is discussed by Nguyen and Baird [52] that exfoliated nanocomposites are mostly only achieved with montmorillonite concentrations up to 5 wt.%. Above this value, agglomeration takes place.

## **2.4 PLA nanocomposites**

### **2.4.1 Preparation of PLA nanocomposites**

PLA nanocomposites were first prepared by Ogata et al. [92] in 1997, who dissolved certain amounts of PLLA and dimethyl distearyl ammonium modified MMT in hot chloroform. However, the clay layers were not delaminated, in fact, they existed in the form of tactoids containing less than four silicate layers. This is probably because the clay content in their sample (10 wt.%) was too high to achieve intercalated dispersion. After the first approach, several people successfully produced delaminated layered silicate in PLA by solution casting. For example, Krikorian and Pochan [93] investigated the compatibility of three different kinds of organic modified silicate in PLLA using a solution film casting method, which presented well intercalated clay structures. McLauchlin and Thomas [94] also produced intercalated PLA / MMT nanocomposites by solution casting from chloroform.

Melt compounding is another popular method for the production of PLA / clay nanocomposites. Ray et al. [42] produced PLA nanocomposites by melt compounding of PLA and octadecyl ammonium modified MMT at 190°C followed by melt-extrusion of the mixture [95]. X-ray diffraction (XRD) and transmission electron microscopy (TEM) techniques were used to probe the clay structure and confirmed that the silicate layers were delaminated and randomly dispersed in the PLA matrix. Paul et al. [96] investigated the feasibility of PLA nanocomposite formation by using a melt intercalation technique. In their research, intercalated PLA nanocomposites were obtained and that was confirmed using XRD. Duan et al. [75] have successfully produced intercalated PLA nanocomposite films also using melt compounding followed by compression moulding.

## 2.4.2 Morphology

Generally the morphology of PLA nanocomposite can be established using wide-angle X-ray diffraction (WAXD) and TEM. WAXD is a convenient way to determine the interlayer spacing of the layered silicate. TEM observation provides a qualitative understanding of the internal structure and distribution of clay phases through direct visualisation. Figure 2.15 shows WAXD patterns and the corresponding TEM images of three morphologies in PLA nanocomposites: intercalated, intercalated and flocculated, and exfoliated by Ray et al. [42]. However, it is noticed that the 'exfoliated' TEM image (in Figure 2.15) does not unambiguously show complete delamination of the silicate layers.

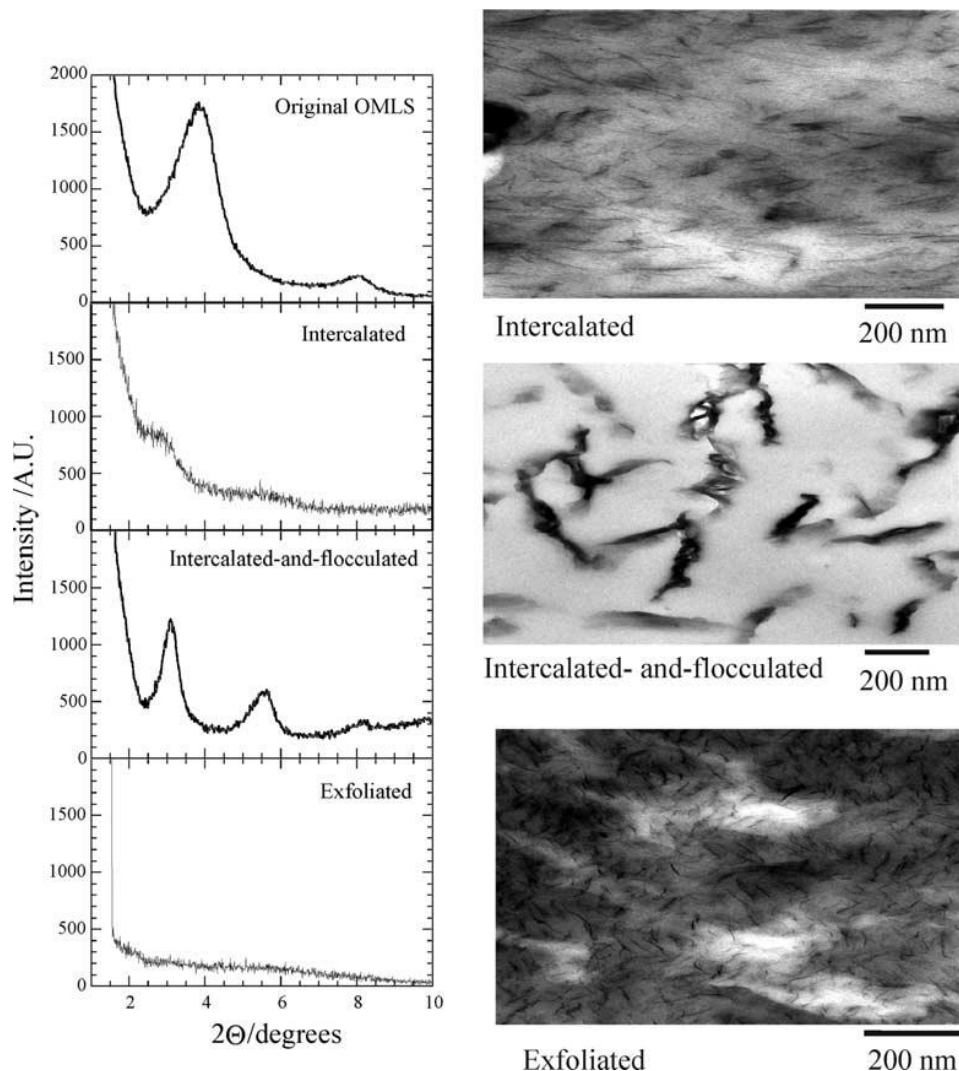


Figure 2.15 WAXD patterns and corresponding TEM images of three different morphologies of PLA nanocomposite [42]

Krikorian and Porchan [93] investigated the morphology of PLA nanocomposites modified by three kinds of montmorillonite clay. Their WAXD and TEM results (see Figures 2.16 - 2.18) showed that the characteristic peak of neat Cloisite 15A corresponded to an interlayer spacing of  $d(001)=3.2$  nm, which was shifted to 3.8 nm in the PLA nanocomposites. The intensity of this intercalated clay peak increased with the clay content. For the Cloisite 25A based nanocomposites, the characteristic peak of the neat organoclay corresponded to a interlayer spacing of  $d(001) = 2$  nm, which was shifted to a higher angle representing a interlayer spacing of  $d(001) = 3.6$  nm (see Figure 2.17.a). With respect to Cloisite 30B, there was no evidence for organoclay basal spacing peak among all the nanocomposite samples (Figure 2.18.a). This implies that all the samples have exfoliated morphology and the clay platelets were evenly distributed in the PLA matrix. The XRD result was supported by TEM in Figure 2.18.b, in which the silicate layers did not aggregate or form intercalated tactoids in the PLLA matrix.

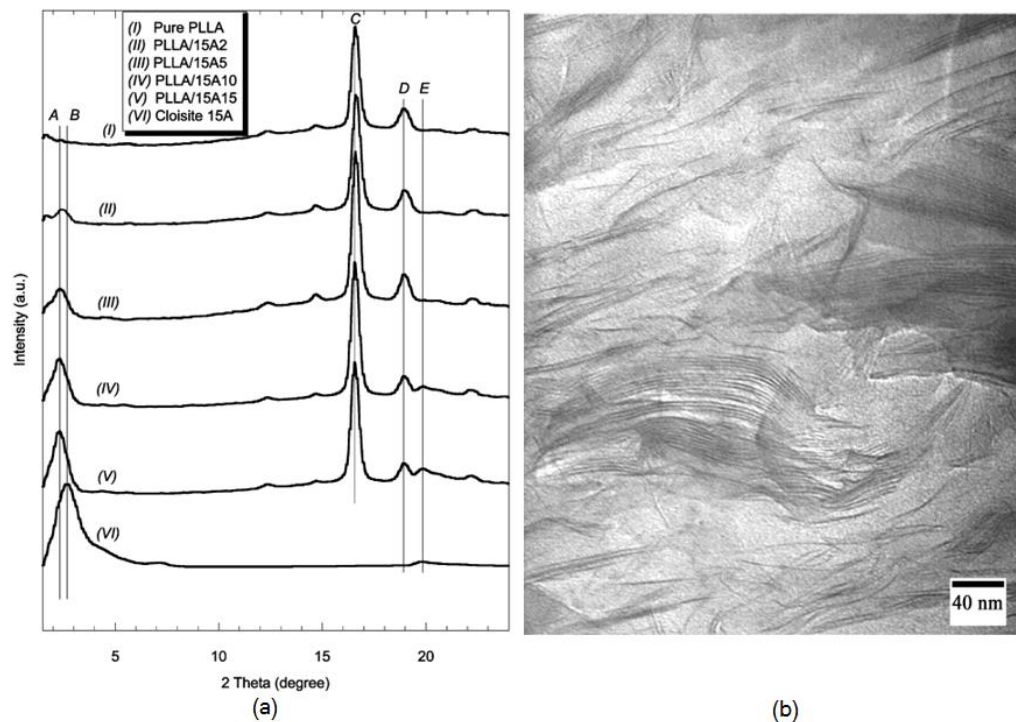


Figure 2.16 a. WAXD patterns for different compositions of neat PLLA and Cloisite 15A; b. TEM image of PLLA nanocomposite sample with 10 wt.% Cloisite 15A [93]

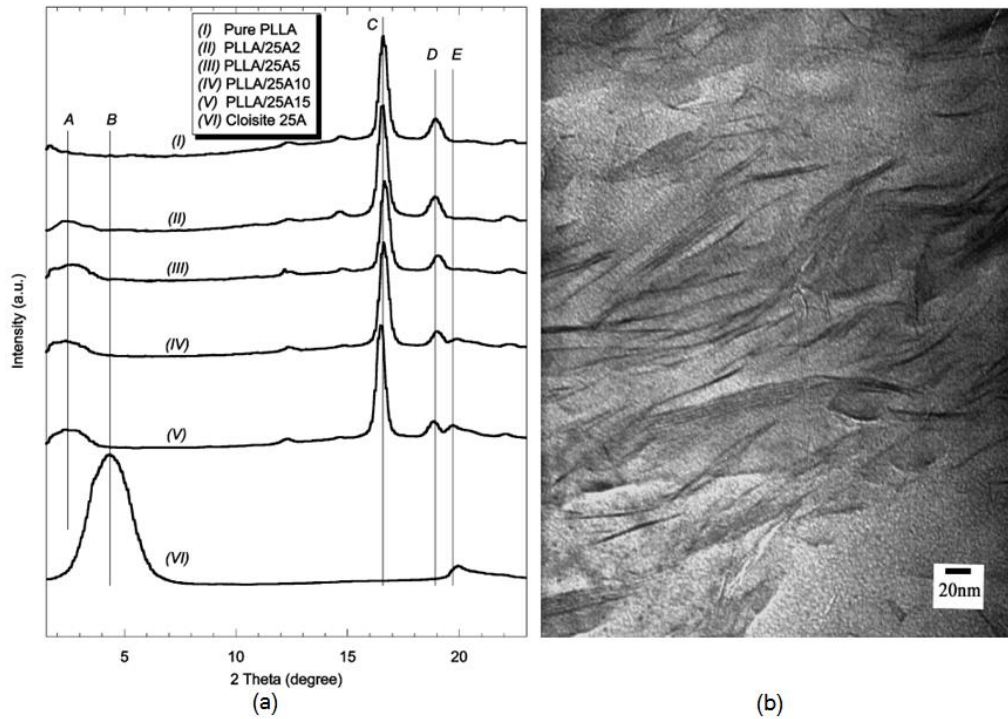


Figure 2.17 a. WAXD patterns for different compositions of neat PLLA and Cloisite 25A; b. TEM image of PLLA nanocomposite sample with 10 wt.% Cloisite 25A [93]

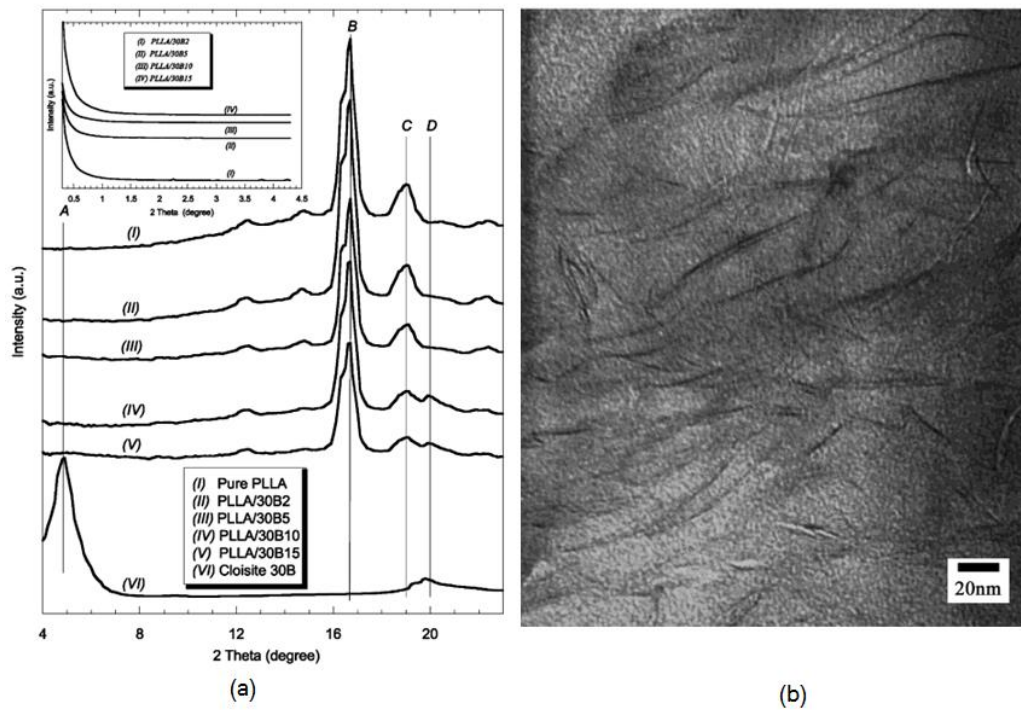


Figure 2.18 a. WAXD patterns for different compositions of neat PLLA and Cloisite 30B; b. TEM image of PLLA nanocomposite sample with 10 wt.% Cloisite 30B [93]

Rhim et al. [97] reported that the initial interlayer spacing of Cloisite 30B and Cloisite 20A were 1.86 nm and 2.41 nm, respectively. The XRD result for the PLA / Cloisite 30B and PLA / Cloisite 20A showed that the d(001) peak of the clay was shifted to a lower angle, as indicated by an increase in the d-spacing to 3.14 nm and 3.24 nm, respectively. McLauchlin and Thomas [94] investigated two kinds of PLA nanocomposites containing cocamidopropylbetaine (CAB) and sodium montmorillonite (MMT), respectively. It was found that the interlayer spacing of MMT organoclay was 1.81 nm and this increased to 3.48 nm in the PLA nanocomposites. The CAB had an interlayer spacing of 1.84 nm, which was expanded to 4.09 nm in the nanocomposite. Duan and Thomas [75] recently reported that Cloisite 30B organoclay has an interlayer spacing of 1.8 nm and that increased to 3.4 nm in their intercalated PLA nanocomposites produce by melt compounding.

### 2.4.3 Oxygen and water vapour barrier properties

The permeability to water vapour and gas is very important for packaging materials. Many researchers [95], [98]–[101] have attempted to incorporate fillers, such as talc, montmorillonite clay, mica, in PLA to improve its gas barrier properties.

Thellen et al. [98] incorporated MMT clay in PLA by melt processing and reported that the PLA nanocomposite showed an increase in the oxygen barrier by 15–48%. The increase in barrier property is dependent on the amount of clay addition. Zenkiewicz and Richert [100] found that the oxygen gas permeability of PLA nanocomposites was reduced by 55% and the carbon dioxide permeability was reduced by 90%. Ray et al. [95], [99] measured the oxygen gas permeabilities of near exfoliated PLA nanocomposites containing 4, 7, 10 wt.% organically modified synthetic mica and 4, 5, 7 wt.% organically modified montmorillonite, respectively. It was found that the oxygen permeability of the PLA nanocomposite declined significantly with the filler loading. The permeability of the mica samples fitted the theoretical line based on the ‘Nielsen model’ with a given aspect ratio of 275 (see Figure 2.19).

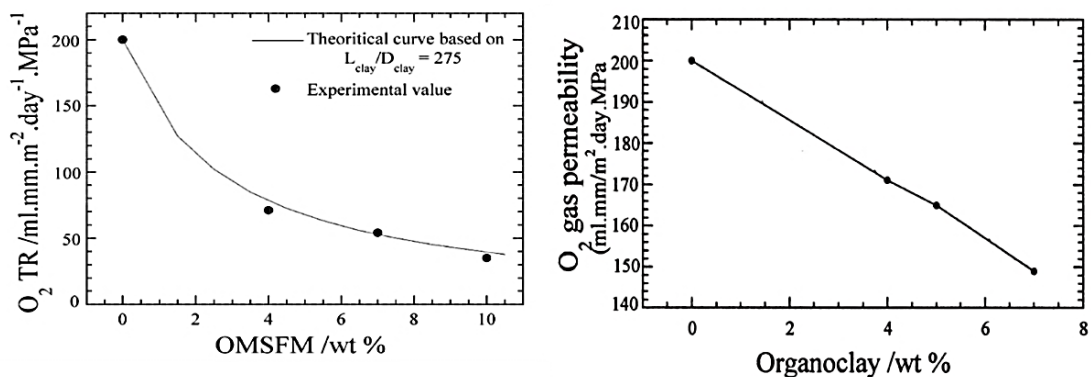


Figure 2.19 Oxygen permeability of PLA / montmorillonite nanocomposites (right), and PLA / synthetic mica nanocomposites (left) [95], [99]

Picard et al. [101] predicted the effect of crystallinity on the oxygen barrier properties of semi-crystalline PLA nanocomposites using the Nielsen model (in the case of L=D), and found a good agreement between the theoretical and experimental permeability for the semi-crystalline PLA films.

There are a limited number of studies on water vapour permeability of PLA nanocomposites. Thellen et al. [98] investigated moisture barrier properties of PLA nanocomposites containing 5 wt.% montmorillonite. It was reported that the PLA nanocomposites exhibit a 40-50% improvement in water vapour barrier, which they attributed to the diffusivity and the water vapour transmission rate of the sample being reduced by water clusters formed at the surface of the clay platelets. Zenkiewicz and Richert [100] investigated the influence of different types of montmorillonite, organic modifier and compatibiliser on the permeability of PLA nanocomposites. They found that the best result was a 60% improvement in water vapour barrier of a PLA nanocomposite containing 5 wt.% nanoclay. Rhim et al. [97] reported that the water vapour permeability of the nanocomposite varied significantly with different types of the nanoclay. The organically modified clay exhibited better water vapour barrier than the natural clay, since the former was more compatible with PLA. The sample containing 13 wt.%, organoclay showed a reduction in water vapour permeability by approximately 67%.

Duan et al. [75] investigated poly(lactic acid) / MMT nanocomposites and found that the water vapour permeability data fitted well with the Nielsen model. In another study, Duan and Thomas [19] modified the Nielsen equation (2.11) to predict the water vapour permeability of semi-crystalline PLA films. They assumed the spherulites were impermeable spherical particles, hence, in equation (2.11)  $L=D$  and the volume fraction ( $\phi_F$ ) is replaced with the degree of crystallinity ( $X_c$ ), then the Nielsen model becomes:

$$\frac{P_{crystalline}}{P_{amorphous}} = \frac{1-X_c}{1+\frac{1}{2}X_c} \dots\dots\dots(2.25)$$

The modified Nielsen model fitted very well with the water vapour permeability of the semi-crystalline PLA samples with crystallinity ranging from 0 to 50%.

#### 2.4.4 Effect of uniaxial and biaxial stretching on PLA and PLA nanocomposites

It is known that orientation can induce crystallisation in polymers. The properties of oriented PLA have been investigated by several workers [102]–[107]. Kokturk et al. [106] reported that upon stretching, PLA films underwent rapid orientation in the amorphous region. Beyond a critical level of orientation the polymer sharply formed highly oriented  $\beta$  crystals. The degree of crystallisation increased during the stretching process. Yu et al. [107] reported that uniaxial stretching of semi-crystalline PLA films significantly increased the crystallinity of the sample, which led to an increase in tensile strength, modulus and toughness. A similar result has been proposed by Xie et al. [103], who found that the crystallinity of PLA films increased with the draw ratio and that reached a maximum value when the samples were stretched to 3 times in length at 90°C .

Simultaneous biaxial stretching of PLA films in the rubbery state has been reported to have in-plane isotropy with poorly ordered crystalline regions, which was due to an insufficient number of chains being oriented in the same direction [102]. The crystallinity of simultaneous biaxial and uniaxial stretched PLA films are plotted against draw ratio in Figure 2.20. The degree of crystallisation showed an increase with increasing draw ratio. On the contrary, the cold crystallisation temperature of the stretched films was reduced with the increase of draw ratio, and nearly disappeared at a draw ratio of 4x4 [102], [104].

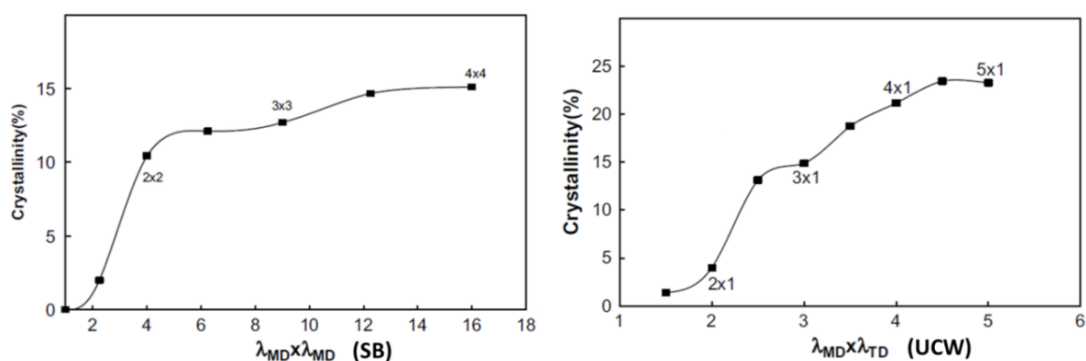


Figure 2.20 Crystallinity of simultaneous biaxial (left) and uniaxial (right) oriented PLA films as a function of draw ratio [102]

In the sequential biaxial stretching mode, the crystallinity of the films increased in the first uniaxial stretching stage, followed by a drop and then increased during

the second stage of drawing in the transverse direction (TD) (see Figure 2.21). This phenomenon was because the extension in TD had destroyed the crystals produced by uniaxial stretching, and re-oriented the chains in the machine direction (MD). After the draw ratio in the TD ( $\lambda_{TD}$ ) equalled that in the MD ( $\lambda_{MD}$ ), sufficient numbers of chains were oriented forming crystals [102].

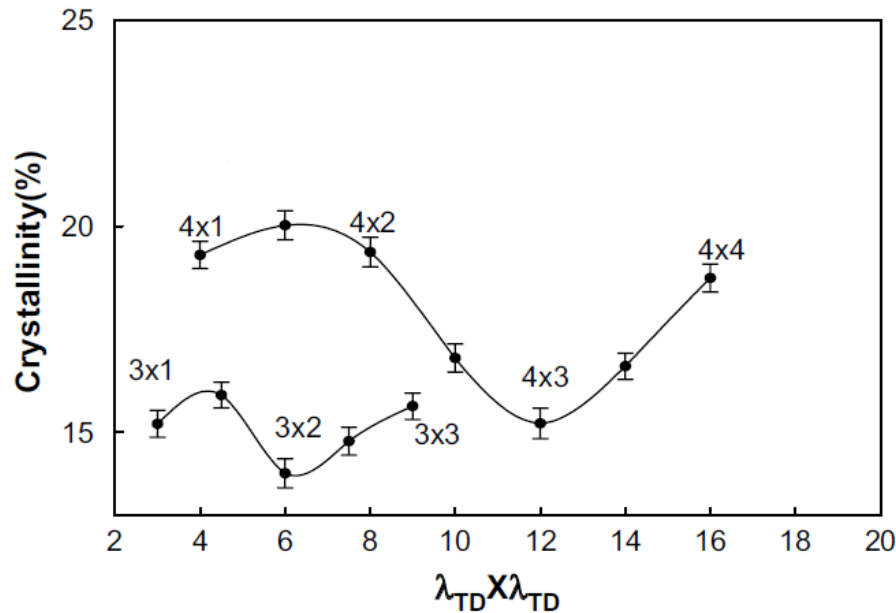


Figure 2.21 Crystallinity of sequential biaxial stretched PLA films as a function of draw ratio [102]

A limited number of studies with respect to oriented PLA nanocomposites have been reported. Tabatabaei and Aji [108], [109] investigated the effect of uniaxial and biaxial stretching on clay orientation and the extent of dispersion in PLA nanocomposites. The XRD patterns of the oriented PLA and PLA nanocomposites (containing 5 wt.% clay) are shown in Figure 2.22. It is found that upon biaxial stretching the peak (203) related to PLA crystallites was decreased, whereas, the peak related to the interlayer spacing of nanoclay remained in the oriented samples.

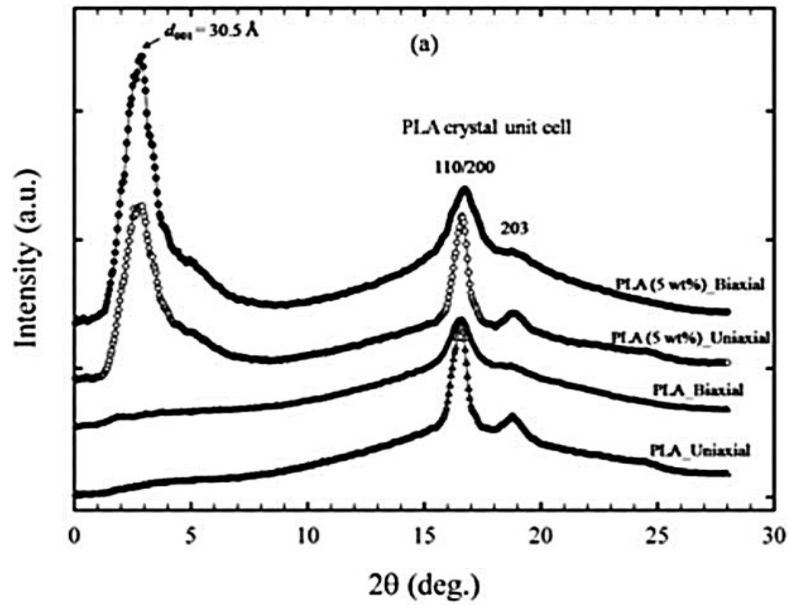


Figure 2.22 XRD patterns of uniaxially and biaxially oriented PLA and its nanocomposite films

The incorporation of nanoclay slightly enhanced the orientation of the crystallite unit cells of orientated films. The alignment of crystallite unit cells was found to be dependent on both uniaxial and biaxial stretching. The orientation of clay platelets in the oriented films is illustrated in Figure 2.23.

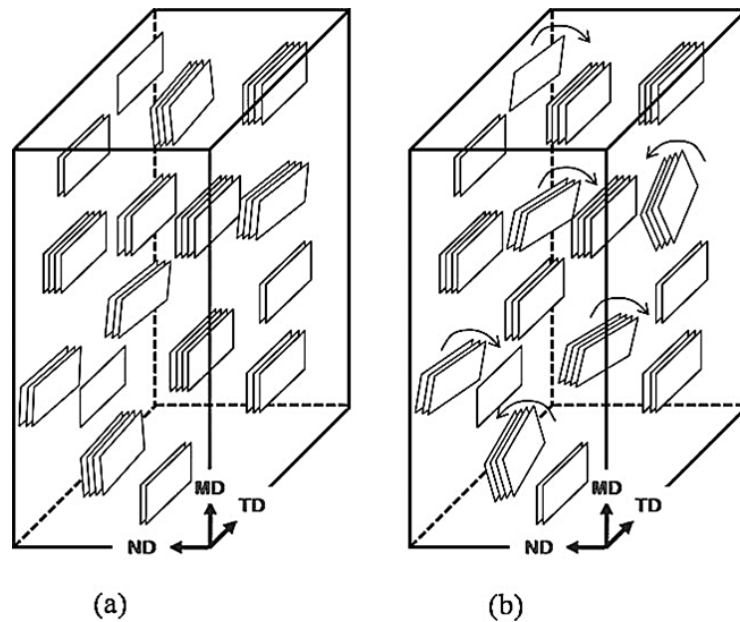


Figure 2.23 Schematic diagram of the orientation of clay tactoids with respect to the film axes, for (a) uniaxially and (b) biaxially stretched PLA nanocomposite films [109]

## 2.5 Orientation of polymers

Orientation is commonly used in the packaging industry to improve the mechanical properties of the products [110]. The extent of chain orientation that is induced in amorphous polymers is dependent on the drawing temperature and the extensional strain rate. The appropriate drawing temperature is approximately 10°C above the glass transition temperature [106], [109], [110].

For semi-crystalline polymers, after a certain draw ratio is reached, stress induced crystallisation occurs, which results in a highly oriented crystalline phase. Stress induced crystallisation can increase the mechanical properties. For example, the tensile strength of polypropylene has been increased more than 10 times after orientation generated by cold drawing [111].

Three typical stretching modes are used in industrial film production (see Figure 2.24):

1. Uniaxial Constant Width (UCW) Stretching: the film is stretched in the MD while its width is constrained in the TD.
2. Simultaneous Biaxial (SB) Stretching: the film is stretched in two perpendicular directions at the same ratio at the same time.
3. Sequential Biaxial (SEQ) Stretching: the film is first stretched in the MD in the UCW mode, and subsequently stretched in the TD in the UCW mode at the same stretching rate

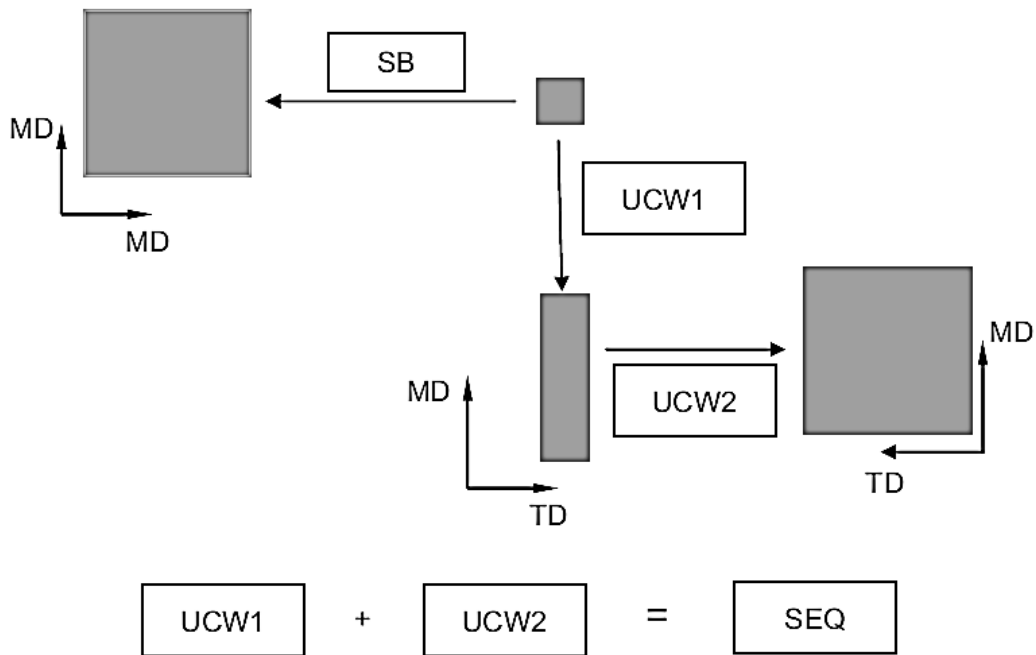


Figure 2.24 Schematic of stretching modes (MD=machine direction; TD=transversal direction) [102]

Structure evolution of semi-crystalline PLA films during simultaneous biaxial and sequential biaxial stretching has been compared by Ou and Cakmak [102], who reported that simultaneous biaxial stretching always induces in-plane isotropy to the film, whereas the orientation in the sequential biaxial stretched film is more complicated. In the first stage (stretching in the MD), orientated crystallisation developed gradually in the MD while the transverse isotropy is maintained. In the second stage (stretching in the TD), the crystalline structure orientated in the MD is gradually destroyed forming a secondary population of orientated crystallites in the TD. As a result, the crystallite size in the MD is reduced. This destruction is caused by the splaying action under the transverse stretching [102].

Physical properties of the PLA films can be enhanced by applying orientation of the polymer chains. A list of typical draw temperatures for PLA film extrusion processes in the MD and TD are shown in Table 2.2.

Table 2.2 Processing temperature profile for biaxial orientation PLA films (screw speed: 20-100rpm)

<b>Section</b>	<b>Temperatures (°C)</b>
Feed throat	45
Feed zone	180
Compression section	190
Metering section	200
Adapter	200
Die	200
Machine direction draw	60-70
Transverse direction draw	70-80
Heat set oven	120-140

## 2.6 Electrospinning of PLA

### 2.6.1 Introduction to electrospinning

Electrospinning is a broadly used technology for producing polymer nanofibres with diameters in the nanometer scale [112]. The process of electrospinning has gained much attention in the last decade due to its versatile spinning in a wide variety of polymeric type, ability to produce continuous fibres and control of fibre diameter in the submicron range, which is difficult to achieve by using standard mechanical fibre-spinning techniques [113], [114]. There is a wide range of polymers and polymer blends that are used in electrospinning and are able to form fine and uniform fibres within the submicron range [115]. With high surface-to-volume ratio and possibly a porous structure, electrospun polymer fibres have shown extensive potential in a number of applications, such as nanocatalysis, tissue engineering scaffolds, protective clothing, filtration, pharmaceuticals, optical electronics, healthcare, biotechnology, and environmental engineering [116], [117].

Another advantage of the electrospinning process is that it is a versatile and cost-efficient method of producing multi-function and high-performance composite fibres by incorporating nanoparticles in the polymer solutions during the electrospinning process [118]. These additive and filler reinforced fibres can display superior mechanical behaviour and functional properties. Inorganic additives such as ZnO, TiO<sub>2</sub>, Ag<sub>2</sub>O, cellulose and carbon nanotubes have been incorporated into electrospun nanofibres to produce composite functional materials [119].

Electrospinning is a simple technique which utilises high electrostatic forces for fibre production. This process was first introduced by Formhals [120] in 1934. The work of Taylor [121] on electrically driven jets has laid the groundwork for electrospinning.

Currently there are two standard electrospinning setups: vertical and horizontal, see Figure 2.25. Basically, an electrospinning system consists of three main components: a high voltage power supply, a spinneret and a ground collector (usually a metal plate or rotating mandrel). The electrospinning is carried out in a high voltage electric field between a needle tipped syringe that contains

polymer based solution and a metal collector for the deposition of nanofibres. When a high voltage is applied to a droplet of polymeric solution on the needle tip, the droplet is charged and forms a conical shape. As the electric force is higher than the surface tension of the solution, a liquid jet is generated from the droplet and spun on the collector [122].

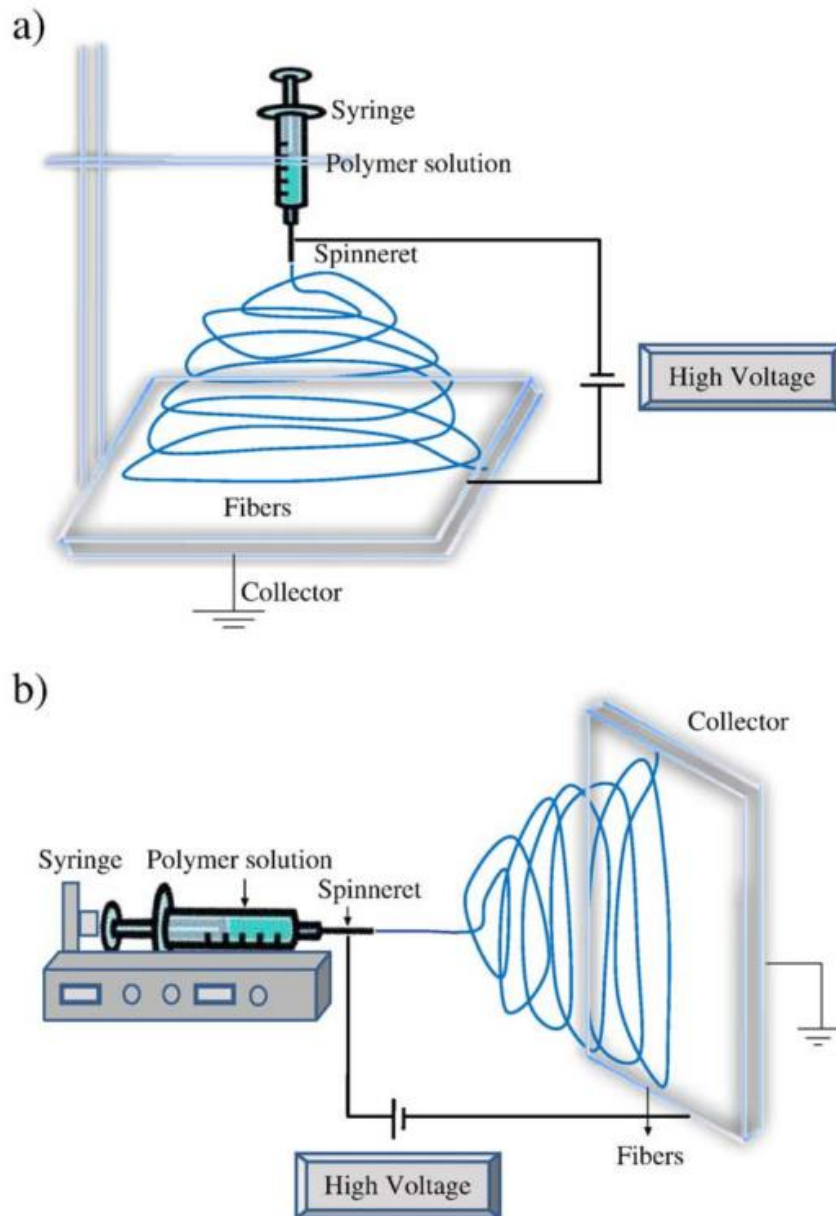


Figure 2.25 Schematic diagrams of set up of electrospinning apparatus (a) typical vertical set up and (b) horizontal set up of electrospinning apparatus [114]

### **2.6.2 Effect of various parameters on electrospinning**

The quality of the electrospinning process is governed by many parameters, which are classified into solution parameters, process parameters and ambient parameters. Fibre morphology and diameter are significantly affected by solution parameters (solution viscosity, conductivity, polymer molecular weight and surface tension) and processing parameters (applied electric field, tip-to-collector distance, and feeding rate). For example, too low a polymer concentration and solution viscosity lead to droplets and beads in the fibres. Fine fibres can be achieved by increasing the voltage and tip to collector distance or reducing the feed rate during the electrospinning process. The optimum fibre quality can be obtained by manipulating these parameters. Ambient parameters, including the temperature and humidity of the surroundings, also play an important role in the final morphology of the electrospun fibres. It is reported that increasing the ambient temperature gives rise to the decrease of fibre diameter, whereas the increase in the humidity causes circular pores on the surface of fibres. Table 2.3 summarises various parameters and their effects on the morphology of fibres produced by electrospinning.

Table 2.3 Summaries of electrospinning parameters and their effect of the fibre morphology [114], [117]

<b>Parameters</b>	<b>Effect on fibre morphology</b>
Solution parameters	
Viscosity (polymer concentration)	Low: cause generation of beads High: increase in fibre diameter, disappearance of beads
Molecular weight	High: reduce the number of beads and droplets
Conductivity	High: decrease fibre diameter
Surface tension	High: instability of jets (surface tension has no effect on fibre morphology)
Processing parameters	
Applied voltage	High: decrease fibre diameter
Distance between tip and collector	High: decrease fibre diameter Too low: cause beads generation
Feed rate	Low: decrease fibre diameter High: easy to cause beads generation
Ambient parameters	
Temperature	High: decrease fibre diameter
Humidity	High: cause circular pores on the fibre surface

### 2.6.3 Electrospinning of PLA based nanofibres

PLA is a bio-based polymer that has been widely commercialised. Since PLA is not only compostable and derived from renewable resources but is also biocompatible, it has been of a great interest in biomedical applications such as tissue scaffolds and wound healing [123]–[126].

Electrospinning has been utilised to prepare PLA based nanofibres and the effect of solution and processing parameters on fibre morphology has been investigated [123], [126]–[129]. Yang et al. [129] dissolved PLLA in dichloromethane / DMF (70:30) at a concentration of 1% (w/w) and obtained a nanofibre scaffold with an average diameter of  $272 \pm 77$  nm. In another work of these authors [128], aligned PLLA fibrous scaffolds with an average diameter of 300 nm were fabricated using electrospinning from PLLA with dichloromethane / DMF (70:30) solution. According to their results, the aligned PLLA nanofibres were more suitable than the random nanofibres as cell carrier in neural tissue engineering. Tsuji et al. [127] dissolved high molecular weight PLLA / PDLA (1:1) in chloroform at a concentration of  $4 \text{ g dL}^{-1}$ . They collected stereocomplex nanofibres with diameters of 830–1400 and 400–970 nm at voltages of -12 and -25 kV, respectively, (negative voltage was applied to the tip of the needle while the collecting drum was grounded). It was found that the crystallinity of the homo-crystallites composed of either PLLA or PDLA decreased from 5% to 1%, whereas the stereocomplex nanofibres increased from 16 to 20%. This finding indicated that stereocomplex nanofibres with a small amount of homo-crystallites can be prepared using electrospinning, even when high-molecular-weight PLLA and PDLA are used. The orientation caused by high voltage (or electrically induced high shearing force) during electrospinning enhanced the formation and growth of stereocomplex crystallites, and thus suppresses the formation of homo-crystallites. In terms of the fibre morphology, the blend fibres exhibited smoother surfaces than that of the pure PLLA fibres, as shown in Figure 2.26.

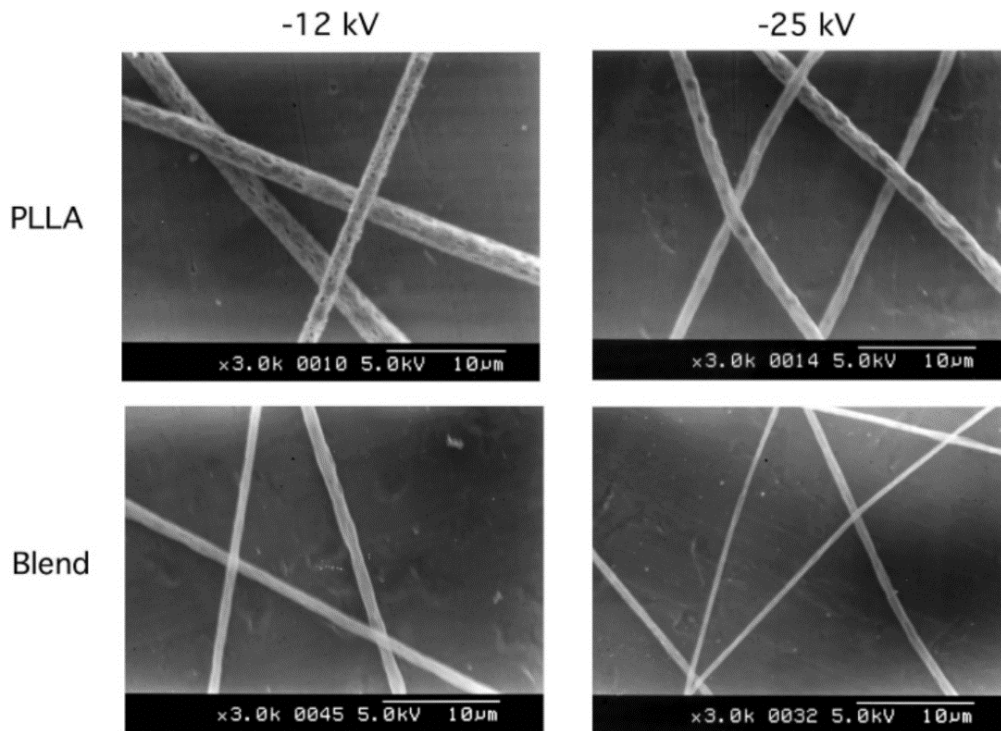


Figure 2.26 SEM images of PLLA and PLLA/PDLA (1:1) blend fibres that were electrospun at applied voltages of -12 and -25 kV [127]

Casasola et al. [130] prepared PLA solutions in various single solvent and binary-solvent systems to investigate the effect of different solution properties on the fibre morphology and diameter. It was found that among all single solvents, only a PLA solution in acetone produced continuous nanofibres, as shown in Figure 2.27. Binary solvent systems based on mixture of acetone and another solvent were able to produce nanofibres. Defect-free nanofibres were collected using solvent systems AC/DMF and AC/DMAc (see Figure 2.28). This result revealed that solvents with higher electrical conductivity resulted in less bead, defect-free nanofibres. In addition, the effect of polymer concentration and solvent ratio were also investigated. It was reported that polymer concentration played an important role in the nanofibre morphology: higher concentration of polymer produced more uniform and defect-free nanofibres with increased diameters.

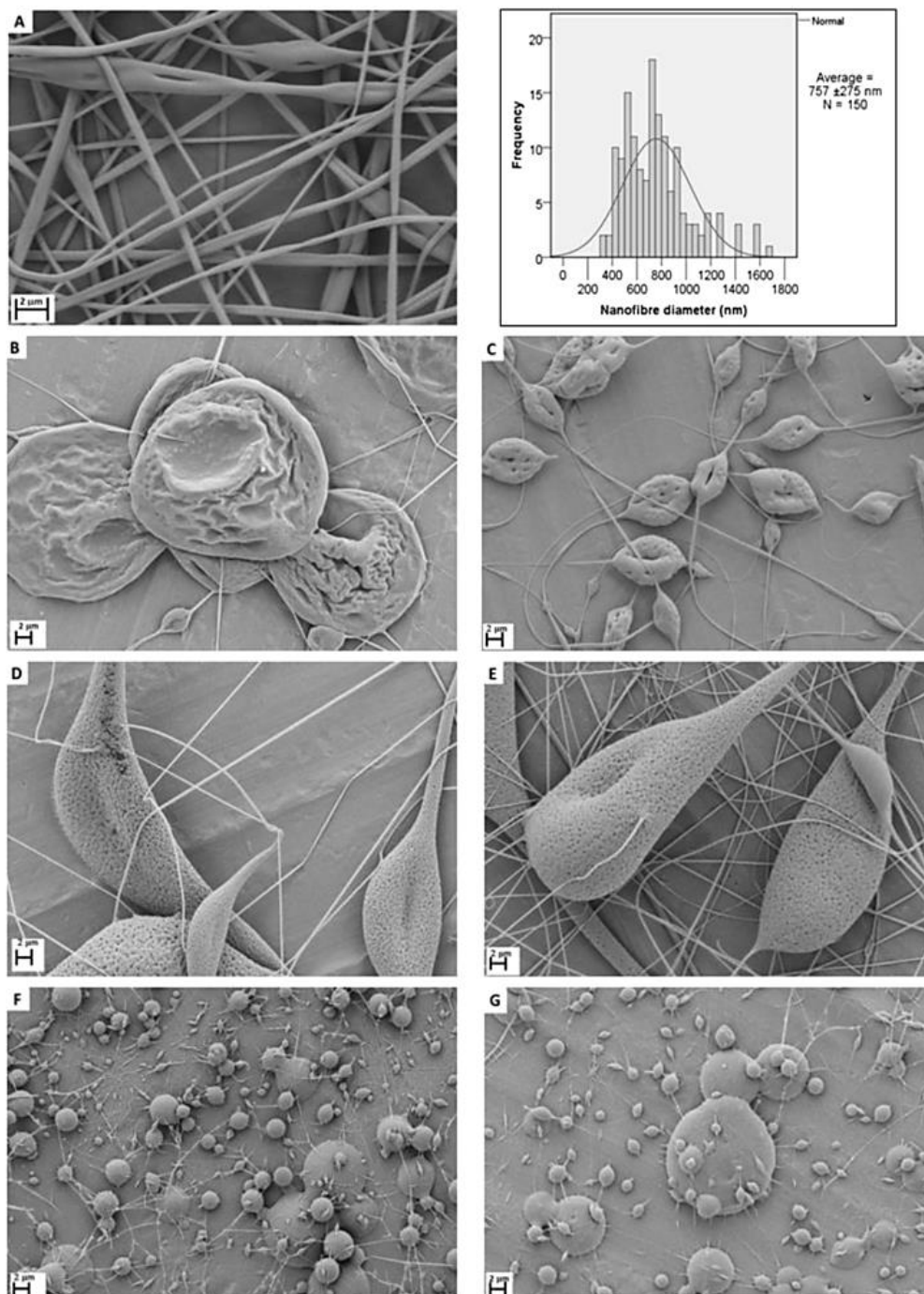


Figure 2.27 Effect of single solvent systems on nanofibre morphology: scanning electron micrographs of PLA nanofibres from solutions of 10% (w/v) of PLA in: (a) acetone with nanofibre diameter distribution, (b) 1,4-dioxane, (c) tetrahydrofuran, (d) dichloromethane, (e) chloroform, (f) dimethylformamide and (g) dimethylacetamide [130]

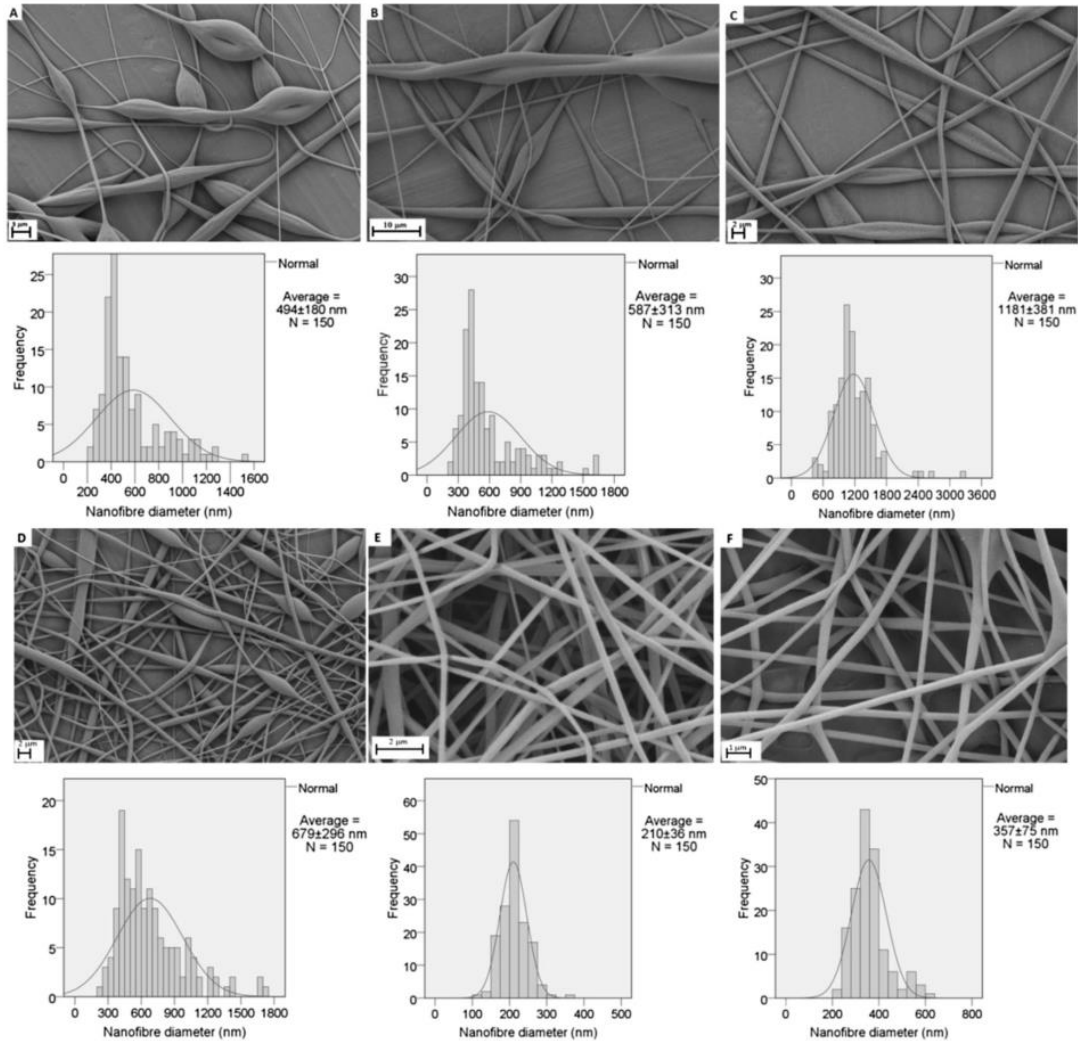


Figure 2.28 Effect of binary-solvent systems on nanofibre morphology: scanning electron micrographs of PLA nanofibres with nanofibre diameter distribution from solutions of 10% (w/ v) of PLA in (a) acetone / 1,4-dioxane, (b) acetone / tetrahydrofuran, (c) acetone / dichloromethane, (d) acetone/chloroform, (e) acetone / dime-thylformamide and (f) acetone / dimethylacetamide [130]

In another study, Casasola et al. [131] proposed a methodology for selection of solvent systems to produce PLA electrospinnable solutions that can form defect-free nanofibres with narrow diameter distribution. The optimum solvent systems were selected firstly using a thermodynamic approach to select the most suitable solvent. The second step was to optimise the solution by adding a solvent with high dielectric constant, which can provide defect-free nanofibres with narrow diameter distribution. The last step was to choose the optimum polymer

concentration; i.e. defect-free nanofibres can be collected when polymer concentration was 2 or 2.5 times the chain entanglement concentration.

#### **2.6.4 Electrospinning of nanoclay composite fibres**

As discussed already in Section 2.2.1, montmorillonite is a layered silicate clay, which belongs to the 2:1 layered phyllosilicate family. Its crystal structure consists of an aluminium and magnesium hydroxide octahedral sheet, which is sandwiched between two silicon oxide tetrahedral sheets. The layer thickness of each platelet is nearly 1 nm and the spacing between two layers is less than 1 nm [42].

Montmorillonite has been widely used as reinforcement for polymers, due to its high aspect ratio and capability of surface modification with both organic and inorganic cations [2]. It has been reported that adding a small amount of MMT nanoclay can increase mechanical and physical properties of polymers such as strength, stiffness, UV-light resistance and thermal stability. For example, the incorporation of MMT (5.79 vol.%) in PLA scaffolds exhibited an increase in tensile modulus from 121.2 MPa for pure PLA scaffolds to 170.1 MPa for nanocomposite scaffolds [132].

MMT has been proved as a highly efficient drug carrier for wound healing, treatment of stomach ulcers and intestinal problems, as it exhibits high drug loading capacity due to high surface area, mucoadhesive properties and nontoxicity [133]. Othman et al. [134] incorporated MMT and paracetamol in PLA nanoparticles as a drug carrier. Single layered clay silicates were included in the paracetamol nanocrystals that were well distributed in PLA matrix, as shown in Figure 2.29. They concluded that the incorporation of MMT improved both the drug encapsulation efficiency and increased the drug loading capacity in PLA nanoparticles.

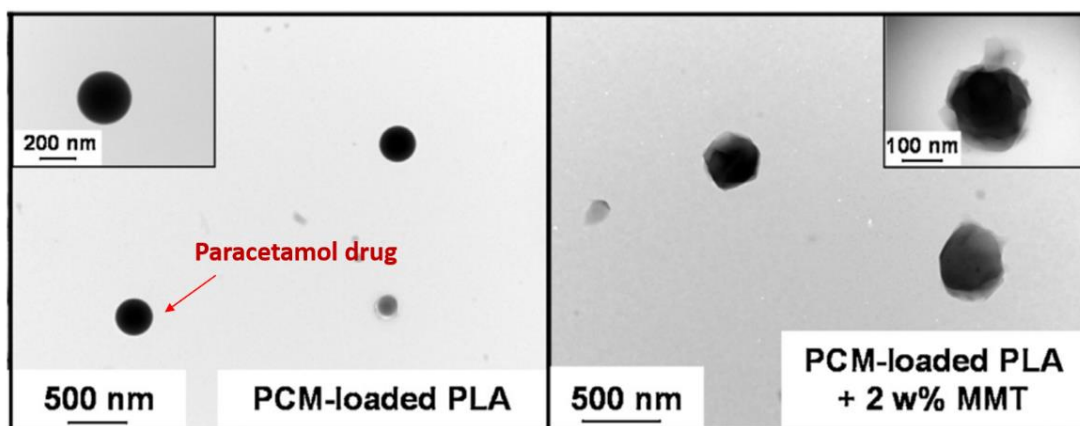


Figure 2.29 TEM images of paracetamol (PCM)-loaded PLA and PCM-loaded PLA nanocomposite with 2 wt.% clay content [134]

MMT has been widely incorporated into polymer nanofibres to enhance the mechanical and thermal properties. For example, nanocomposite fibres based on poly( $\epsilon$ -caprolactone) (PCL) and organically modified montmorillonite were prepared by electrospinning from the intercalated nanocomposite solution. The fibrous PCL / MMT membrane showed enhanced stiffness without sacrificing polymer ductility due to the high aspect ratio of the nanoclay [135]. Electrospun composite fibres of poly(vinyl alcohol) (PVA), chitosan oligosaccharide and montmorillonite clay were fabricated by Park et al. [136], who found that the nanoclay concentration had an important role in the control of the nanofibre qualities. They reported that mechanical properties and thermal stability of the nanofibres were increased with the concentration of nanoclay. Yoon and Kelarakis [137] reported that the incorporation of organically modified Luccentite nanoclay dramatically modified the structure and morphology of the polyvinylidene fluoride (PVDF) electrospun nanofibres by reducing beads in the fibres and stabilising the formation of  $\beta$ -crystallites from  $\alpha$ -spherulites of the polymer. Wang et al. [138] found that adding nanoclay enhanced molecular alignment of polymer chains in electrospun nanofibres, and hence improved optical and mechanical properties of the nanofibres.

Only a few researchers have studied the electrospinning of PLA / nanoclay nanofibres. Badrinarayanan et al. [139] investigated the effect of nanoclay on the thermal behaviour of electrospun PLA and obtained well dispersed nanoclay

structure as shown in Figure 2.30. They found that the incorporation of nanoclay (from 15 to 25 wt.%) reduced the degree of crystallinity and the T<sub>g</sub> for both amorphous and semicrystalline PLA nanofibres.

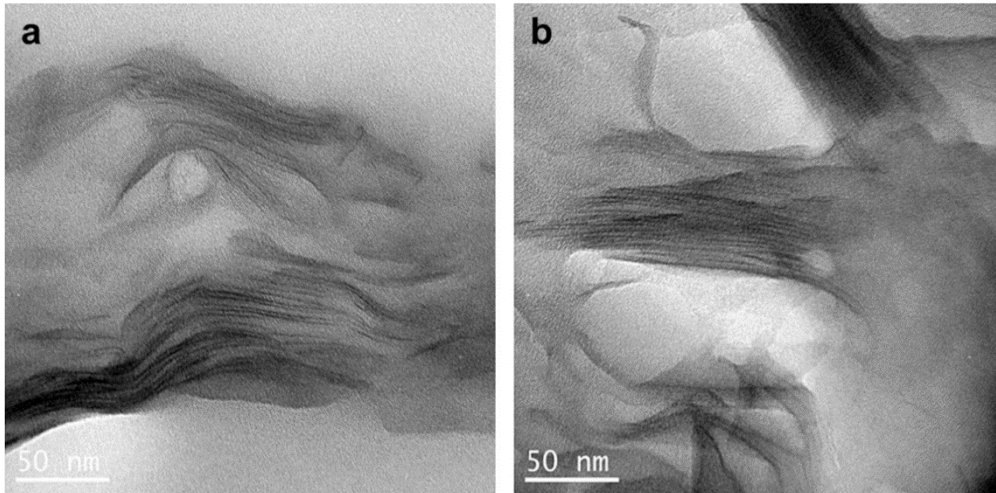


Figure 2.30 TEM images of PLA nanocomposite containing (a) 15.3 wt.% and (b) 25 wt.% clay [139]

Ayutthaya et al. [140] prepared clay incorporated keratin/PLA core-shell nanofibres via electrospinning. It was found that with the addition of 1-2 pph Na-montmorillonite clay, the processability and the morphology of the nanofibres were improved. The nanoclay also acted as nucleating agent to keratin. Lee et al. [141] dissolved PLLA with 2, 3 and 5 phr montmorillonite in chloroform at a concentration of 0.1 g/ml and collected porous nanofibres scaffolds. The nanocomposite scaffolds exhibited increased strength and improved structural integrity during biodegradation.

### 2.6.5 Electrospinning of zinc oxide composite fibres

Nano-sized zinc oxide (ZnO) is an attractive component for incorporation in fibrous materials for medical applications due to its antibacterial properties. ZnO nanoparticles have been incorporated in several biocompatible and biodegradable polymer nanofibres using electrospinning. For example, the electrospinning of a solution of sodium alginate (SA) and poly (vinyl alcohol) was carried out with ZnO nanoparticles with different concentrations to get SA/PVA/ZnO composite nanofibres. The presence of ZnO in the fibrous mats was found to improve the thermal stability and antibacterial activity against *S. aureus* and *E. coli* [142]. Anitha et al. [143] fabricated ZnO-embedded cellulose acetate fibrous membrane by electrospinning. The addition of ZnO contributed to a strong antibacterial activity against the *S. aureus*, *E. coli* and *Citrobacter* and changed the wettability on the surface of the membrane. Augustine et al. [144] prepared polycaprolactone (PCL)/ZnO non-woven membrane by electrospinning and found that the concentration of ZnO has a strong effect on the morphology of the fibre. The surfaces of the nanofibres became rougher with the addition of ZnO (see Figure 2.31). With high ZnO concentrations (5 wt.% and 6 wt.%) the PCL membrane effectively inhibited the growth of *S. aureus* and *E. coli*, as shown in Figure 2.32. The composite membrane also showed excellent fibroblast cell attachment, which is therefore appealing for tissue engineering applications.

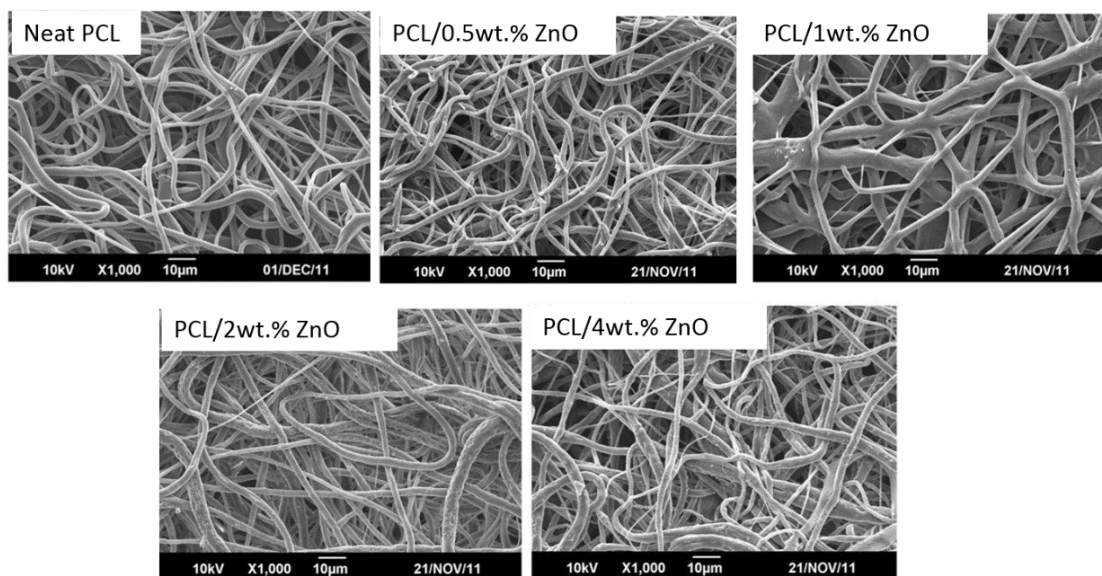


Figure 2.31 SEM image of PCL and PCL nanocomposite membrane with different ZnO nanoparticles [144]

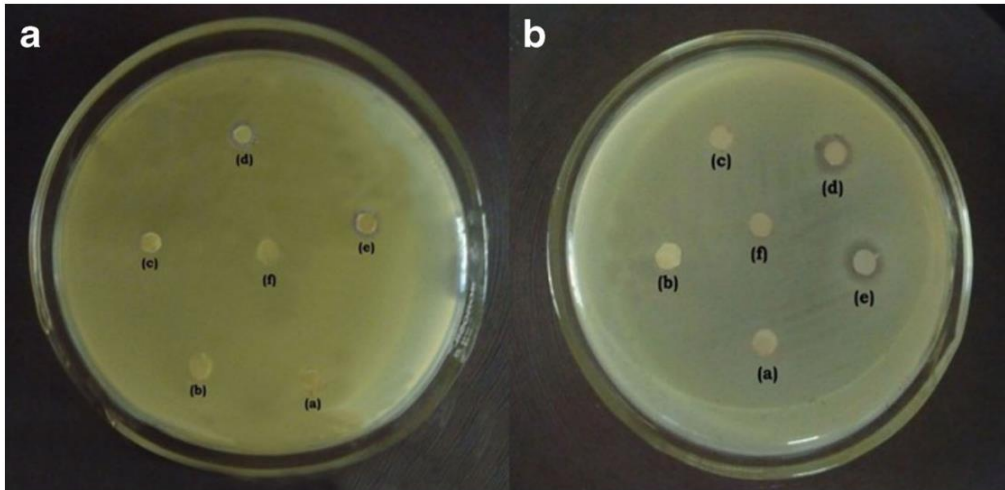


Figure 2.32 Plates showing the antibacterial activity of the fabricated PCL membranes with different concentrations of ZnO nanoparticles against *E. coli* (plate (a)) and *S. aureus* (plate (b)). In both plates are (a) 2 wt.%, (b) 3 wt.%, (c) 4 wt.%, (d) 5 wt.%, and (e) 6 wt.% ZnO nanoparticles, and PCL membrane alone (f) [144]

Only a few researchers [145]–[148] have reported the electrospinning of PLA / ZnO nanofibres. Rodríguez-Tobías et al. [146] investigated the morphology, mechanical and antibacterial properties of PLA / ZnO nanocomposite mats with ZnO concentrations from 0 to 5 wt.%. A good distribution of ZnO nanoparticles was obtained with some agglomerations in the PLA nanofibres, as shown in the SEM and elemental mapping images in Figure 2.33. Tensile strength and Young's modulus were slightly increased with an optimal ZnO concentration of 3 wt.%. The composite nanofibres exhibited a growth inhibition of the Gram-negative *E. coli* and the Gram-positive *S. aureus* bacteria.

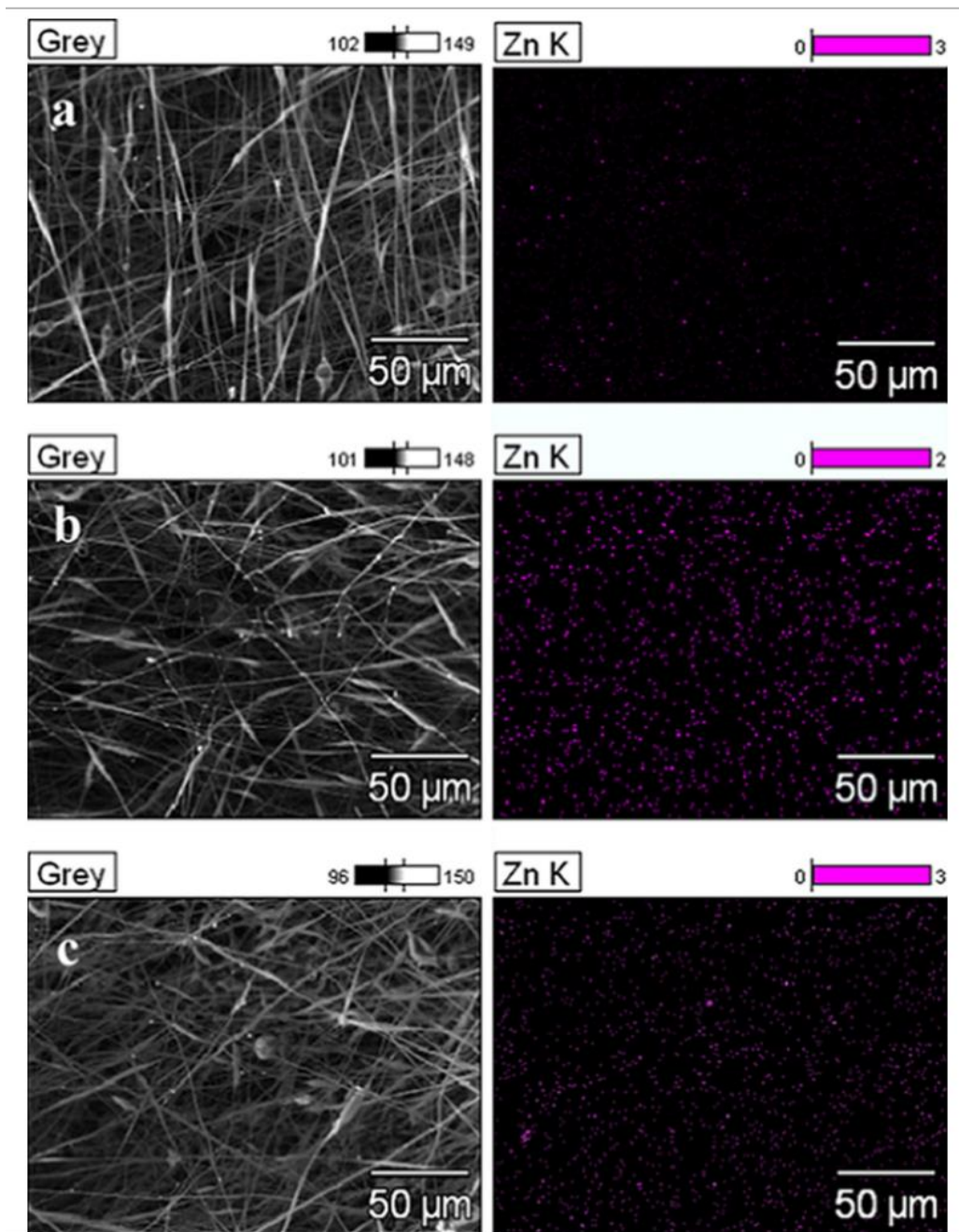


Figure 2.33 SEM images (left) and elemental mapping (right) of electrospun mats obtained by electrospinning of a PLA solution and electrospaying of nano-ZnO dispersed in MeOH at (a) 1, (b) 3, and (c) 5 wt.% with respect to PLA [146]

Virovska et al. [148] fabricated PLA / ZnO non-woven nanofibres of two types: ZnO nanoparticles deposited on the surface of PLA fibres and ZnO nanoparticles in the bulk. Figure 2.34 shows the morphology of the two types of nanofibres. It was found that the type ZnO–on-PLA exhibited higher photocatalytic activity and antimicrobial activity against *S. aureus* when compared with the type ZnO–in-

PLA. Therefore, the use of electrospinning and electrospraying for producing ZnO-on-PLA nanofibres was more efficient for preparation of hybrid materials with significant activities.

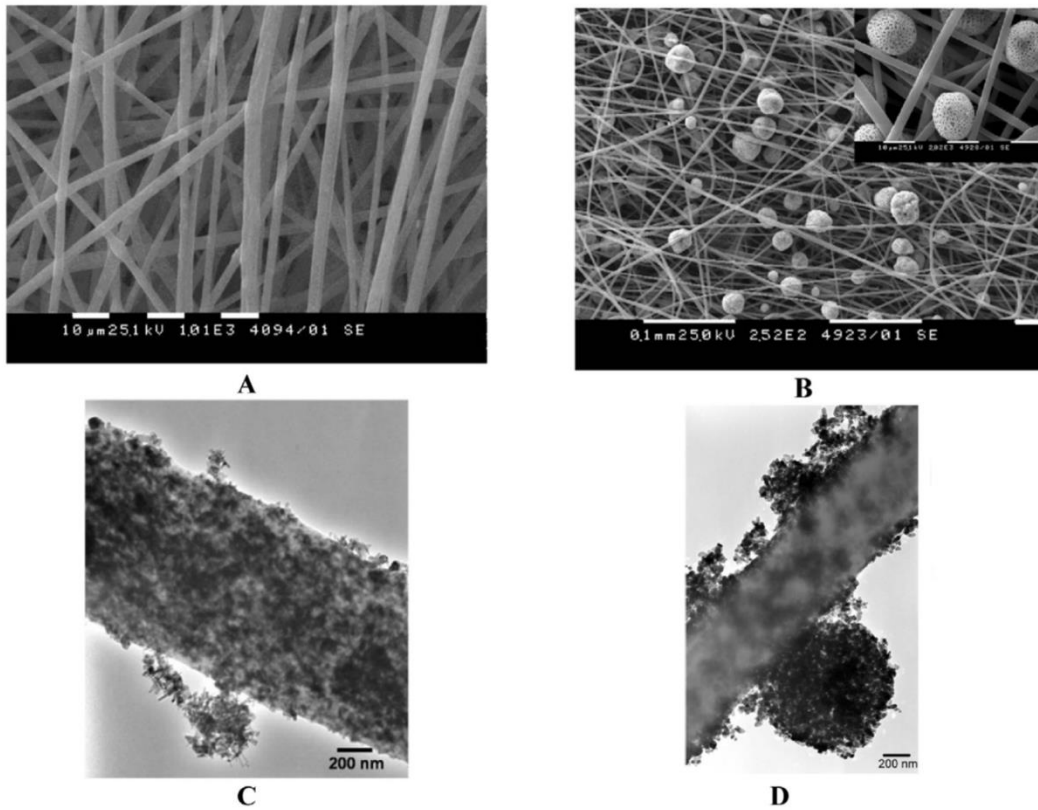


Figure 2.34 morphology of the ZnO-on-PLA nanofibres: (A) SEM images (C) TEM images; and the ZnO-in-PLA nanofibres: (B) SEM images (D) TEM images [148]

### 3 Experimental

#### 3.1 Raw materials

##### *PLA*

Two grades of Polylactic Acid (Ingeo™ Biopolymer 4060D and 4032D), supplied by NatureWorks LLC, were used as the composite matrix. Information about the PLA polymers is shown in Table 3.1, which was supplied by the manufacturer.

Table 3.1 Information of PLA 4060D and PLA 4032D

Raw materials	State	D content	Tg / °C	Tm / °C
PLA 4060D	Amorphous	1.4 wt. %	55-60	N/A
PLA 4032D	Semi-crystalline	12 wt. %	55-60	155-170

##### *Nanoclay*

The organoclay used was Cloisite® 30B, supplied by Southern Clay Products. It is a montmorillonite layered silicate which has been modified with an alkyl quaternary ammonium salt.

##### *Zinc oxide (ZnO)*

ZnO was used to improve antimicrobial activity of electrospun PLA nanofibres. It was supplied as a powder (99.5+%) by Fisher Scientific. The average particle size was measured to be ac. 100 nm.

##### *Acetone (AC)*

AC used as the solvent to prepare PLA solutions for electrospinning was purchased from Fisher Scientific. It was analysis grade (99.5+%): boiling point 56°C, electrical conductivity 0.2  $\mu\text{S cm}^{-1}$ , dielectric constant 20.6, and solubility parameter 10  $\text{cal}^{1/2} \text{cm}^{-3/2}$ .

##### *Chloroform (CHL)*

CHL used as the second solvent to prepare PLA 4032D solutions for electrospinning was purchased from Sigma-Aldrich. It was analysis grade (99+%): boiling point 61°C, electrical conductivity 1.0E-04  $\mu\text{S cm}^{-1}$ , dielectric constant 4.8, and solubility parameter 9.3  $\text{cal}^{1/2} \text{cm}^{-3/2}$ .

## 3.2 Sample preparation

### 3.2.1 Pre-drying of PLA

PLA easily absorbs water molecules from the air, which can cause degradation during later melt processing. Therefore, PLA granules were pre-dried in a vacuum oven for about 24 hours at 60°C and 600 mbar to remove excess moisture from the material.

### 3.2.2 Compounding (Haake Rheomix OS)

The dried PLA was then melt compounded with organoclay in a counter-rotating mixer (Haake Rheomix OS) (see Figure 3.1). This procedure can promote dispersive and distributive mixing of the materials.

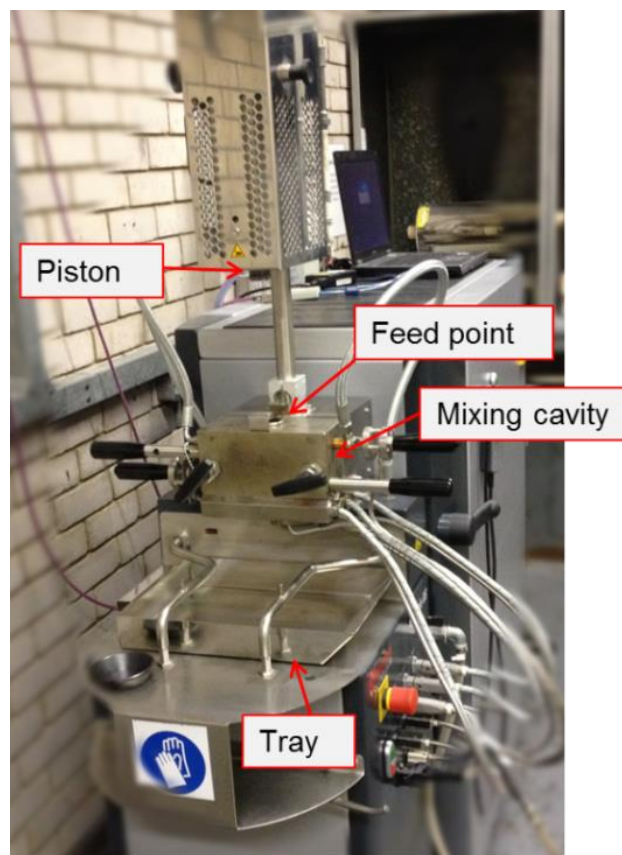


Figure 3.1 Parts of Haake Rheomix OS

The compounding of PLA and organoclay was carried out at 170°C for 10 mins at a constant rotor speed of 60 rpm. The total sample weight for each batch was 58 g. The mixing cavity was heated up to 170°C before the rotors were started. Then materials were slowly added into the mixing cavity through a hopper on top of the cavity. A piston was dropped through the hopper into the feed point of the

mixing cavity to seal the system. After 10 mins mixing, the machine stopped automatically. The piston was raised and the cavity and rotors were taken apart. The mixed compound was then quickly removed from the cavity and the rotors using two stripping knives and left on a steel tray to cool before being collected in a sealed plastic bag for later use.

For preparing PLA nanocomposite compounds, a masterbatch containing 20 wt.% organoclay and 80 wt.% PLA was first made. A certain amount of masterbatch was diluted with pure PLA granules in a second batch to produce further compositions ranging from 1 wt.% to 5 wt.% clay content. The formulations of the masterbatch and PLA nanocomposites are listed in Tables 3.2 and 3.3.

Table 3.2 Masterbatch formulation

	<b>PLA (g)</b>	<b>Cloisite® 30B (g)</b>	<b>Total (g)</b>
Reference sample	58	0	58
Masterbatch (20 wt.%)	46.4	11.6	58

Table 3.3 Sample formulations

	<b>PLA (g)</b>	<b>Masterbatch (g)</b>	<b>Total (g)</b>
Reference sample	58	0	58
1 wt.% Nanocomposite	55.1	2.9	58
2 wt.% Nanocomposite	52.2	5.8	58
3 wt.% Nanocomposite	49.3	8.7	58
4 wt.% Nanocomposite	46.4	11.6	58
5 wt.% Nanocomposite	43.5	14.5	58

After the mixed compound had been collected, the machine was cleaned using HDPE as the cleaning agent and a range of brushes. 44.4 g HDPE was added into the cavity for 5 mins to dilute the residual PLA. The HDPE and the residual PLA were blended and removed. Then the cavity and the rotors were cleaned using different kinds of brushes.

### 3.2.3 Compression moulding

#### 3.2.3.1 Quenching process

PLA nanocomposites sheets were compression moulded in a 20 ton hydraulic press (see Figure 3.2). Figure 3.3 shows two moulds that were used to produce different shape sheets: a 12x12 cm<sup>2</sup> square mould was used to produce square sheets for the biaxial stretching test; a hexagonal mould was used to produce samples for the water vapour permeability test. The mould was placed on a steel plate and the polymer resin was placed on the mould sandwiched between two PET films. As the temperature reached 180°C, the plate as well as the sample was placed in the press machine to soften the polymer resin for around 10 mins before the top plate was placed on top of the sample. The sample plate was then raised close to the upper platen of the machine. 5 mins were allowed for further heating of the sample. After which time, the sample was slowly pressed up to 15 tons for 3 mins, followed by cold pressing of the sample in a different machine for 2 mins at 5 tons at room temperature.



Figure 3.2 Compression moulding sample setup and hot press machine

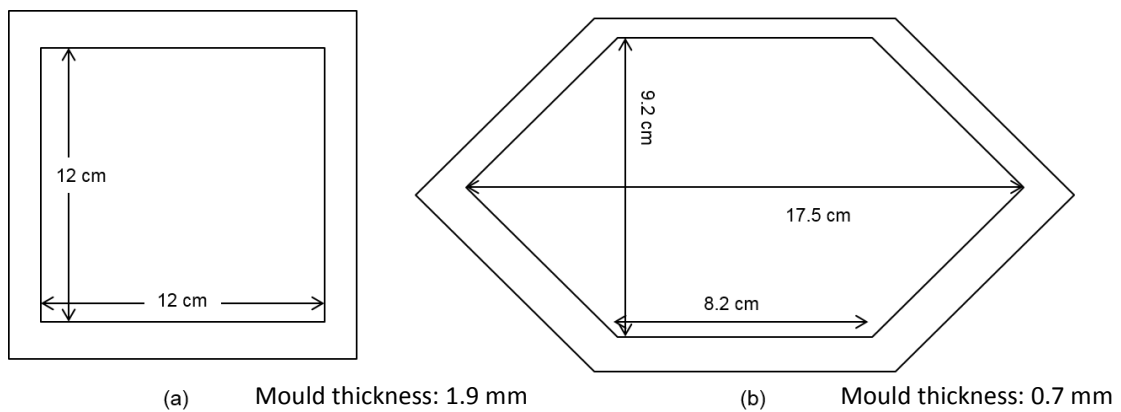


Figure 3.3 Dimensions of the moulds

### 3.2.3.2 Annealing process

The quenched PLA nanocomposites sheets were annealed at 115 °C and 5 tons for 15 mins in a hot press machine. Then the sheet was quenched at room temperature for 2 mins in a cold machine at 5 tons.

### 3.2.4 Uniaxial stretching

A stretching test on the PLA nanocomposite films was carried out using a biaxial stretching machine. Figure 3.4 shows the main parts of the machine.

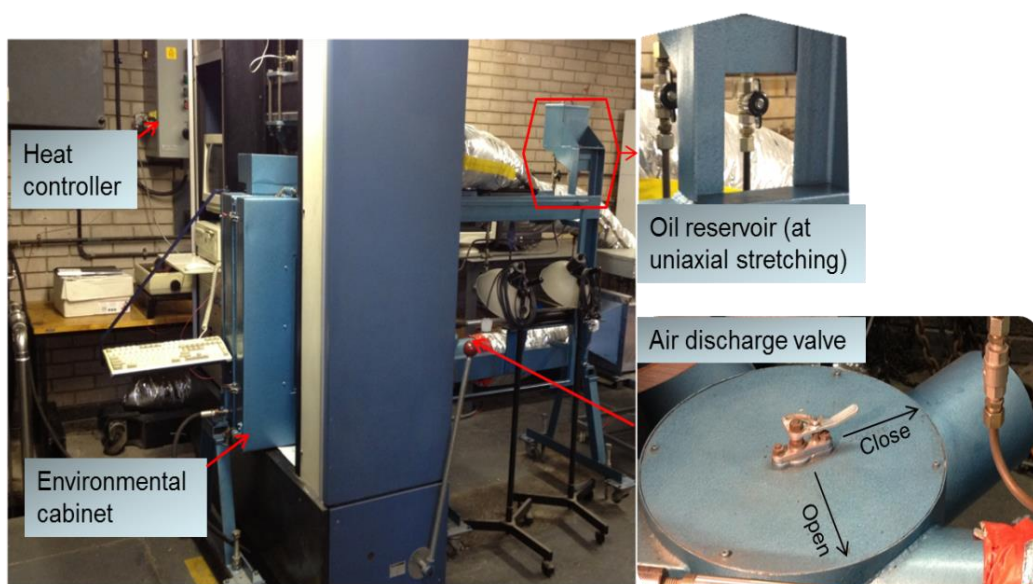


Figure 3.4 Main parts of biaxial stretching machine

A 12x12 cm<sup>2</sup> sample sheet was placed in a slot in the stretching head, which was then adjusted to its onset position. Nitrogen gas pressure of 100 psi was applied to the grips of the crosshead to make sure all the grips had engaged the sample edges. Then the environmental cabinet was closed allowing the sample to be heated to the drawing temperature. As the temperature reached the set drawing temperature, the grip pressure was increased to 200 psi (i.e. 1.38 MPa), which was the recommend value for stretching PLA. After about 5 mins pre-heating, the crosshead started to move at a constant drawing speed and stopped automatically at the maximum displacement set previously. When the test was finished the air heater was switched off and the air discharge valve was opened to cool down the sample in the environmental cabinet for about 5 mins. After this the sample was taken out from the crosshead. The stretching parameters are listed in Table 3.4.

Table 3.4 Stretching parameters of PLA nanocomposites

	<b>Drawing temperature</b>	<b>Drawing rate</b>	<b>Draw ratio</b>	<b>Gas pressure</b>
Uniaxial stretching	60°C	10 mm/min	3 X 1	1.38 MPa

*PS:* crosshead displacement = sample dimension × (draw ratio – 1)

### 3.2.5 Electrospinning of PLA nanocomposite solution

#### 3.2.5.1 Preparations of PLA / clay solutions

The electrospinning solutions were prepared by dissolving PLA in a single solvent (acetone or chloroform) or a binary-solvent system of acetone and chloroform (50/50 v/v) to obtain a 12.5% w/v PLA concentration. Two grades of PLA (4060D and 4032D) solutions were prepared separately. PLA 4060D can be dissolved in acetone at room temperature. However, the grade 4032D is only dissolved in chloroform at room temperature or in a binary-solvent of acetone and chloroform (50/50 v/v) at 45°C, since it is crystalline.

The optimum solvent system for the two grades of PLA was selected for further

nanocomposite preparation according to the morphology of the electrospun nanofibres, which will be discussed in Section 6.1 in detail.

For the preparation of all solutions, the solvents were added to a pre-weighed amount of polymer or polymer nanocomposite in a glass bottle. The polymer nanocomposites used were prepared from melt compounding (same processing as Section 3.2.2). This is to make sure the clay layered silicates were well dispersed in the polymer solution. The solutions were magnetically stirred for 5 hours. The stirring temperature was dependent on the crystallinity of the polymer grade. For the 4060D solutions it was stirred at room temperature (23 °C), whereas the 4032D solutions was stirred at 45 °C. For the preparation of the polymer nanocomposite solutions, the nanoclay at concentrations of 1, 3, and 5 wt.% to PLA were dispersed in the solvent system in a sonic bath for 1 hour followed by magnetic stirring for 1 hour. Then PLA was added to the solution and magnetically stirred at room temperature for about 5 hours.

### **3.2.5.2 Preparations of PLA / ZnO solutions**

The electrospinning solutions were prepared by dissolving PLA 4060D in acetone to obtain a 12.5 % w/v PLA concentration. For the preparation of the PLA / nanoparticle solutions, the ZnO powders (at concentrations of 1, 3, 5, 7 and 9 wt.% to PLA) were dispersed in acetone in a sonic bath for 1 hour and then magnetically stirred for 1 hour. Then PLA was added to the solution and magnetically stirred at room temperature for about 5 hours.

### **3.2.5.3 Electrospinning process**

The electrospinning experiment was carried out with a spraybase electrospinning instrument by Profector Life Sciences Ltd. as shown in Figure 3.5. During the experiment, a high voltage supply was used to generate an electric field of 20 kV between a collector and a needle, which was set up vertically to the collector and connected to a plastic syringe by a polyethylene capillary tube. A pump system was used to feed a constant rate of solution (1 ml/h) through the needle. The

solution droplet at the tip of the needle was charged and drawn to produce nanofibres, which were randomly sprayed onto the collector. A camera was located inside the chamber to observe the spinning process at the tip of the needle. The process parameters are listed in Table 3.5.

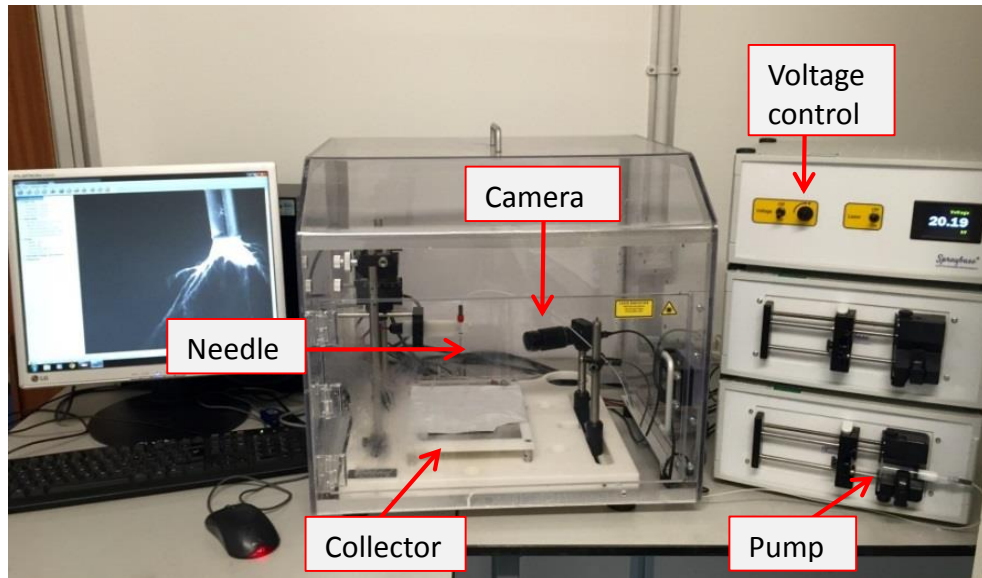


Figure 3.5 The spraybase electrospinning instrument

Table 3.5 Process parameter of electrospinning

Fire composition	Solvent type	Temperature of mixing	Flow rate	Voltage	Needle to collector distance
PLA 4060D/clay	AC	Room temperature	1 ml/min	20 kV	10 cm
PLA 4032D/clay	AC/CHL	45 °C	1 ml/min	20 kV	10 cm
PLA 4060D/ZnO	AC	Room temperature	1 ml/min	20 kV	10 cm

### 3.3 Characterisation

#### 3.3.1 Differential scanning calorimetry (DSC)

The thermal properties of PLA nanocomposite were investigated using differential scanning calorimetry (DSC). The measurement was carried out using a TA DSC Q200 calorimeter fitted with a TA refrigerated cooling system. Sample pieces of approximately 10-15 mg were cut and encapsulated in aluminium pans, covered with aluminium lids, and sealed using a crimper. A reference pan was loaded with a sample pan into the cell of the equipment, which was sealed in a nitrogen atmosphere at a gas purging rate of 50 ml/min during the test. The samples were heated from 20°C to 200°C at a heating rate of 10 °C/min. Five individual samples were tested for each formulation. Then data was analysed using the TA universal analysis software.

The amount of overall crystallinity was calculated from the following equation:

$$\% Crystallinity = \left[ \frac{\Delta H_m - \Delta H_c}{93.1 \times w} \right] \times 100\% \dots \dots \dots (3.1)$$

Where,  $\Delta H_m$  is the measured heat of fusion;  $\Delta H_c$  is the enthalpy of cold crystallisation; 93.1(J/g) is the enthalpy of fusion for 100% crystalline PLA; and  $w$  is the weight fraction of PLA in PLA nanocomposites.

#### 3.3.2 Water vapour transmission rate test

Water vapour transmission rate is actually the flux, which is the amount of water (Q) diffusing across unit area (A) in unit time (t).

$$WVTR = Q/At \dots \dots \dots (3.2)$$

Water vapour permeability P is given by

$$P = WVTR \frac{l}{\Delta p} \dots \dots \dots (3.3)$$

where  $l$  is the film thickness;  $\Delta p$  is pressures difference of water vapour on either side of the film.

WVTR of various sample sheets was measured using a MOCON Permatran-W@398 operated with permeability system software. The machine has two

separate cells in each side, so two samples can be tested at the same time. The test setup parameters are listed in Table 3.6. The main parts of the sample insertion system are illustrated in Figure 3.6.

Table 3.6 MOCON WVTR test setup parameters

Temperature setpoint	37.8 °C
Barometric pressure	760 mmHg
Relative humidity (RH)	90%
Compensate RH to	100%
Ambient temperature	23 °C
Sample area	50 cm <sup>2</sup>
Test range	5% RH
Dry side setpoint	10% RH
Nitrogen gas flow rate	0.5 L/min

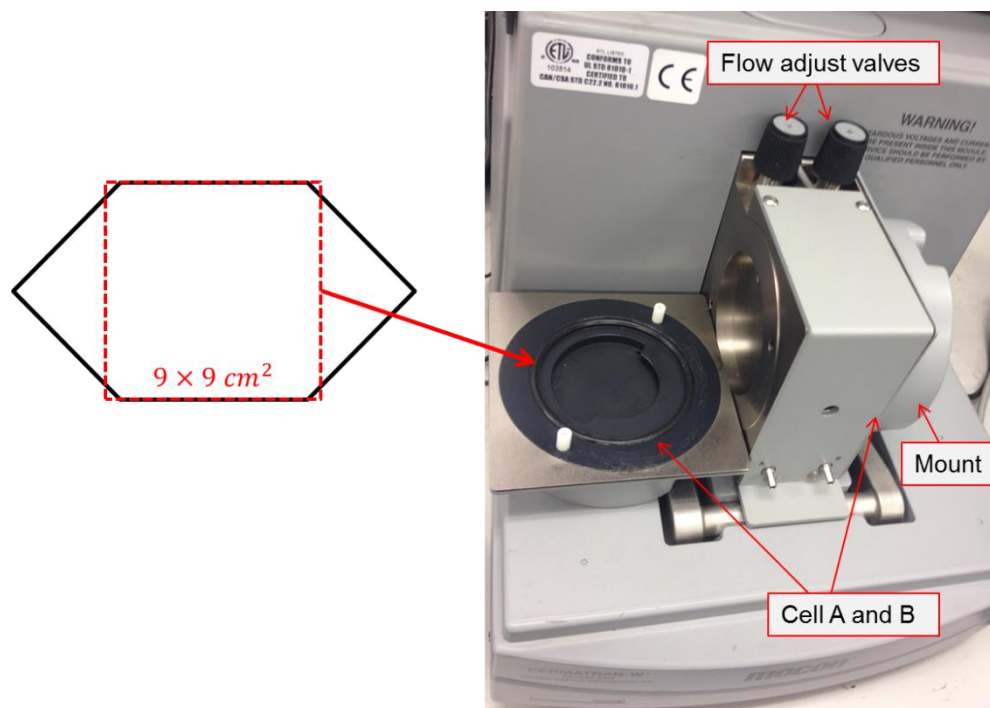


Figure 3.6 Main parts of sample insertion system of MOCON

The sample was cut out into a 9x9 cm<sup>2</sup> square. The average thickness of the sample sheet was measured using a digital micrometer and inputted into the permeability system software. Since the thicknesses of the samples are different, the WVTR value is normalised to a film of 25 μm or 1 mil (1/1000 inch) thickness, with the same unit as raw WVTR, given by:

$$WVTR (normalised) = WVTR(raw) \times \frac{l}{25} \dots\dots\dots(3.4)$$

Figure 3.6 shows parts of the sample insertion system. An appropriate silicon sealant was lightly greased on the rim edge of the cells where sample was to be mounted. After the samples were properly placed the cells were closed and the test was started. The data was calibrated using a ‘Certified Yellow Film’ standard with a WVTR of 23.53 gm/m<sup>2</sup>/day at 37.8°C. The WVTR value collected from the machine is normalised WVTR.

### 3.3.3 Wide angle X-ray diffraction (WAXD)

Wide-angle X-ray diffraction was used to investigate the extent of dispersion and delamination of the organoclay in the PLA nanocomposite samples. WAXD traces of pure PLA, organoclay and PLA nanocomposite samples were collected on a Brucker D8 Diffractometer using the  $Cu - K\alpha$  radiation ( $\lambda = 1.542 \text{ nm}$ ). The diffractometer was controlled using Diffract Plus XRD Commander and WAXD data was analysed using EVA software. A piece of sample sheet (about 2 x 2 cm<sup>2</sup>) was laid flat on a plastic block. A piece of plasticine was stuck between the sample and the block to adjust the sample surface to the same level as the reference plane of the instrument. Samples were scanned in the angular region ( $2\theta$ ) of 1°-10°.

### 3.3.4 Birefringence

Birefringence measurements were carried out using a Leica microscope equipped with a tilting compensator B (measurement range from  $1-5\lambda$  orders) and compensator K ( $30\lambda$  orders).

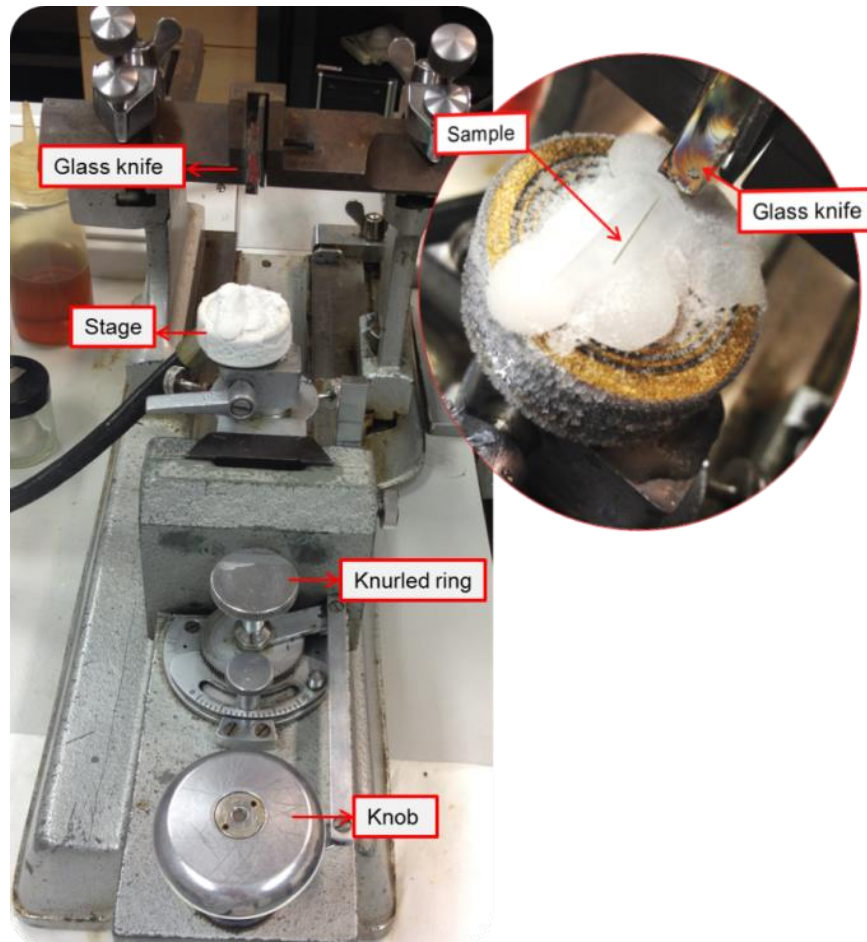


Figure 3.7 Parts of cold stage microtome and a sample being cut on it.

The birefringence sample was prepared on a cold stage microtome operated with glass knife. Figure 3.7 shows parts of the cold stage microtome and a sample being cut on it. A piece of sample (around 3mm x 10mm) was cut off and placed straight to the cutting direction on the brass block of the microtome. A drop of water was put on the sample and frozen on the stage by giving a quick blast (about 3-4 seconds) of liquid CO<sub>2</sub>. This is to make sure the sample was held steady on the stage. More drops of water were added onto the sample and left to be frozen until the sample was fully covered in ice. The height of the stage was then adjusted to align the ice just below the knife blade before cutting. The

thickness of the microtomed cross-section was set by rotating the smooth round knob (usually 10  $\mu m$  for birefringence samples). Sample slices were cut off and left on the glass knife, which were collected using tweezers and dried using a piece of filter paper. Then the sample was mounted in an appropriate liquid on a glass slide and covered by a coverslip for observation.

The orientation of the sample was determined using a polarised optical microscope. The sample slide was observed using a 10x magnification objective lens and a 546 nm filter. The sample was moved into the extinction position by rotating the object stage. Then the object stage was rotated by 45° to find the diagonal position for the object (in which the maximum brightness of the object can be obtained). A tilting compensator B was inserted into the tube slot and tilted by rotating the drum on the compensator in two directions. When the object turned back (extinguished), the tilting angles ( $i'$  and  $i''$ ) can be read from a scale on the compensator knob. Therefore, the value of  $2i = i' + i''$  can be calculated, which was used to evaluate the phase difference ( $\Gamma$ ) of the object from a given table in the instructions of the compensator. Then the birefringence of the object can be calculated from the following equation:

$$\Delta n = \frac{\Gamma}{d} \dots\dots\dots(3.5)$$

where  $\Gamma$  is the phase difference;  $d$  is the thickness of the sample, which was 10  $\mu m$  in this case.

### 3.3.5 Transmission electron microscopy (TEM)

TEM samples were prepared on a Cambridge Instruments ultra-microtome fitted with a diamond edge blade. The melt compounded sample pellet was firstly sharpened into a pencil-like point and then mounted on the ultra-microtome to shave off thin slices (~ 100 nm thick), as shown in Figure 3.8. A reservoir of de-ionised water was used to contain the sliced off sample pieces, which were then scooped onto a copper mesh and left on an absorbent paper to dry before being observed.

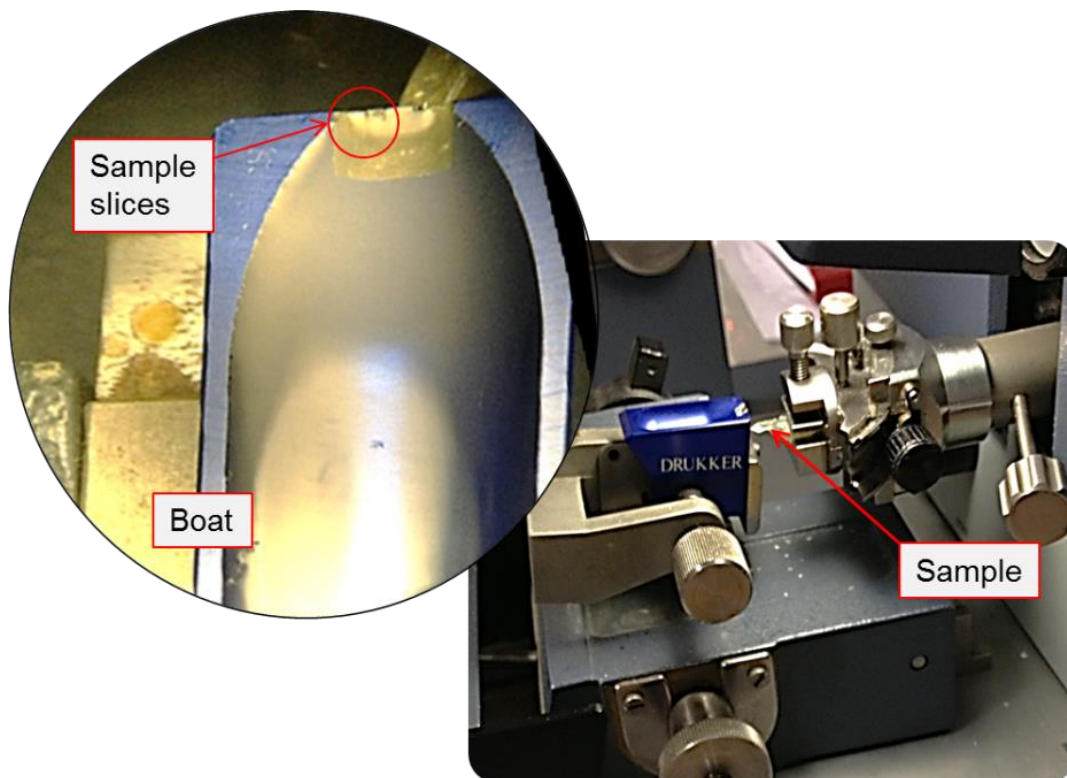


Figure 3.8 Cutting of TEM samples

TEM observation was carried out a JEOL, JEM-2000FX electron microscope operated at an accelerating voltage of 100kV. PLA nanocomposite samples were observed at various magnifications of 25, 40, 100, 200 and 400 thousand times. Image J photograph software was used to measure the aspect ratios of the clay platelets from TEM images.

### 3.3.6 Scanning electron microscopy (SEM)

The surface morphology of electrospun PLA based nanofibres was evaluated using a Carl Zeis (Leo) 1530VP field emission gun scanning electron microscope (FEGSEM). Samples for SEM were coated using a gold/palladium sputter for 1 min (SC7604, Emitech). The average diameter of the nanofibres was measured on the SEM images using image softwares (ImageJ and IBM SPSS Statistics).

### 3.3.7 Tensile testing of electrospun mats

The mechanical properties of PLA nanofibre mats were analysed by tensile tests following the ISO257-2-5A specification. For the sample preparation, PLA nanofibre mats were firstly peeled off from the foil as shown in Figure 3.9. The nanofibre mats for tensile test should be electrospun for about 4 hrs at a rate of 1ml/hr, as to obtain thick and consistent nanofibre mats. The average thickness of the mats was about 0.09 mm. Then the nanofibre mats were cut into tensile bar specimens using cutting equipment (Ray-Ran RR/PCP). The profile of the specimens was Dumbbell shaped ISO 257-2-5A. For each PLA solution 3 tensile specimens were cut for tensile testing.



Figure 3.9 PLA nanofibre mats peeled off

Tensile testing on PLA nanofibres was carried on an INSTRON 5944 Micro Tester. During the test, PLA nanofibre specimens were clamped between two rubbery clamps. A load force of 2 kN was used. The tensile speed was firstly 2 mm/min until the load was up to 0.1N, and then changed to 3 mm/min until the sample was broken. Tensile strength, Young's modulus and elongation at break of PLA nanofibres were calculated from each test.

### **3.3.8 Antibacterial testing of electrospun mats**

Bacterial cultures of *E. coli* – K12 (Wild Type) were prepared in 100 ml Lysogeny Broth (LB), which were inoculated and incubated at 37 °C for 24 hrs in an autoclave. Then LB Agar Petri plates were seeded with 1 ml of the incubated bacterial culture (prepared according to manufacturer's instructions). Electrospun PLA/ ZnO fibre mats were folded and pressed into discs and placed onto the incubated Agar Petri plates to have further incubation at 37°C for 24 h. Then clear zones of inhibition were observed and the diameter of the inhibition zone was measured.

## 4 Effect of clay on the water barrier property of PLA nanocomposites

### 4.1 Effect of clay concentration on quenched PLA nanocomposites

#### 4.1.1 DSC of quenched PLA nanocomposites

The DSC first heating scans for PLA4060D and PLA nanocomposites of various clay concentrations are displayed in Figure 4.1. The step change at 56°C relates to the glass transition temperature ( $T_g$ ) of the polymer. An endothermic peak is observed just after the glass transition temperature. This is associated with relaxation of non-equilibrium structure. It was observed that as the clay concentration increased the endothermic peak tended to decrease in intensity, which suggested that the nanoclay had a confining effect on polymer chain relaxation. However, the glass transition temperature (see Table 4.1) decreased slightly as the nanoclay content increased in the PLA nanocomposites. This phenomenon may be due to a plasticising effect of the nanoclay surfactant that enhanced the glass transition process. A decrease in  $T_g$  for PLA nanocomposites has also been reported in some previous studies [149]–[151].

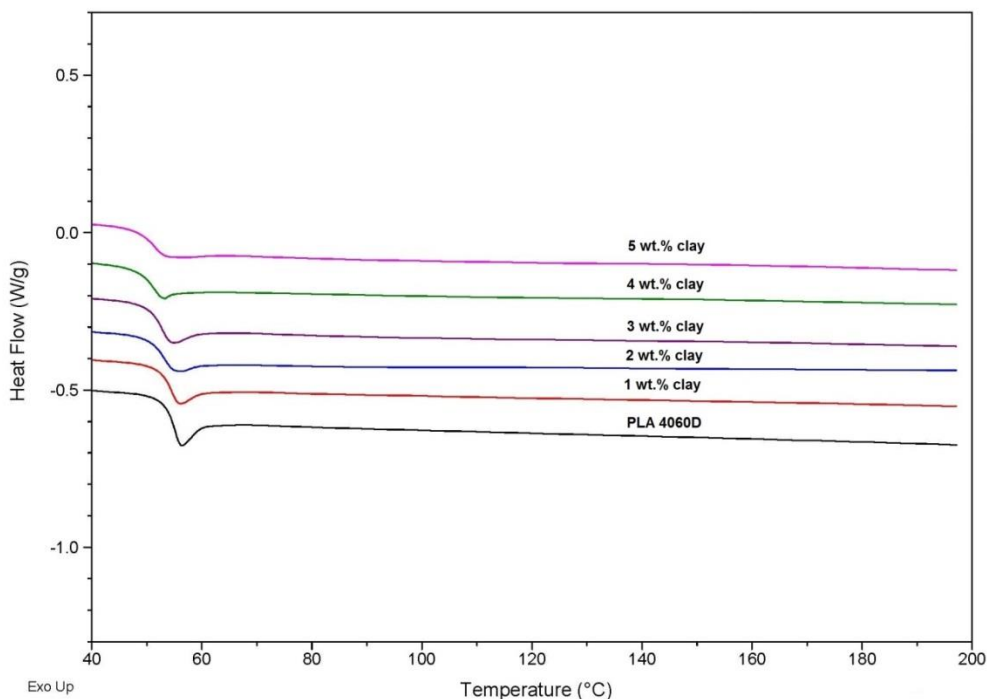


Figure 4.1 DSC curves of pure PLA4060D and its nanocomposites containing 1-5 wt.% clay contents

Table 4.1 DSC data for all samples

Sample	Tg
Quenched PLA	56±1 °C
Quenched PLA+1wt.%nanoclay	55±1 °C
Quenched PLA+2wt.%nanoclay	52±1 °C
Quenched PLA+3wt.%nanoclay	53±1 °C
Quenched PLA+4wt.%nanoclay	51±1 °C
Quenched PLA+5wt.%nanoclay	52±1 °C

#### 4.1.2 TEM of quenched PLA nanocomposites

The transmission electron micrographs of PLA nanocomposites containing 1, 2 and 3 wt.% clay at different magnifications are shown in Figure 4.2. From the low magnification images, it is observed that the clay particles are aligned and evenly distributed in the PLA matrix. The alignment of the clay particles took place during the polymer melt compounding, and remained in the same direction as the polymer melt flow after cooling. The intercalated structures of the nanoclay are shown in the high magnification images. It is also observed that single layered silicates are delaminated in the PLA matrix.

A micrograph of a 3 wt.% nanoclay sample at 200k magnification is shown in Figure 4.3, in which the intercalated clay structure can be clearly seen. A micrograph of a 1 wt.% nanoclay sample at 200k magnification, as shown in Figure 4.4, clearly presents exfoliated single layered clay platelets in the polymer matrix. A more detailed view of the delamination structure of clay platelets is given in Figure 4.5 and Figure 4.6, which are 400K magnification TEM images of a 1 wt.% and a 3 wt. % nanoclay sample. In these micrographs, the dark lines are the edges of exfoliated single layered clay platelets.

The length and thickness of the clay platelets are able to be measured from the TEM micrographs using Image J software. More than 200 clay platelets were measured from 7 high magnification micrographs with different clay content. The

average length and thickness of the clay platelets was found to be  $90 \pm 15$  nm and  $2.1 \pm 0.5$  nm, respectively. Hence, the average aspect ratio (length/thickness) of the organoclay within PLA matrix was approximately 40.

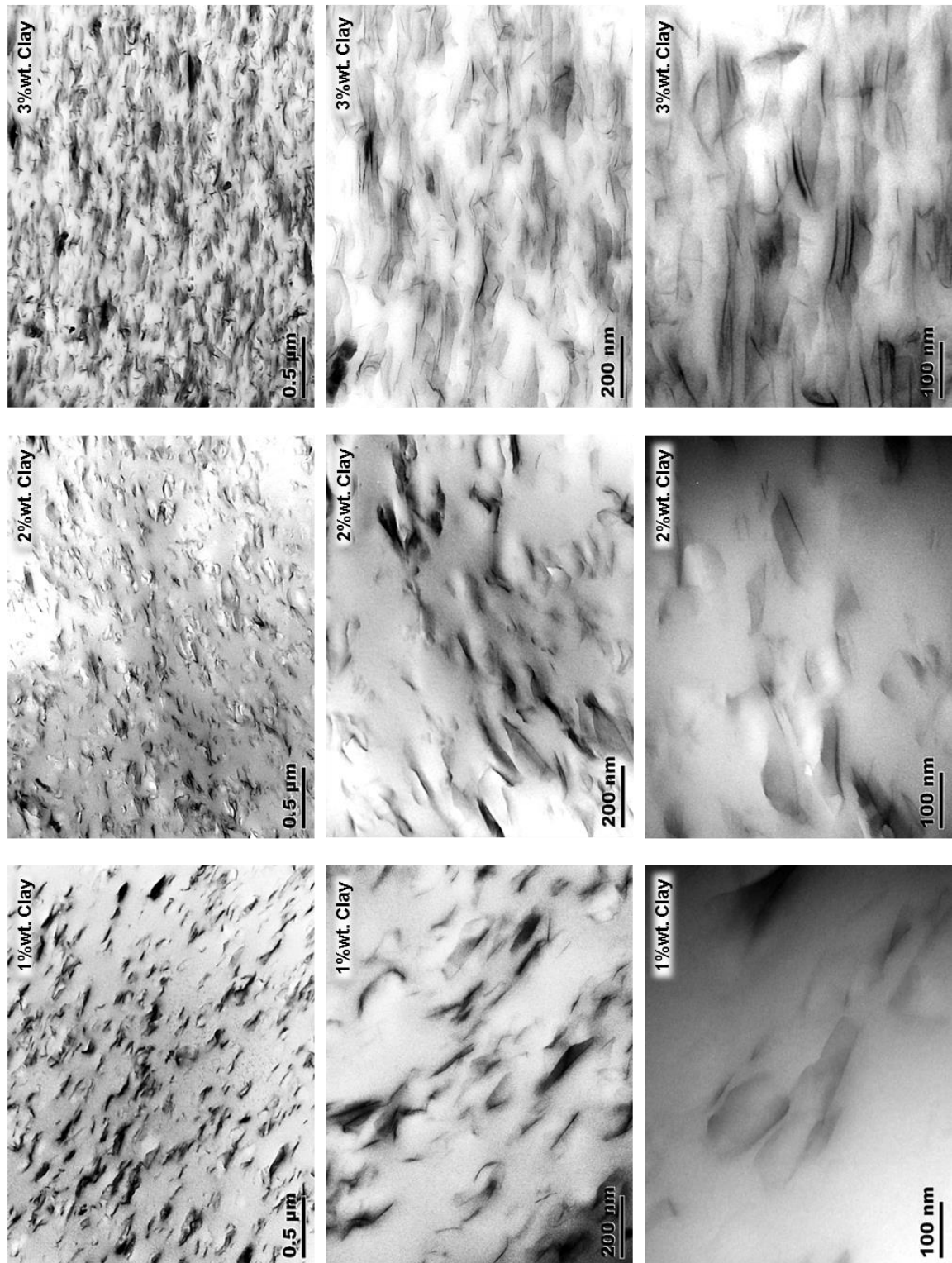


Figure 4.2 TEM images of PLA nanocomposites containing 1, 2, 3 wt. % clay at 40k, 100k and 200k magnifications

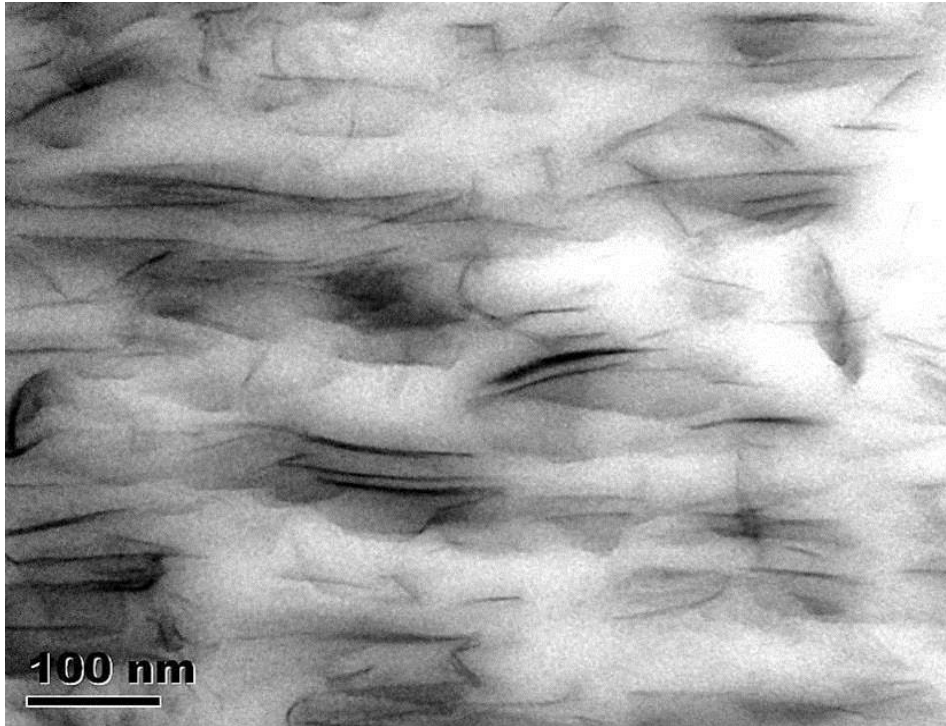


Figure 4.3 Transmission electron micrograph of PLA nanocomposite with 3 wt.% clay at 200K magnification

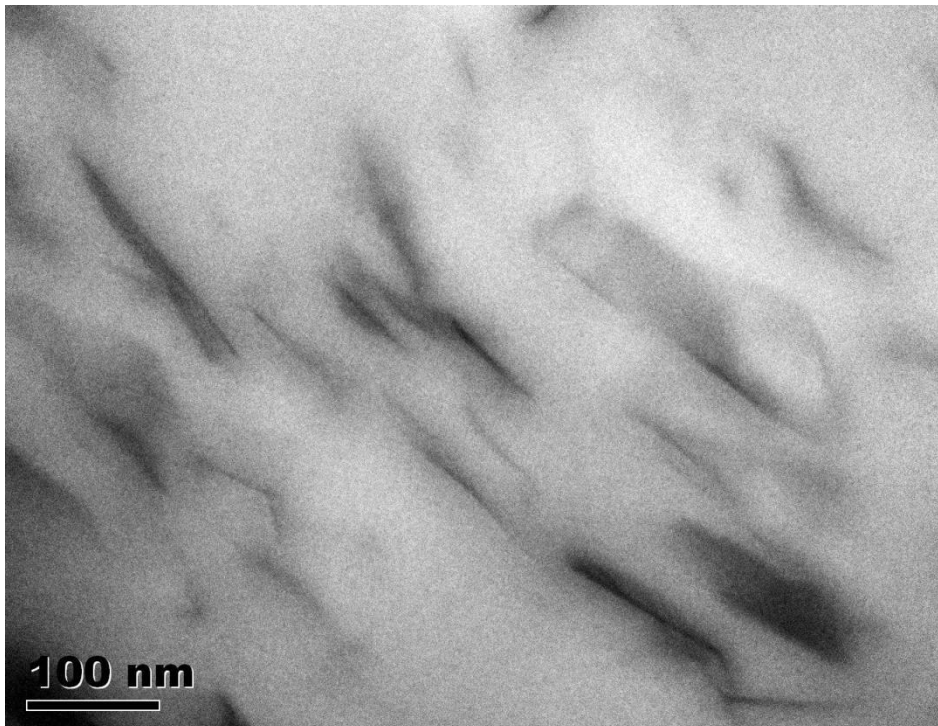


Figure 4.4 Transmission electron micrograph of PLA nanocomposite with 1 wt.% clay at 200K magnification

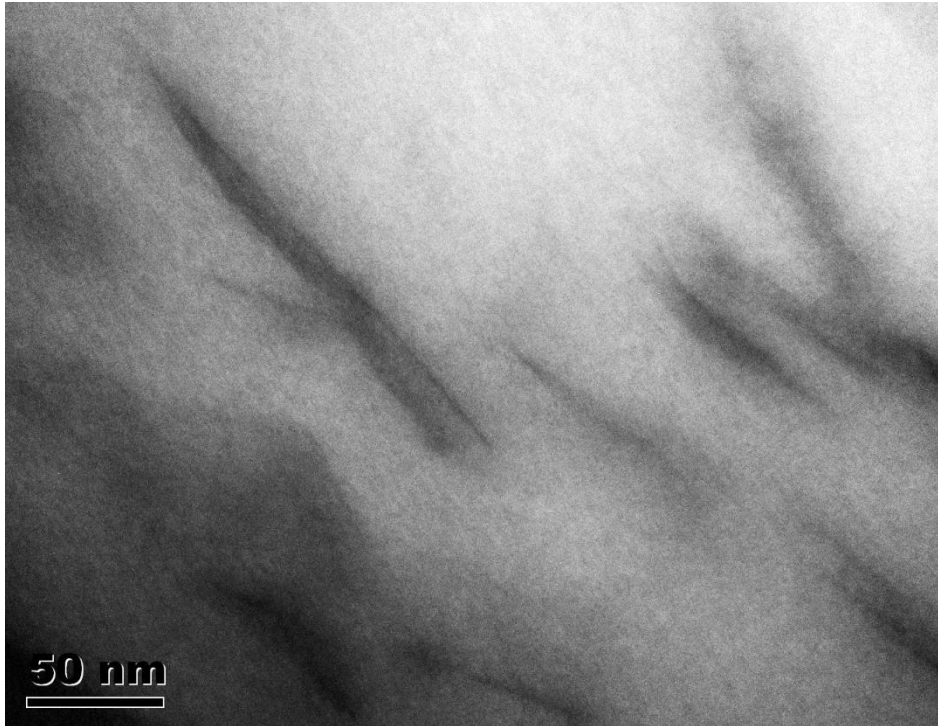


Figure 4.5 Transmission electron micrograph of PLA nanocomposite with 1 wt.% clay at 400K magnification

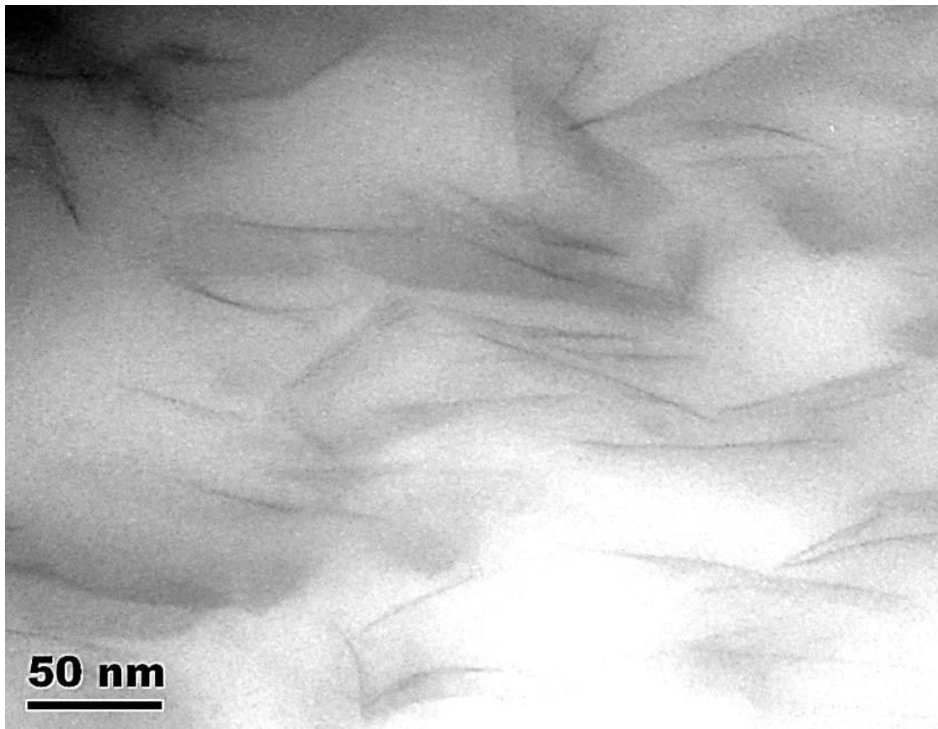


Figure 4.6 Transmission electron micrograph of PLA nanocomposite with 3 wt. % clay at 400K magnification

### 4.1.3 WAXD of quenched PLA nanocomposites

WAXD traces for Cloisite 30B organoclay, PLA and PLA nanocomposite containing 3 wt.% clay are shown in Figure 4.7. In the trace of the nanoclay, the peak at  $2\theta = 4.8^\circ$  corresponds to a clay interlayer spacing ( $d_{001}$ ) of 1.8 nm. In the PLA nanocomposite, the peak shifted to  $2.7^\circ$  corresponding to an interlayer spacing of 3.3 nm. This result indicates that the layered platelet had been exfoliated and widened within the PLA matrix, which means that an intercalated structure has been produced. The XRD result is consistent with TEM observations on the nanocomposites samples.

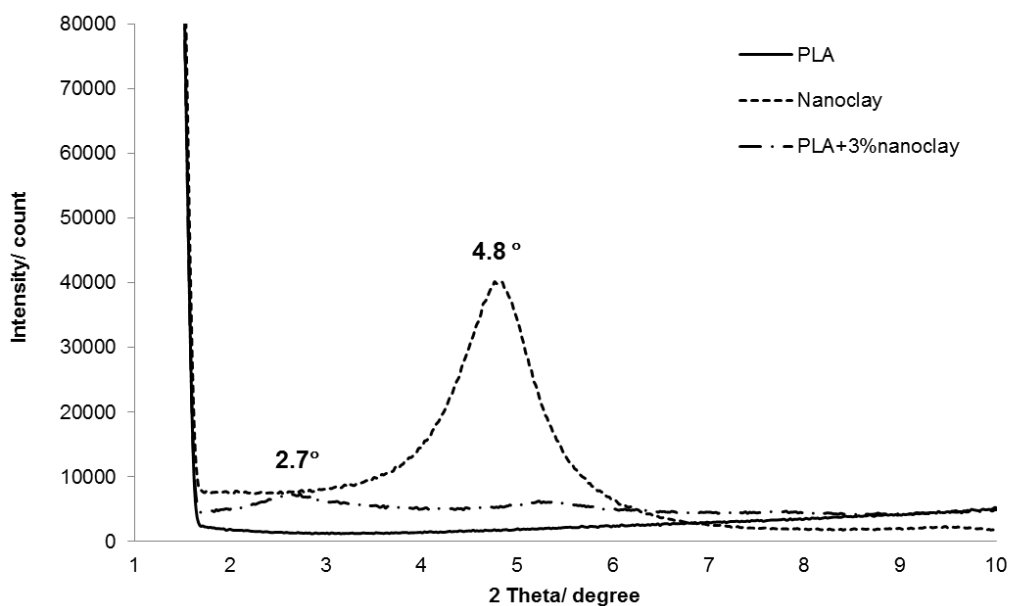


Figure 4.7 WAXD traces of organoclay, PLA and PLA nanocomposite

The XRD result is in agreement with some other published WAXD data for PLA nanocomposites. McLauchlin and Thomas [152] have reported that Cloisite 30B clay has an interplanar spacing of 1.8 nm, which increased to 3.5 nm in the intercalated PLA nanocomposites produced by solvent casting. Rhim et al. [97] found that the interlayer distance of Cloisite 30B was 1.86 nm, while that for PLA / Cloisite 30B nanocomposite was increased to 3.14 nm. Thellen et al. [98] reported that the interlayer spacing in montmorillonite layered silicate was increased from 1.8 to 3.2 nm in PLA nanocomposite produced by blow film extrusion. Duan et al. [75] reported that the interlayer spacing of Cloisite 30B nanoclay was increased from 1.84 nm to 3.4 nm after melt compounding with PLA.

#### 4.1.4 Water vapour permeability results

Water vapour transmission rate (WVTR) data for the PLA and PLA nanocomposite sheets is plotted as a function of weight % nanoclay, as shown in Figure 4.8. Five individual samples were measured for each data point. The results show a significant decrease with increasing clay content and level off at clay content of 5 wt.%. The sample with 5 wt.% nanoclay addition shows the lowest permeability, which was reduced by about 37% compared with the neat PLA. The results of WVTR are listed in Table 4.2.

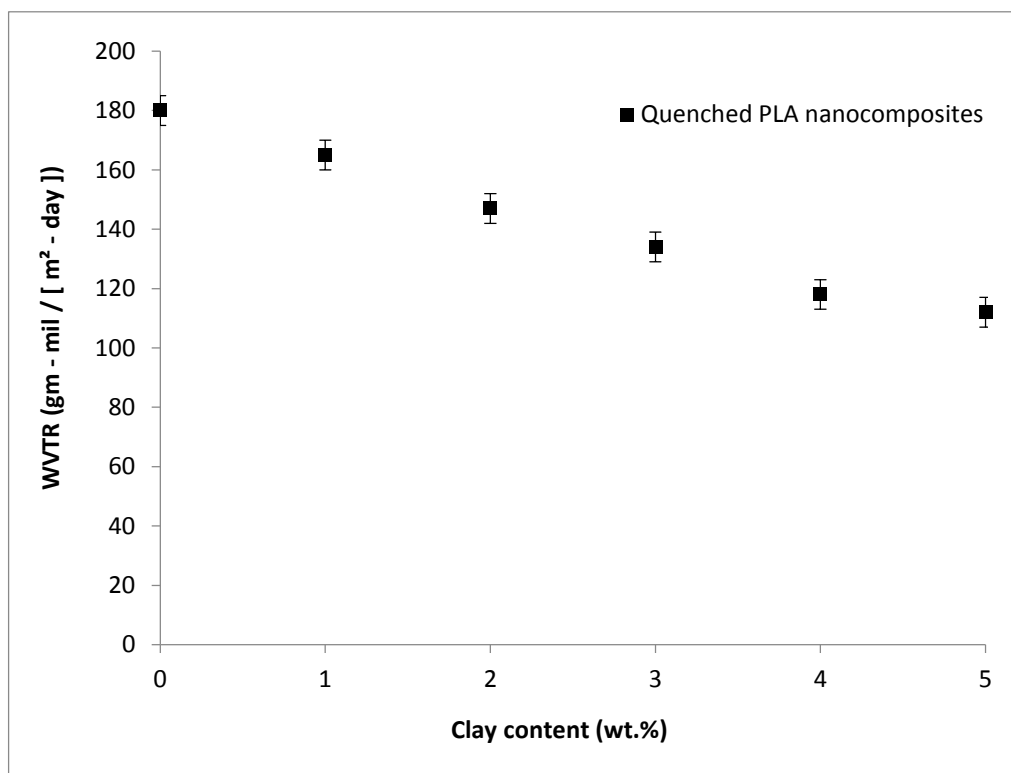


Figure 4.8 Water vapour permeabilities of neat PLA and PLA nanocomposites

Table 4.2 Water vapour transmission rate of quenched PLA nanocomposites

Sample	WVTR (gm-mil/[m <sup>2</sup> -day])
Quenched PLA	180 ± 3
Quenched PLA+1wt.%nanoclay	165 ± 3
Quenched PLA+2wt.%nanoclay	147 ± 2
Quenched PLA+3wt.%nanoclay	134 ± 3
Quenched PLA+4wt.%nanoclay	118 ± 1
Quenched PLA+5wt.%nanoclay	112 ± 3

### Interpretation by tortuous path models

Since the samples are amorphous PLA, the reduction in water vapour permeability originates from the incorporation of nanoclay. As it is discussed in Section 2.3, the mechanism by which the barrier properties of polymer nanocomposites are improved is by a so-called ‘tortuous path’ effect, which was first proposed by Nielsen [73]. In the model, the diffusion path length of gas or water vapour molecules is dramatically increased due to obstacles created by nanofiller particles.

In the present study, the Nielsen equation was used to calculate the theoretical permeability of PLA nanocomposite given that the aspect ratio (L/D) is 40, as shown below:

$$\frac{P_F}{P_u} = \frac{\phi_P}{1+(L/2D)\phi_F} \dots\dots\dots(4.1)$$

where L/D=40;  $P_F$  is the theoretical permeability of PLA nanocomposite

$P_u$  is the permeability of neat PLA, which was found to be 180 gm - mil / [ m<sup>2</sup> - day;  $\phi_P$  and  $\phi_F$  are the volume fractions of the PLA matrix and nanoclay, which can be obtained by knowing that the density of PLA is 1.24 g/cm<sup>3</sup> and the density of nanoclay is 1.98 g/cm<sup>3</sup>;

To fit our experimental data with the Nielsen model, the weight fraction of nanoclay should be converted to volume fraction since it is required in the Nielsen

equation.

$$\phi_F = \frac{W_F/\rho_F}{W_F/\rho_F + W_P/\rho_P}$$

Where  $W_F$  and  $W_P$  are the weight fraction of the nanoclay and PLA;  $\rho_F$  and  $\rho_P$  are the densities of nanoclay and PLA.

Take a sample with 1 wt.% nanoclay for example, the volume fraction of the nanoclay is:

$$\phi_F = \frac{1\%/1.98}{1\%/1.98 + 99\%/1.24} = 0.6\%$$

The weight to volume fraction conversion for samples containing 1-5 wt.% clay is shown in Table 4.3.

Table 4.3 Weight fraction to volume fraction conversion

<b>Weight fraction</b>	<b>Volume fraction</b>
1 wt. %	0.6 vol%
2 wt. %	1.3 vol%
3 wt. %	1.9 vol%
4 wt. %	2.6 vol%
5 wt. %	3.2 vol%

A plot of the permeability versus volume fraction of clay content is shown in Figure 4.9, in which the Nielsen theoretical permeability is compared with the experimental data. It is found that the predicted line of the Nielsen permeability lay just below the experimental data points, which indicates that the experimental data fit the 'Nielsen theory' well. This result is in agreement with the work of Duan et al. [75], who first fitted the permeability of the polymer nanocomposites with the Nielsen model.

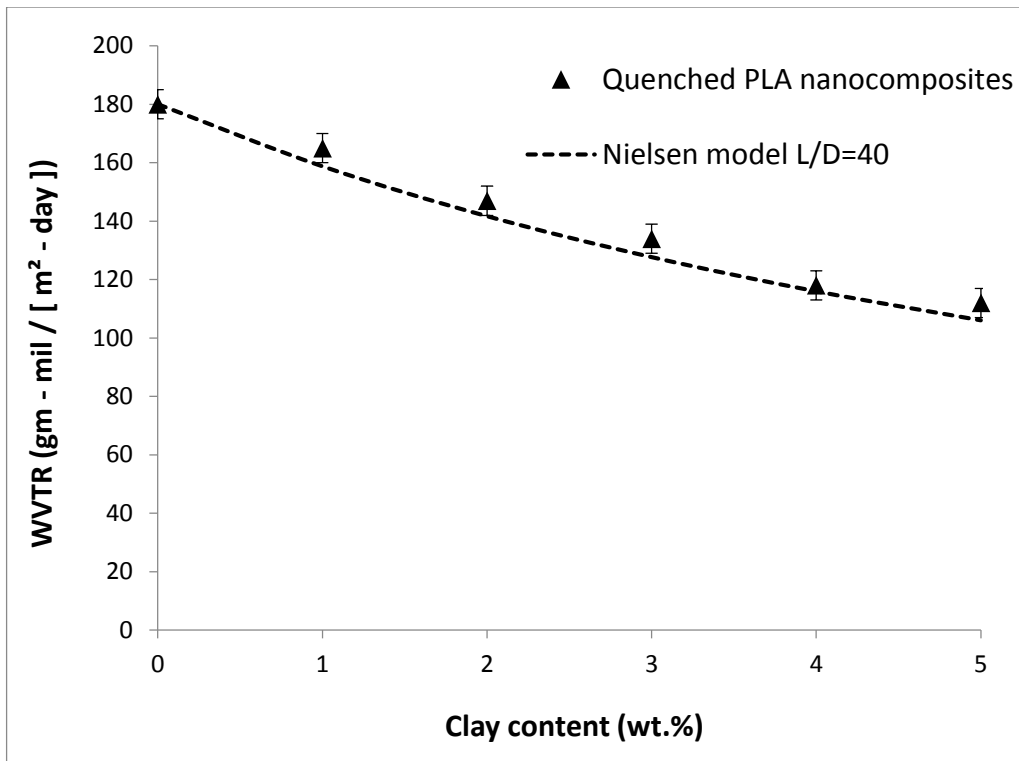


Figure 4.9 Water vapour permeabilities of PLA and PLA nanocomposites in comparison with Nielsen theoretical values

The difference between the experimental and predicted data is probably due to the clay platelets not being 100% exfoliated and not orientated perpendicularly to the diffusion direction. Therefore, in the next section annealing was introduced to the PLA sheets to obtain crystallinity in order to improve the barrier property of PLA nanocomposites.

## 4.2 Effect of annealing on PLA nanocomposites

### 4.2.1 DSC of annealed PLA nanocomposites

Figure 4.10 shows the DSC first heating scan for the crystallisable PLA, grade 4032D, that had been annealed. The glass transition temperature is 57 °C and the melting point is 170 °C . There is a small peak at about 162 °C merging into the main melting peak. The occurrence of such a double melting peak in PLA has been previously reported [25], [26], [29]–[31], [101]. One explanation of double melting is associated with melt-recrystallisation, which suggests that the high-temperature endotherm can be attributed to the melting of original crystals and the low-temperature endotherms are due to crystals formed through recrystallisation due to cold crystallisation. Sometimes double melting peaks can be associated with different crystalline forms. For example, Sawai et al. [26] obtained both  $\alpha$  crystal and  $\beta$  crystals in uniaxially orientated PLLA and found double melting peaks in the DSC scan. The main melting peak corresponded to the melting of  $\alpha$  crystals, whereas the lower temperature peak, at about 10°C below the main peak, was due to the melting of orientated  $\beta$  crystal phases. In other cases the double peak is due to disordered crystallites. Pan et al. [29], [30] observed double melting in PLLA and attributed it to the formation of a disordered  $\alpha'$  crystal phase. They proposed that the high temperature melting peak corresponded to melting of the  $\alpha$  phase, which is the ordered crystalline form, whereas the lower peak corresponded to melting of the disordered  $\alpha'$  phase.

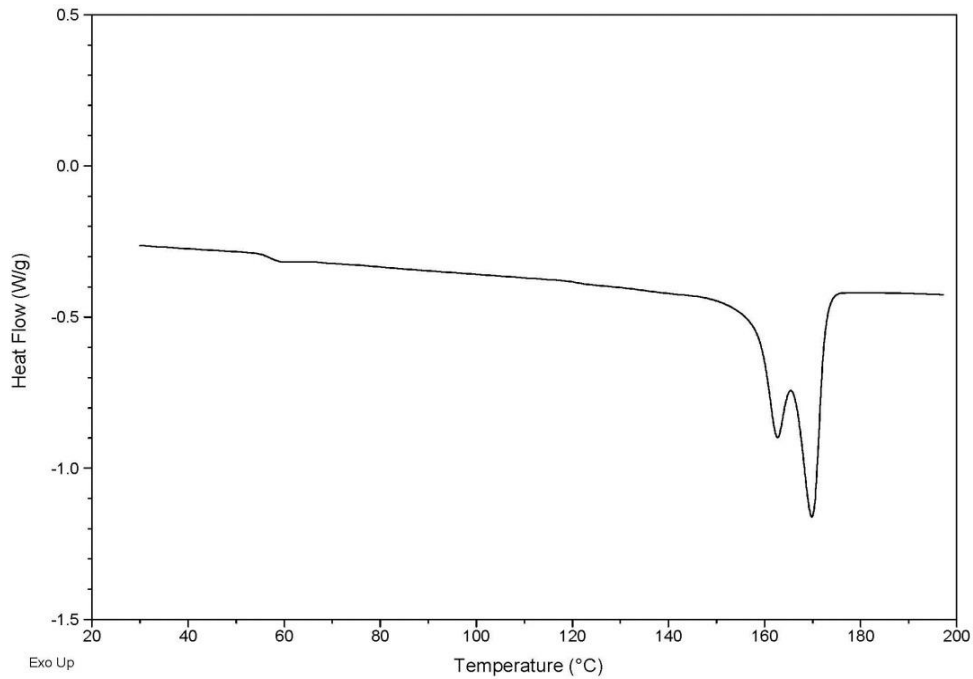


Figure 4.10 DSC heating scan for the annealed PLA 4032D

Annealed PLA nanocomposites were found to exhibit different melting behaviours from the annealed neat PLA. Figures 4.11 - 4.13 show DSC heating scans of the annealed PLA nanocomposites with 1, 3 and 5 wt.% nanoclay. Although, the glass transition temperature and the melting point are still at 57°C and 170°C, respectively, the lower melting peak has virtually disappeared as the clay loading increased up to 5 wt.%, showing that the nanoclay has promoted formation of the more stable  $\alpha$  crystal phase during annealing.

Table 4.4 Summarises the DSC result of samples with various clay concentrations. It is seen that the crystallinity of annealed PLA nanocomposites was about 30%. The clay concentration had no effect on the extent of crystallinity of the annealed samples.

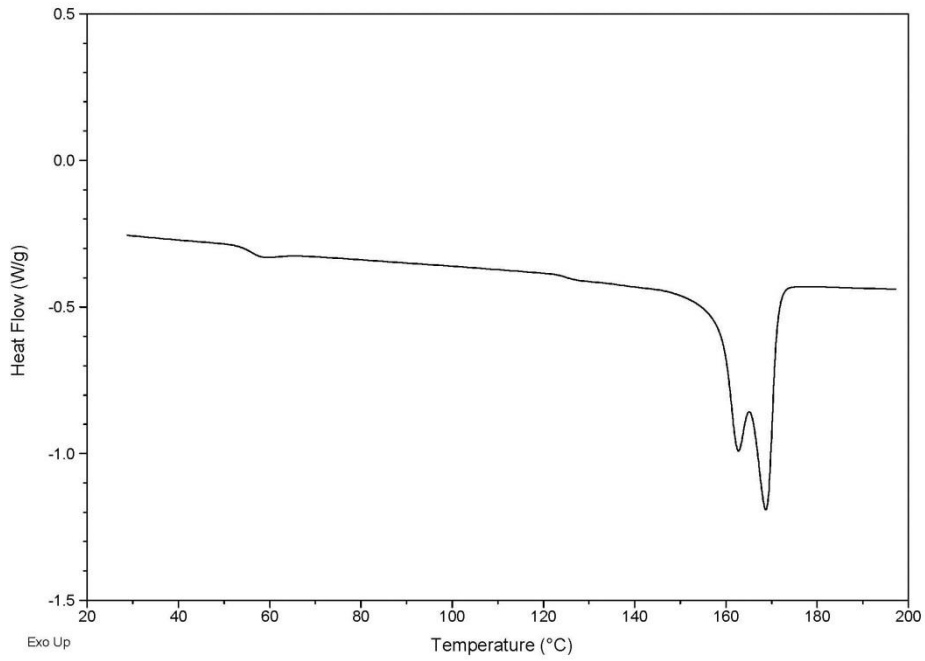


Figure 4.11 DSC heating scan for the annealed PLA 4032D nanocomposite with 1 wt.% nanoclay

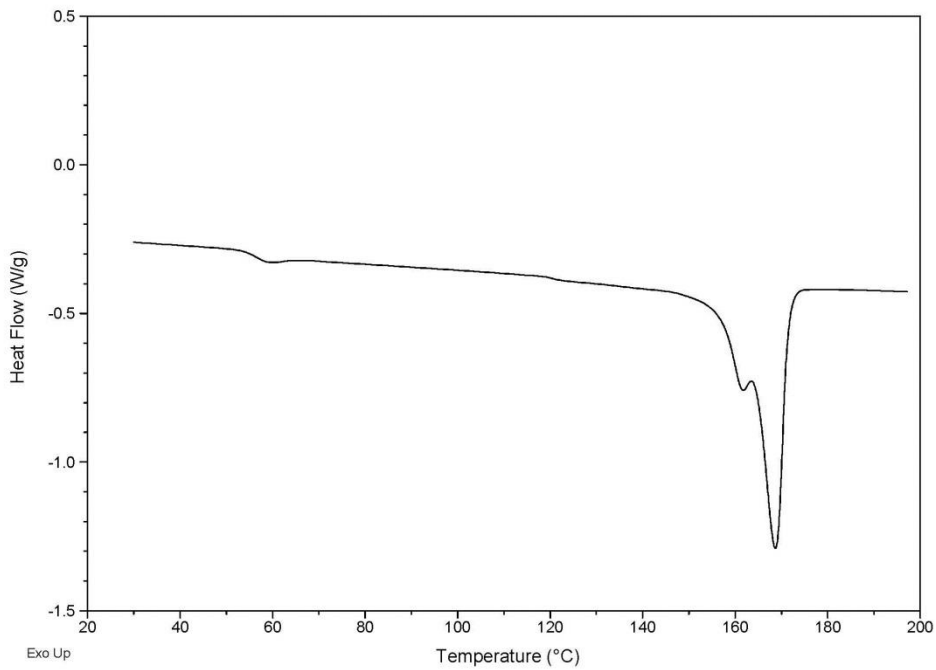


Figure 4.12 DSC heating scan for the annealed PLA 4032D nanocomposite with 3 wt.% nanoclay

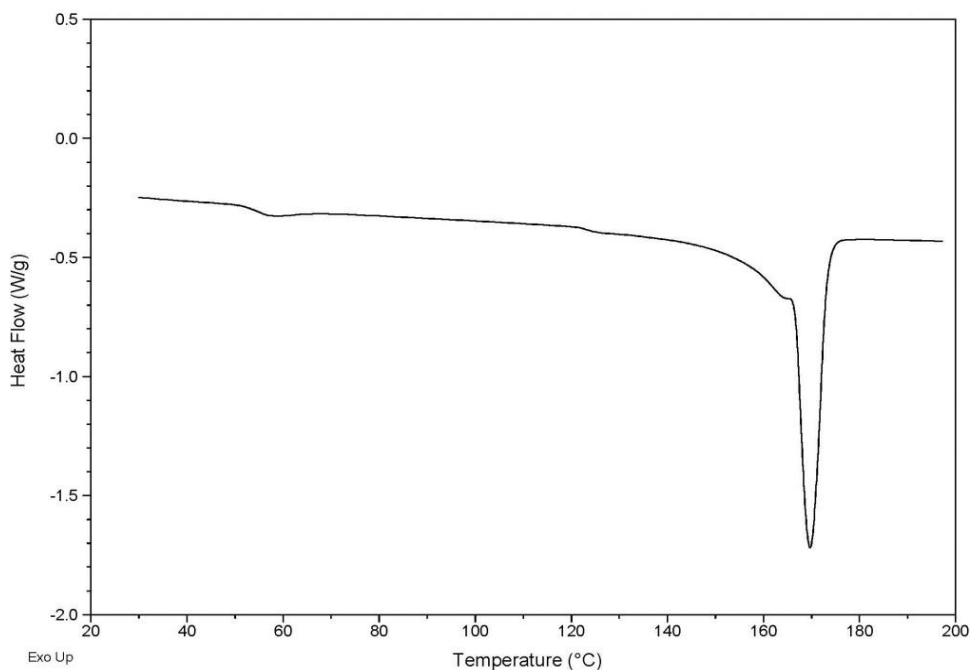


Figure 4.13 DSC heating scan for the annealed PLA 4032D nanocomposite with 5 wt.% nanoclay

Table 4.4 DSC data for all samples

Sample	T <sub>g</sub>	T <sub>m</sub>	Crystallinity
Quenched PLA	56±1 °C	----	0%
Quenched PLA+1wt.%nanoclay	55±1 °C	----	0%
Quenched PLA+2wt.%nanoclay	52±1 °C	----	0%
Quenched PLA+3wt.%nanoclay	53±1 °C	----	0%
Quenched PLA+4wt.%nanoclay	51±1 °C	----	0%
Quenched PLA+5wt.%nanoclay	52±1 °C	----	0%
Annealed PLA	57±1 °C	170±1 °C	30±1%
Annealed PLA+1wt.%nanoclay	56±1 °C	170±1 °C	32±1%
Annealed PLA+2wt.%nanoclay	56±1 °C	169±1 °C	31±1%
Annealed PLA+3wt.%nanoclay	57±1 °C	169±1 °C	32±1%
Annealed PLA+4wt.%nanoclay	56±1 °C	170±1 °C	31±1%
Annealed PLA+5wt.%nanoclay	56±1 °C	170±1 °C	30±1%

#### **4.2.2 Optical microscopy results of annealed PLA nanocomposites**

The crystalline morphology of a semi-crystalline PLA 4032D film produced by annealing at 115 °C for 15 min was investigated in a hot stage and the crystallite morphology was observed between crossed polars in a Leica® DM LM binocular transmitted light microscope. Figure 4.14 shows a series of micrographs of the sample taken at different temperatures in the hot stage microscope when heated at a rate of 10°C per minute. The change in the crystallite morphology can be interpreted in relation to the DSC scan in Figure 4.10. Some coarser spherulites in a background of tiny crystallites are observed at 115 °C during the heating process. As the temperature reaches 160 °C, some small crystallites begin to blur, whereas some large crystallites grow. When the temperature reaches the melting point, 166-168 °C, the small crystallites blur into the dark background, whereas the large crystallites still exist. At 170 °C the image becomes completely dark, indicating that all the crystallites have melted.

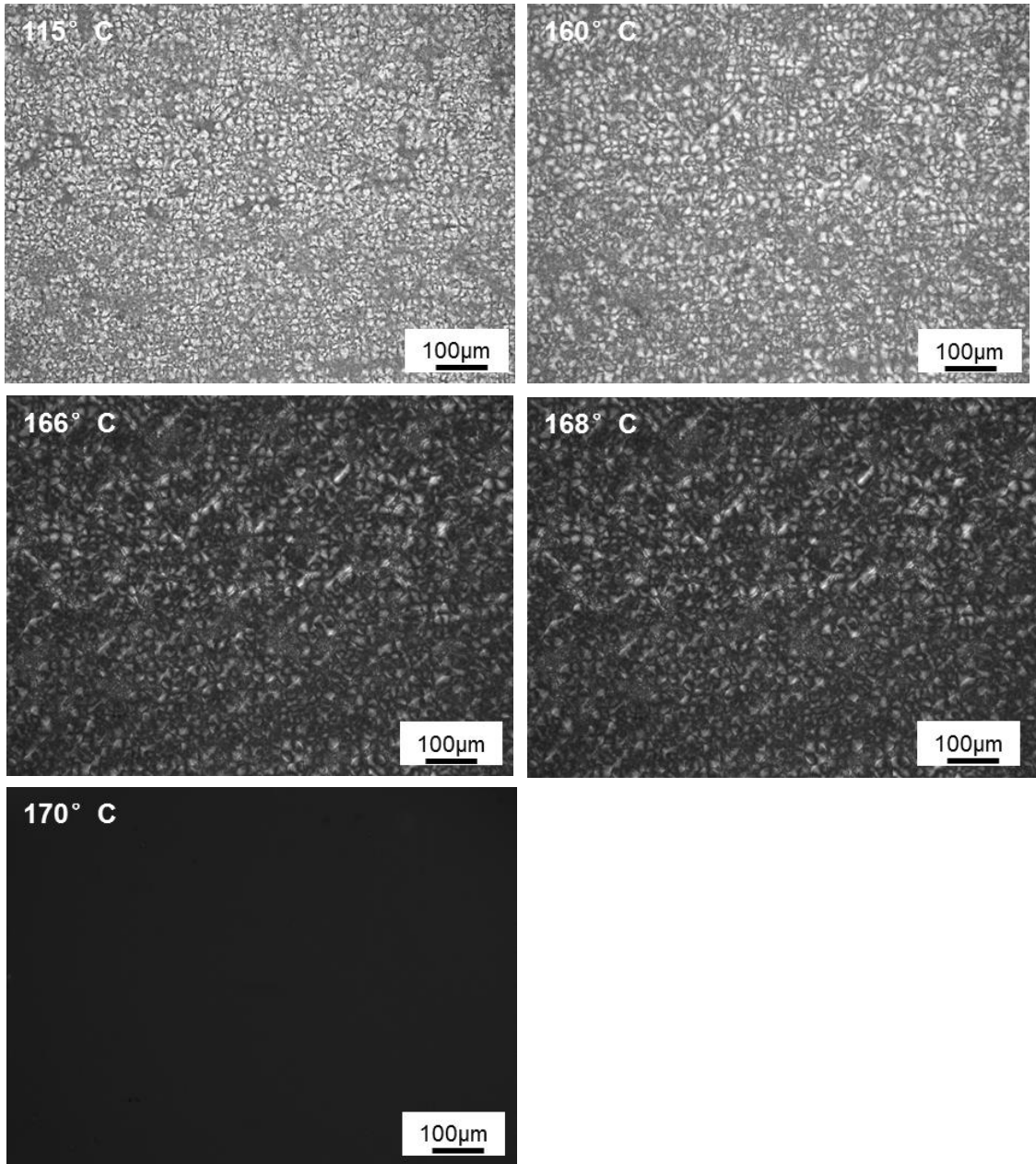


Figure 4.14 Annealed PLA 4032D viewed in hot stage polarised optical microscope when heated at 115 °C and 168 °C and 170 °C

### 4.2.3 XRD results of annealed PLA nanocomposites

Figure 4.15 shows the comparison between the WAXD traces of a quenched and an annealed PLA nanocomposites with 3 wt.% nanoclay. It is found that the  $2\theta$  peak associated with the clay interlayer structure is still at  $2.7^\circ$  after annealing, giving a clay interlayer spacing of 3.3 nm in the samples. This result indicates that the dispersion of clay platelets did not change during annealing.

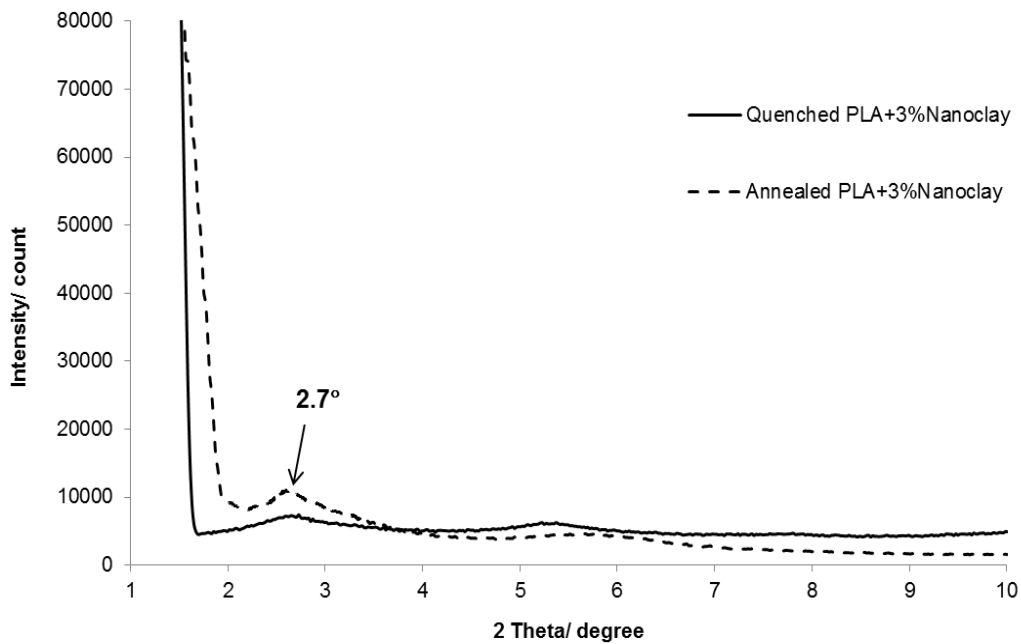


Figure 4.15 WAXD traces of quenched and annealed PLA nanocomposites with 3 wt.% nanoclay

### 4.2.4 TEM results of annealed PLA nanocomposites

The transmission electron micrographs of the quenched and annealed PLA nanocomposites containing 1 wt.% clay at low and high magnifications are shown in Figure 4.16. As discussed in Section 4.1, the quenched samples showed good alignment of the clay layers as seen in the low magnification images (Figure 4.2). The alignment of the clay particles took place during polymer melt compounding, and remains in the same direction as the polymer melt flow after cooling. The higher magnification image shows intercalated structures of the nanoclay. It is observed that the single layered silicates were

also delaminated in the PLA matrix.

However, for the annealed samples, the clay layers are randomly aligned in the low magnification image and well dispersed single layered clay platelets can be observed in the high magnification image. Compared with the XRD result in Figure 4.15, it is concluded that the crystallisation process did not affect the dispersion state of the nanoclay but has changed the alignment of the nanoclay particles.

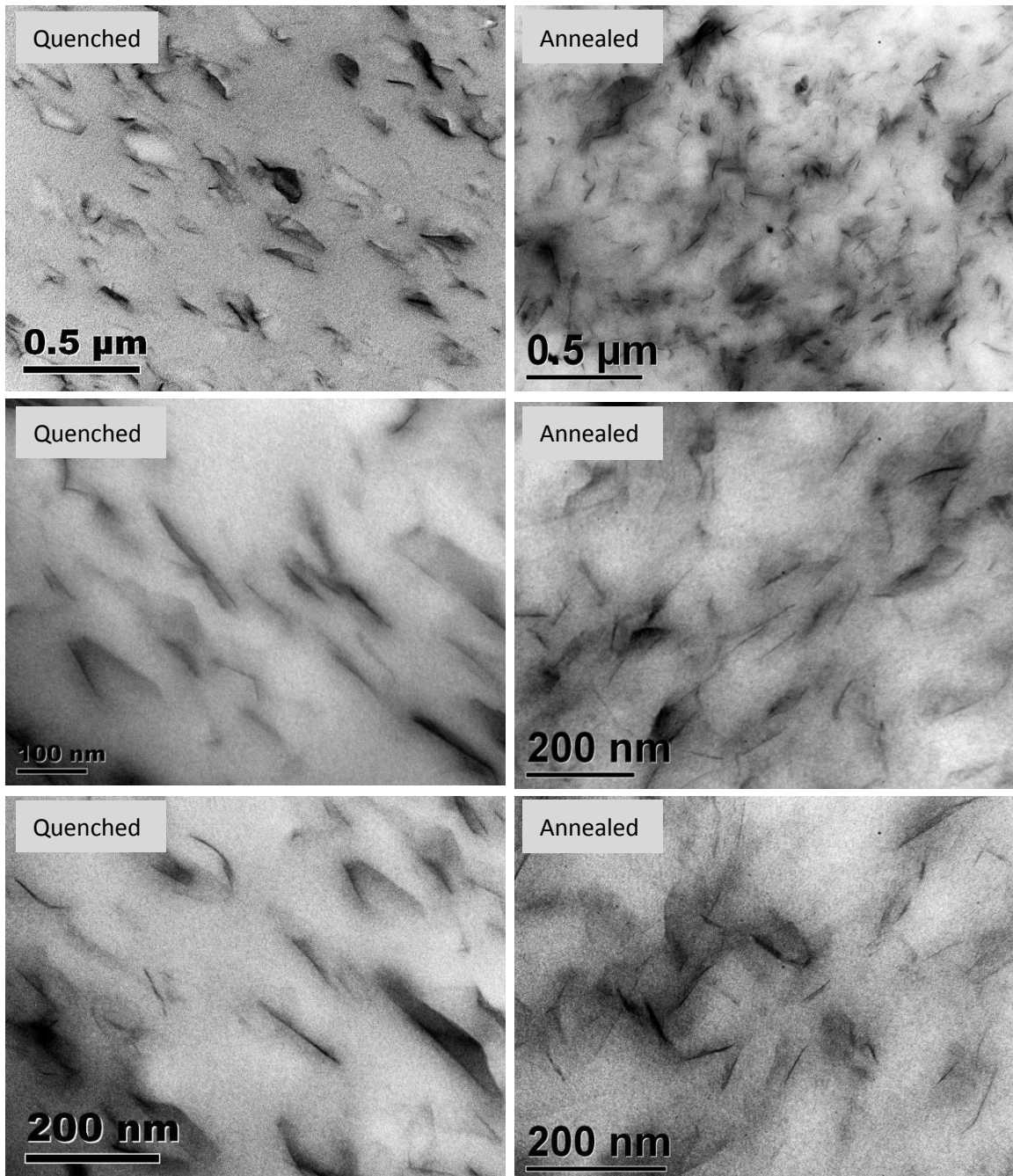


Figure 4.16 TEM images of quenched and annealed PLA nanocomposites

containing 1 wt. % clay at 60k , 100k and 200k magnifications

The transmission electron micrographs a 1 wt.% nanoclay sample at 400k magnification are shown in Figure 4.17 and Figure 4.18, in which intercalated clay structure can be clearly observed. In these micrographs, the dark lines are the edges of the single layered silicate. The length and thickness of clay platelets after annealing were measured from the TEM micrographs using Image J<sup>®</sup> software. More than 200 clay platelets were measured from 7 high magnification micrographs. The average length and thickness of the clay platelets in the annealed nanocomposite were found to be  $155 \pm 35$  nm and  $3.8 \pm 1.6$  nm, therefore, the aspect ratio of the nanoclay was about 41, which is similar to the value measure on the quenched nanocomposite samples.

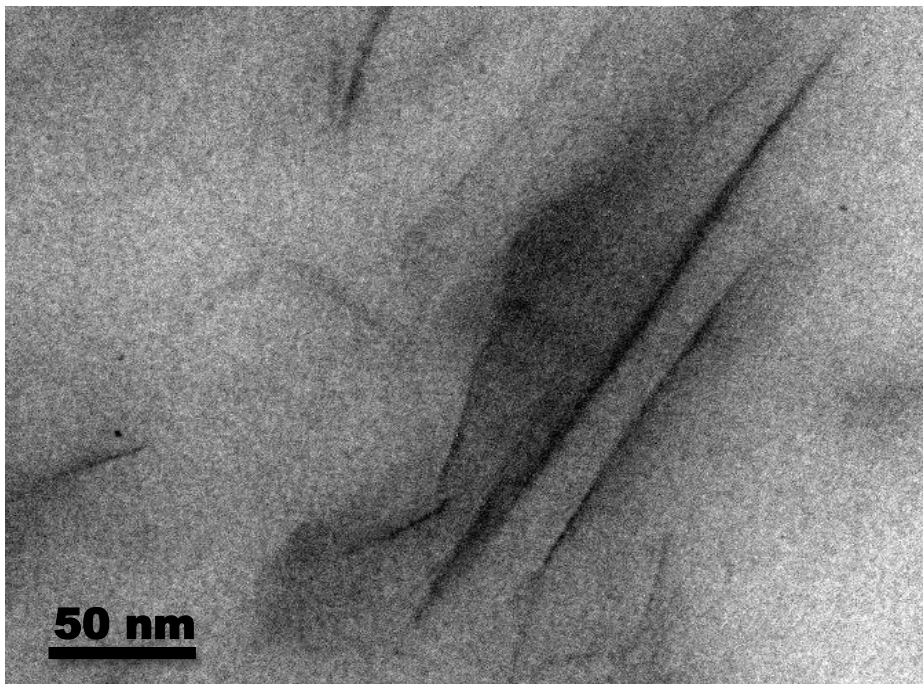


Figure 4.17 TEM images of annealed PLA nanocomposite with 1 wt.% clay at 400k magnifications

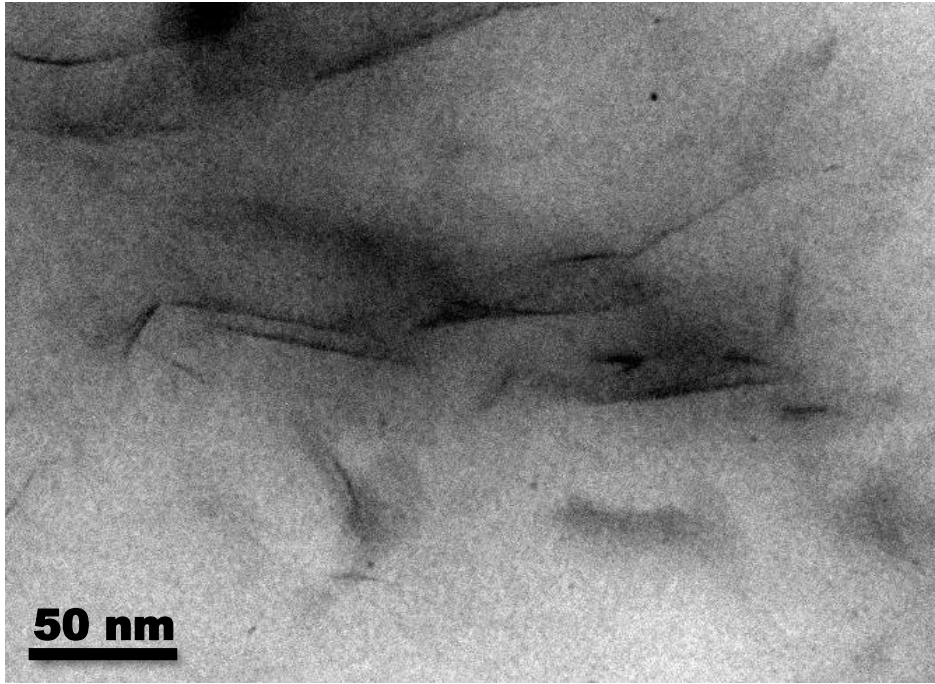


Figure 4.18 TEM images of annealed PLA nanocomposite with 1 wt.% clay at 400k magnifications

## 4.2.5 Water vapour permeability results

### 4.2.5.1 Interpretation by tortuous path models

Water vapour transmission rate (WVTR) data for quenched and annealed PLA nanocomposite sheets was measured through the PLA sheets processed from the amorphous PLA, 4060D, and the crystallisable PLA, 4032D, respectively. The experimental data is shown in Table 4.5. Five individual samples were measured for each data point. It is clearly seen that the measured water vapour permeability data for the annealed samples is much lower than that of the quenched samples due to the crystallinity of the annealed PLA nanocomposite.

Table 4.5 Results of water vapour transmission rate of annealed and quenched PLA nanocomposites

Sample	Crystallinity	WVTR (gm-mil/[m <sup>2</sup> -day])
Quenched PLA 4060D	0%	180 ± 3
Quenched PLA 4060D +1wt.%nanoclay	0%	165 ± 3
Quenched PLA 4060D +2wt.%nanoclay	0%	147 ± 2
Quenched PLA 4060D +3wt.%nanoclay	0%	134 ± 3
Quenched PLA 4060D +4wt.%nanoclay	0%	118 ± 1
Quenched PLA 4060D +5wt.%nanoclay	0%	112 ± 3
Annealed PLA 4032D	30±1%	111 ± 2
Annealed PLA 4032D +1wt.%nanoclay	32±1%	108 ± 6
Annealed PLA 4032D +2wt.%nanoclay	31±1%	107 ± 3
Annealed PLA 4032D +3wt.%nanoclay	32±1%	87 ± 2
Annealed PLA 4032D +4wt.%nanoclay	31±1%	86 ± 2
Annealed PLA 4032D +5wt.%nanoclay	30±1%	88 ± 1

The WVTR data of the quenched PLA nanocomposites is discussed in Section 4.2.5. Water vapour permeability significantly decreased with increasing clay content and tended to level off at a clay content of 5 wt.%. A prediction line from the Nielsen model was plotted in same figure and fitted very well with the experimental data.

Figure 4.19 shows the plot of WVTR data for the annealed PLA nanocomposite samples as a function of wt.% nanoclay. A theoretical line predicted from the Nielsen model is plotted in the same graph. It is found that all the experimental data is higher than the theoretical line and the reduction of permeability does not fit the Nielsen model. This is thought to be due to the effect of annealing on increasing crystallinity but also changing the alignment of the clay particles.

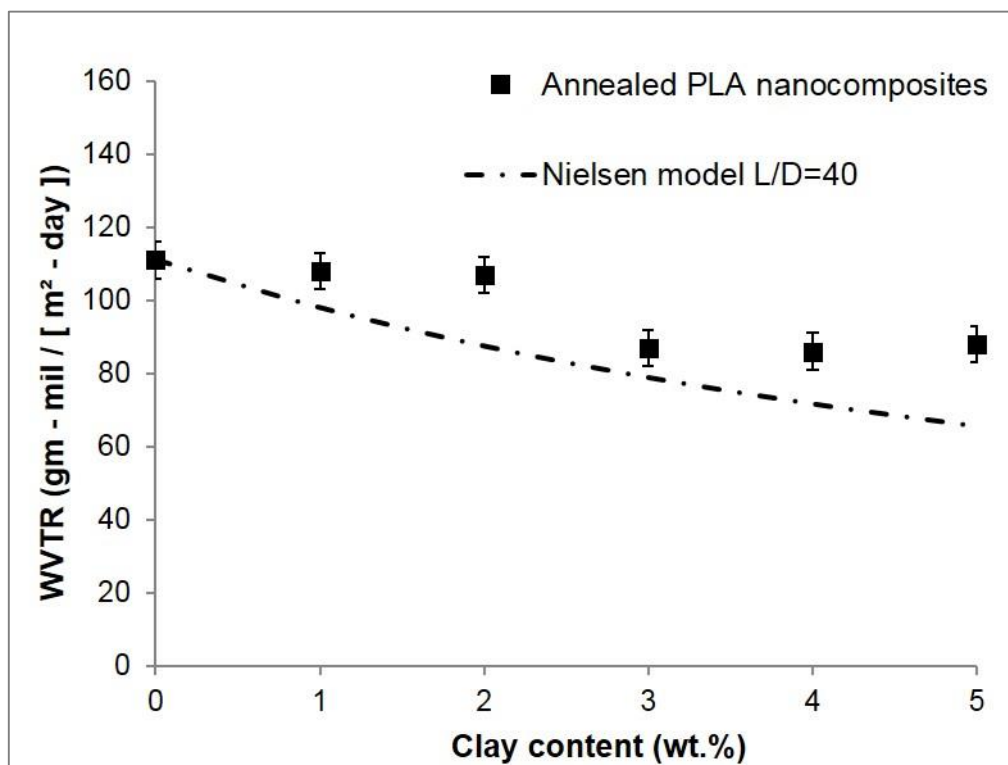


Figure 4.19 Water vapour permeabilities of annealed PLA and PLA nanocomposites in comparison with Nielsen theoretical values

According to the TEM images in Figure 4.16, the clay layers became more randomly oriented after annealing. Therefore, a model, due to Bharadwaj [79], that takes into account the orientation of the particles, was applied to the

annealed data. Unlike the Nielsen model, which assumes the filler particles are aligned at right angles to the diffusion direction, this model allows for the filler particles to be oriented in different directions. In this model there is an orientation factor,  $S$ , included in the tortuosity factor. The orientation factor is shown in equation (4.2), where  $\theta$  is the angle between the perfect diffusion direction and the normal to the filler particles.

$$S = \frac{1}{2} \langle 3 \cos^2 \theta - 1 \rangle \dots\dots\dots(4.2)$$

It is seen from equation (4.2) that when the filler particles are orientated perpendicular to the direction of diffusion (i.e.  $\theta=0$ ) then  $S=1$  and the equation becomes the same as the Nielsen model. However, if the filler particles are orientated parallel to the direction of diffusion (i.e.  $\theta=\pi/2$ ) then  $S=-1/2$ . When there is random orientation, then  $S=0$ .

The order parameter is inserted into the Nielsen equation to allow for orientation [79], as shown in equation (4.3)

$$\frac{P_F}{P_0} = \frac{1-\phi_F}{1 + \frac{L\phi_F}{2D} \left(\frac{2}{3}\right) \left(S + \frac{1}{2}\right)} \dots\dots\dots(4.3)$$

This model is fitted to the WVTR data from the annealed samples in Figure 4.20. The best fit between the experimental data and the predicted line was found with a regression coefficient,  $R^2$ , of 0.8 when  $S = 0.15$ , which indicates that the orientation of the clay particles was in a nearly random state.

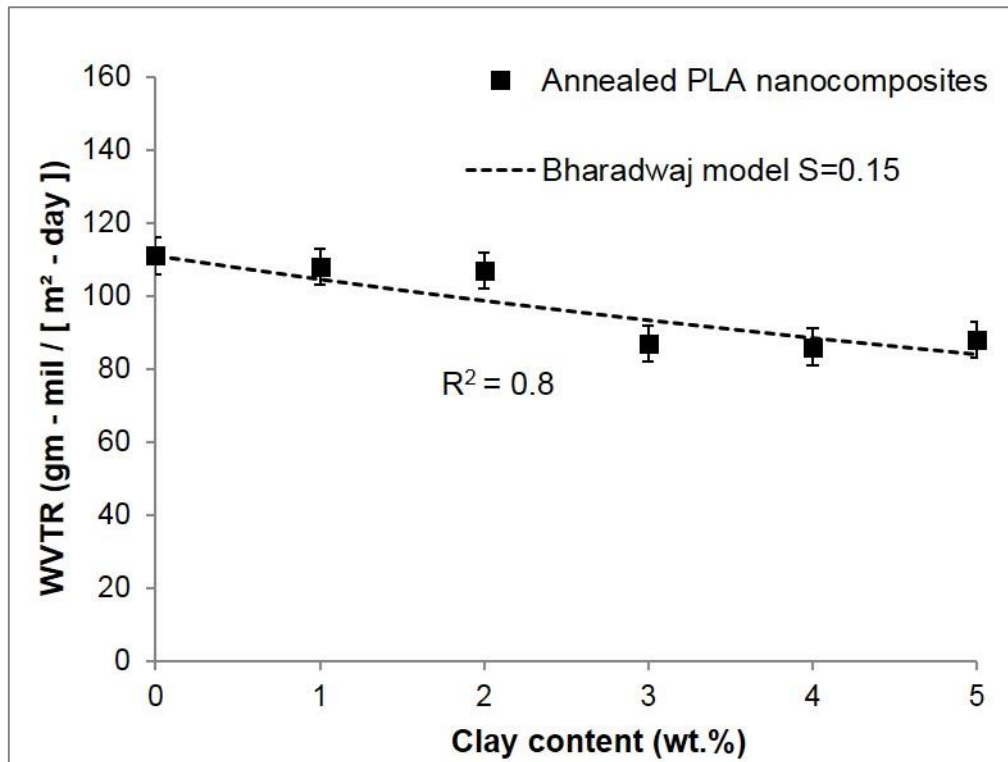


Figure 4.20 Water vapour permeabilities of annealed PLA and PLA nanocomposites in comparison with theoretical values predicted from the Bharadwaj model

#### 4.2.5.2 Building a new tortuous model and interpretation

In the Nielsen model, the tortuosity factor is the maximum possible value given by

$$\tau = 1 + (L/2D)\phi_F \dots\dots\dots(4.4)$$

In the case of a crystalline polymer, the spherical crystals are assumed to be impermeable fillers with the same L and D. Exchanging the volume fraction of fillers for the fraction of crystallinity  $X_c$ , the tortuosity factor is given by

$$\tau = 1 + \frac{1}{2}X_c \dots\dots\dots(4.5)$$

Then the Nielsen equation is modified to give equation (4.6), in which  $P_c$  is the permeability of the semi-crystalline polymer,  $P_0$  is the permeability of the amorphous polymer, and  $X_c$  is the fractional degree of crystallinity [19].

$$\frac{P_c}{P_0} = \frac{1-X_c}{1+\frac{1}{2}X_c} \dots\dots\dots(4.6)$$

In the present study, the permeability of the annealed PLA ( $P_{C+0\%clay}$ ) can be predicted by using equation (4.6) with a known crystallinity of  $X_c = 0.3$  (Table 4.4) and  $P_0 = 180 \text{ gm - mil} / [\text{m}^2 - \text{day}]$ , therefore, it becomes

$$P_{C+0\%clay} = P_0 * \left(\frac{1-X_c}{1+\frac{1}{2}X_c}\right) \dots\dots\dots(4.7)$$

This gives a value of  $110 \text{ g - mil} / [\text{m}^2 - \text{day}]$ , which is in good agreement with the measured value of  $111 \text{ g - mil} / [\text{m}^2 - \text{day}]$ .

As discussed previously, the model of Bharadwaj (equation (4.3)) has been fitted well with the experimental data of annealed PLA nanocomposites (see Figure 4.20). Therefore the permeability of the annealed PLA nanocomposites containing 0 to 5wt.% nanoclay can be expressed as following:

$$P_{C+n\%clay} = P_{C+0\%clay} * \left(\frac{1-\phi_F}{1+\frac{L\phi_F}{2D}\left(\frac{2}{3}\right)\left(S+\frac{1}{2}\right)}\right) \dots\dots\dots(4.8)$$

By inserting equation (4.7) into equation (4.8), the theoretical permeability of semi-crystalline polymer nanocomposites becomes

$$P_{C+n\%clay} = P_0 * \left(\frac{1-X_c}{1+\frac{1}{2}X_c}\right) * \left(\frac{1-\phi_F}{1+\frac{L\phi_F}{2D}\left(\frac{2}{3}\right)\left(S+\frac{1}{2}\right)}\right) \dots\dots\dots(4.9)$$

Permeability predicted from equation (4.9) was plotted together with the experimental data from the semi-crystalline PLA nanocomposites, as shown in Figure 4.21. When  $S = 0.15$ , the experimental data gives a reasonable fit to the predicted line with  $R^2 = 0.8$ . This confirms that the new model fits the experimental data well as the model of Bharadwaj, showing that the new tortuous path model gives a good prediction of the combined effect of crystallinity and nanoclay on water vapour permeability of polymer films.

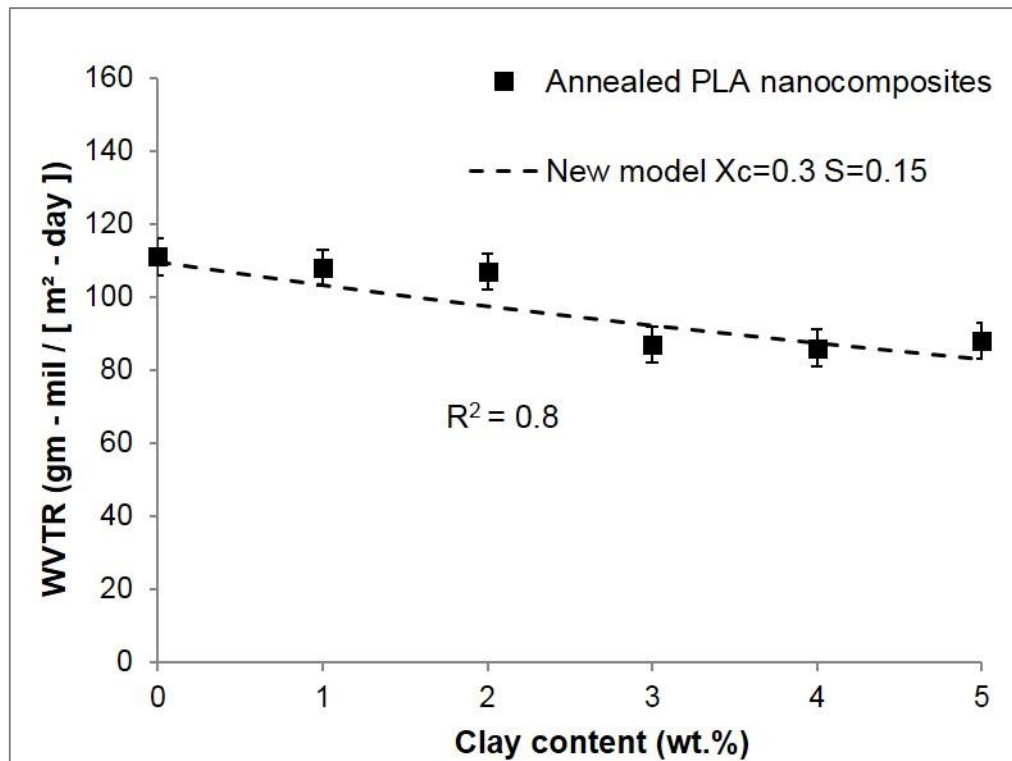


Figure 4.21 Water vapour permeabilities of annealed PLA nanocomposites in comparison with theoretical value predicted from the new model, equation (4.9)

More details of the interpretation of the new model can be found in a recent journal article [153].

### 4.3 Summary

1. PLA nanocomposites containing 0 to 5 wt.% montmorillonite layered silicate were prepared by melt compounding followed by compression moulding with two different thermal treatments (i.e. quenching and annealing). Both amorphous and semi-crystalline PLA nanocomposite samples were obtained.
2. Thermal properties of the samples were measured by DSC. The crystallinity of the annealed PLA and PLA nanocomposites was 30%. The morphology of crystallites was observed by polarised optical microscopy.
3. The nanoclay structure was measured using TEM and WAXD. It was confirmed that the nanocomposite structures were intercalated and the clay aspect ratio was about 40 in both quenched and annealed samples. The clay layers were aligned in the same direction in the quenched samples. However, there was random orientation in the annealed samples due to the crystallisation process.
4. Water vapour transmission rates through the film samples were measured at 38°C and at a relative humidity of 90%. It was found that the measured values of WVTR of the quenched PLA nanocomposites decreased consistently with clay concentration and the data showed a good fit with the Nielsen model. The measured WVTR data of the annealed PLA nanocomposites fitted the model of Bharadwaj when the clay orientation was assumed to be nearly random.
5. A new tortuous model was built based on the models of Nielsen and Bharadwaj to predict the combined effects of crystallinity and nano-filler on the water vapour transmission rates through the polymer films. The new model showed a good fit with the experimental data from the annealed PLA nanocomposites.

## 5 Uniaxial stretching of PLA nanocomposites

### 5.1 Uniaxial stretching of neat PLA sheets

Before processing to stretch the PLA nanocomposite sheets, the optimum stretching temperature for each grade of PLA was determined by uniaxial stretching of the neat PLA 4060D sheets at four different temperatures (60, 65, 70 and 75°C). The lowest stretching temperature was selected at 60°C, which was 5°C above the T<sub>g</sub> of the PLA 4060D. The sheets were stretched to 3 times the original length at a crosshead speed of 10 mm/min. The optimum drawing temperature was determined depending on the quality of the stretched samples. To understand how well the sheet was stretched, equally spaced dots were drawn on the 12x12 cm<sup>2</sup> sheets before stretching (see Figure 5.1). The dots are used to determine the quality of the deformation in each area of the sheets after stretching. For example, in Figure 5.1, at a stretch temperature of 60°C, the sample was uniformly deformed, since the majority of the dots are evenly distributed. When the temperature was increased to 75°C, the deformation of the sample was not uniform as the dots in the same line are shifted from each other.

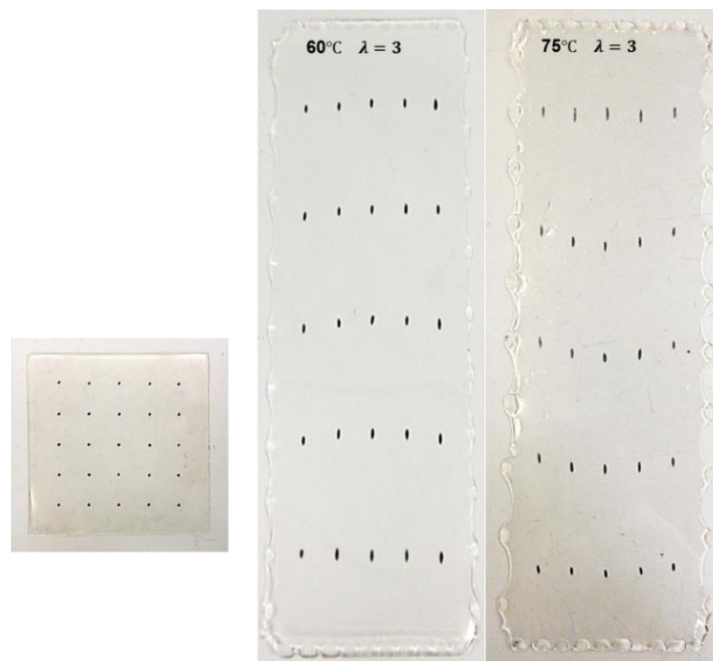


Figure 5.1 Photos of an unstretched PLA sheet and two uniaxially stretched PLA sheets

The curves of drawing force versus displacement for the process of uniaxial stretching are plotted in Figure 5.2. It is observed that the initial force applied at 60°C was much higher than that at 75°C, which is because, above  $T_g$ , as the temperature increases the chain segment motion allows polymer chains to align more easily during stretching. Therefore, lower force is needed to align the polymer chains at higher temperature.

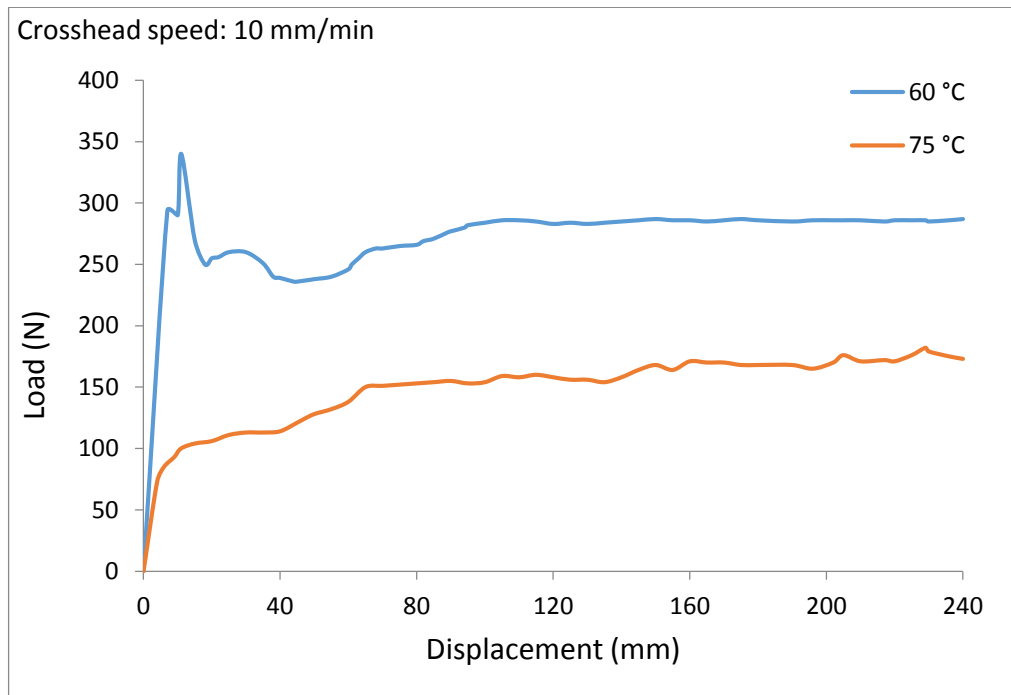


Figure 5.2 Force versus displacement curve at 60°C and 75°C uniaxially stretching on PLA sheets

In addition, the shapes of the curves are quite different: the 60°C curve exhibited a yield point at 340 N, after which it levelled out at about 285 N; whereas, the 75°C curve increased at the beginning until reaching equilibrium at about 170 N. This result implies that as the drawing temperature increases, the behaviour of the polymer is changed from ductile (60°C) to rubbery (75°C).

### 5.1.1 Birefringence test on uniaxially stretched PLA films

In-plane birefringence ( $\Delta n_{xz}$  and  $\Delta n_{xy}$ ) of the uniaxially stretched samples was measured using a Leica microscope equipped with the tilting compensator B (measurement range from 1-5  $\lambda$  orders) and compensator K (30  $\lambda$  orders). Figure 5.3 shows a diagram of the dimensions of a stretched sample.

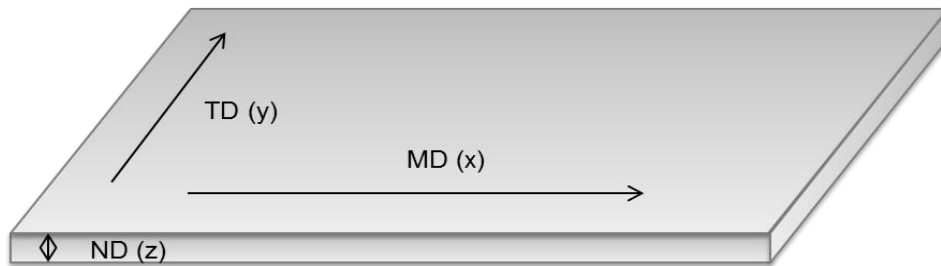


Figure 5.3 A diagram of the dimensions of a stretched sheet (MD=machine direction; TD=transversal direction; ND= normal direction of the sample)

Table 5.1 shows the birefringence values of samples that had been stretched at various temperatures. The trend of the birefringence versus drawing temperature is presented in Figure 5.4 ( $x=MD$ ;  $y=TD$ ;  $z=ND$ ). It is not surprising that the unstretched normal sample exhibits no birefringence in both directions.

Table 5.1 Birefringence for drawn PLA at different temperatures

Drawing temperature	$\Delta n_{xz} \times 10^{-3}$	$\Delta n_{xy} \times 10^{-3}$
60°C	$9.7 \pm 2$	$8.4 \pm 2.3$
65°C	$8.4 \pm 2.4$	$4.7 \pm 2.9$
70°C	$7.3 \pm 0.6$	$3.2 \pm 2.5$
75°C	$4.3 \pm 0.8$	$1.2 \pm 1.8$

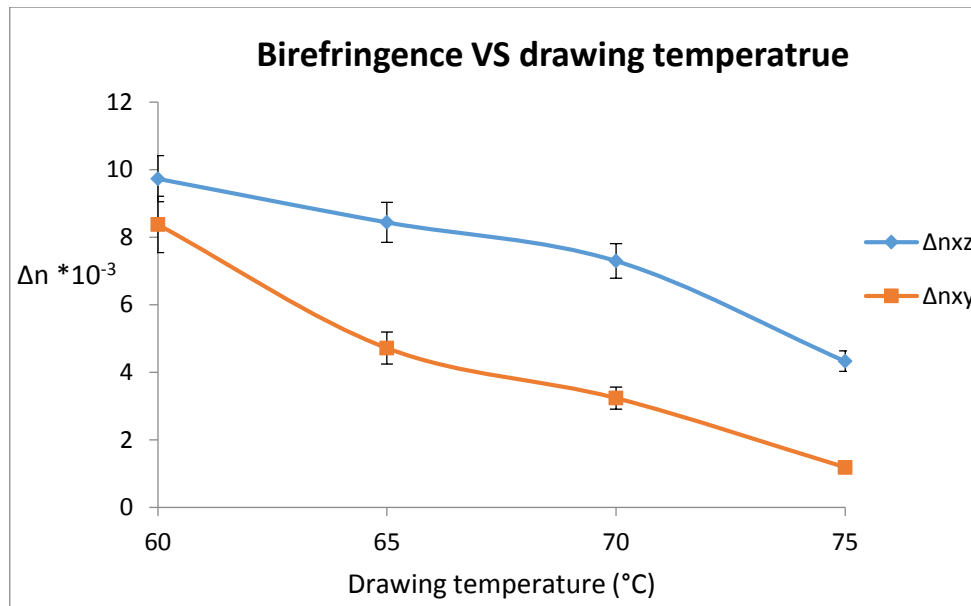


Figure 5.4 Birefringence of PLA sheets stretched at different temperatures

For the drawn samples, both  $\Delta n_{xy}$  and  $\Delta n_{xz}$  show a decrease with the increase of drawing temperature. High birefringence represents high orientation for the sample. Therefore, this result suggests that the sample stretched at 60°C exhibits the highest degree of chain orientation.

As expected, the birefringence  $\Delta n_{xz}$  is found to be higher than  $\Delta n_{xy}$  for all stretching temperatures indicating that the refractive index in TD ( $n_y$ ) is higher than that in ND ( $n_z$ ), since  $\Delta n_{xy} = n_x - n_y$  and  $\Delta n_{xz} = n_x - n_z$ . This result suggests that a high level of chain orientation was developed in the machine direction. A small amount of orientation was generated in the transverse direction, since the width of the sample in TD is constrained during stretching.

The birefringence result is similar to published birefringence data by Ou and Cakmak [105], who found that the in-plane birefringences for 3x1 uniaxially stretched PLA at a stretching temperature of 70°C is  $\Delta n_{xz} = 9 \times 10^{-3}$ .

### 5.1.2 DSC results of uniaxially stretched PLA films

DSC heating scans for the PLA sheets stretched at various drawing temperatures are displayed in Figure 5.5. The step change at the glass transition temperature was increased after stretching, probably because the alignment of the polymer chains had induced an increase of the relaxation time distribution for the polymer. A widened enthalpy relaxation peak next to the glass transition was noticed in the stretched samples, which was quite different from the normal quenched sample (Figure 4.1). This is probably because in the stretched films polymer chains were highly orientated, which needs more relaxation time during glass transition. A similar phenomenon has been found in the DSC results of biaxial drawn PLA films by Delpouve et al. [154], who reported that a wide glass transition step was founded in the biaxial drawn PLA films as the structural heterogeneities of polymer chains induced a widening of the relaxation time distribution. Since the grade 4060D is amorphous the curves do not show cold crystallisation or melting peaks.

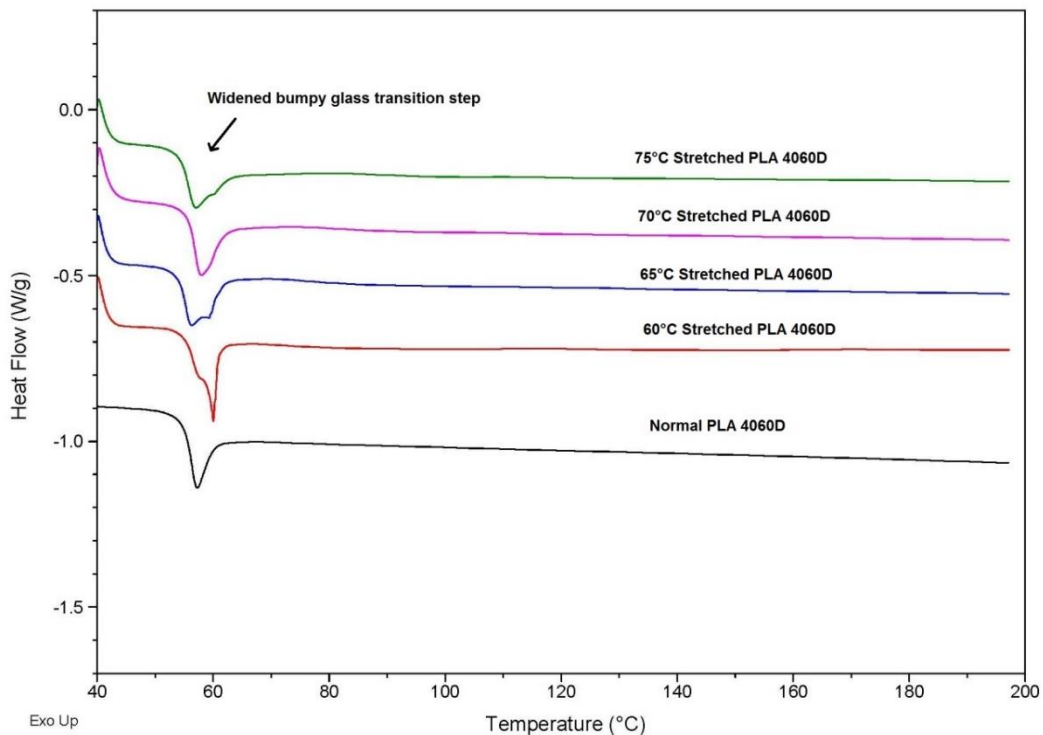


Figure 5.5 DSC heating scans for normal PLA and four stretched PLA samples at various drawing temperatures

The T<sub>g</sub> values for stretched PLA samples are shown in Table 5.2. A plot of T<sub>g</sub> as a function of drawing temperature is illustrated in Figure 5.6. The horizontal line represents the T<sub>g</sub> value of the unstretched PLA. Three samples were tested for each data point. The samples stretched at 60°C exhibited a shift in T<sub>g</sub> to about 3°C higher than the unstretched (normal PLA) samples. While the other samples drawn at 65, 70 and 75°C showed the same value of T<sub>g</sub> as the normal PLA samples. The shift in T<sub>g</sub> for the 60°C stretched samples was probably due to the polymer chains being highly orientated, which required more energy for relaxation. This result correlates with the birefringence result showing that the samples stretched at 60°C had the highest degree of orientation. A similar phenomenon has been reported by Tsai et al. [155], who investigated thermal properties of biaxially stretched PLA and attributed the increase in T<sub>g</sub> to limited polymer chain motion in the stretched film due to the alignment and packing of polymer molecules.

Table 5.2 T<sub>g</sub> values of the stretched PLA sheets

<b>Sample</b>	<b>T<sub>g</sub> (°C)</b>
60°C stretched PLA	59±1
65°C stretched PLA	59±1
70°C stretched PLA	57±1
75°C stretched PLA	55±1
Unstretched PLA	56±1

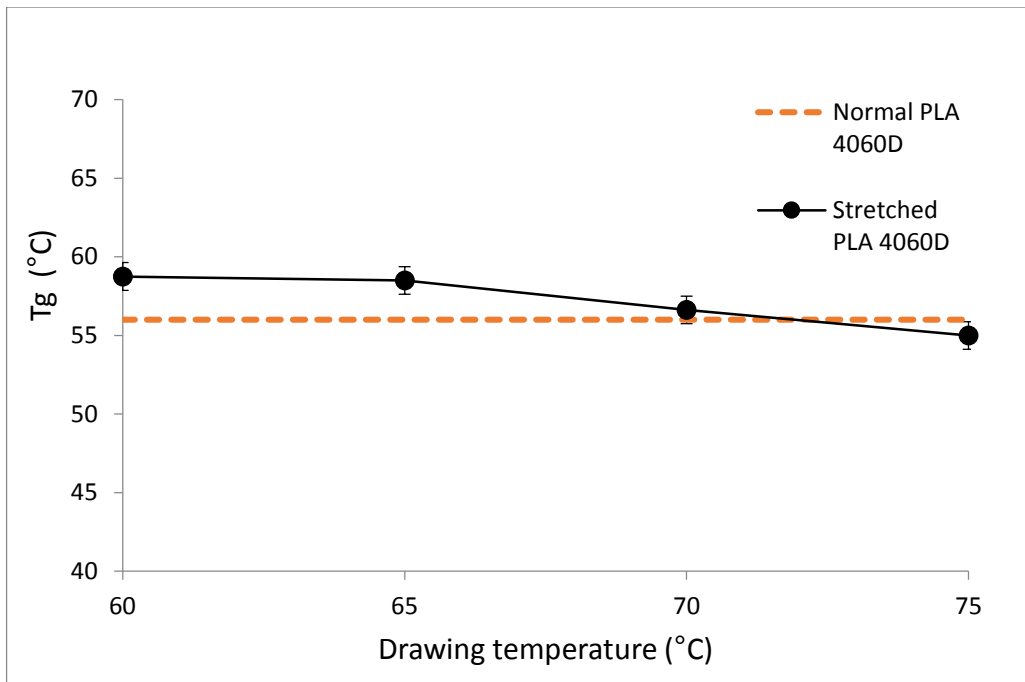


Figure 5.6 T<sub>g</sub> of the stretched PLA samples as a function of drawing temperature

### 5.1.4 XRD of uniaxially stretched PLA films

The wide-angle X-ray diffraction (WAXD) traces of the unstretched (normal) PLA and the stretched PLA sheets are presented in Figure 5.7. A very broad diffraction peak at  $2\theta=16^\circ$  corresponds to the orientated amorphous phase in the polymer. Comparing with the normal PLA, this peak in the traces of the stretched samples is sharper and higher according to the drawing temperature. All stretched samples exhibited diffraction peaks at  $2\theta=26^\circ$  and  $29^\circ$ , which could correspond to some crystalline phase formed by stretching. However grade 4060D PLA is amorphous and the peaks at  $26^\circ$  and  $29^\circ$  are too sharp to be due to crystalline phase.

WAXD data for stretched crystalline PLA showing similar  $2\theta$  values has been published. For example, Xie et al. [103] investigated the strain-induced crystallinity of stretched PLA at 80, 90 and 120 °C and found that the XRD traces of all the samples showed a diffraction peak at  $29^\circ$ , which corresponded to the  $\alpha$  crystal form of PLA. Another study showed a diffraction peak at  $2\theta=30^\circ$ , however, this reflection was reported to correspond to the  $\beta$  crystal form of orientated PLA [26]. There is no report on an XRD reflection peak at  $26^\circ$  for PLA films in the literature.

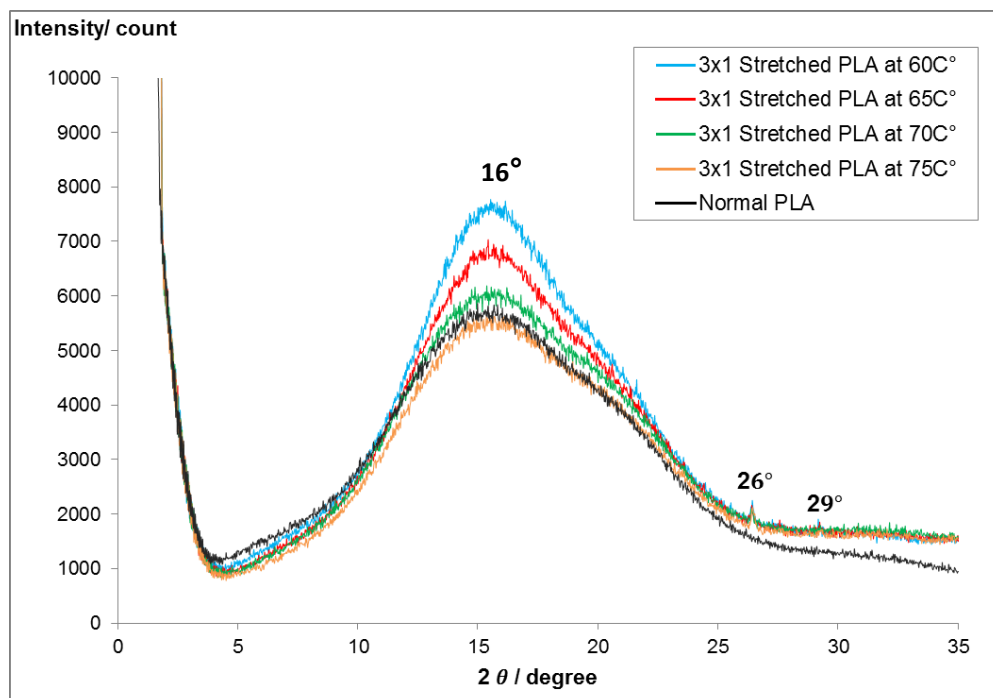


Figure 5.7 WAXD traces for normal PLA and stretched PLA at various drawing temperatures

### 5.1.5 Water vapour permeability results

The water vapour transmission rate data for all the stretched samples are shown in Table 5.3. Three to four samples were tested for each data point. It is found that the average thickness of the stretched samples was ca. 0.28 mm with different standard deviations that increased with the drawing temperature. This reveals that the samples tended to become uneven as the drawing temperature increased since the polymer chains are more flowable at higher temperature. The uniformity of the stretched sample is significant to the water barrier properties of the sample. As the drawing temperature increase the permeability value tends to become higher with increased deviations. For example, the sample stretched at 75°C showed high WVTR value of 261 gm-mil/[ m<sup>2</sup> - day ] with a standard deviation of 111. The samples drawn at a temperature of 60 °C showed the most stable and best barrier behaviour compared with those drawn at other drawing temperatures (note that the WVTR data shown in Table 5.3 are already normalised for sample thickness).

Table 5.3 WVTR data for stretched PLA

<b>Drawing temperature</b>	<b>Sample thickness (mm)</b>	<b>Mean (gm - mil / [ m<sup>2</sup> - day ])</b>
60 °C	0.27 ± 0.02	209±19
	0.29 ± 0.01	
65 °C	0.28 ± 0.01	214±26
	0.29 ± 0.02	
70 °C	0.29 ± 0.05	210±29
	0.29 ± 0.04	
75 °C	0.27 ± 0.9	261±111
	0.27 ± 0.08	
Normal PLA 4060D	0.60 ± 0.01	180 ± 3

The plot of WVTR as a function of drawing temperature is shown in Figure 5.8. The red dashed line represents the WVTR value of the unstretched normal PLA samples, which is much lower than the value points of the stretched samples due to the thickness of the normal samples being 2-3 times of the stretched ones. However, it is noteworthy that, the difference in thickness has been already taken into account in the WVTR measurement assuming a linear inverse relationship, as discussed in Section 3.3.2. The reduction in water vapour permeability of the stretched films indicates that there are other factors accounting for the WVTR measurement.

One possibility is that there may be some invisible air bubbles or defects in the sample that were expanded along with the stretching of the samples, hence resulting in poor barrier properties of the samples. Another factor is that polymer films that have been stretched tend to bend and have an uneven surface, especially for the thin films. Therefore, after stretching PLA films were more likely to be bent and exhibited less uniformity. This is also crucial to the WVTR result, because samples of less uniformity tend to have worse barrier properties in the WVTR test because they are more difficult to seal.

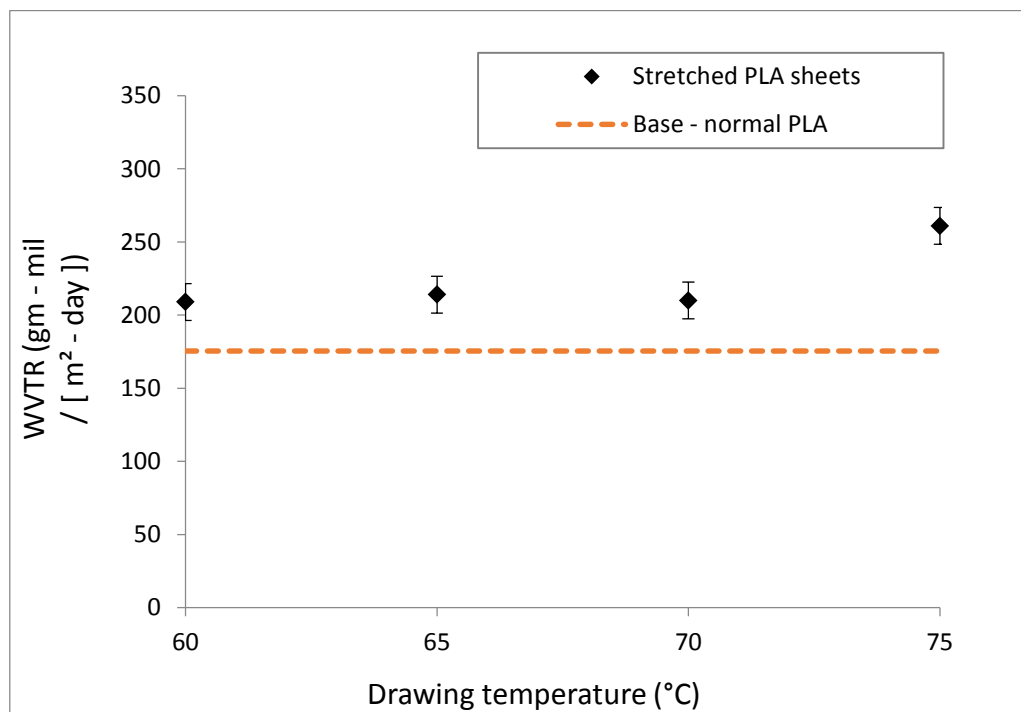


Figure 5.8 WVTR data for stretched PLA versus drawing temperature

To minimise these effects, it was necessary to keep the thickness constant for all the samples in the WVTR test. The amorphous PLA sheets for uniaxial stretching were prepared to be three times thicker than the normal quenched sheets using a deep mould (see Section 3.2.3.1) during compression moulding. After being uniaxially stretched at a 3x1 draw ratio, the samples showed similar thickness (ca.  $0.6 \pm 0.01$  mm) compared with the normal quenched samples. Water vapour permeability of the PLA films at different thickness are shown in Table 5.4. The stretched PLA with higher thickness showed a much lower average WVTR with a smaller deviation compared with that of the low thickness sample. The WVTR value of the stretched PLA samples was  $177 \pm 1$  gm-mil/[m<sup>2</sup>-day], which is similar to that of the quenched PLA with the same thickness.

Table 5.4 WVTR of stretched PLA in different thickness compared with the quenched PLA

<b>Sample</b>	<b>Sample thickness (mm)</b>	<b>WVTR (gm-mil/[m<sup>2</sup>-day])</b>
Stretched PLA4060D at 60 °C	$0.28 \pm 0.01$	$209 \pm 19$
Stretched PLA4060D at 60 °C	$0.60 \pm 0.01$	$177 \pm 1$
Quenched PLA4060D	$0.60 \pm 0.01$	$180 \pm 3$

In summary, the optimum drawing temperature was 60 °C. In the sample preparation, the amorphous PLA sheets for uniaxial stretching need to be prepared three times thicker than the normal quenched ones during compression moulding.

## 5.2 Effect of mechanical stretching on PLA nanocomposites

### 5.2.1 DSC of uniaxially stretched PLA nanocomposites

PLA nanocomposites with clay content from 1 to 5 wt.% were uniaxially stretched at 60 °C. Thermal properties of the stretched PLA nanocomposites were measured by DSC and the DSC heating scans for the samples are shown in Figure 5.9. The step change at the glass transition temperature, at 60°C, of the pure stretched PLA sample was widened and became more undulating. This is due to the alignment of the polymer chains induced by stretching, which causes an increase in the relaxation time of the polymer chains. It is found that with the presence of nanoclay, the undulating step change at T<sub>g</sub> was smooth, similar to the unstretched PLA DSC curve in Figure 5.5. As the clay loading increased to 3 wt.% the enthalpy relaxation peak after the step at T<sub>g</sub> became sharp. The clay particles were aligned with the polymer chain orientation playing a confining role in polymer chain relaxation. As a result, the enthalpy relaxation peak became sharper and smooth with the increase of clay loading. Since the grade 4060D is amorphous the curves do not show cold crystallisation or melting peaks.

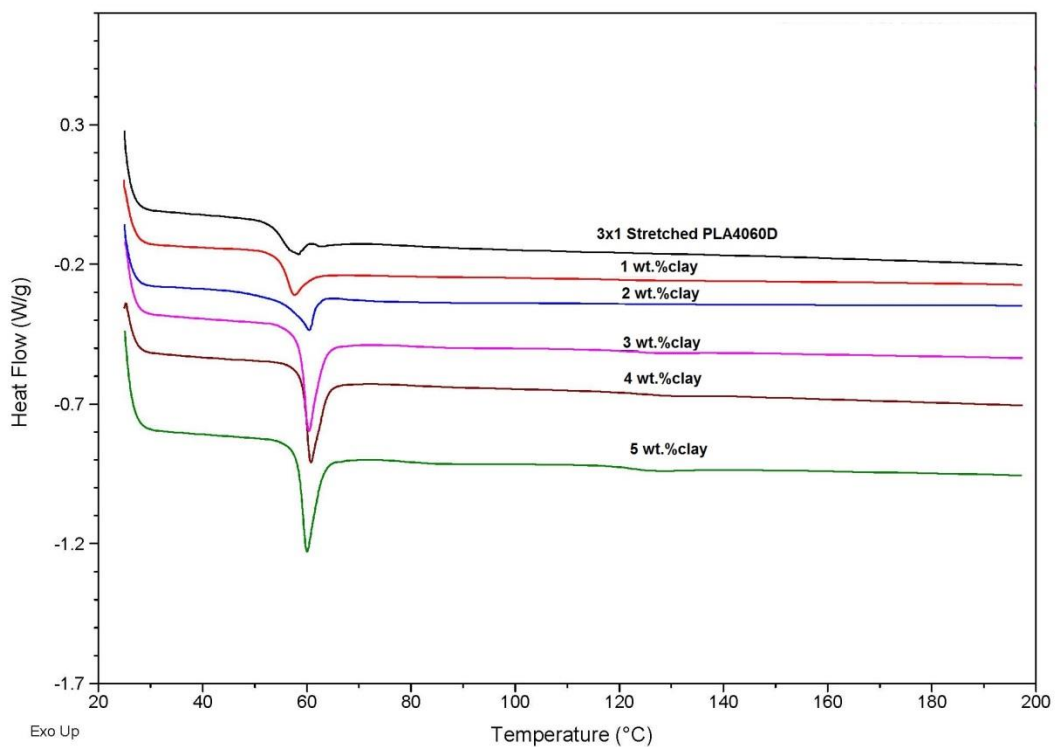


Figure 5.9 DSC curves of 3x1 stretched PLA4060D and its nanocomposites at 60 °C

The T<sub>g</sub> values of the stretched PLA nanocomposites are compared with normal PLA nanocomposite as shown in Table 5.5. Also, the effect of clay content on T<sub>g</sub> values for stretched and normal quenched PLA nanocomposite samples is shown in Figure 5.10. Compared with the normal samples, the stretched samples showed similar T<sub>g</sub> values at clay content of 1 wt.%, around 55-56°C. However, at high clay content, of 2, 3, 4, and 5 wt.%, T<sub>g</sub> of the stretched samples significantly increased to around 60±1 °C, which indicates that the mobility of stretched polymer chains is reduced with higher clay content. This finding corresponds to the DSC curves in Figure 5.9, in which sharp enthalpy relaxation peaks after the T<sub>g</sub> step change can be clearly observed in the stretched samples with 3, 4, and 5 wt.% clay. This finding is well explained by an observation noted during the uniaxial stretching: samples containing higher clay content were more difficult to be stretched.

Table 5.5 DSC results of stretched PLA 4060D nanocomposites in comparison with unstretched PLA 4060D nanocomposites

Sample	T <sub>g</sub>
Quenched PLA4060D	56±1°C
Quenched PLA4060D +1wt.%nanoclay	55±1°C
Quenched PLA4060D +2wt.%nanoclay	52±1 °C
Quenched PLA4060D +3wt.%nanoclay	53±1 °C
Quenched PLA4060D +4wt.%nanoclay	51±1 °C
Quenched PLA4060D +5wt.%nanoclay	52±1 °C
Stretched PLA4060D	55±1°C
Stretched PLA4060D+1wt.%nanoclay	56±1°C
Stretched PLA4060D+2wt.%nanoclay	60±1°C
Stretched PLA4060D+3wt.%nanoclay	60±1°C
Stretched PLA4060D+4wt.%nanoclay	60±1°C
Stretched PLA4060D+5wt.%nanoclay	60±1°C

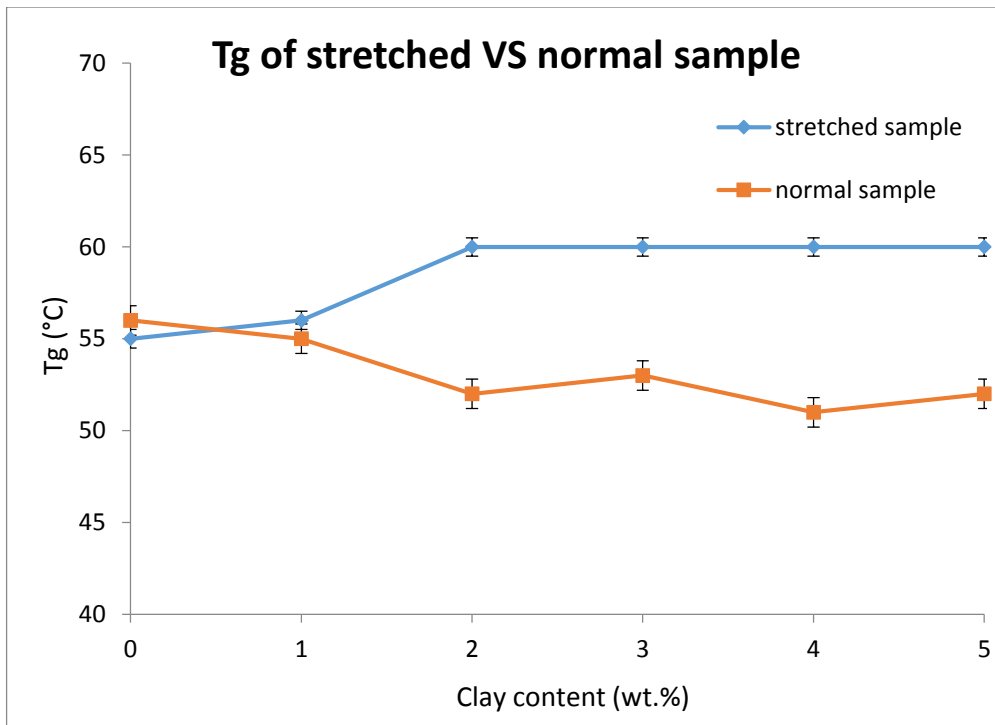


Figure 5.10 Tg trend of PLA nanocomposite against clay content for both stretched samples and normal quenched samples

### 5.2.2 TEM of uniaxially stretched PLA nanocomposites

Transmission electron micrographs of normal quenched and stretched PLA nanocomposite samples containing 1 wt.% nanoclay are shown in Figure 5.11. In the quenched film, the clay layers are mostly aligned and well dispersed in the nanocomposite. An alignment of the clay structure was obtained during melt compounding and remained in the same direction as the polymer melt flow after compression moulding.

In the uniaxially stretched film, the clay particles are found to align more uniformly in the vertical direction, and the clay platelets are more exfoliated in the matrix, implying that a better delamination of the clay layers were obtained during uniaxially stretching.

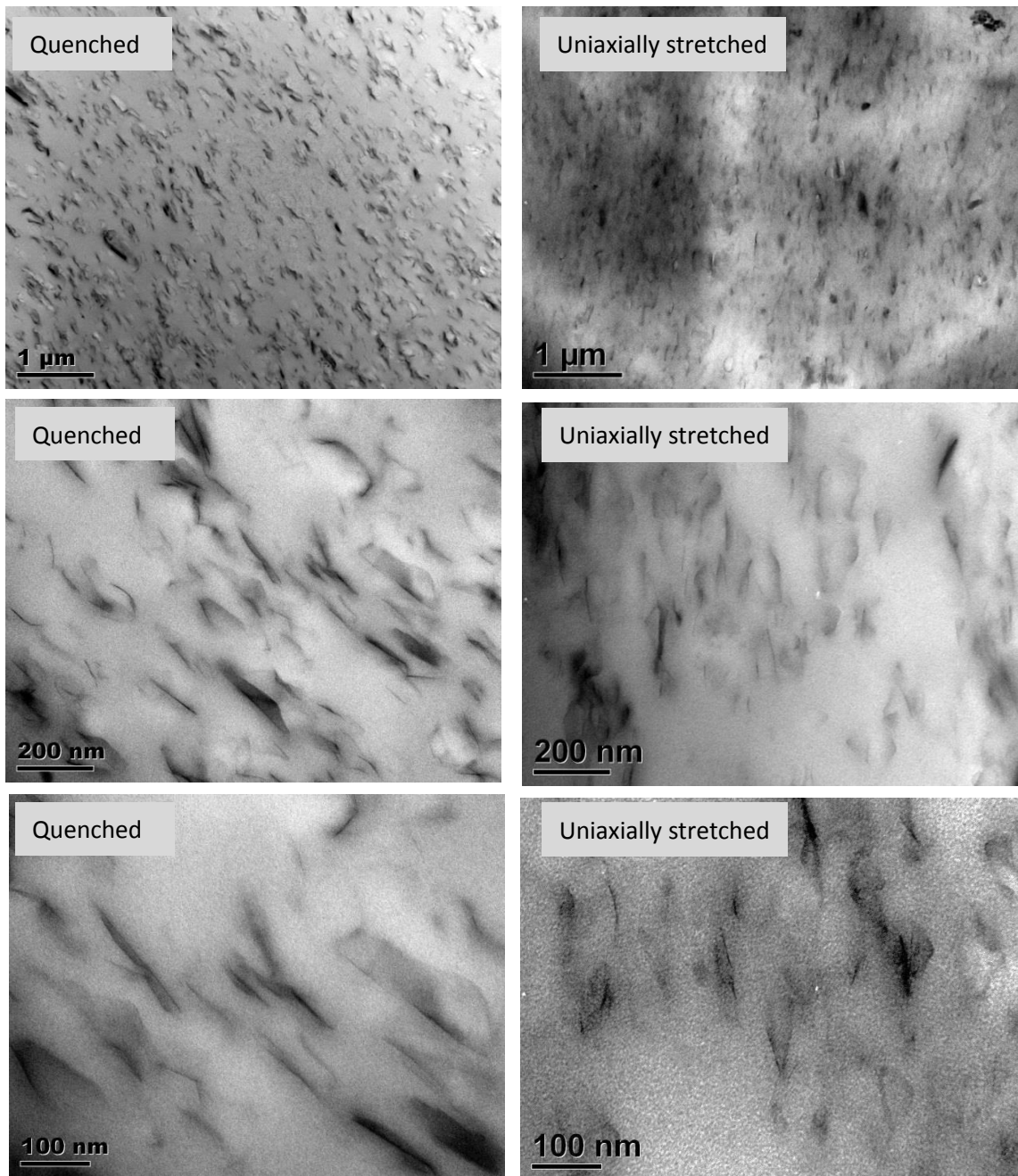


Figure 5.11 TEM images of quenched and stretched PLA nanocomposites containing 1 wt. % clay at 25k, 100k and 200k magnifications

A diagram of how the nanoclay structure was changed during uniaxially stretching is shown in Figure 5.12.

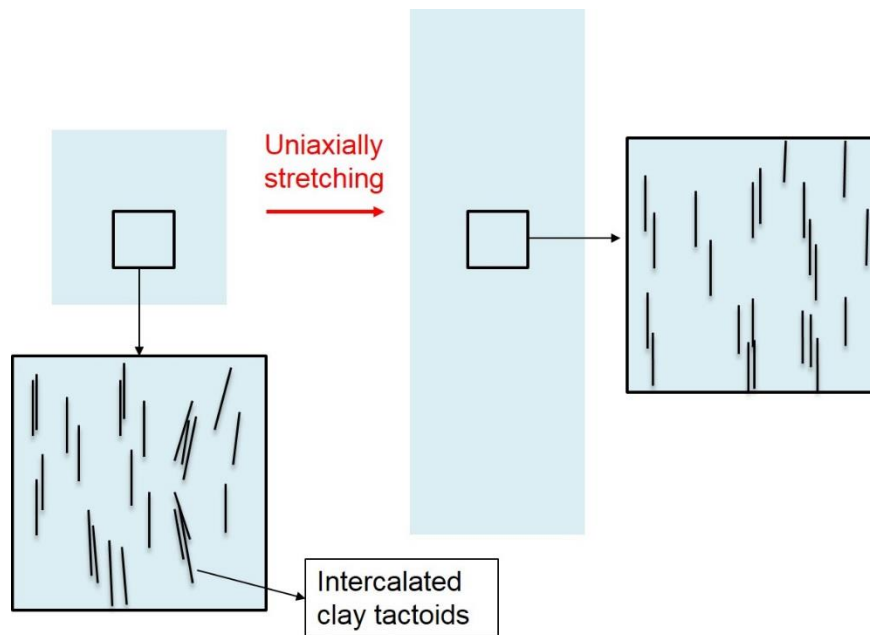


Figure 5.12 Schematic diagram of how intercalated clay tactoids is drawn during uniaxially stretching

A better observation of the stretching induced delamination on the clay layers can be seen in Figure 5.13, which is a TEM image of a stretched PLA nanocomposites containing 1 wt.% clay at 200k magnification. The length and thickness of the clay layers were measured from the images of the uniaxially stretched samples using Image J<sup>®</sup> software. More than 100 clay platelets were measured from 5 high magnification micrographs. The average length and thickness of the clay platelets in the stretched nanocomposite were found to be  $105 \pm 29$  nm and  $2.1 \pm 0.9$  nm, respectively. Therefore, the aspect ratio (length/thickness) of the nanoclay in the uniaxially stretched samples was approximately 48, which is higher than the measured aspect ratio of quenched PLA nanocomposite samples. This is because the intercalated clay tactoids were sheared by the drawing force during the uniaxially stretching making the clay tactoids look longer and thinner in the TEM images, hence resulting in a higher aspect ratio value.

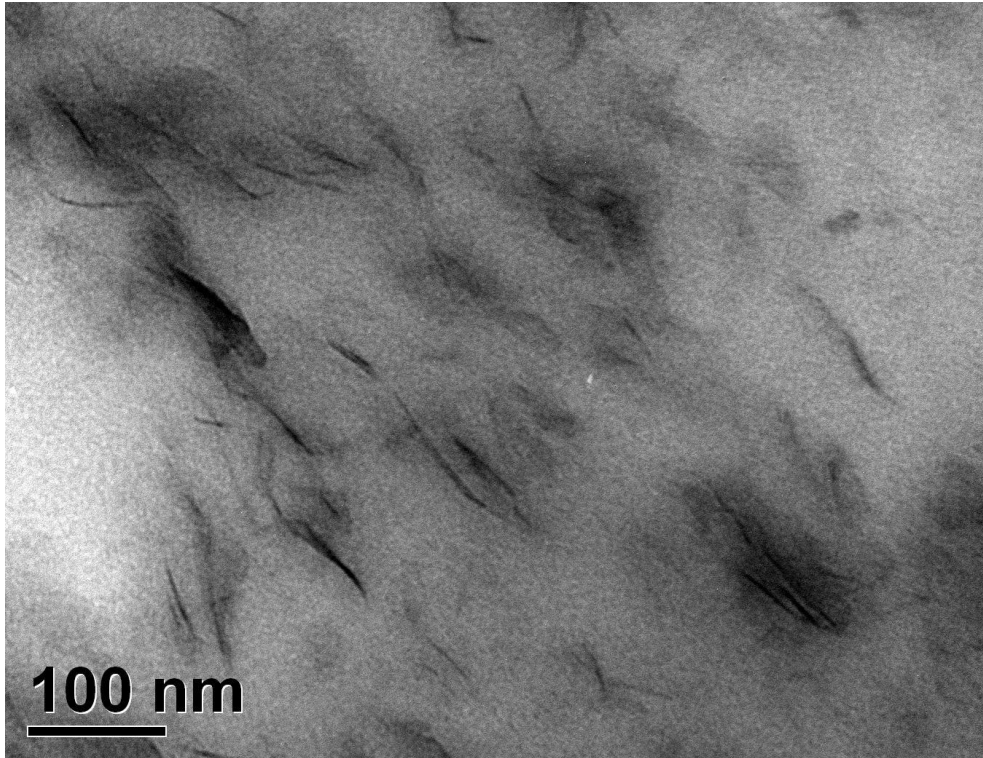


Figure 5.13 TEM images of a stretched PLA nanocomposites containing 1 wt.% clay at 200k magnification

### 5.2.3 XRD of uniaxially stretched PLA nanocomposites

Figure 5.14 shows WAXD traces of a normal quenched sample and a uniaxially stretched PLA nanocomposite samples containing 3 wt.% nanoclay. The peak at  $2.7^\circ$  in the normal PLA corresponds to a clay interlayer spacing ( $d_{001}$ ) of 3.3 nm, showing that the clay structure in the normal nanocomposite sample was intercalated. A broad diffraction peak at  $2\theta=16^\circ$  represents the amorphous phase of PLA. Whereas, in terms of the stretched sample, the peak at  $2\theta=16^\circ$  sharpen, corresponding to the orientated polymer chains in the stretched sample. The peak at  $2.7^\circ$  in the normal PLA nanocomposite has slightly shifted to  $2.5^\circ$ , corresponding to a  $d_{001}$  of 3.5 nm. This means the clay galleries had been further delaminated along with the uniaxial stretching on the polymer chains. This result agrees with the TEM observation that the intercalated clay galleries were shifted and delaminated during uniaxially stretching. The widened interlayer spacing of nanoclay in the stretched nanocomposite films can be observed in the TEM micrographs (Figure 5.11).

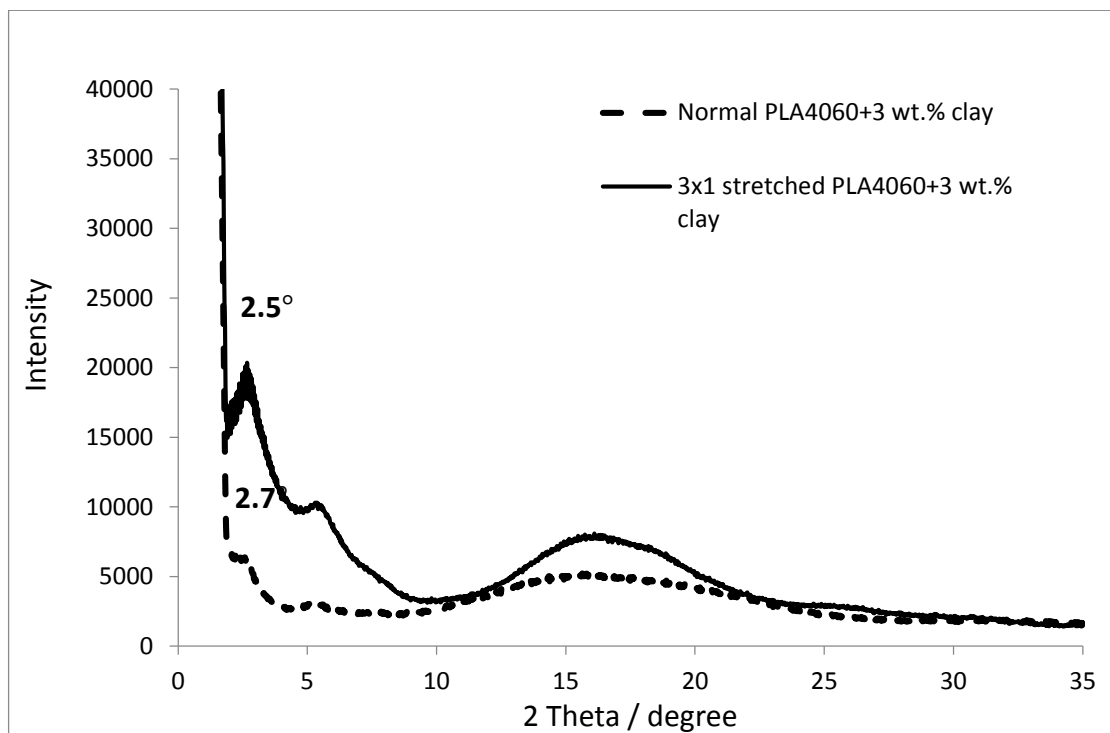


Figure 5.14 WAXD traces of quenched and uniaxially stretched PLA nanocomposites with 3 wt.% nanoclay

### 5.2.4 Water vapour permeability results

Water vapour transmission rate (WVTR) data of the stretched PLA nanocomposites are shown in Table 5.6. The WVTR values of the quenched and uniaxially stretched PLA nanocomposites are plotted as a function of wt.% nanoclay in Figure 5.15. It is found that the measured value of WVTR of pure PLA samples that were quenched and stretched are similar, which indicates that orientation of the PLA chains has no significant effect on the water barrier properties. However, the WVTR values for the uniaxially stretched nanocomposite films are significantly lower than those quenched, which is ascribed to the change of clay structure.

Table 5.6 WVTR result of uniaxially stretched PLA nanocomposite in comparison with quenched PLA nanocomposites

Sample	WVTR (gm-mil/[m <sup>2</sup> -day])
Quenched PLA4060D	180 ± 3
Quenched PLA4060D + 1wt.%nanoclay	165 ± 3
Quenched PLA4060D + 2wt.%nanoclay	147 ± 2
Quenched PLA4060D + 3wt.%nanoclay	134 ± 3
Quenched PLA4060D + 4wt.%nanoclay	118 ± 1
Quenched PLA4060D + 5wt.%nanoclay	112 ± 3
Stretched PLA4060D	177 ± 1
Stretched PLA4060D + 1wt.%nanoclay	145 ± 6
Stretched PLA4060D + 2wt.%nanoclay	129 ± 5
Stretched PLA4060D + 3wt.%nanoclay	125 ± 7
Stretched PLA4060D + 4wt.%nanoclay	106 ± 8
Stretched PLA4060D + 5wt.%nanoclay	111 ± 3

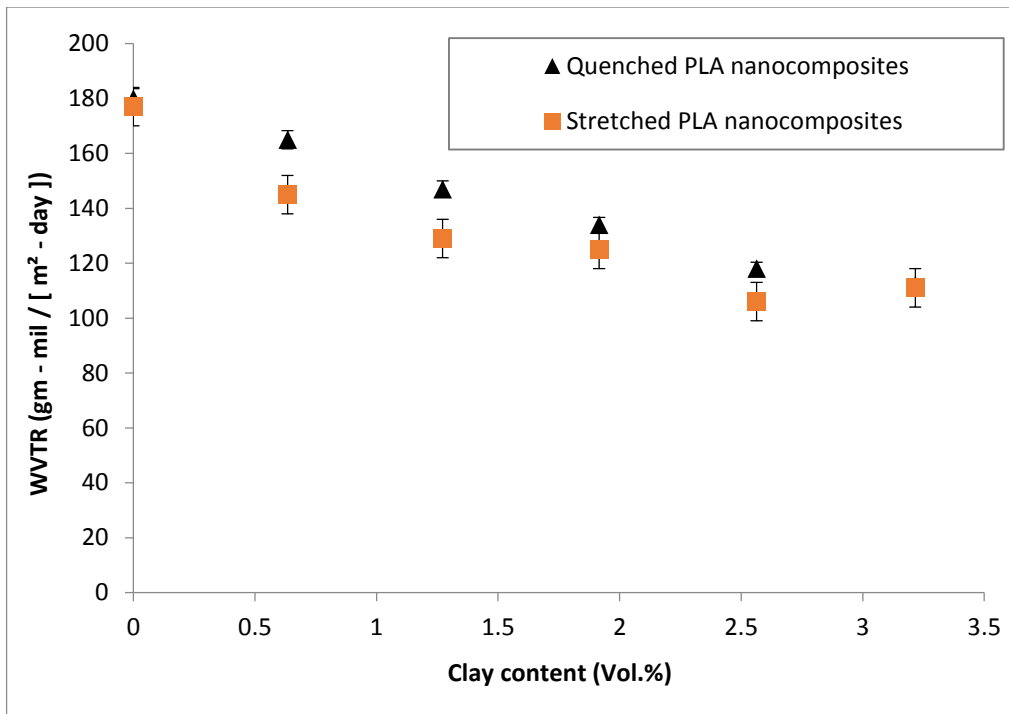


Figure 5.15 Water vapour permeabilities of uniaxially stretched PLA nanocomposites in comparison with quenched PLA nanocomposites

According to the TEM observation, the clay aspect ratio for the nanocomposite films was increased to 48 after uniaxial stretching. A plot of the predicted permeability from the Nielsen model (see Section 2.3.2, here  $L/D = 48$ ) is shown in Figure 5.16. The Nielsen model was found to fit well with the experimental data of the stretched nanocomposite except the sample with 5 wt.% nanoclay, which shows no difference from the quenched sample with the same clay content. It is concluded that stretching has enhanced the barrier property of the nanocomposite by increasing the clay tortuosity (due to drawing force applied on the intercalated tactoids during uniaxially stretching) within the samples. The fact that the 5 wt.% clay samples did not change water permeability after being stretched is because of clay agglomeration in the samples. When the clay layers are agglomerated the clay galleries cannot be further delaminated during mechanical stretching. Therefore, the samples with 5 wt.% clay did not show any improvement in the water barrier properties.

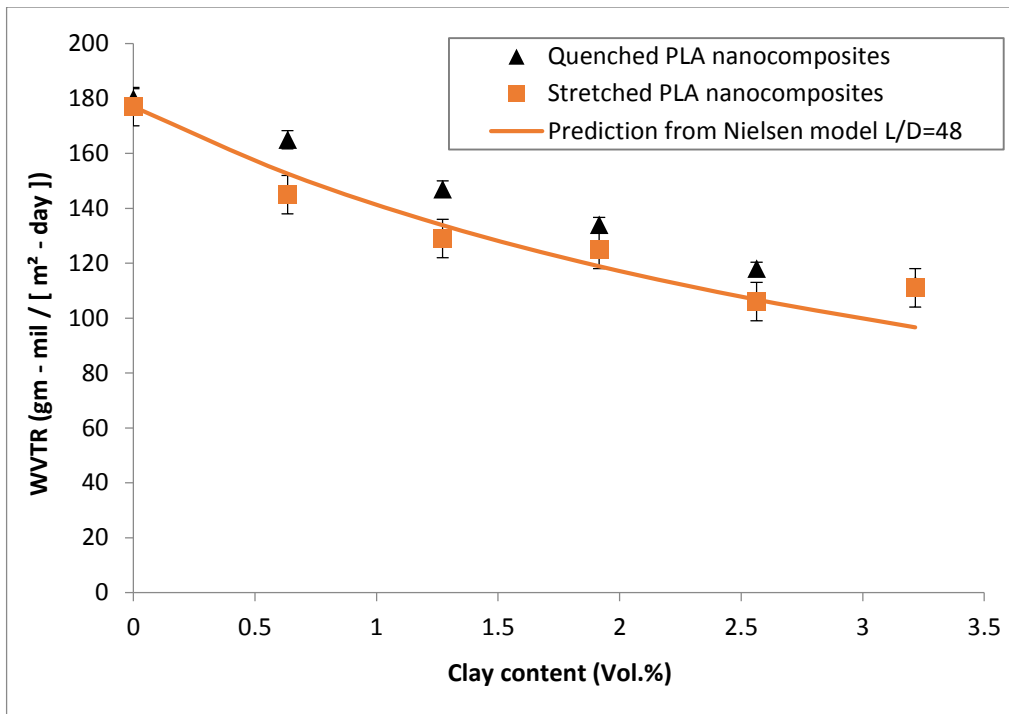


Figure 5.16 Water vapour permeabilities of quenched and uniaxially stretched PLA nanocomposites in comparison with Nielsen theoretical values (when  $L/D=48$ )

### 5.3 Summary

1. Uniaxial stretching at 60 °C and a draw ratio of 3 was applied to quenched PLA 4060D sheets using a BASE stretching machine. The stretching temperature was found to have a significant effect on the quality of the products. The optimum drawing temperature was selected from tests on samples in the range of temperature from 60°C to 75°C using various characterisation techniques. The results of birefringence test showed that the degree of orientation in the stretched PLA films reduced with the increase in drawing temperature. The DSC results showed that only the samples stretched at 60°C exhibited an increase in T<sub>g</sub> by 4°C due to the polymer chains being highly orientated, which requires more energy for chain relaxation. PLA films that had been stretched at 60°C showed the most stable and best water barrier properties compared with the other samples. Therefore, the optimum stretching temperature for the PLA nanocomposite sheets was chosen as 60 °C.
2. The thickness of the samples was found to be very sensitive in the WVTR test due to defects and air bubbles in the sample and the non-uniformity of the sample. To keep the thickness consistent, the sheets for uniaxial stretching were prepared to be three times thicker than the normal quenched samples during compression moulding.
3. Thermal properties of the uniaxially stretched PLA nanocomposite samples were measured by DSC. The T<sub>g</sub> values did not change after stretching at low clay content. However, as the clay content increased the T<sub>g</sub> value of the stretched films significantly increased by 5 °C. This indicates that the appearance of nanoclay has reduced the polymer chains mobility and therefore increased chain relaxation time at T<sub>g</sub>.
4. The nanoclay structure was measured using TEM and WAXD. It was found that a better delamination of the clay layers were obtained during uniaxial stretching. The clay aspect ratio in the uniaxially stretched samples was approximately 48. The WAXD analysis confirmed that the clay interlayer spacing had been increased during uniaxial stretching by 0.2 nm. This was attributed to the intercalated clay tactoids being drawn and sheared during

uniaxially stretching, thus the distance between the clay layers was increased.

5. Water vapour transmission rates through the stretched nanocomposite films were measured to be lower than values for the quenched nanocomposite. The WVTR data of the stretched PLA nanocomposites decreased consistently with clay concentration except the sample with 5 wt.% nanoclay, which increased to the same value as the quenched sample with 5 wt.% clay presumably due to the agglomeration of the nanoclay in the sample. The WVTR data of the stretched nanocomposite showed a good fit to the Nielsen model.

## 6 Electrospinning of PLA based nanofibres

### 6.1 Electrospinning of PLA - Selecting the optimum solvent system

Two grades of PLA were separately dissolved in single solvent (acetone or chloroform) and binary-solvent systems of acetone and chloroform (50/50 v/v) to obtain a 12.5% w/v PLA concentration. The concentration was selected according to the work of Casasola et al. [130], who reported that defect-free PLA nanofibres can be collected from a PLA/acetone solution when the polymer concentration is above 12.5% w/v. As the polymer concentration increases more chain entanglements are obtained, hence leading to an increase of the viscoelastic force, which will counterbalance the Coulombic stretching force and therefore results in fewer beads [130].

Details of the preparation method are given in Section 3.2.5. The optimum solvent system for the two grades of PLA was selected according to the morphology of the electrospun nanofibres. Table 6.1 shows the composition of the PLA solutions. Electro-spinning was carried out in a spray-base electrospray instrument manufactured by Profector Life Sciences Ltd. A flow rate of 1 ml/h and a voltage of 20 kV were used as described in Section 3.2.5.3.

Table 6.1 Composition of two grades of PLA solutions with different solvent systems

PLA grade	Solvent system	PLA concentration in solution (g/ml)
PLA 4060D	AC	12.5
	CHL	12.5
	AC/CHL (50/50 v/v)	12.5
PLA 4032D	AC	Undissolved
	CHL	12.5
	AC/CHL (50/50 v/v)	12.5

AC (acetone); CHL(chloroform)

The SEM images of amorphous PLA (grade 4060D) electrospun fibres from AC, CHL, and AC/CHL solvent systems and crystallisable PLA (grade 4032D) from CHL and AC/CHL solvent systems are shown in Figure 6.1. It is obvious that for PLA 4060D, only AC provides sufficient quantity of non-beaded fibres, whereas the other two solvent systems (CHL and AC/CHL) were found to produce nanofibres with bead-string morphologies. This is due to the conductivity and the dielectric constant of acetone being much higher than that of chloroform (see Section 3.1). As the solution conductivity of the solvent (CHL) is increased by adding another solvent with higher dielectric constant (e.g. AC), more charges are created on the jet surface, which would enhance the stability of the charged jet and help the jet flow because of a strong Coulomb repulsion force to overcome the surface tension. Hence, on increasing the high dielectric constant of the solvent, defect-free fibres are produced by electrospinning [130], [131].

Since the crystallisable PLA did not dissolve in acetone, only CHL and AC/CHL solvents were used to produce electrospun nanofibres. The AC/CHL solvent system was found to produce smooth and defect-free nanofibres, whereas the CHL single solvent produced fibres with bead-string morphology. Therefore, it is concluded that the optimum solvent systems for electrospinning PLA 4060D and PLA 4032D are AC and AC/CHL, respectively.

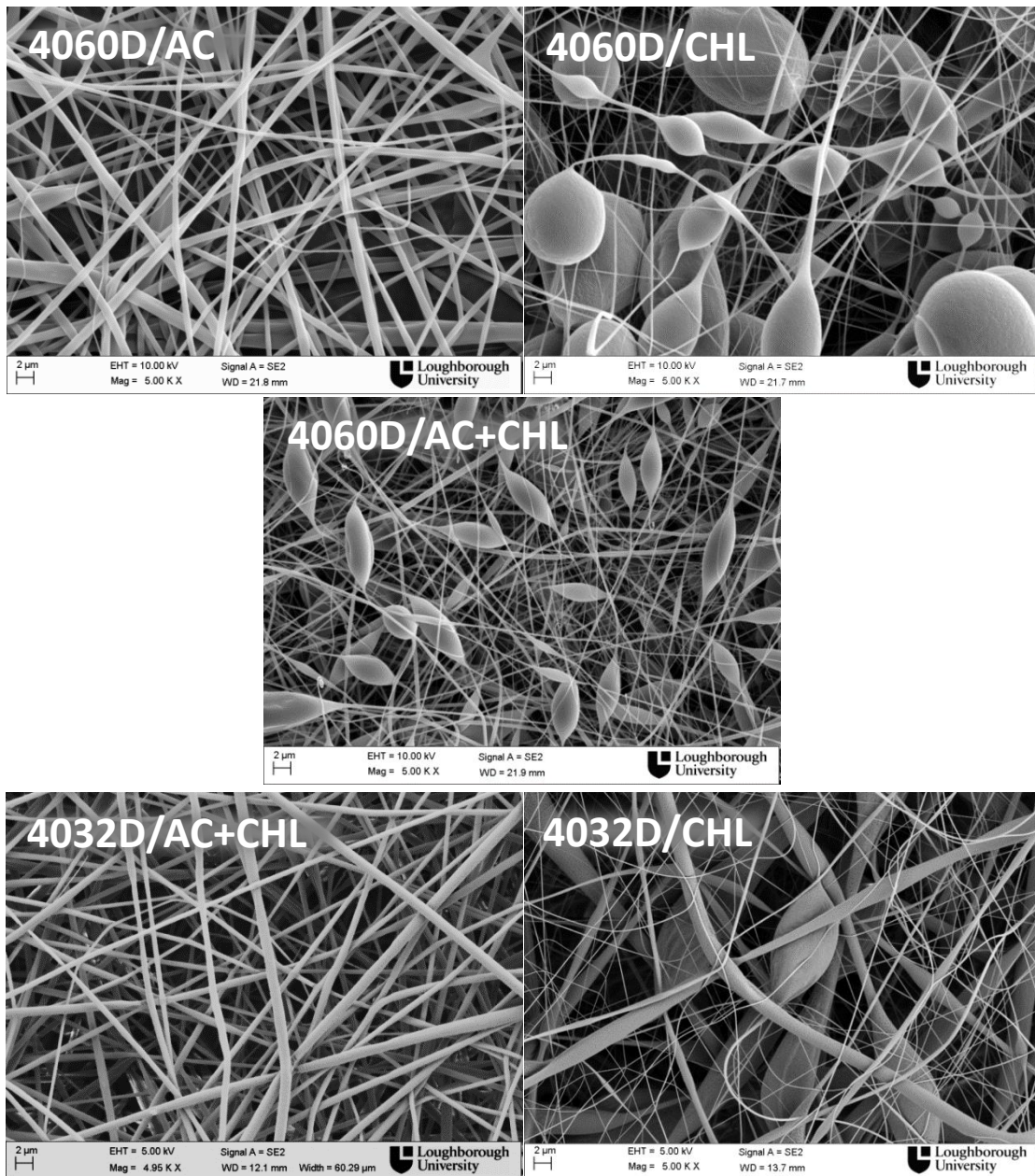


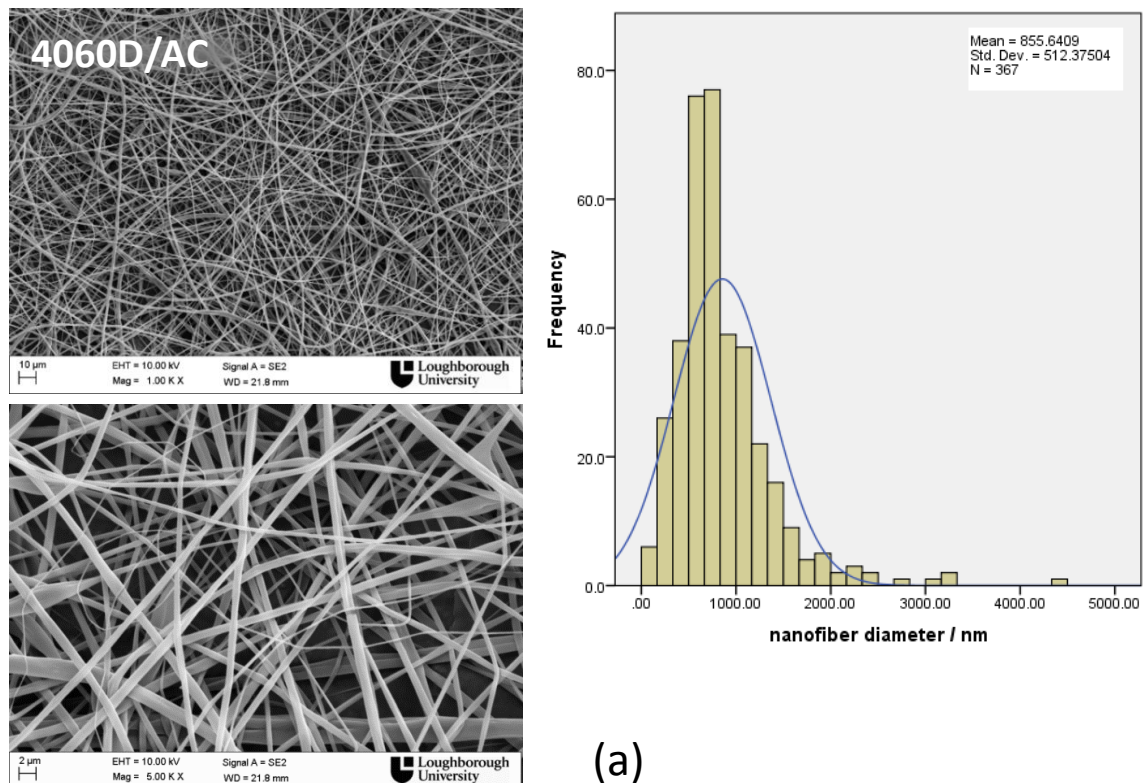
Figure 6.1 SEM images of PLA nanofibres from solutions of 12.5% (w/v) amorphous PLA (grade 4060D) in acetone, chloroform, and acetone/chloroform and crystallisable PLA (grade 4032D) in chloroform, and acetone/chloroform solvent systems

## 6.2 Electrospinning of PLA / clay nanofibres

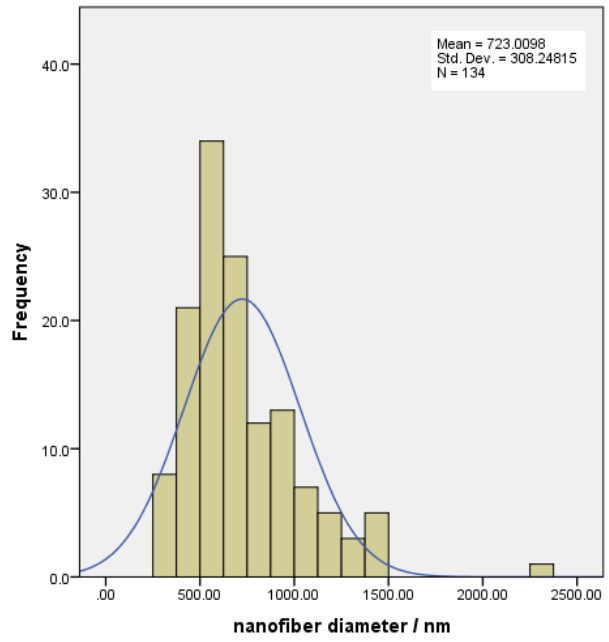
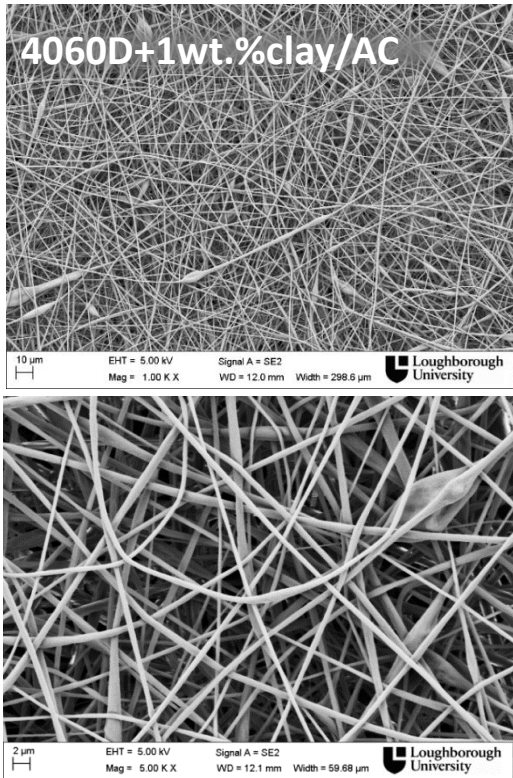
### 6.2.1 Morphology of PLA / clay nanofibres (SEM and diameter distribution)

PLA 4060D nanocomposite nanofibres containing 1, 3, and 5 wt.% montmorillonite clay were electrospun from acetone solution at 12.5% w/v concentration; and PLA 4032D nanocomposite nanofibres containing 1, 3, and 5 wt.% montmorillonite clay were electrospun from AC/CHL (50/50 v/v) solution at 12.5% w/v concentration. Details of the preparation method are given in Section 3.2.5.1.

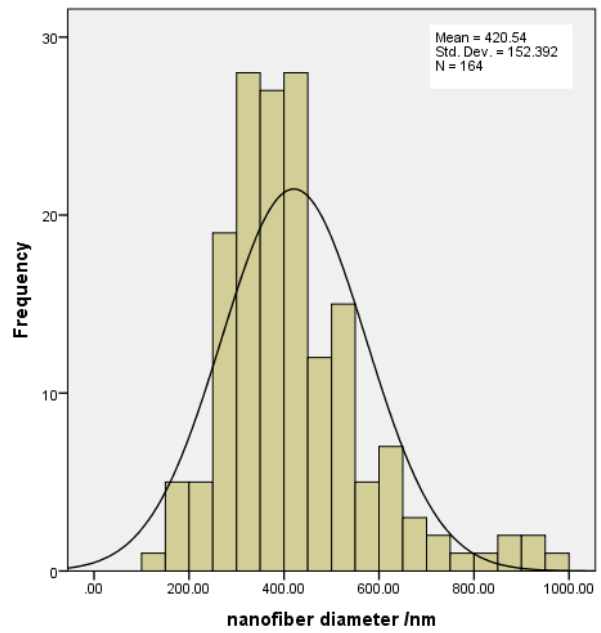
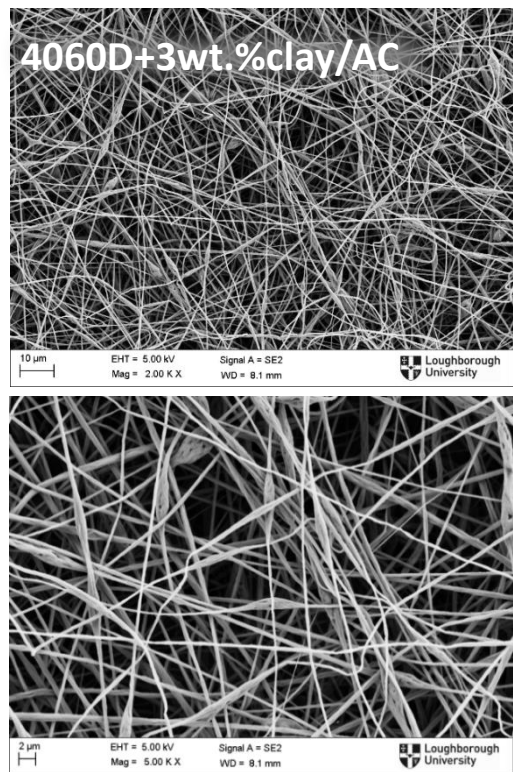
The SEM images and nanofiber diameter distribution of amorphous and crystallisable PLA / clay nanofibres are shown in Figure 6.2 and Figure 6.3, respectively. Continuous and smooth nanofibres were obtained from all the samples. Only a few beads were collected in the nanocomposite fibrous mats, which is due to the viscosity of the polymer nanocomposite solutions being lower than that of the pure polymer solution at the same concentration.



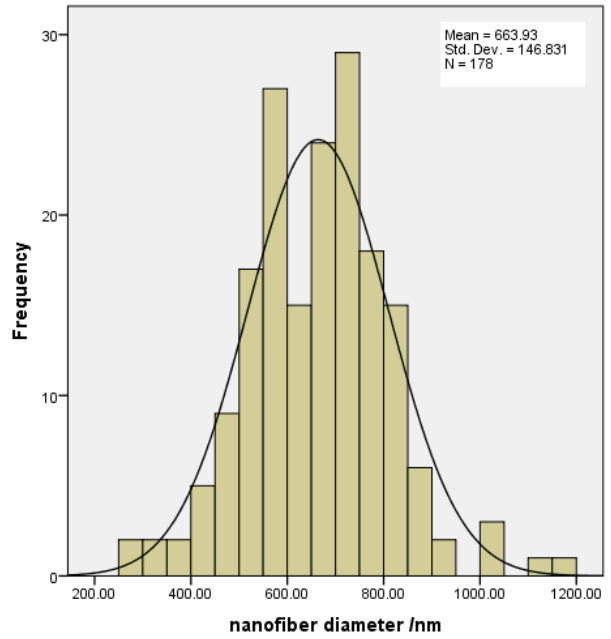
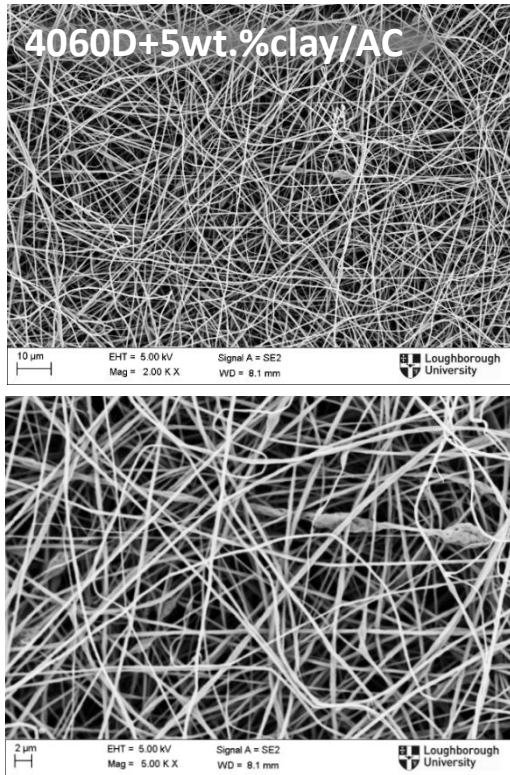
(a)



(b)

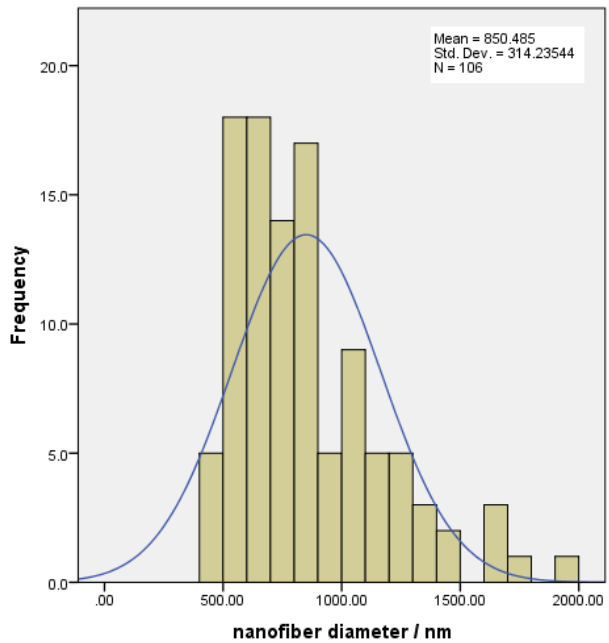
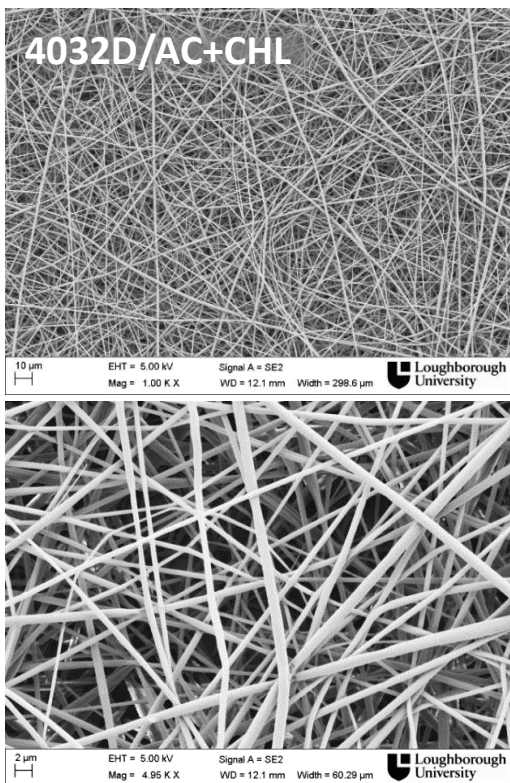


(c)

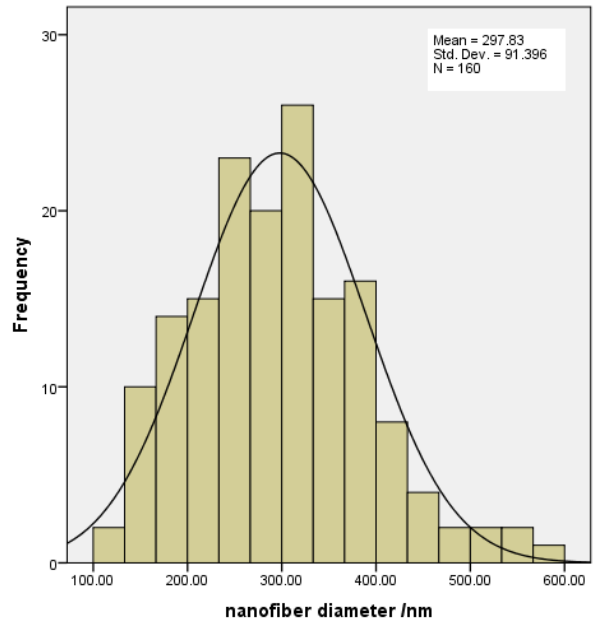
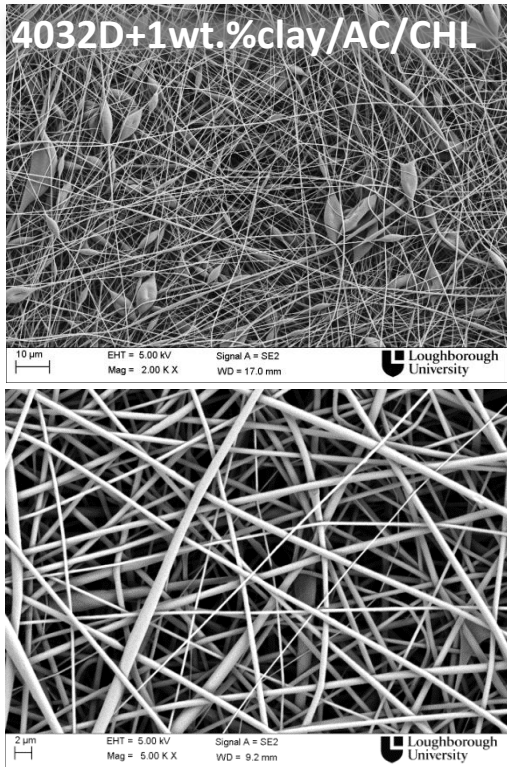


(d)

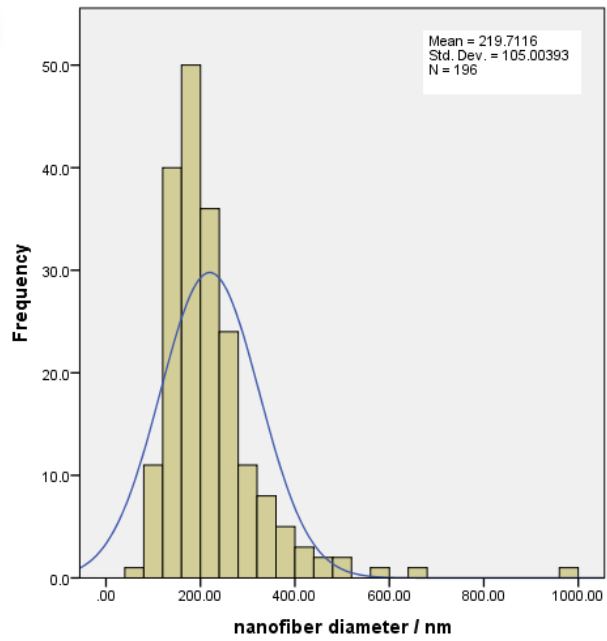
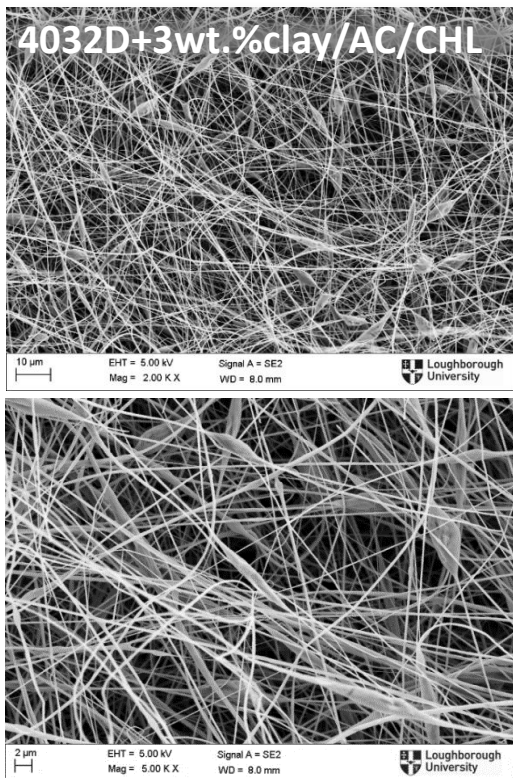
Figure 6.2 SEM images of PLA 4060D/clay nanofibres containing (a) 0 wt.%, (b) 1 wt.%, (c) 3 wt.% and (d) 5 wt.% nanoclay



(a)



(b)



(c)

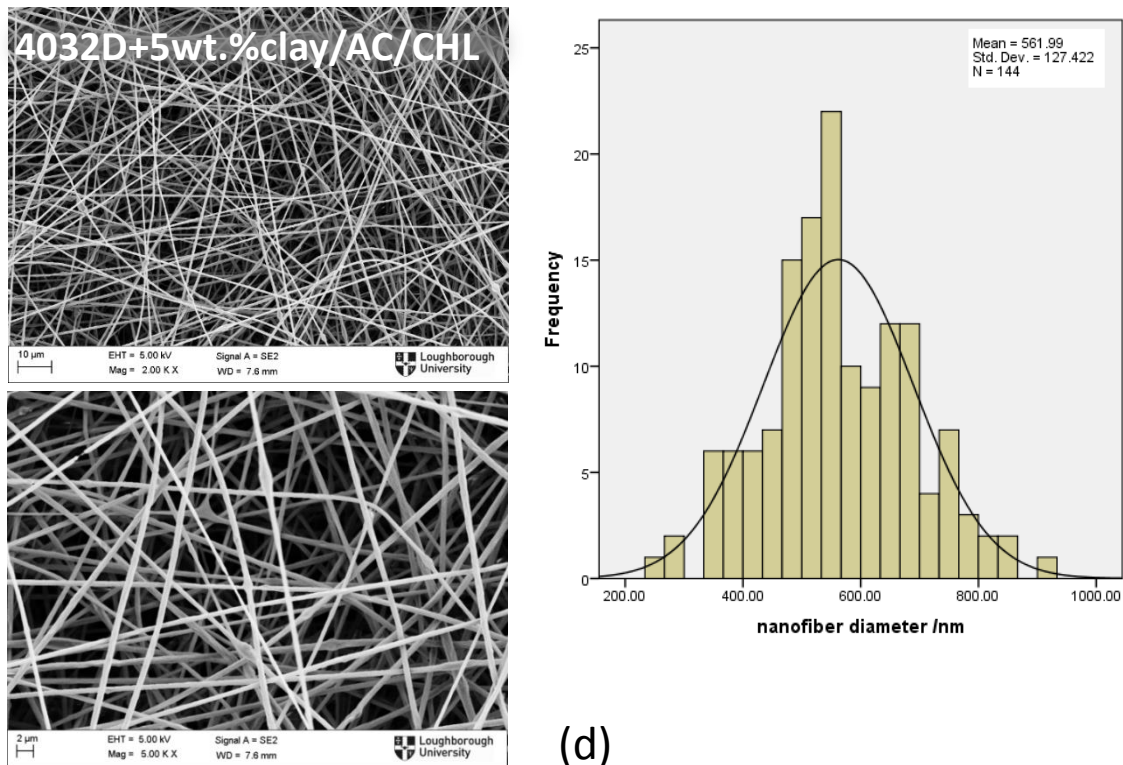


Figure 6.3 SEM images of PLA 4032D/clay nanofibres containing (a) 0 wt.%, (b) 1 wt.%, (c) 3 wt.% and (d) 5 wt.% nanoclay

The diameter of the nanofibres was measured using Image J<sup>®</sup> software and the diameter distribution was analysed using IBM SPSS Statistics 22.0. Table 6.2 shows the average diameter of the nanocomposite fibres containing various clay concentrations. The effect of clay concentration on the diameter of the nanofibres is also presented in Figure 6.4.

Table 6.2 Nanofibre diameter of PLA and PLA/clay nanocomposite fibres

Sample	PLA 4060D	PLA 4032D
Neat PLA nanofibres	856 ± 512 nm	850 ± 314 nm
1 wt.% clay	723 ± 308 nm	298 ± 91 nm
3 wt.% clay	421 ± 153 nm	220 ± 105 nm
5 wt.% clay	664 ± 147 nm	562 ± 127 nm

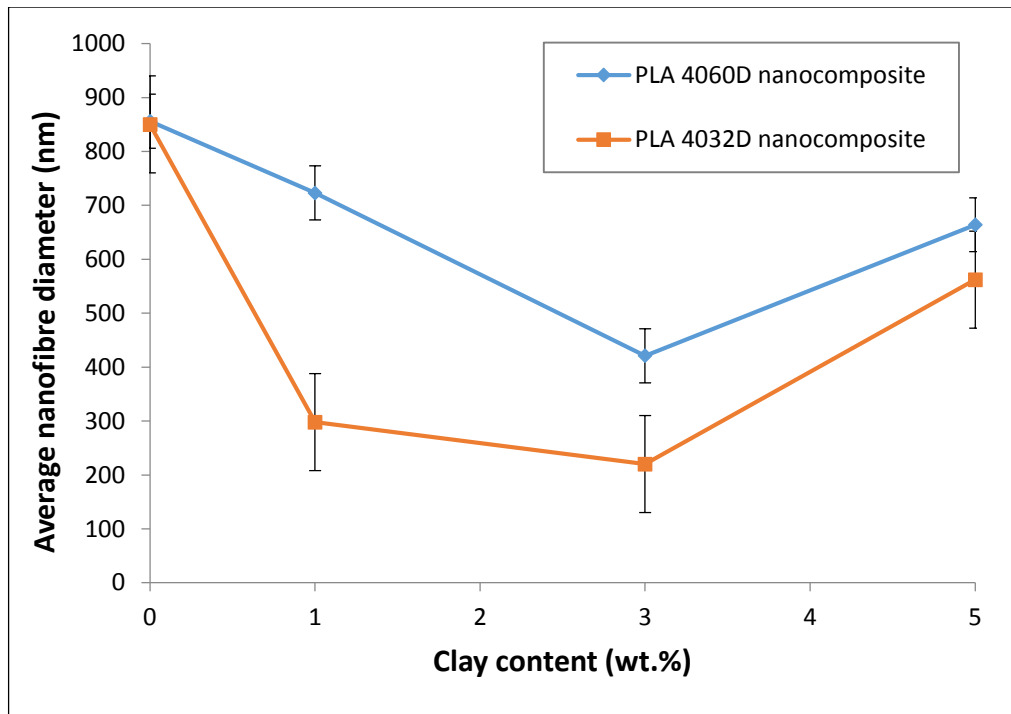


Figure 6.4 Average diameters of PLA/clay nanofibres as a function of clay concentration

It is found that for the PLA 4060D samples, the fibre diameter greatly reduced with the increase of nanoclay concentration from 1 to 3 wt.%. At 3 wt.% clay loading, the average diameter was  $421 \pm 152$  nm, which was the half of the pure PLA nanofibres. It is also noticed that more uniform nanofibres with lower standard deviation of diameter from the mean value were produced with the increase of clay content. These results occur because on adding inorganic clay to the polymer the electrical conductivity and viscosity of the polymer solution increased, which gives rise to production of finer fibres with fewer beads and narrower fibre size distributions [156][135]. However, as the clay concentration reached 5 wt.%, the nanofibre diameter increased to  $664 \pm 147$  nm, probably due to the agglomeration of the clay platelets.

These results are consistent with the observation of Touny et al. [157], who reported that the average diameter of electrospun PLA nanofibre significantly reduced on the addition of 2.5 wt.% inorganic clay (Halloysite), and then increased with more loadings of nanoclay from 5 to 15 wt.% content.

The average diameter of crystalline PLA nanofibres was  $850 \pm 314$  nm, which is

similar to the diameter of the amorphous nanofibres. Nanocomposite fibres with low clay concentrations exhibited much finer and more homogenous average diameter with reduced standard deviation. Especially at 3 wt.% clay the average nanofibre diameter was  $219 \pm 105$  nm. However the diameter of nanofibres increased when 5 wt.% clay was incorporated in the fibres, which gave an average diameter of  $562 \pm 127$  nm. The increase of the nanofibre diameter with high nanoclay loading was attributed to the aggregated silicate clay layers in the fibres. It is noteworthy that the average diameter of crystalline PLA nanofibres was much lower compared with the amorphous nanocomposite, which reveals that the nanofibres became much finer and more uniform due to the combined effect of crystallinity and clay.

### **6.2.2 TEM of PLA / clay nanofibres**

TEM images of PLA 4060D / clay nanofibres are shown in Figure 6.5, which shows the dispersion state of clay layers in PLA nanofibres. It is clearly seen that the nanoclay platelets are aligned in the spinning direction of the nanofibres. Single layered clay platelets can be seen in 1 wt.% and 3 wt.% clay samples. Aggregated clay structures are observed in the sample with 5 wt.% clay, which corresponds to the increased average diameter of this sample. The dimensions of the dispersed nanoclay platelets was measured using Image J<sup>®</sup> software. Length and thickness of the nanoclay were  $260 \pm 90$  nm and  $5 \pm 2$  nm, respectively. Therefore, the aspect ratio the nanoclay in the PLA nanofibres was about 52, which is higher compared with the aspect ratio measured from melt produced PLA nanocomposite films (Chapter 4), because the nanoclay structure was more dispersed after being dissolved and sonic stirred in the polymer solution.

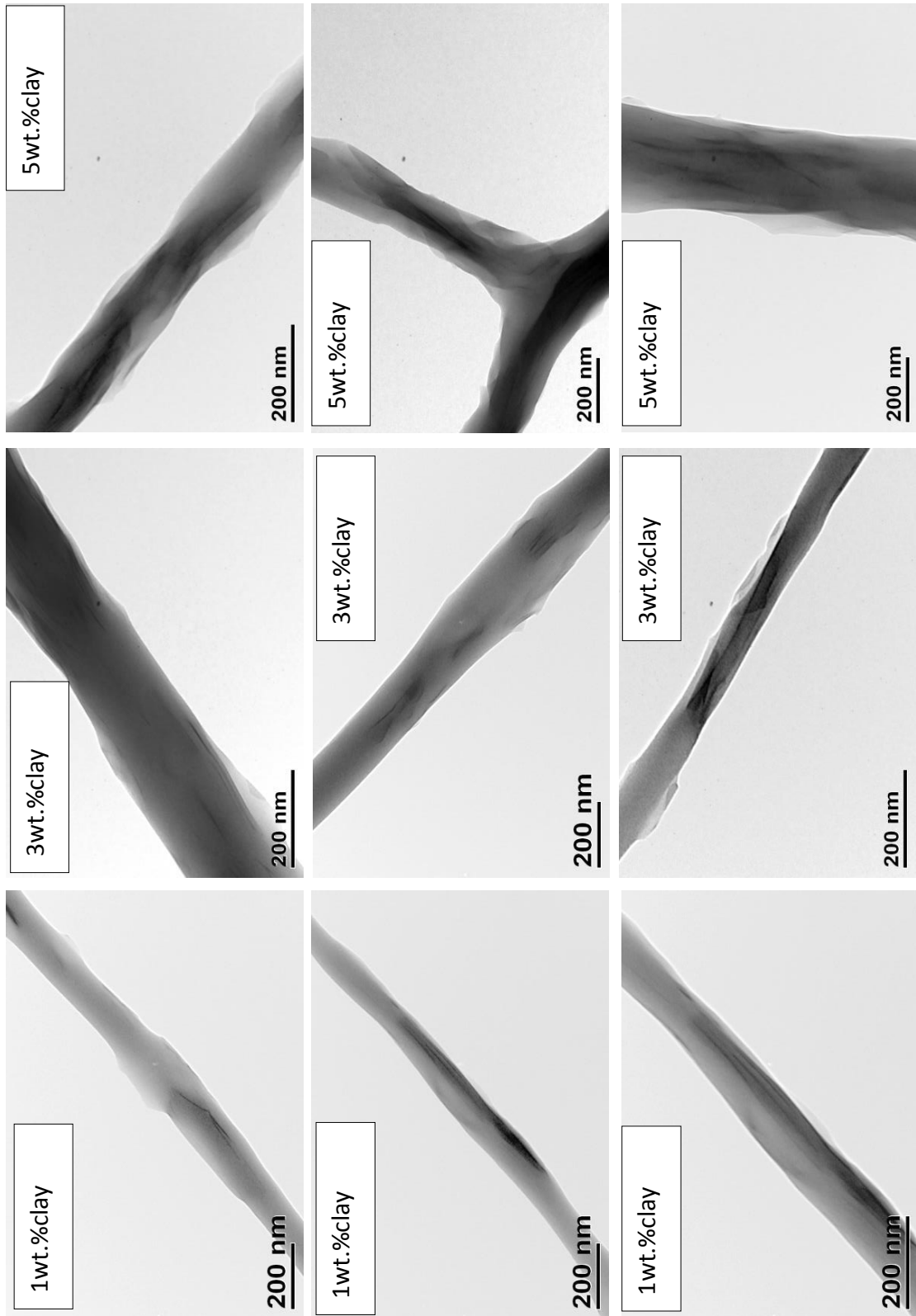


Figure 6.5 TEM images of PLA4060D / MMT nanofibres with different clay contents

### 6.2.3 DSC results of PLA / clay nanofibres

DSC scan curves of the amorphous PLA and PLA / montmorillonite clay nanofibres are shown in Figure 6.6. The step change at 58 °C is the glass transition temperature. It is found that the incorporation of nanoclay did not affect the glass transition temperature (see Table 6.3). The sharp peak following the glass transition temperature is associated with chain relaxation. However, it is noticed that the significant enthalpy relaxation peak only occurred in the sample with 1 wt.% nanoclay, whereas for the neat PLA fibres and PLA with 3 and 5 wt.% clay fibres the enthalpy relaxation peak is minimal in the DSC scan curves. Since grade 4060D is amorphous the curves do not show cold crystallisation or melting peaks.

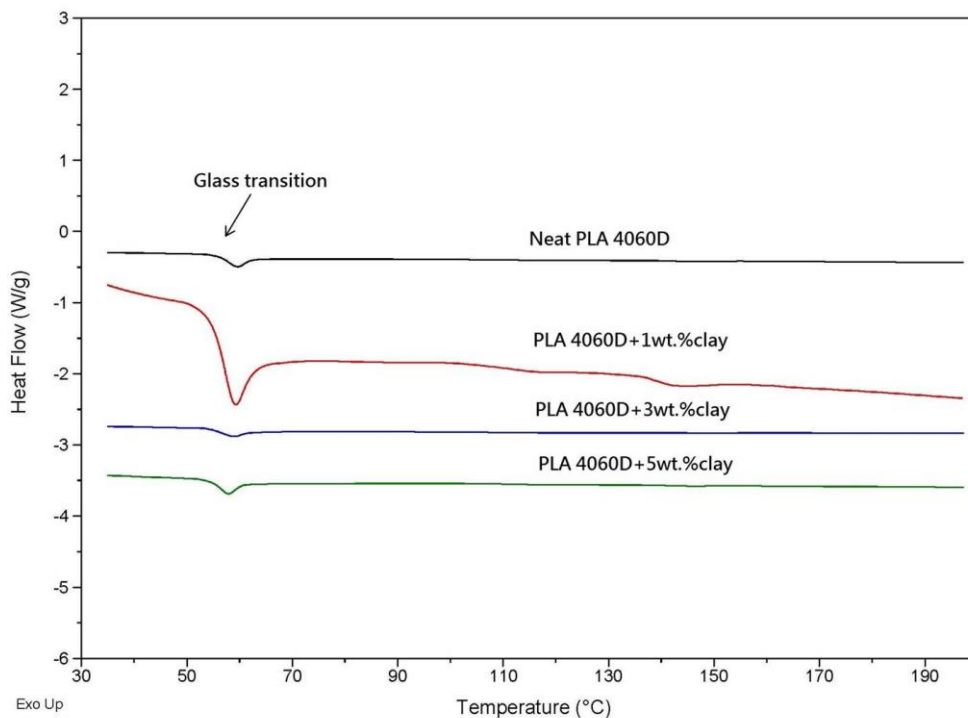


Figure 6.6 DSC scans of amorphous PLA and PLA/MMT nanofibres containing 1, 3, and 5 wt.% MMT

Figure 6.7 shows DSC curves of the crystallisable grade of PLA and PLA/MMT nanofibres. The step change caused by the glass transition was at around 60°C for the neat PLA and PLA with 1 and 3 wt.% MMT nanofibres. In the case of PLA with 5 wt.% MMT, the glass transition temperature reduced to 56°C (see Table 6.3). A minimal enthalpy relaxation peak accompanying the glass transition step

was observed in the curves for all samples. This result was also found by Badrinarayanan et al. [139], who investigated the effect of nanoclay on the thermal behaviour of electrospun PLA and found that the incorporation of nanoclay (from 15 to 25 wt.%) reduced the degree of crystallinity and the T<sub>g</sub> for both amorphous and semicrystalline PLA nanofibres. In a study of PLLA / clay scaffolds by Lee et al. [132], the decrease in T<sub>g</sub> value was attributed to enhanced PLLA chain mobility due to the presence of the MMT nanoparticles.

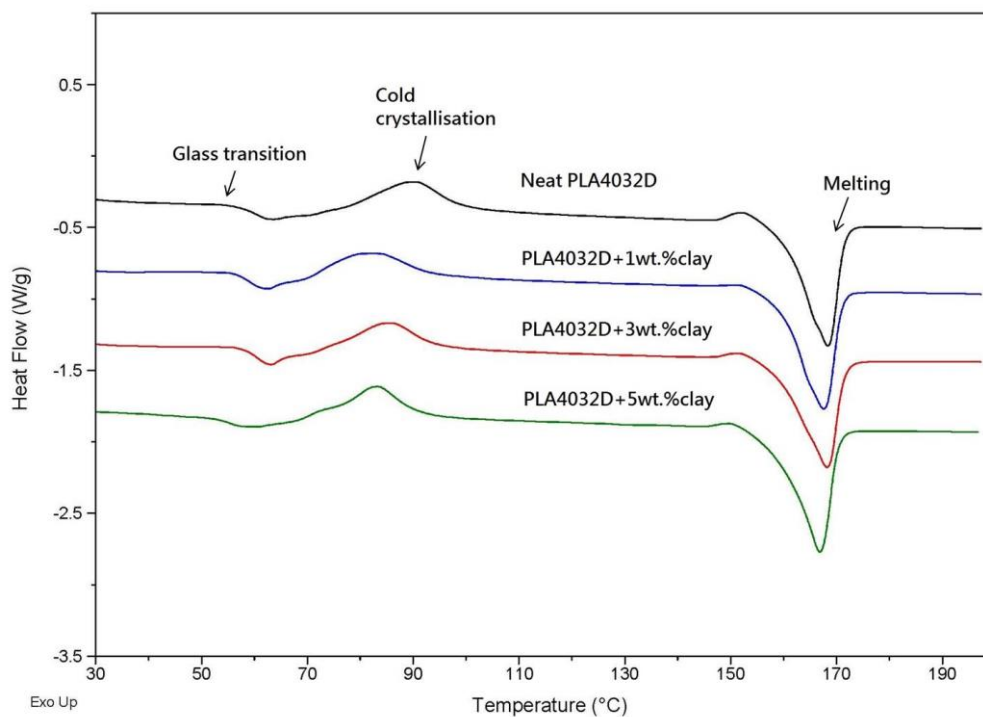


Figure 6.7 DSC scans of semi-crystalline PLA and PLA / clay nanofibres containing 1, 3, and 5 wt.% clay

A cold crystallisation exothermic peak occurred in the range 82-89°C, showing that the electrospun nanofibres had not completely crystallised during the electrospinning process. Comparing with the melt produced PLA films (Table 4.4), the T<sub>c</sub> range of electrospun PLA nanofibres is generally slightly lower, probably due to a different crystal modification ( $\beta$ -crystal) being formed during electrospinning.

It is noticed that the cold crystallisation temperatures, T<sub>c</sub>, of all the PLA / clay samples were lower than that of the pure PLA (Table 6,3). This result may be due to the nanoclay being aligned in the spinning direction, thus enhancing the formation of PLA crystals. The nano-sized clay layers provide a large surface

area due to their high aspect ratio (ca. 50). As the clay aligned in the flow direction, the particles may have acted as effective nucleating sites for PLA, which facilitated the PLA crystallisation process. Conclusively,  $T_c$  is decreased with the addition of clay [132].

Table 6.3 DSC result for electrospun PLA and PLA / clay nanofibres

Sample	$T_g$ (°C)	$T_c$ (°C)	$T_m$ (°C)	Crystallinity %
Neat PLA4060D	$58 \pm 1$	-----	-----	0
PLA4060D+1 wt.% clay	$57 \pm 1$	-----	-----	0
PLA4060D+3 wt.% clay	$56 \pm 1$	-----	-----	0
PLA4060D+5 wt.% clay	$57 \pm 1$	-----	-----	0
Neat PLA4032D	$61 \pm 1$	$89 \pm 1$	$168 \pm 1$	$21 \pm 1$
PLA4032D+1 wt.% clay	$59 \pm 1$	$82 \pm 1$	$167 \pm 1$	$29 \pm 1$
PLA4032D+3 wt.% clay	$60 \pm 1$	$86 \pm 1$	$168 \pm 1$	$29 \pm 1$
PLA4032D+5 wt.% clay	$56 \pm 1$	$84 \pm 1$	$167 \pm 1$	$31 \pm 1$

A melting endothermic peak was observed at  $168^\circ\text{C}$ , before which a small exothermic peak at  $151 \pm 1^\circ\text{C}$  was found in all PLA 4032D samples, corresponding to a change of crystal morphology before melting. Pure PLA samples had a crystallinity of  $21 \pm 1\%$  obtained from the electrospinning process. The degree of crystallinity increased up to  $31 \pm 1\%$  as the nanoclay concentration increased to 5 wt.% in the electrospun PLA nanofibres. The increase in the crystallinity is attributed to the nanoclay acting as a nucleating agent in the system, thus the crystallinity increased with the addition of clay. This result is consistent with a study of PLA / Halloysite (HNT) nanofibres by Touny et al. [157],

who found that the degree of crystallinity of neat PLA nanofibres was increased from 14% to 25% by the incorporation of 10 wt.% HNT due to the nucleating effect of the nanoclay particles.

#### 6.2.4 Mechanical properties of PLA / clay nanofibres

The mechanical properties of PLA nanofibres were analysed by tensile tests following the ISO257-2-5A specification. Five to six specimens of  $0.09 \pm 0.03$  mm thickness were investigated for each sample concentration. Figure 6.8 shows stress-strain curves of PLA 4060D based nanofibre mats containing 0, 1, 3, and 5 wt.% clay concentrations. Figure 6.9 shows the stress-strain curves of PLA 4032D nanofibres containing 3 wt.% clay. All the nanofibre samples exhibited ductile-brittle mechanical properties. Since the nanofibre mats were porous, the tensile curves are variable.

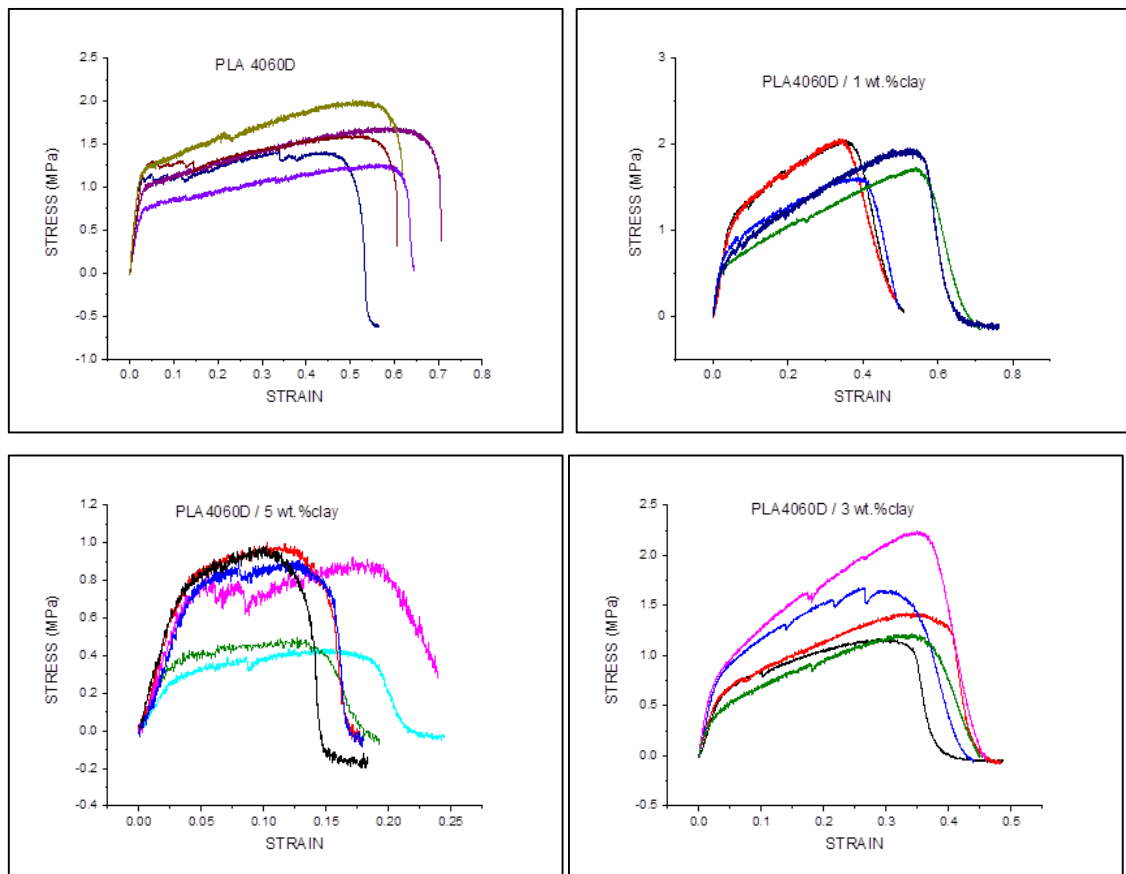


Figure 6.8 Strain - stress curves of PLA 4060D and its nanocomposite mats

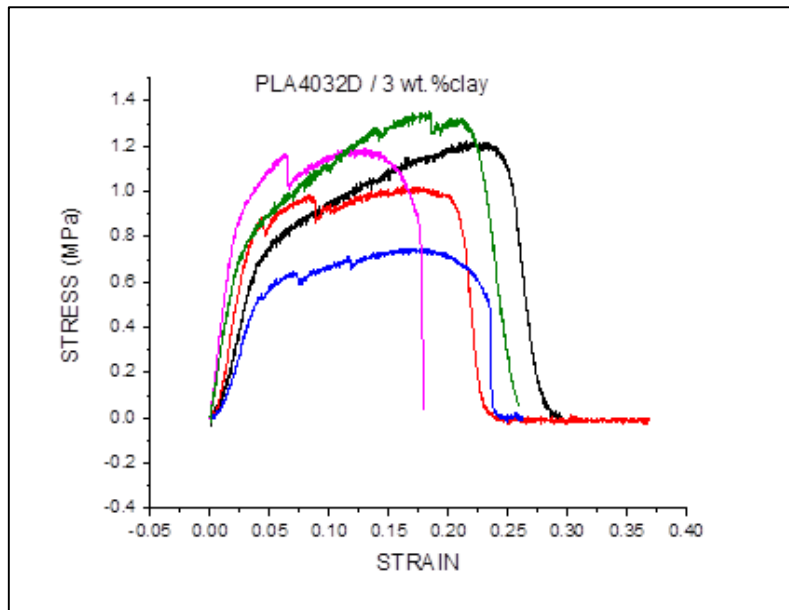


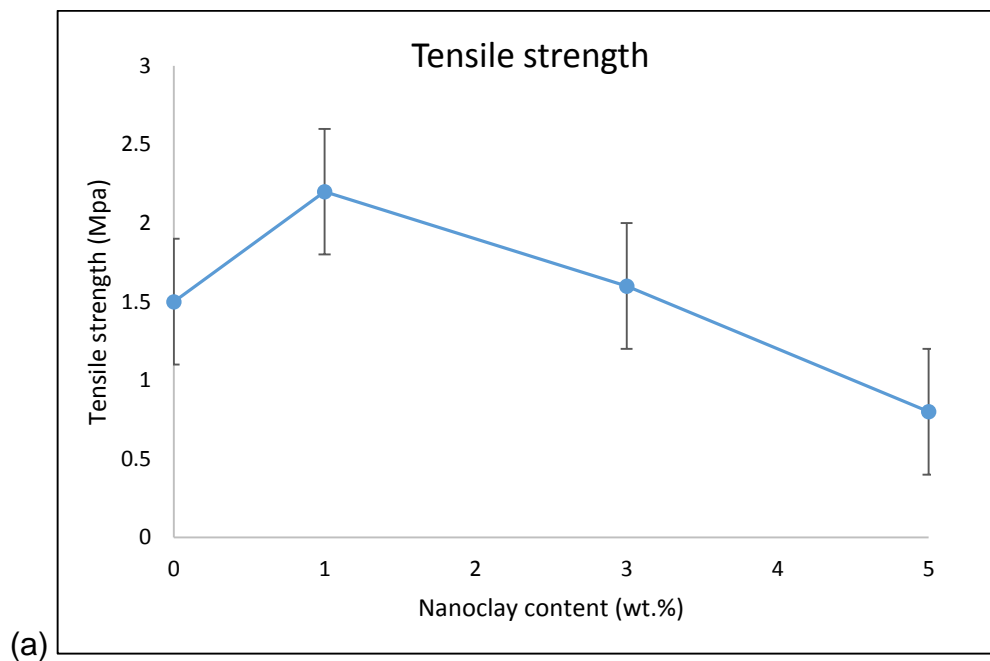
Figure 6.9 Strain - stress curves of PLA 4032D / 3wt.% clay nanocomposite mats

The tensile strength, Young's modulus and elongation at break values of the measured nanofibres are shown in Table 6.4 and the trends of the tensile properties of the amorphous nanofibres are plotted as a function of clay concentration in Figure 6.10. It is noticed that tensile strength of the nanofibres was increased with adding 1 wt.% clay, but then decreased with further addition of clay concentration. At 5 wt.% clay loading, the tensile strength was  $0.8 \pm 0.2$  MPa, which was lower than the pure PLA nanofibres. The addition of 5 wt.% nanoclay had reduced the Young's modulus and the elongation at break by 62% and 69% respectively compared with the neat nanofibres. The tensile test results lead to the conclusion that adding nanoclay of 3 wt.% or more had made the nanofibre more brittle and weaker.

It is interesting to note that crystallinity, even as high as 29%, did not enhance the mechanical properties of the PLA 4032D nanofibres. The tensile strength and Young's modulus of the PLA 4032D / 3 wt.% clay nanofibres are only  $1.1 \pm 0.2$  MPa and  $31 \pm 10$  MPa, respectively, which are the same as the values for the PLA 4060D / 3 wt.% clay nanofibres. The elongation at break of the crystalline nanocomposite sample is lower than that of the amorphous nanofibres at same clay concentration, probably due to the presence of crystallites in the fibres.

Table 6.4 Mechanical properties of PLA and PLA/clay nanofibre mats obtained from electrospinning

Sample	Tensile strength / MPa	Young's modulus / MPa	Elongation at break / %
PLA 4060D	1.5±0.3	47 ± 11	55± 9
PLA 4060D +1 wt.% clay	2.2±0.9	34± 16	48 ± 12
PLA 4060D +3 wt.% clay	1.6±0.4	26± 8	36± 3
PLA 4060D +5 wt.% clay	0.8±0.2	18± 5	17± 2
PLA 4032D+3 wt.% clay	1.1±0.2	31 ± 10	21± 3



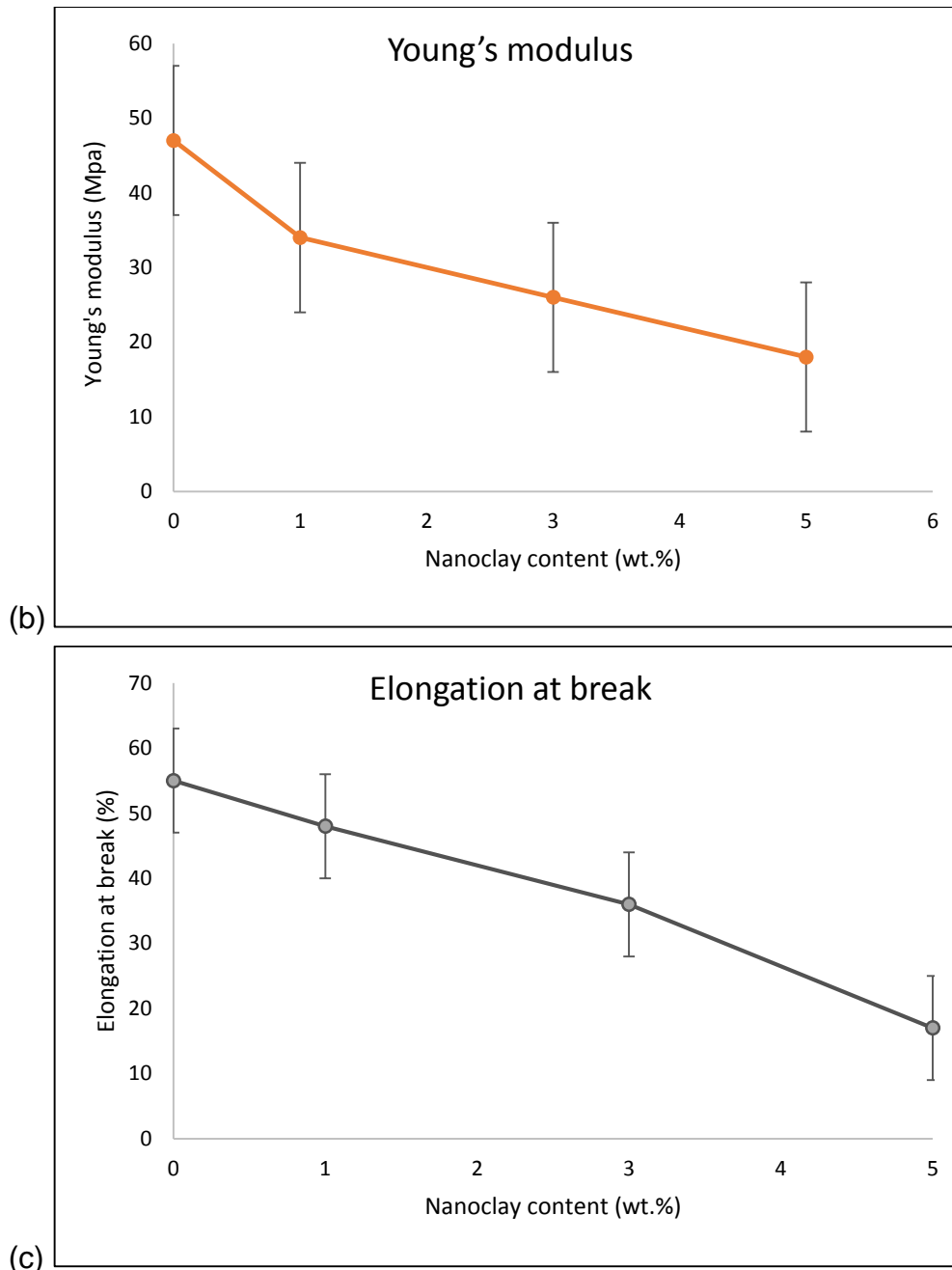


Figure 6.10 Tensile properties of amorphous PLA/clay nanofibre mats as a function of clay concentration (a) tensile strength (b) Young's modulus (c) Elongation at break

This result does not agree with the research by Shi et al. [158], who studied the mechanical properties of PLA / cellulose fibres produced by electrospinning. They found that the PLA nanocomposite mats gave excellent mechanical properties at cellulose content below 5wt.%. The tensile strength and Young's modulus of the PLA nanocomposite mats with 5wt.% cellulose increased by

about 5 and 22 fold (i.e., 6.3 and 125.6 MPa) comparing with the neat PLA nanofibre mats. The improvement of the mechanical properties was ascribed to the reinforcement of cellulose, increased crystallinity of PLA matrix and more uniform and finer fibre morphology. In the case of PLLA / clay scaffold, Lee et al. [132] investigated the mechanical properties of the PLLA nanocomposite scaffolds produced by salt / leaching gas foaming method and found that the modulus of the composite fibres were increased by the presence of clay particles. In their case, the exfoliated clay particles acted as a mechanical reinforcement of the polymer chains in the scaffold.

In our case, the reason of poor mechanical properties of PLA / clay nanofibres could that be the size of montmorillonite clay particles was too large to reinforce PLA nanofibres. Nanofillers with small size (i.e. diameter less than 100 nm) would be better a choice to enhance the mechanical properties PLA nanofibres.

### 6.2.5 Summary of PLA / clay nanofibres

1. Two grades of PLA were dissolved in a single solvent (acetone or chloroform) and binary-solvent systems of acetone and chloroform (50/50 v/v) to obtain a 12.5% w/v PLA concentration. Electrospinning was carried out in a spray-base electrospay instrument (Profector Life Sciences Ltd.) using a flow rate of 1 ml/h and a voltage of 20 kV. The optimum solvent systems for electrospinning PLA 4060D and PLA 4032D are AC and AC/CHL, respectively, from which continuous and non-beaded nanofibres were collected.
2. PLA nanocomposite nanofibres containing 1, 3, and 5 wt.% montmorillonite clay were produced from the optimum solution at 12.5% w/v concentration using electrospinning.
3. The morphology of the nanofibres was investigated using SEM. Continuous nanofibres with the existence of a few beads were obtained. The diameter of the nanofibres was measured using Image J<sup>®</sup> and the diameter distribution was analysed using IBM SPSS Statistics 22.0. For both of the grades, the fibre diameter firstly reduced with the increase of nanoclay loading when the clay content is below 3 wt.%, then tended to increase as the clay content increased to 5 wt.%. The average diameters of the crystallisable PLA (grade 4032D) / clay nanofibres are lower than those of the respective amorphous PLA (grade 4060D) / clay nanofibres.
4. The nanoclay structure in the nanofibres was investigated using TEM. The nanoclay platelets were fully exfoliated and aligned in the flow direction of drawn force. The aspect ratio of the nanoclay in the PLA nanofibres was measured to be about 52.
5. Thermal properties of the nanofibres were investigated using DSC. In both of the two grades of PLA nanofibres, T<sub>g</sub> decreased with the addition of nanoclay. The crystallisable PLA / clay nanofibres had a degree of crystallinity in the range 21% - 31%. The crystallinity increased with clay content. The crystallisation temperature range of electrospun PLA fibres (82 - 89°C) is much lower than that of melting produced PLA films, probably due to the formation of  $\beta$ -crystal during electrospinning.
6. The mechanical properties of PLA nanofibres were analysed by tensile tests following the ISO257-2-5A specification. All the nanofibre samples exhibited

ductile-brittle mechanical properties. The addition of nanoclay in excess of 1 wt.% reduced mechanical properties of the PLA nanofibres.

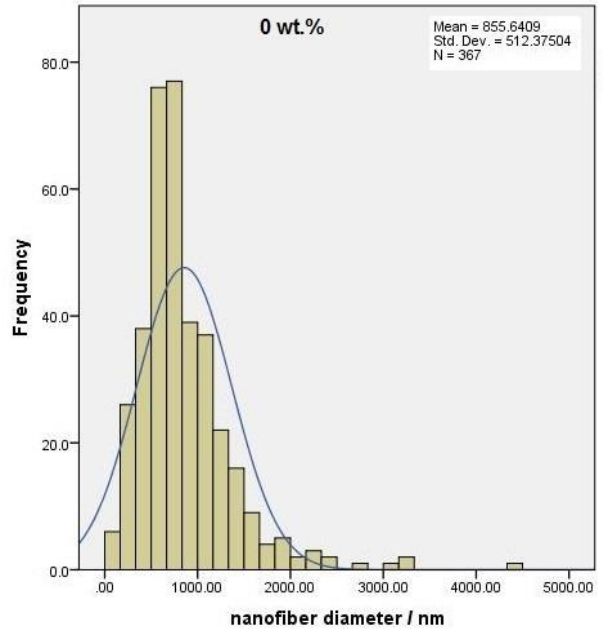
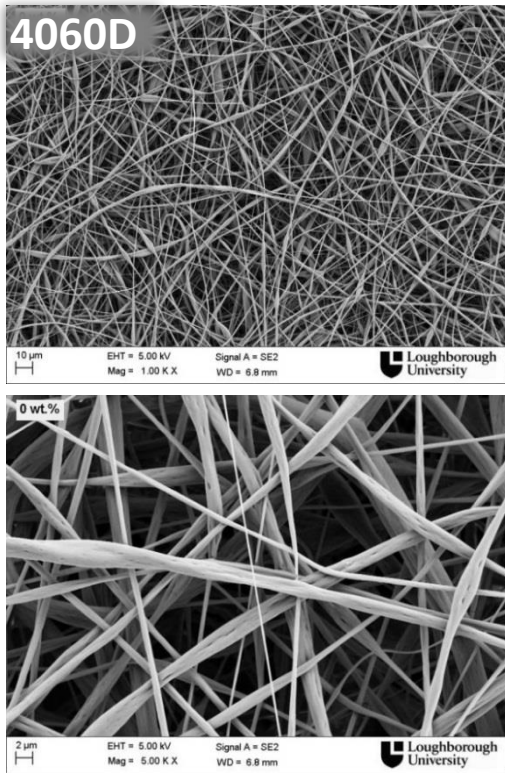
## **6.3 Electrospun PLA / ZnO nanofibres**

### **6.3.1 Preparation and morphology of PLA / ZnO nanofibres**

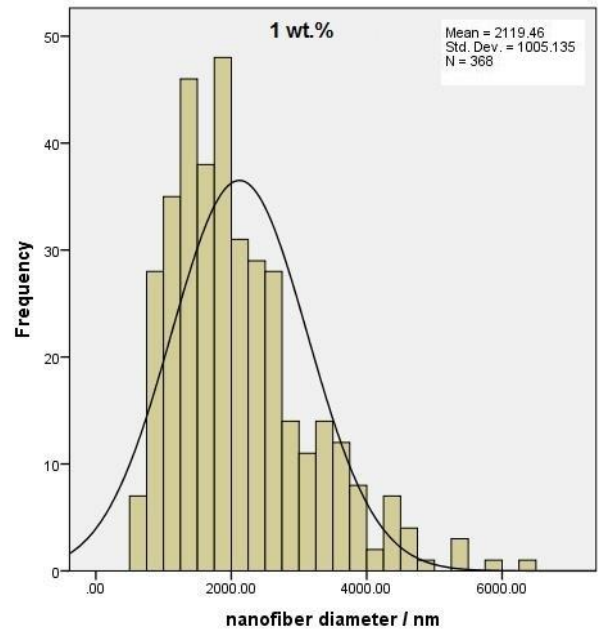
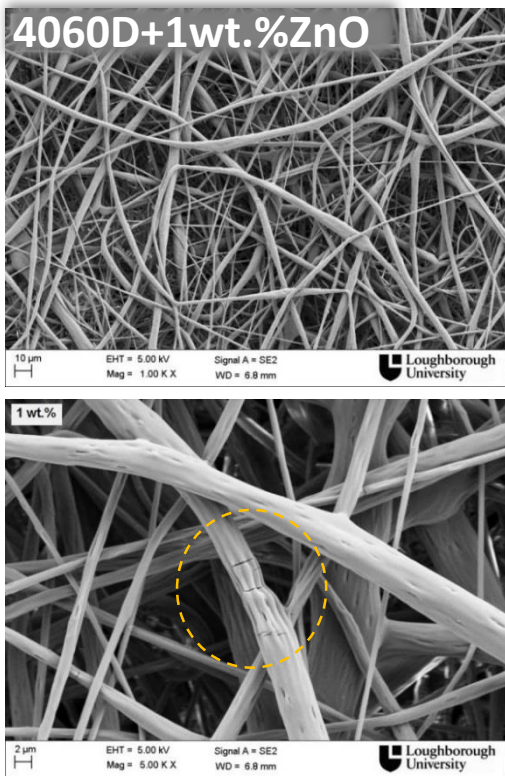
PLA 4060D nanocomposite nanofibres containing 1, 3, 5, 7 and 9 wt.% zinc oxide (ZnO) were electrospun from acetone solution at 12.5% w/v concentration. The preparation method is described in detail in Section 3.2.5.2.

The SEM images of the surface morphology of PLA / ZnO nanofibres are shown in Figure 6.11. It is noticed that the surface roughness is significantly affected by the ZnO concentration. The neat PLA nanofibres are smooth with some pores on the surface. However, with the incorporation of ZnO nanoparticles, the nanofibres turned to become a 'ridged' and porous surface (as shown in the 1 wt.% SEM images). As more ZnO nanoparticles are added, more 'ridged' nanofibres are formed. At the concentration of ZnO above 5 wt.%, some clusters of ZnO particles are aggregated and emerge on the surface of the PLA nanofibres.

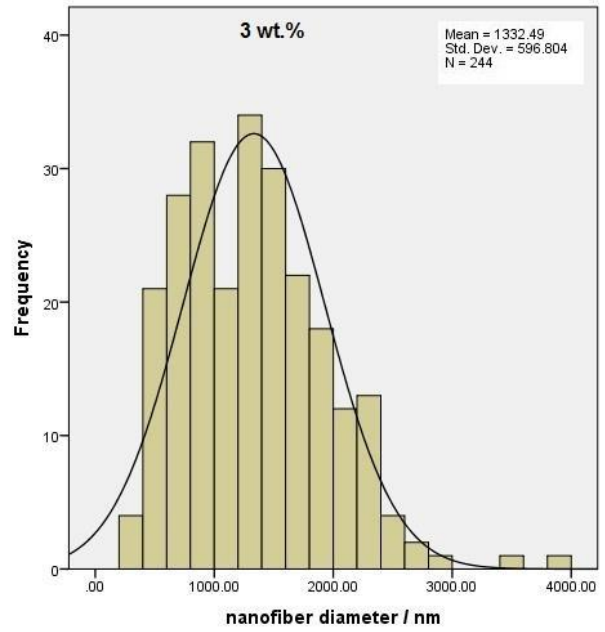
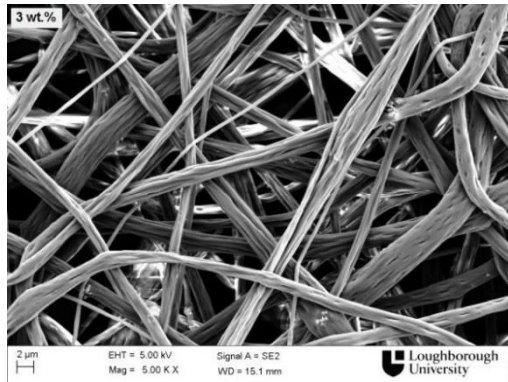
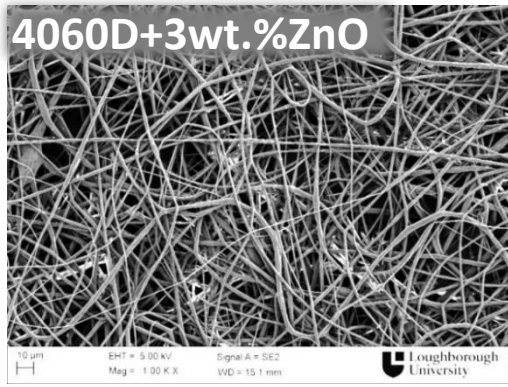
Figure 6.12 shows backscattered electron microscopy images of PLA nanocomposite fibres with 5 wt.% ZnO that gives a representation of the particle distribution. The white regions in Figure 6.12 indicate ZnO nanoparticles. It is found that a good distribution of the ZnO particle was obtained through out the electrospun nanofibres, accompanied by some nanoparticle agglomerations.



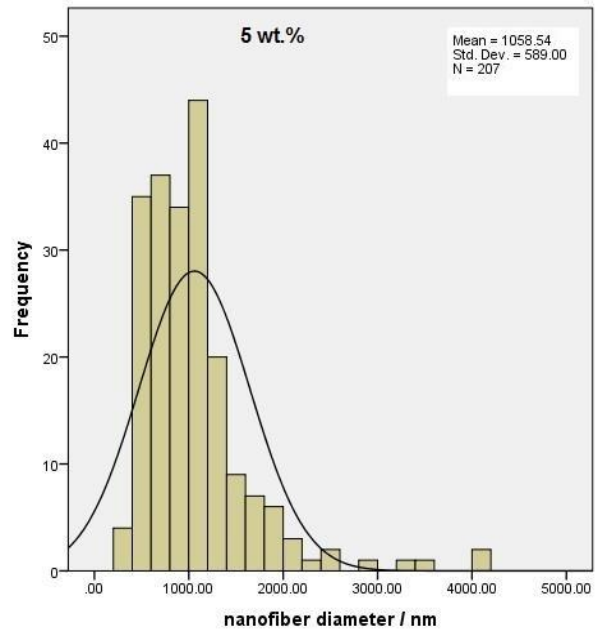
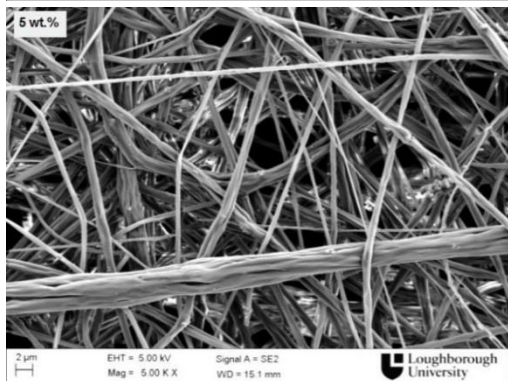
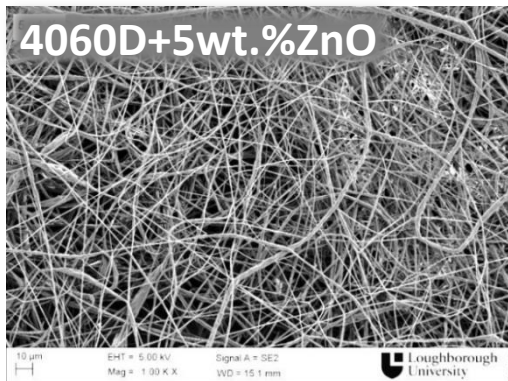
(a)



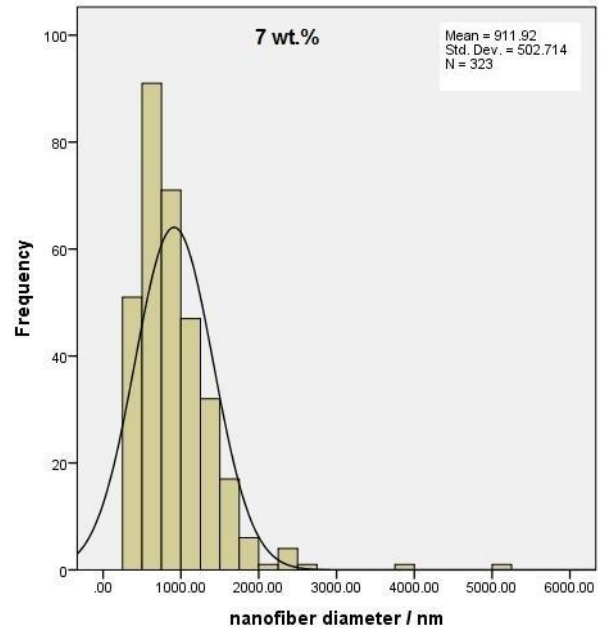
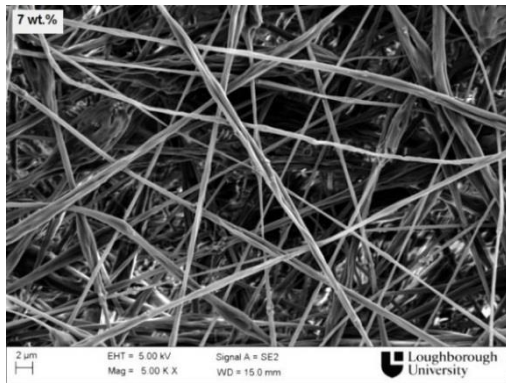
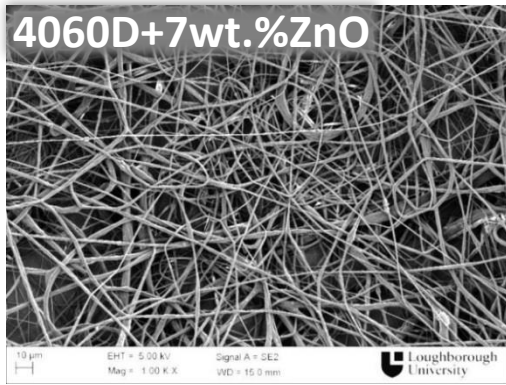
(b)



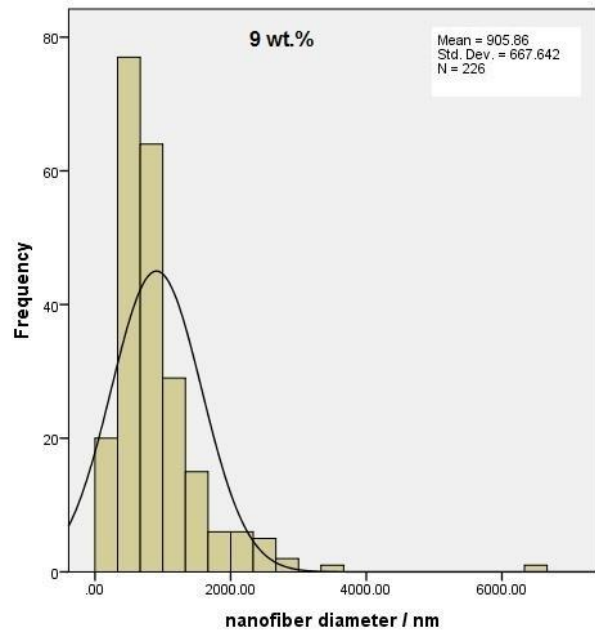
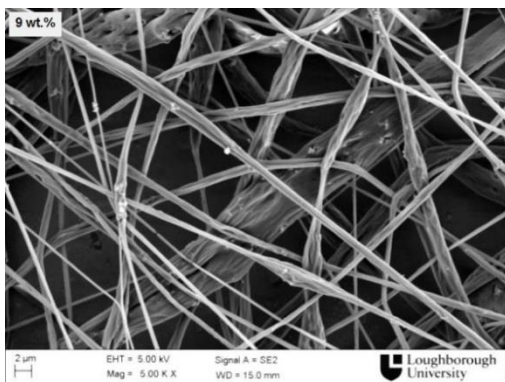
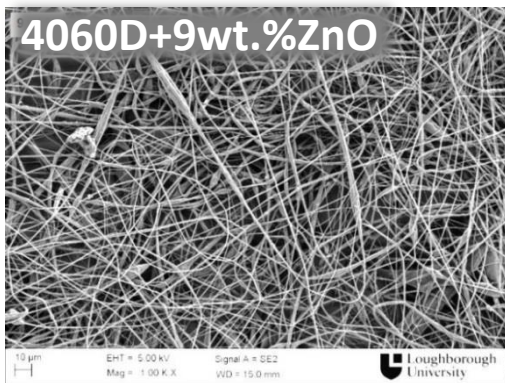
(C)



(d)



(e)



(f)

Figure 6.11 SEM images of (a) PLA and PLA/ZnO nanofibres containing (b) 1 wt.%, (c) 3 wt.%, (d) 5 wt.%, (e) 7 wt.%, (f) 9 wt.% ZnO

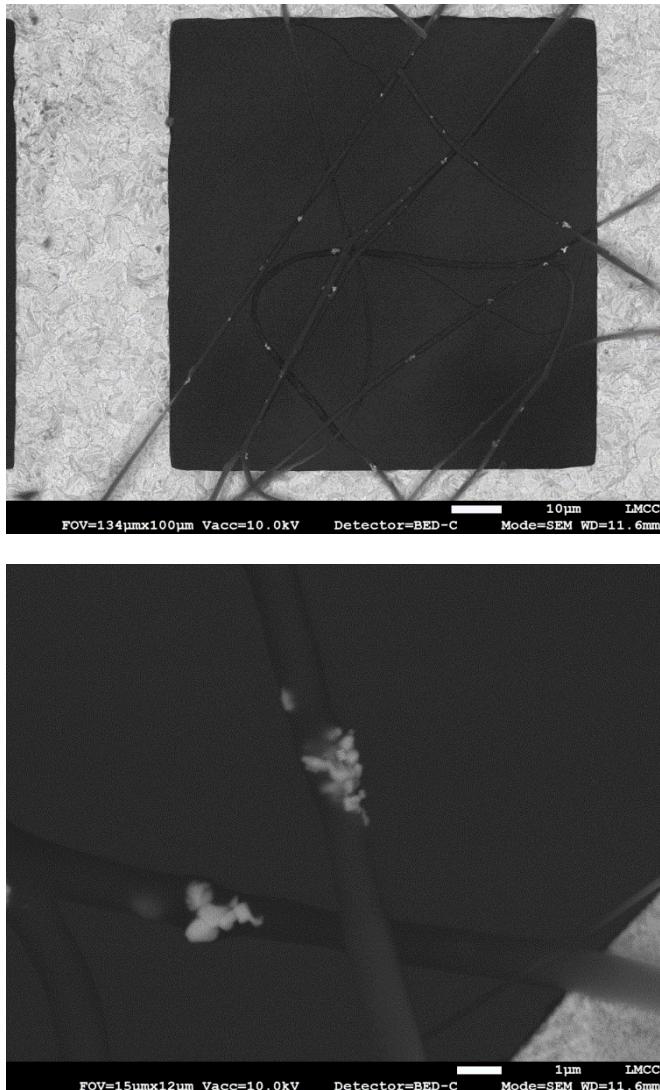


Figure 6.12 SEM images of PLA/ZnO nanofibres containing 5 wt.% ZnO at different magnifications using backscattered electrons

Table 6.5 shows the average diameter of nanocomposite fibres containing various clay concentrations and the effect of ZnO concentration on the diameter of the nanofibres is presented in Figure 6.13. The average diameter of pure PLA nanofibres was  $856 \pm 512$  nm. However, unlike the nanoclay, as 1 wt.% ZnO was incorporated the average fibre diameter increased to 2119 nm with a large standard deviation of 1005. This could be due to the large size of the ZnO particles and the porous structure of the nanofibres in the nanocomposite samples. With further addition of ZnO, the average diameter reduced continuously to  $906 \pm 668$  nm for the 9 wt.% ZnO nanofibres, which was still higher than that of pure PLA nanofibres.

Table 6.5 Nanofibre diameter of PLA/ZnO nanocomposite mats

Fibre composition	Nanofibre diameter
Neat PLA nanofibres	856 ± 512 nm
PLA + 1 wt.% ZnO	2119 ± 1005 nm
PLA + 3 wt.% ZnO	1332 ± 597 nm
PLA + 5 wt.% ZnO	1059 ± 589 nm
PLA + 7 wt.% ZnO	912 ± 503 nm
PLA + 9 wt.% ZnO	906 ± 668 nm

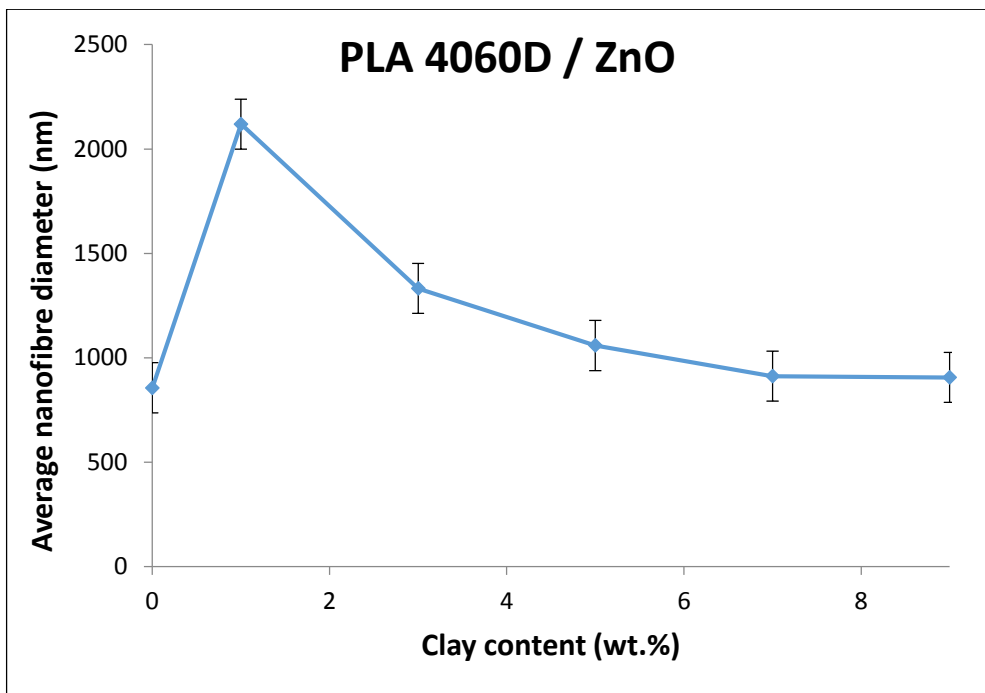


Figure 6.13 Average diameters of PLA/ZnO nanofibres as a function of ZnO concentration

Rodríguez-Tobías et al. [146] also obtained porous PLA / ZnO nanofibre continuous nanofibres by electrospinning from PLA, ZnO and 2,2,2-trifluoroethanol solution. The PLA / ZnO nanofibres showed a uniform morphology with an average porosity about 55%. However, the diameter of their nanocomposite fibres was consistent with ZnO content, giving an average value of 810, 700, 710 and 790 nm with standard deviation of 200-400 nm for the nanofibres with 0, 1, 3 and 5 wt.% ZnO.

### 6.3.2 TEM of PLA / ZnO nanofibres

TEM images of PLA / ZnO nanofibres with 1, 3, 5 wt.% ZnO concentrations are shown in Figure 6.14, where single and aggregated ZnO particles can be observed. Some aggregation and clusters of ZnO particles were observed in the samples containing 1 wt.% ZnO, which resulted in high nanofibre diameter to the nanocomposite mats. The diameter of the dispersed ZnO nano-particles was measured to be  $95 \pm 50$  nm using Image J® software.

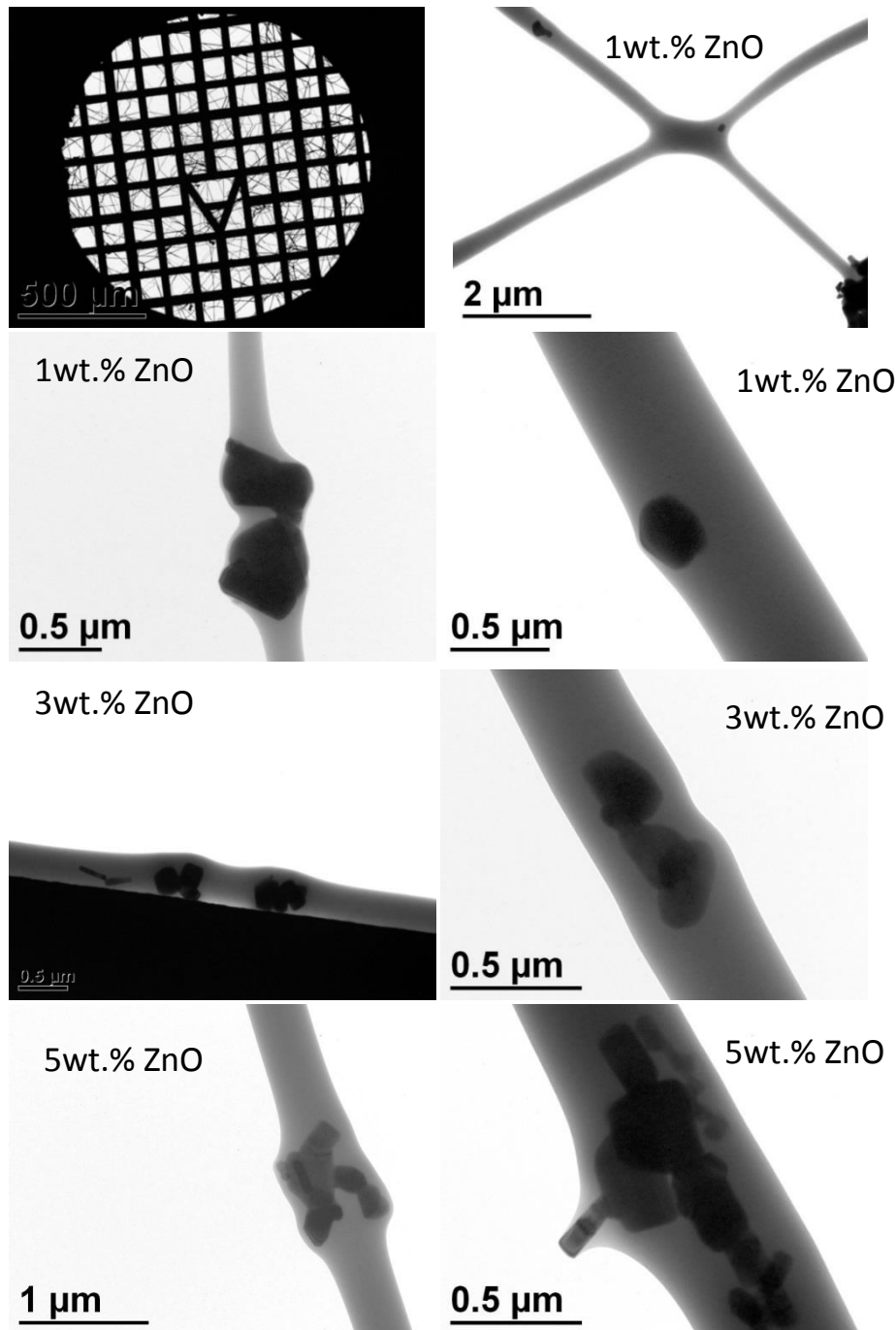


Figure 6.14 TEM images of PLA/ZnO nanofibres containing 1, 3, 5 wt.% ZnO

### 6.3.3 DSC result of PLA / ZnO nanofibres

Thermal properties of PLA / ZnO nanofibres were investigated using DSC. The heat scan curves of PLA and PLA nanocomposite nanofibres are shown in Figure 6.15. The step change at 58°C is related to the glass transition temperature. The sharp peak next to the glass transition temperature is associated with polymer chain relaxation. The measured values of T<sub>g</sub> are shown in Table 6.6. Unlike nanoclay, the incorporation of ZnO in PLA nanofibres did not affect the T<sub>g</sub> value of the polymer. However, it is noteworthy that the area under the enthalpy relaxation peak became larger with the addition of ZnO. This indicates that the addition of ZnO particles has enhanced the relaxation of the polymer chains. Since the polymer is amorphous the curves do not show any crystallisation or melting peaks.

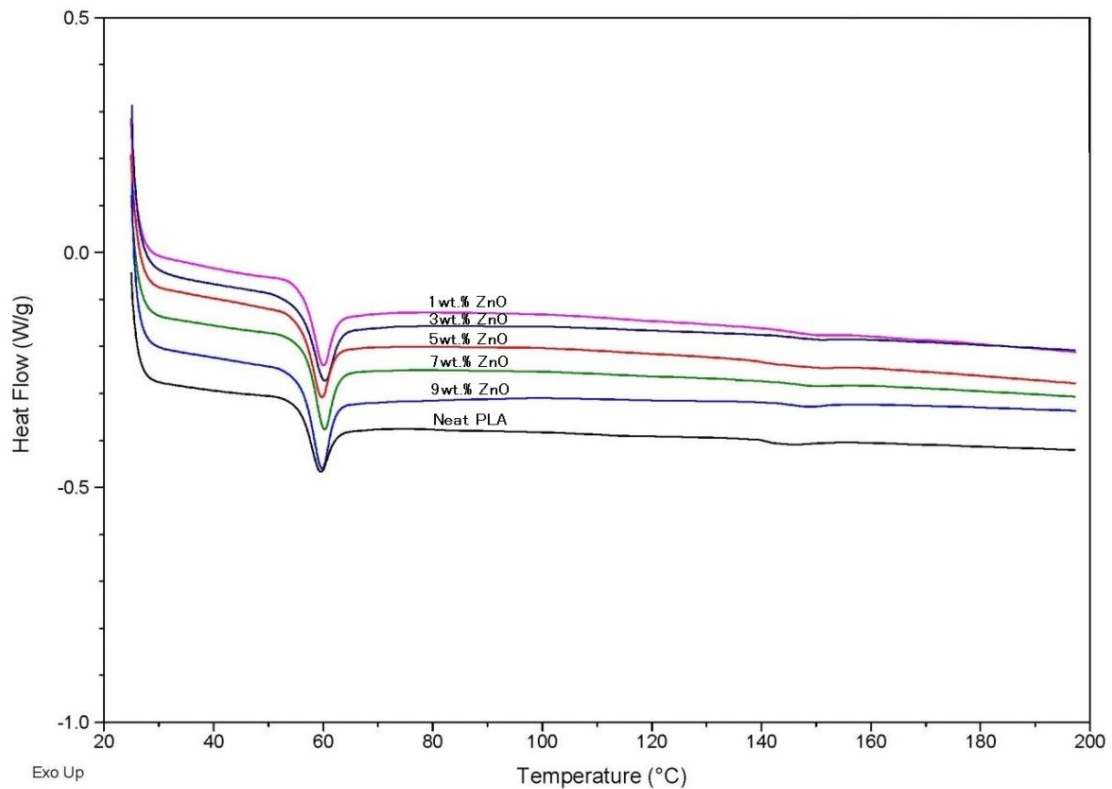


Figure 6.15 DSC scans of PLA / ZnO nanofibres containing 1 to 9 wt.% ZnO

Table 6.6 DSC result of electrospun PLA / ZnO nanofibres

Sample	Tg (°C)
Pure PLA	58 ± 1
PLA + 1 wt.% ZnO	59 ± 1
PLA + 3 wt.% ZnO	59 ± 1
PLA + 5 wt.% ZnO	58 ± 1
PLA + 7 wt.% ZnO	59 ± 1
PLA + 9 wt.% ZnO	58 ± 1

#### 6.3.4 Wettability of PLA / ZnO nanofibres

The wetting properties of the fibrous mats were evaluated by water contact angle measurement. Figure 7.16 shows the contact angle of a water droplet on the fibrous mats containing ZnO at various concentrations. Since PLA is a hydrophobic polymer, the measured contact angle for the pure PLA fibrous mat was found to be  $133 \pm 2^\circ$ . In the case of the hybrid fibrous mats containing 1 wt.%, 5 wt.% and 9 wt.% ZnO, the measured contact angle was  $131 \pm 2^\circ$ ,  $130 \pm 3^\circ$ , and  $134 \pm 3^\circ$ , respectively. Hence, the incorporation of ZnO nanoparticles did not affect the wettability of PLA nanofibres.

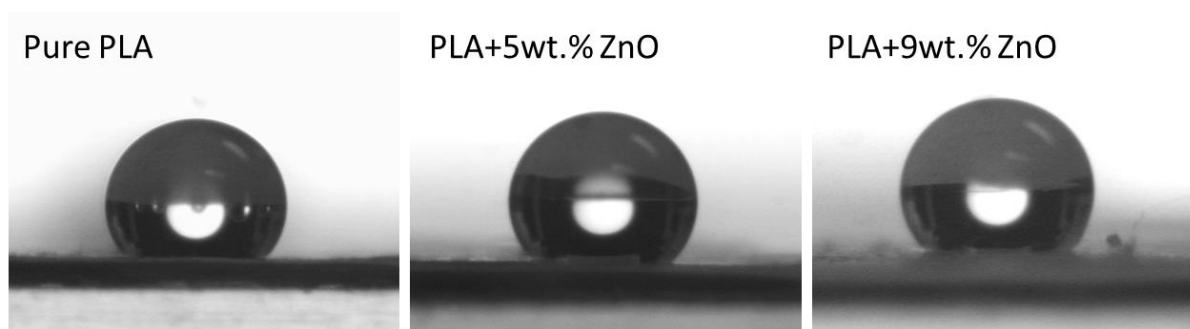


Figure 6.16 Water droplet contact angle on the surface of PLA fibrous mats containing 0, 5, and 9 wt.% ZnO nanoparticles

### 6.3.5 Antimicrobial properties of PLA / ZnO nanofibres

Antimicrobial properties of a pure PLA fibrous mat and the ZnO impregnated mats were evaluated against E.coli bacteria at 37°C . The pure PLA fibrous mat was used as a control. Figure 6.17 shows inhibition zone results of a neat PLA mat and a PLA composite mat with 9 wt.% ZnO, respectively. An inhibition zone around the composite mat can be clearly seen.

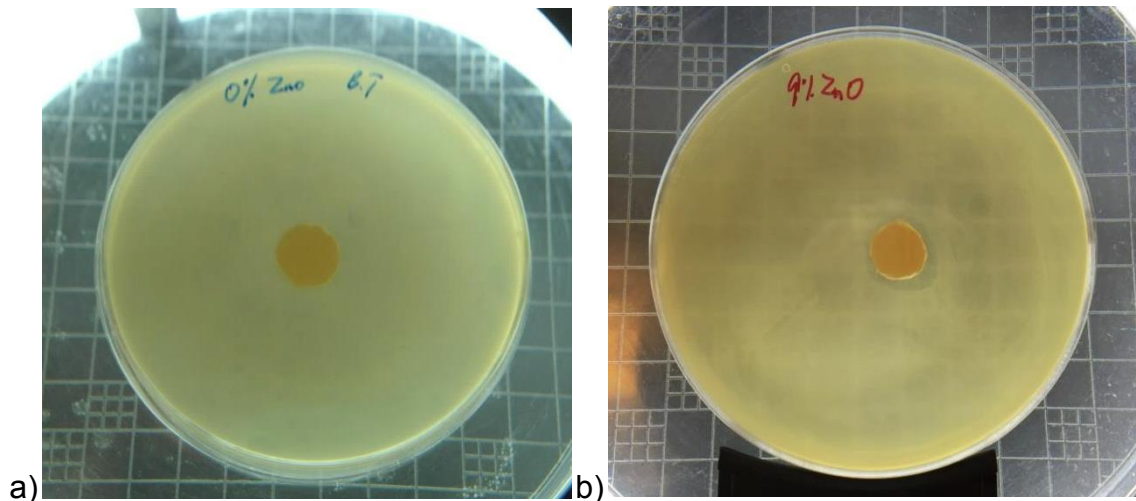


Figure 6.17 Antimicrobial test of electrospun PLA fibrous mats containing (a) 0 wt.% and (b) 9 wt.% ZnO nanoparticles

The antibacterial activity result of the nanofibres of various ZnO concentrations is shown in Figure 6.18. It is found that the neat PLA fibres and the fibres with ZnO concentration of 1 and 3 wt.% exhibited no activity against the E.coli bacteria since there was no zone inhibitions around the fibre mats. In the 5 wt.% ZnO sample, the area around the sample mat was slightly clear, which shows a light inhibiting effect on bacteria, even though no evidently clear zone inhibition is present. The antimicrobial activity was clearly evident with the 7 wt.% and 9 wt.% of ZnO concentrations, which showed an inhibition zone diameter of  $17 \pm 1$  mm and  $21 \pm 1$  mm, respectively. It is because at low ZnO concentrations the particles were trapped in the PLA nanofibres, thus, no ZnO particles were directly in contact with the agar. As the concentration of ZnO reached 5 wt.%, the particles were exposed on the fibre surface and an inhibition zone appeared around the fibrous mats. The measured diameter of the inhibition zone is shown in Table 6.7.

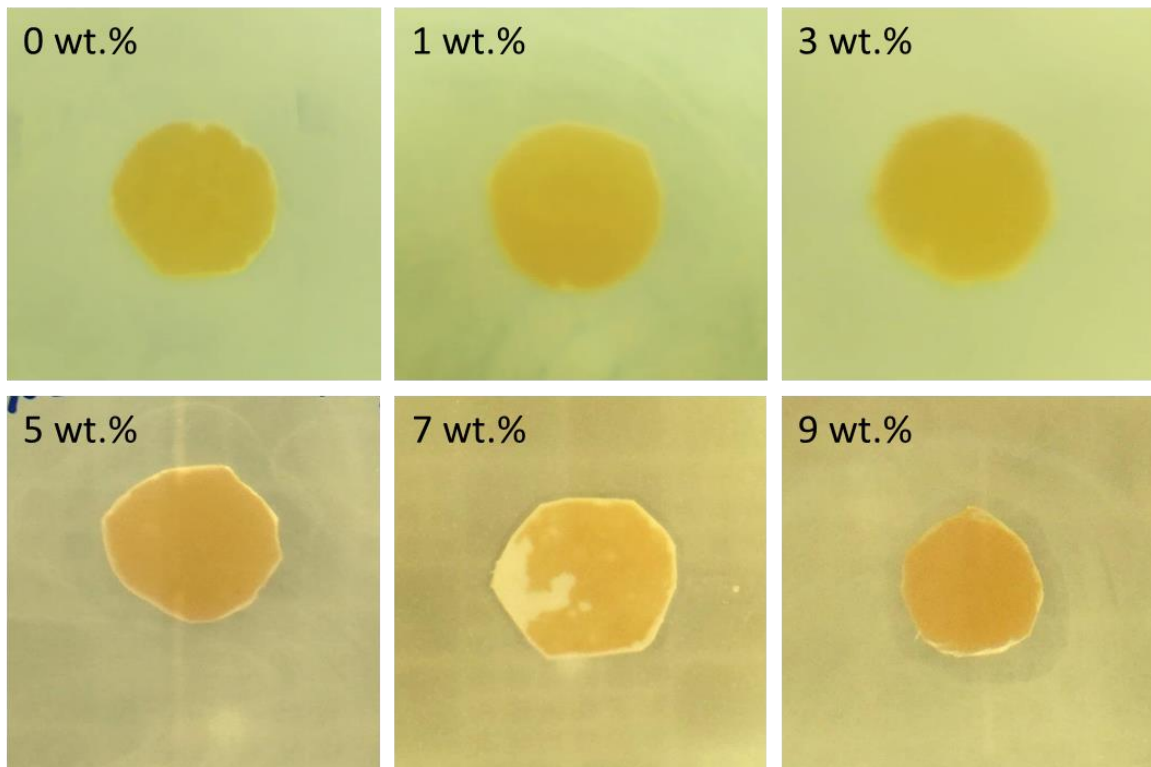


Figure 6.18 Image of bacterial zone inhibition of PLA/ZnO fibrous mats against E.coli

Table 6.7 Diameter of bacterial zone inhibition

Sample	Inhibition zone diameter / mm
Pure PLA	15
PLA + 1 wt.% ZnO	15
PLA + 3 wt.% ZnO	15
PLA + 5 wt.% ZnO	>15
PLA + 7 wt.% ZnO	17±1
PLA + 9 wt.% ZnO	21±1

Similarly, in a study of electrospun PCL / ZnO non-woven membrane, the composite fibrous membrane showed effective inhibiting growth for *S. aureus* and *E. coli* when the ZnO concentration above 5 wt.% [144].

### 6.3.6 Summary of PLA/ZnO nanofibres

1. PLA 4060D nanocomposite nanofibres containing 1, 3, 5, 7 and 9 wt.% ZnO were electrospun from acetone solution at 12.5% w/v concentration using electrospinning.
2. The morphology of the nanofibres was investigated using SEM. The addition of ZnO has increased the roughness and porosity of the nanofibres' surface. The diameter of the nanofibres was measured using Image J<sup>®</sup> and the diameter distribution was analysed using IBM SPSS Statistics 22.0. It is noted that the nanofibre diameter increased with the addition of ZnO particles due to the large size of the ZnO particles and the porous structure of the nanofibres.
3. ZnO particle structure was measured using TEM. A good distribution of the ZnO particle was obtained with some nanoparticles agglomerates. The dispersed ZnO nanoparticles showed an average diameter of  $95 \pm 50$  nm.
4. Thermal properties of the nanofibres were investigated using DSC. The incorporation of ZnO did not change the T<sub>g</sub> value of the polymer, but enhanced the enthalpy relaxation of the polymer chains at the glass transition.
5. The wetting properties of the fibrous mats were evaluated by water contact angle measurement. PLA nanocomposite mats exhibited hydrophobic properties. The incorporation of ZnO nanoparticles did not affect the wettability of PLA nanofibres.
6. Antimicrobial properties of a pure PLA fibrous mat and the ZnO impregnated mats were evaluated against E.coli bacterial at 37°C . Zone inhibition was observed when ZnO content was above 5 wt.%.

## 7 Conclusions

In Chapter 4, the effects of incorporating nanoclay and crystallinity (by annealing) on the nanoclay structure and water barrier properties of PLA films were investigated. PLA nanocomposites containing 0 to 5 wt.% montmorillonite layered silicate were prepared. Both amorphous and semi-crystalline PLA nanocomposite samples were obtained by compression moulding with different thermal treatments, i.e. quenching and annealing, respectively. Thermal properties of the samples were measured by DSC. The crystallinity of the annealed PLA and PLA nanocomposites was found to be about 30%. The morphology of crystallites was also observed using polarised optical microscopy. The nanoclay structure was measured using TEM and WAXD. The nanocomposite structures in both quenched and annealed films were intercalated and the clay aspect ratio was measured to be 40. The clay layers were aligned in the same direction in the quenched samples, whereas they were random orientated in the annealed samples due to annealing.

Water vapour transmission rates through the film samples were measured using a MOCON Permatran-W@398. It was found that the WVTR value of the quenched PLA nanocomposites decreased consistently with clay concentration and this data showed a good fit with the Nielsen model. The measured WVTR value of the annealed PLA nanocomposites fitted the model of Bharadwaj assuming the clay orientation was nearly random. A new tortuous model was built based on the models of Nielsen and Bharadwaj to predict the combined effects of crystallinity and nano-filler on the water vapour transmission rates through the polymer films. The new model showed a good fit with the experimental data from the annealed PLA nanocomposites.

Chapter 5 gives results of how mechanical stretching affects water barrier properties of PLA nanocomposite films. Uniaxial stretching was applied to quenched PLA 4060D sheets at a draw ratio of 3 using a BASE stretching machine. Since stretching temperature has a significant effect on the quality of the products, the optimum drawing temperature (in the range of 60°C to 75°C) was selected in the first step. Results of birefringence showed that the degree of orientation in the stretched PLA films reduced with the increasing drawing temperature. DSC results suggested that only the sample stretched at 60°C

exhibited an increase in  $T_g$  by  $4^\circ\text{C}$ , due to the polymer chains being highly orientated, which requires more energy for chain relaxation. In the end, PLA films that had been stretched at  $60^\circ\text{C}$  showed the most stable and best water barrier properties compared with the other samples. Therefore, the optimum stretching temperature for the PLA nanocomposite sheets was selected to be  $60^\circ\text{C}$ .

On the other hand, the WVTR results were very sensitive to the thickness of the tested samples due to the defects and air bubbles in the samples and their uniformity. To keep the thickness consistent, the nanocomposite sheets for uniaxial stretching were prepared three times thicker than the normal quenched ones during compression moulding. Thermal properties were measured by DSC. It was found that the  $T_g$  values of the stretched films did not change at low clay content. However, as the clay content increased the  $T_g$  value of the stretched films significantly increased by  $5^\circ\text{C}$ . This indicates that the appearance of nanoclay has resisted the polymer chain relaxation. The nanoclay structure was measured using TEM and WAXD. Better delamination of the clay layers was obtained by shearing the intercalated clay tactoids during uniaxial stretching. The clay aspect ratio in the uniaxially stretched samples was measured to be 48. The WAXD analysis confirmed that the clay interlayer spacing had been increased during uniaxial stretching by 0.2 nm. WVTR values of the stretched nanocomposite films were slightly lower than those of the quenched nanocomposite films. The WVTR values of the stretched PLA nanocomposites decreased consistently with clay concentration, except the sample with 5 wt.% nanoclay, which had the same value as the quenched sample with 5 wt.% clay. This was due to agglomeration of the nanoclay at high clay content. The WVTR data of the stretched nanocomposite showed a good fit with the Nielsen model.

Chapter 6 investigates fibrous PLA nanocomposite mats produced from PLA solutions using electrospinning. To prepare polymer solutions, two grades of PLA (4060D and 4032D) were dissolved in acetone, chloroform, and binary-solvent systems of acetone and chloroform (50/50 v/v), respectively, to obtain a 12.5% w/v PLA concentration. Electrospinning was carried out in a spray-base electrospay instrument by Profector Life Sciences Ltd. using a flow rate of 1 ml/h and a voltage of 20 kV. The optimum solvent systems for electrospinning PLA 4060D and PLA 4032D were found to be AC and AC / CHL, respectively, from

which continuous and non-beaded nanofibres were collected.

A further study on nanoclay incorporated PLA nanofibres was shown in Chapter 6.1. Electrospinning is a novel technique in polymer nanocomposite. Nobody has investigated PLA / montmorillonite nanofibres produced using electrospinning. In this research, PLA nanofibres containing 1, 3, and 5 wt.% montmorillonite clay were produced from the optimum solution at 12.5% w/v concentration using electrospinning. The morphology of the nanofibres was investigated using SEM. Continuous nanofibres with the existence of a few beads were observed in both grades of PLA nanocomposite fibres. The diameter of the nanofibres was measured using Image J<sup>®</sup> software and the diameter distribution was analysed using IBM SPSS Statistics 22.0. For both PLA grades, the fibre diameter decreased with increasing nanoclay loading until the clay content was below 3 wt.%, then increased as the clay content increased to 5 wt.%. The average diameters of the crystallisable PLA (grade 4032D) / clay nanofibres were lower than those of the amorphous PLA (grade 4060D) / clay nanofibres. The nanoclay structure in the nanofibres was measured using TEM. The nanoclay platelets were fully exfoliated and aligned to the flow direction of drawn force. The aspect ratio the nanoclay in the PLA nanofibres was about 52. Thermal properties of the nanofibres were investigated using DSC. Both PLA grades showed a reduction in T<sub>g</sub> with the addition of nanoclay. The crystallisable PLA / clay nanofibres showed the degree of crystallinity increased with clay content from 21% to 31%. The crystallisation temperature of electrospun PLA fibres is much lower than that of melting produced PLA films, probably due to the formation of  $\beta$ -crystal during electrospinning. The mechanical properties of PLA nanofibres were analysed by tensile tests following the ISO257-2-5A specification. All the nanofibre samples exhibited ductile-brittle mechanical properties. The addition of nanoclay has reduced mechanical properties of the PLA nanofibres.

ZnO has been introduced in polymer fibres for medical and water treatment applications due to its anti-bacteria property. The effect of ZnO nanoparticles on PLA nanofibres was investigated in Chapter 6.2. PLA 4060D nanocomposite nanofibres containing 1, 3, 5, 7 and 9 wt.% ZnO were electrospun from acetone solution at 12.5% w/v concentration. The morphology of the nanofibres was investigated using SEM. The addition of ZnO enhanced the roughness and

porosity of the nanofibres' surface. The diameter of the nanofibres was measured using Image J<sup>®</sup> software and the diameter distribution was analysed using IBM SPSS Statistics 22.0. It is noted that the nanofibre diameter increased with the addition of ZnO particles due to the large size of the ZnO particles and the porous structure of the nanofibres. The particle structure in the nanofibres was measured using TEM. A good distribution of the ZnO particle was obtained with the some nanoparticle agglomerates. The dispersed ZnO nano-particles showed an average diameter of  $95 \pm 50$  nm. Thermal properties of the nanofibres were investigated using DSC. The incorporation of ZnO did not change the T<sub>g</sub> value of the polymer, but enhanced the enthalpy relaxation of the polymer chains at the glass transition. The wetting properties of the fibrous mats were evaluated by water contact angle measurement. PLA nanocomposite mats exhibited hydrophobic property. The incorporation of ZnO nanoparticles did not affect the wettability of PLA nanofibres. Antimicrobial properties of a pure PLA fibrous mat and the ZnO impregnated mats were evaluated against E.coli bacterial at 37°C. Zone inhibition was observed when ZnO content was above 5 wt.%.

## 8 Further work

The following further work is suggested.

1. Incorporate mechanical stretching on crystallisable PLLA and investigate the effect of stretching induced crystallinity on water barrier property of PLLA. Mechanical stretching induces a certain degree of crystallinity in PLLA, which can significantly improve barrier property of the polymer. As we know, the crystal modification of stretching induced crystals,  $\beta$ -crystal, is unlike  $\alpha$ -crystal that is produced from annealing. It is worth to study the effect of different crystal forms on barrier property of PLA membrane films.
2. Repeat tensile test on electrospun PLA 4032D / clay nanofibre mats. Since the nanofibre mats are porous, the results of tensile test in the present thesis are very variable.
3. Incorporate paracetamol in PLA / clay nanofibres and investigate the optimum clay concentration as drug carrier in PLA nanofibres. PLA nanofibres can be used in wound healing and other medical applications because of its good biocompatibility. Nanoclay has been proved as being a good drug carrier in PLA matrix. Therefore, it is necessary to investigate the optimum composition of drug-loaded PLA / clay composite solution for electrospinning.
4. Investigate mechanical properties of PLA / ZnO nanofibre mats. The size of ZnO particles is smaller than the nanoclay. Hence, the incorporation of ZnO nanoparticles could enhance the mechanical properties of PLA nanofibres. To obtain a good dispersion of ZnO nano-particles surfactant (e.g. sodium di-2-ethylhexyl-sulfosuccinate) and dispersant (e.g. ethylene glycol) can be used in solution preparation.

## References

- [1] D. E. Henton, P. Gruber, J. Lunt, and J. Randall, "Polylactic acid technology," in *Natural Fibers, Biopolymers, and Biocomposites*, A. K. Mohanty, M. Misra, and L. T. Drzal, Eds. Boca Raton, FL : Taylor & Francis, 2005, pp. 527–577.
- [2] G. Choudalakis and A. Gotsis, "Permeability of polymer/clay nanocomposites: a review," *European Polymer Journal*, vol. 45, no. 4, pp. 967–984, 2009.
- [3] C. A. Growth, "World Plastics Production 1950 – 2015," *PlasticsEurope Market Research Group (PEMRG) / Consultic Marketing & Industrieberatung GmbH*, 2015.
- [4] A. A. Shah, F. Hasan, A. Hameed, and S. Ahmed, "Biological degradation of plastics: A comprehensive review," *Biotechnology Advances*, vol. 26, no. 3, pp. 246–265, 2008.
- [5] K. Madhavan Nampoothiri, N. R. Nair, and R. P. John, "An overview of the recent developments in polylactide (PLA) research.," *Bioresource Technology*, vol. 101, no. 22, pp. 8493–8501, Nov. 2010.
- [6] D. Garlotta, "A Literature Review of Poly ( Lactic Acid )," *Journal of Polymers and the Environment*, vol. 9, no. 2, pp. 63–84, 2002.
- [7] B. Tan and N. L. Thomas, "A review of the water barrier properties of polymer/clay and polymer/graphene nanocomposites," *Journal of Membrane Science*, vol. 514, pp. 595–612, 2016.
- [8] L. T. Lim, R. Auras, and M. Rubino, "Processing technologies for poly(lactic acid)," *Progress in Polymer Science*, vol. 33, no. 8, pp. 820–852, Aug. 2008.
- [9] R. Auras, B. Harte, and S. Selke, "An overview of polylactides as packaging materials.," *Macromolecular Bioscience*, vol. 4, no. 9, pp. 835–864, Sep. 2004.
- [10] M. H. Hartmann, "High Molecular Weight Polylactic Acid Polymers," in *Biopolymers from Renewable Resources*, 1st ed., D. L. Kaplan, Ed. Berlin: Springer Berlin Heidelberg, 1998, pp. 367–411.
- [11] K. Jamshidi, S. H. Hyon, and Y. Ikada, "Thermal characterization of polylactides," *Polymer*, vol. 29, no. 12, pp. 2229–2234, 1988.
- [12] D. Garlotta, "A Literature Review of Poly ( Lactic Acid )," *Journal of polymer and the environment*, vol. 9, no. 2, 2002.
- [13] A. Celli and M. Scandola, "Thermal properties and physical ageing of poly (l-lactic acid)," *Polymer*, vol. 33, no. 13, pp. 2699–2703, 1992.
- [14] J. R. Dorgan, J. Janzen, M. P. Clayton, S. B. Hait, and D. M. Knauss, "Melt rheology of variable L-content poly(lactic acid)," *Journal of Rheology*, vol. 49, no. 3, p. 607, 2005.
- [15] H. Cai, V. Dave, R. a Gross, and S. P. McCarthy, "Effects of physical aging, crystallinity, and orientation on the enzymatic degradation of poly(lactic acid)," *Journal of Polymer Science Part B: Polymer Physics*, vol. 34, no. 16, pp. 2701–2708, 1996.
- [16] H. Tsuji and Y. Ikada, "Crystallization from the melt of poly(lactide)s with

- different optical purities and their blends,” *Macromolecular Chemistry and Physics*, vol. 197, pp. 3483–3499, 1996.
- [17] J.-R. Sarasua, R. E. Prud’homme, M. Wisniewski, A. Le Borgne, and N. Spassky, “Crystallization and Melting Behavior of Polylactides,” *Macromolecules*, vol. 31, no. 12, pp. 3895–3905, 1998.
- [18] J. R. Sarasua, A. L. Arraiza, P. Balerdi, and I. Maiza, “Crystallinity and mechanical properties of optically pure polylactides and their blends,” *Polymer Engineering and Science*, vol. 45, no. 5, pp. 745–753, 2005.
- [19] Z. Duan and N. L. Thomas, “Water vapour permeability of poly(lactic acid): Crystallinity and the tortuous path model,” *Journal of Applied Physics*, vol. 115, no. 6, p. 064903(1-9), 2014.
- [20] E. W. Fischer, H. J. Sterzel, and G. Wegner, “Investigation of the structure of solution grown crystals of lactide copolymers by means of chemical reactions,” *Kolloid-Zeitschrift & Zeitschrift für Polymere*, vol. 251, no. 11, pp. 980–990, 1973.
- [21] P. De Santis and A. J. Kovacs, “Molecular conformation of poly(S-lactic acid),” *Biopolymers*, vol. 6, no. 3, pp. 299–306, 1968.
- [22] B. Eling, S. Gogolewski, and a. J. Pennings, “Biodegradable materials of poly(l-lactic acid): 1. Melt-spun and solution-spun fibres,” *Polymer*, vol. 23, no. 11, pp. 1587–1593, 1982.
- [23] J. Zhang, Y. Duan, H. Sato, H. Tsuji, I. Noda, S. Yan, and Y. Ozaki, “Crystal Modifications and Thermal Behavior of Poly ( L -lactic acid ) Revealed by Infrared Spectroscopy,” *Macromolecules*, vol. 38, no. 19, pp. 8012–8021, 2005.
- [24] W. Hoogsteen and A. Postema, “Crystal structure, conformation and morphology of solution-spun poly (L-lactide) fibers,” *Macromolecules*, vol. 23, pp. 634–642, 1990.
- [25] X. Ling and J. E. Spruiell, “Analysis of the Complex Thermal Behavior of Poly ( L -lactic acid ) Film . I . Samples Crystallized from the Glassy State,” *Journal of Polymer Science: Part B: Polymer Physics*, vol. 44, no. 22, pp. 3200–3214, 2006.
- [26] D. Sawai, K. Takahashi, T. Imamura, K. Nakamura, T. Kanamoto, and S.-H. Hyon, “Preparation of Oriented  $\beta$  -Form Poly ( L -lactic acid ) by Solid-State Extrusion,” *Journal of Polymer Science Part B: Polymer Physics*, vol. 40, no. 1, pp. 95–104, 2002.
- [27] L. Cartier, T. Okihara, Y. Ikada, H. Tsuji, J. Puiggali, and B. Lotz, “Epitaxial crystallization and crystalline polymorphism of polylactides,” *Polymer*, vol. 41, no. 25, pp. 8909–8919, 2000.
- [28] M. Cocca, M. L. Di Lorenzo, M. Malinconico, and V. Frezza, “Influence of crystal polymorphism on mechanical and barrier properties of poly(l-lactic acid),” *European Polymer Journal*, vol. 47, no. 5, pp. 1073–1080, 2011.
- [29] P. Pan, W. Kai, B. Zhu, T. Dong, and Y. Inoue, “Polymorphous Crystallization and Multiple Melting Behavior of Poly ( L -lactide ): Molecular Weight Dependence,” *Macromolecules*, vol. 40, pp. 6898–6905, 2007.

- [30] P. Pan, B. Zhu, W. Kai, T. Dong, and Y. Inoue, "Polymorphic Transition in Disordered Poly ( L -lactide ) Crystals Induced by Annealing at Elevated Temperatures," *Macromolecules*, vol. 41, pp. 4296–4304, 2008.
- [31] M. Yasuniwa, S. Tsubakihara, Y. Sugimoto, and C. Nakafuku, "Thermal Analysis of the Double-Melting Behavior of Poly ( L-lactic acid )," *Journal of Polymer Science: Part B: Polymer Physics*, vol. 42, no. 1, pp. 25–32, 2004.
- [32] Q. Fang and M. a Hanna, "Rheological properties of amorphous and semicrystalline polylactic acid polymers," *Industrial Crops and Products*, vol. 10, no. 1, pp. 47–53, 1999.
- [33] J. J. Cooper-white and M. E. Mackay, "Rheological Properties of Poly ( lactides ). Effect of Molecular Weight and Temperature on the Viscoelasticity of Poly ( l-lactic acid )," pp. 1803–1814, 1999.
- [34] J. R. Dorgan, J. S. Williams, and D. N. Lewis, "Melt rheology of poly(lactic acid): Entanglement and chain architecture effects," *Journal of Rheology*, vol. 43, no. 5, pp. 1141–1156, 1999.
- [35] A. Södergård and M. Stolt, "Properties of lactic acid based polymers and their correlation with composition," *Progress in Polymer Science*, vol. 27, no. 6, pp. 1123–1163, 2002.
- [36] N. Ljungberg, T. Andersson, and B. Wessle, "Film Extrusion and Film Weldability of Poly ( lactic acid ) Plasticized with Triacetine and Tributyl Citrate," *Journal of Applied Polymer Science*, vol. 88, pp. 3239–3247, 2003.
- [37] F. Kopinke, M. Remmler, K. Mackenzie, and M. Milder, "Thermal decomposition of biodegradable polyesters -II. Poly ( lactic acid )," *Polymer Degradation and Stability*, vol. 53, pp. 329–342, 1996.
- [38] G. Perego, G. D. Cella, and C. Bastloll, "Effect of Molecular Weight and Crystallinity on Poly ( lactic acid ) Mechanical Properties," *Journal of Applied Polymer Science*, vol. 59, pp. 37–43, 1996.
- [39] S. S. Ray, K. Yamada, M. Okamoto, and K. Ueda, "Control of Biodegradability of Polylactide via Nanocomposite Technology," *Macromolecular Materials and Engineering*, vol. 288, no. 3, pp. 203–208, 2003.
- [40] S. Sinha, K. Yamada, M. Okamoto, and K. Ueda, "New polylactide-layered silicate nanocomposites. 2. Concurrent improvements of material properties, biodegradability and melt rheology," *Polymer*, vol. 44, no. 3, pp. 857–866, 2003.
- [41] C. Lu and Y.-W. Mai, "Influence of aspect ratio on barrier properties of polymer-clay nanocomposites.," *Physical Review Letters*, vol. 95, no. 8, p. 088303(1-4), 2005.
- [42] S. S. Ray and M. Okamoto, "Polymer/layered silicate nanocomposites: a review from preparation to processing," *Progress in Polymer Science*, vol. 28, no. 11, pp. 1539–1641, 2003.
- [43] A. Blumstein, "Polymerization of Adsorbed Monolayers . 11 . Thermal Degradation of the Inserted Polymer," *Journal of Polymer Science Part A: Polymer Chemistry*, vol. 3, no. 7, pp. 2665–2672, 1965.

- [44] R. Krishnamoorti, R. A. Vaia, and E. P. Giannelis, "Structure and Dynamics of Polymer-Layered Silicate Nanocomposites," *Chemistry of Materials*, vol. 8, no. 8, pp. 1728–1734, 1996.
- [45] D. R. Paul and L. M. Robeson, "Polymer nanotechnology: Nanocomposites," *Polymer*, vol. 49, no. 15, pp. 3187–3204, Jul. 2008.
- [46] E. Giannelis, "Polymer layered silicate nanocomposites," *Advanced Materials*, vol. 8, no. 1, pp. 29–35, 1996.
- [47] S. Pavlidou and C. D. Papaspyrides, "A review on polymer-layered silicate nanocomposites," *Progress in Polymer Science (Oxford)*, vol. 33, no. 12, pp. 1119–1198, 2008.
- [48] V. Mittal, "Polymer layered silicate nanocomposites: A review," *Materials*, vol. 2, no. 3, pp. 992–1057, 2009.
- [49] S. Marais, Q. T. Nguyen, C. Devallencourt, M. Metayer, T. U. Nguyen, and P. Schaetzel, "Permeation of water through polar and nonpolar polymers and copolymers: determination of the concentration-dependent diffusion coefficient," *Journal of Polymer Science, Part B: Polymer Physics*, vol. 38, pp. 1998–2008, 2000.
- [50] M. Alexandre and P. Dubois, "Polymer-layered silicate nanocomposites: Preparation, properties and uses of a new class of materials," *Materials Science and Engineering R: Reports*, vol. 28, no. March, pp. 1–63, 2000.
- [51] P. C. LeBaron, Z. Wang, and T. J. Pinnavaia, "Polymer-layered silicate nanocomposites: An overview," *Applied Clay Science*, vol. 15, pp. 11–29, 1999.
- [52] Q. T. Nguyen and D. G. Baird, "Preparation of polymer-clay nanocomposites and their properties," *Advances in Polymer Technology*, vol. 25, no. 4, pp. 270–285, 2006.
- [53] A. Giannakas, C. G. Spanos, N. Kourkoumelis, T. Vaimakis, and A. Ladavos, "Preparation, characterization and water barrier properties of PS/organo-montmorillonite nanocomposites," *European Polymer Journal*, vol. 44, no. 12, pp. 3915–3921, 2008.
- [54] Y. Cui, S. Kumar, B. Rao Kona, and D. van Houcke, "Gas barrier properties of polymer/clay nanocomposites," *RSC Advances*, vol. 5, no. 78, pp. 63669–63690, 2015.
- [55] A. Chien and K. Lin, "Morphology and Permeability of Exfoliated PVAc-MMT Nanocomposite Films Cast From Soap-Free Emulsion-Polymerized Latices," *Journal of Polymer Science Part A: Polymer Chemistry*, vol. 45, no. 32, pp. 5583–5589, 2007.
- [56] C. F. Dai, P. R. Li, and J. M. Yeh, "Comparative studies for the effect of intercalating agent on the physical properties of epoxy resin-clay based nanocomposite materials," *European Polymer Journal*, vol. 44, no. 8, pp. 2439–2447, 2008.
- [57] O. Gain, E. Espuche, E. Pollet, M. Alexandre, and P. Dubois, "Gas barrier properties of poly( $\epsilon$ -caprolactone)/clay nanocomposites: Influence of the morphology and polymer/clay interactions," *Journal of Polymer Science, Part B: Polymer Physics*, vol. 43, no. 2, pp. 205–214, 2005.

- [58] J. Crank and G. S. Park, *Diffusion in Polymers*. London: Academic Press, 1968.
- [59] N. L. Thomas, "The barrier properties of paint coatings," *Progress in Organic Coatings*, vol. 19, no. 2, pp. 101–121, May 1991.
- [60] P. Meares, *Polymers: Structure and Bulk Properties. chapter 12*. Van Nostrand, 1965.
- [61] S. Pauly, *Polymer Handbook. section VI*, 3rd ed. Wiley Interscience, 1989.
- [62] T. Alfrey, E. F. Gurnee, and W. G. Lloyd, "Diffusion in glassy polymers," *Journal of Polymer Science Part C: Polymer Symposia*, vol. 12, no. 1, pp. 249–261, Mar. 2007.
- [63] H. B. Hopfenberg and V. Stannet, *The Physics of Glassy Polymers-chapter 9*. Applied Science Publishers Ltd., 1973.
- [64] N. L. Thomas and A. . Windle, "A theory of Case II diffusion," vol. 23, pp. 529–542, 1982.
- [65] J. Yoon, H. Jung, M. Kim, and E. Park, "Diffusion Coefficient and Equilibrium Solubility of Water Molecules in Biodegradable Polymers," *Journal of Applied Polymer Science*, vol. 77, no. 8, pp. 1716–1722, 2000.
- [66] H. Tsuji, R. Okino, H. Daimon, and K. Fujie, "Water vapor permeability of poly(lactide)s: Effects of molecular characteristics and crystallinity," *Journal of Applied Polymer Science*, vol. 99, no. 5, pp. 2245–2252, 2006.
- [67] M. Drieskens, R. Peeters, J. Mullens, D. Franco, P. J. Lemstra, and D. G. Hristova-Bogaerds, "Structure versus properties relationship of poly(lactic acid). I. Effect of crystallinity on barrier properties," *Journal of Polymer Science Part B: Polymer physics*, vol. 47, no. 22, pp. 2247–2258, 2009.
- [68] A. S. Michaels, W. R. Vieth, and J. a. Barrie, "Diffusion of gases in polyethylene terephthalate," *Journal of Applied Physics*, vol. 34, no. 1, pp. 13–20, 1963.
- [69] H. Tsuji and T. Tsuruno, "Water Vapor Permeability of Poly(L-lactide)/Poly(D-lactide) Stereocomplexes," *Macromolecular Materials and Engineering*, vol. 295, no. 8, pp. 709–715, Aug. 2010.
- [70] P. W. Morgan, "Structure and Moisture Permeability of Film-Forming Polymers," *Industrial and Engineering Chemistry*, vol. 45, no. 10, pp. 2296–2306, 1953.
- [71] S. W. Lasoski and W. H. Cobbs, "Moisture permeability of polymers. I. Role of crystallinity and orientation," *Journal of Polymer Science Part A: Polymer Chemistry*, vol. 36, no. 130, pp. 21–33, 1959.
- [72] K. Yano, A. Usuki, and A. Okada, "Synthesis and Properties of Polyimide-Clay Hybrid Films," *Journal of Polymer Science Part A: Polymer Chemistry*, vol. 35, no. 11, pp. 2289–2294, 1997.
- [73] Lawrence E. Nielsen, "Models for the Permeability of Filled Polymer Systems," *Journal of Macromolecular Science: Part A - Chemistry*, vol. 1, no. 5, pp. 929–942, 1967.
- [74] K. Yano, A. Usuki, A. Okada, T. Kurauchi, and Kamigaito, O., "Synthesis and Properties of Polyimide-Clay Hybrid," *Journal of Polymer Science Part*

- A: *Polymer Chemistry* polymer since, vol. 31, pp. 2493–2498, 1993.
- [75] Z. Duan, N. L. Thomas, and W. Huang, “Water vapour permeability of poly(lactic acid) nanocomposites,” *Journal of Membrane Science*, vol. 445, pp. 112–118, 2013.
- [76] E. L. Cussler, S. E. Hughes, W. J. Ward, and R. Aris, “Barrier Membranes,” *Journal of Membrane Science*, vol. 38, pp. 161–174, 1988.
- [77] G. H. Fredrickson and J. Bicerano, “Barrier properties of oriented disk composites,” *The Journal of Chemical Physics*, vol. 110, no. 4, p. 2181, 1999.
- [78] H. R. Gusev, A. A. and Lusti, “Rational Design of Nanocomposites for Barrier Applications,” *Advanced Materials*, vol. 13, no. 21, pp. 1641–1643, Nov. 2001.
- [79] R. K. Bharadwaj, “Modeling the Barrier Properties of Polymer-layered Silicate Nanocomposites,” *Macromolecules*, vol. 34, no. 2, pp. 9189–9192, 2001.
- [80] S. Nazarenko, P. Meneghetti, P. Julmon, B. G. Olson, and S. Qutubuddin, “Gas barrier of polystyrene montmorillonite clay nanocomposites: Effect of mineral layer aggregation,” *Journal of Polymer Science Part B: Polymer Physics*, vol. 45, no. 13, pp. 1733–1753, 2007.
- [81] B. Xu, Q. Zheng, Y. Song, and Y. Shangguan, “Calculating barrier properties of polymer/clay nanocomposites: Effects of clay layers,” *Polymer*, vol. 47, no. 8, pp. 2904–2910, 2006.
- [82] A. A. Gusev, “Numerical Identification of the Potential of Whisker- and Platelet-Filled Polymers,” *Macromolecules*, vol. 34, no. 9, pp. 3081–3093, 2001.
- [83] N. K. Lape, E. E. Nuxoll, and E. L. Cussler, “Polydisperse flakes in barrier films,” *Journal of Membrane Science*, vol. 236, pp. 29–37, 2004.
- [84] C. Lu and Y.-W. Mai, “Permeability modelling of polymer-layered silicate nanocomposites,” *Composites Science and Technology*, vol. 67, no. 14, pp. 2895–2902, 2007.
- [85] J. Kim, C. Hu, R. Woo, and M. Sham, “Moisture barrier characteristics of organoclay-epoxy nanocomposites,” *Composites Science and Technology*, vol. 65, no. 5, pp. 805–813, Apr. 2005.
- [86] S. S. Ray, K. Okamoto, and M. Okamoto, “Structure - Property Relationship in Biodegradable Poly ( butylene succinate )/ Layered Silicate Nanocomposites,” *Macromolecules*, vol. 36, pp. 2355–2367, 2003.
- [87] A. Sorrentino, M. Tortora, and V. Vittoria, “Diffusion behavior in polymer-clay nanocomposites,” *Journal of Polymer Science Part B: Polymer Physics*, vol. 44, no. 2, pp. 265–274, 2006.
- [88] V. Bugatti, U. Costantino, G. Gorrasi, M. Nocchetti, L. Tammaro, and V. Vittoria, “Nano-hybrids incorporation into poly( $\epsilon$ -caprolactone) for multifunctional applications: Mechanical and barrier properties,” *European Polymer Journal*, vol. 46, no. 3, pp. 418–427, 2010.
- [89] G. Gorrasi, M. Tortora, V. Vittoria, E. Pollet, B. Lepoittevin, M. Alexandre, and P. Dubois, “Vapor barrier properties of polycaprolactone

- montmorillonite nanocomposites: effect of clay dispersion,” *Polymer*, vol. 44, no. 8, pp. 2271–2279, 2003.
- [90] B. Alexandre, D. Langevin, P. Médéric, T. Aubry, H. Couderc, Q. T. Nguyen, A. Saiter, and S. Marais, “Water barrier properties of polyamide 12/montmorillonite nanocomposite membranes: Structure and volume fraction effects,” *Journal of Membrane Science*, vol. 328, no. 1–2, pp. 186–204, 2009.
- [91] E. Picard, A. Vermogen, J. Gerard, and E. Espuche, “Barrier properties of nylon 6-montmorillonite nanocomposite membranes prepared by melt blending: Influence of the clay content and dispersion stateConsequences on modelling,” *Journal of Membrane Science*, vol. 292, no. 1–2, pp. 133–144, 2007.
- [92] N. Ogata, G. Jimenez, H. Kawai, and T. Ogihara, “Structure and Thermal / Mechanical Properties of Poly ( l-lactide ) -Clay Blend,” *Journal of Polymer Science Part B: Polymer Physics*, vol. 35, pp. 389–396, 1997.
- [93] V. Krikorian and D. J. Pochan, “Poly (L-Lactic Acid)/ Layered Silicate Nanocomposite: Fabrication , Characterization , and Properties,” *Chemistry of Materials*, vol. 15, no. 22, pp. 4317–4324, 2003.
- [94] A. R. McLauchlin and N. L. Thomas, “Biodegradable nanocomposites,” in *Advances in Polymer Nanocomposites*Woodhead Publishing, F. Gao, Ed. Cambridge, 2012, pp. 398–430.
- [95] S. S. Ray, K. Yamada, M. Okamoto, A. Ogami, and K. Ueda, “New Polylactide / Layered Silicate Nanocomposites . 3 . High-Performance Biodegradable Materials,” no. 13, pp. 1456–1465, 2003.
- [96] M. Paul, C. Delcourt, M. Alexandre, P. Degee, F. Monteverde, and P. Dubois, “Polylactide/montmorillonite nanocomposites: study of the hydrolytic degradation,” *Polymer Degradation and Stability*, vol. 87, no. 3, pp. 535–542, 2005.
- [97] J.-W. Rhim, S.-I. Hong, and C.-S. Ha, “Tensile, water vapor barrier and antimicrobial properties of PLA/nanoclay composite films,” *Food Science and Technology*, vol. 42, no. 2, pp. 612–617, 2009.
- [98] C. Thellen, C. Orroth, D. Froio, D. Ziegler, J. Lucciarini, R. Farrell, N. A. D’Souza, and J. A. Ratto, “Influence of montmorillonite layered silicate on plasticized poly(l-lactide) blown films,” *Polymer*, vol. 46, no. 25, pp. 11716–11727, 2005.
- [99] S. Sinha Ray, K. Yamada, M. Okamoto, and K. Ueda, “Biodegradable Polylactide/Montmorillonite Nanocomposites,” *Journal of Nanoscience and Nanotechnology*, vol. 3, no. 6, pp. 503–510, 2003.
- [100] M. Zenkiewicz and J. Richert, “Permeability of polylactide nanocomposite films for water vapour, oxygen and carbon dioxide,” *Polymer Testing*, vol. 27, no. 7, pp. 835–840, 2008.
- [101] E. Picard, E. Espuche, and R. Fulchiron, “Effect of an organo-modified montmorillonite on PLA crystallization and gas barrier properties,” *Applied Clay Science*, vol. 53, no. 1, pp. 58–65, 2011.
- [102] X. Ou and M. Cakmak, “Influence of biaxial stretching mode on the

- crystalline texture in polylactic acid films,” *Polymer*, vol. 49, no. 24, pp. 5344–5352, 2008.
- [103] H. L. Xie, K. Guo, J. Z. Chen, W. J. Wang, M. J. Niu, and X. F. Li, “The Effect of Uniaxial Stretching on the Crystallization Behaviors of Polylactic Acid Film,” *Advanced Materials Research*, vol. 418–420, no. 2012, pp. 625–628, 2012.
- [104] J.-H. Wu, M.-S. Yen, C.-P. Wu, C.-H. Li, and M. C. Kuo, “Effect of Biaxial Stretching on Thermal Properties, Shrinkage and Mechanical Properties of Poly (Lactic Acid) Films,” *Journal of Polymers and the Environment*, vol. 21, pp. 303–311, 2013.
- [105] X. Ou and M. Cakmak, “Comparative study on development of structural hierarchy in constrained annealed simultaneous and sequential biaxially stretched polylactic acid films,” *Polymer*, vol. 51, no. 3, pp. 783–792, 2010.
- [106] G. Kokturk and T. F. Serhatkulu, “Evolution of Phase Behavior and Orientation in Uniaxially Deformed Polylactic Acid Films,” *Polymer Engineering and Science*, vol. 42, no. 8, pp. 1619–1628, 2002.
- [107] L. Yu, H. Liu, F. Xie, L. Chen, and X. Li, “Effect of Annealing and Orientation on Microstructures and Mechanical Properties of Polylactic Acid,” *Polymer Engineering and Science*, vol. 48, no. 4, pp. 634–641, 2008.
- [108] S. H. Tabatabaei and A. Ajji, “Orientation , Mechanical , and Optical Properties of Poly ( Lactic Acid ) Nanoclay Composite Films,” *Polymer Engineering and Science*, vol. 51, no. 11, pp. 2151–2158, 2011.
- [109] S. H. Tabatabaei and A. Ajji, “Crystal Structure and Orientation of Uniaxially and Biaxially Oriented PLA and PP Nanoclay Composite Films,” *Journal of Applied Polymer Science*, vol. 124, pp. 4858–4863, 2012.
- [110] A. J. De Vries, C. Bonnebat, and J. Beautemps, “Uni- and biaxial orientation of polymer films and sheets,” *Journal of Polymer Science: Polymer Symposia*, vol. 58, no. 1, pp. 109–156, 2007.
- [111] H. P. Nadella, J. E. Spruiell, and J. L. White, “Drawing and Annealing of Polypropylene Fibers: Structural Changes and Mechanical Properties.,” *Journal of Applied Polymer Science*, vol. 22, no. 11, pp. 3121–3133, 1978.
- [112] Y. Dzenis, “Spinning Continuous Fibers for Nanotechnology,” *Material Science*, vol. 304, no. 5679, pp. 1917–1919, 2004.
- [113] A. Baji, Y. W. Mai, S. C. Wong, M. Abtahi, and P. Chen, “Electrospinning of polymer nanofibers: Effects on oriented morphology, structures and tensile properties,” *Composites Science and Technology*, vol. 70, no. 5, pp. 703–718, 2010.
- [114] N. Bhardwaj and S. C. Kundu, “Electrospinning: A fascinating fiber fabrication technique,” *Biotechnology Advances*, vol. 28, no. 3, pp. 325–347, 2010.
- [115] J. D. Schiffman and C. L. Schauer, “A Review: Electrospinning of Biopolymer Nanofibers and their Applications,” *Polymer Reviews*, vol. 48, no. 2, pp. 317–352, 2008.
- [116] I. S. Chronakis, “Novel nanocomposites and nanoceramics based on polymer nanofibers using electrospinning process - A review,” *Journal of*

- Materials Processing Technology*, vol. 167, no. 2–3, pp. 283–293, 2005.
- [117] T. J. Sill and H. a von Recum, “Electrospinning: applications in drug delivery and tissue engineering.,” *Biomaterials*, vol. 29, no. 13, pp. 1989–2006, 2008.
- [118] S. Homaeigohar and M. Elbahri, “Nanocomposite Electrospun Nanofiber Membranes for Environmental Remediation,” *Materials*, vol. 7, no. 2, pp. 1017–1045, 2014.
- [119] Z.-M. Huang, Y.-Z. Zhang, M. Kotaki, and S. Ramakrishna, “A review on polymer nanofibers by electrospinning and their applications in nanocomposites,” *Composites Science and Technology*, vol. 63, no. 15, pp. 2223–2253, 2003.
- [120] A. Formhals, “Process and apparatus for preparing artificial threads,” 1934.
- [121] G. Taylor, “Electrically Driven Jets,” *Proceedings of the Royal Society A: Mathematical, Physical and Engineering Sciences*, vol. 313, no. 1515. pp. 453–475, 1969.
- [122] J. Doshi and D. H. Reneker, “Electrospinning process and applications of electrospun fibers,” *Conference Record of the 1993 IEEE Industry Applications Conference Twenty-Eighth IAS Annual Meeting*, vol. 35, pp. 151–160, 1993.
- [123] K. Kim, M. Yu, X. Zong, J. Chiu, D. Fang, Y. S. Seo, B. S. Hsiao, B. Chu, and M. Hadjiargyrou, “Control of degradation rate and hydrophilicity in electrospun non-woven poly(D,L-lactide) nanofiber scaffolds for biomedical applications,” *Biomaterials*, vol. 24, no. 27, pp. 4977–4985, 2003.
- [124] S. R. Bhattarai, N. Bhattarai, P. Viswanathamurthi, H. K. Yi, P. H. Hwang, and H. Y. Kim, “Hydrophilic nanofibrous structure of polylactide; fabrication and cell affinity,” *Journal of biomedical materials research. Part A*, vol. 78, no. 2, pp. 247–257, 2006.
- [125] I. Armentano, M. Dottori, E. Fortunati, S. Mattioli, and J. M. Kenny, “Biodegradable polymer matrix nanocomposites for tissue engineering: A review,” *Polymer Degradation and Stability*, vol. 95, no. 11, pp. 2126–2146, 2010.
- [126] B. Gupta, N. Revagade, and J. Hilborn, “Poly(lactic acid) fiber: An overview,” *Progress in Polymer Science (Oxford)*, vol. 32, no. 4, pp. 455–482, 2007.
- [127] H. Tsuji, M. Nakano, M. Hashimoto, K. Takashima, S. Katsura, and A. Mizuno, “Electrospinning of poly(lactic acid) stereocomplex nanofibers,” *Biomacromolecules*, vol. 7, no. 12, pp. 3316–3320, 2006.
- [128] F. Yang, R. Murugan, S. Wang, and S. Ramakrishna, “Electrospinning of nano/micro scale poly(l-lactic acid) aligned fibers and their potential in neural tissue engineering,” *Biomaterials*, vol. 26, no. 15, pp. 2603–2610, 2005.
- [129] F. Yang, C. Y. Xu, M. Kotaki, S. Wang, and S. Ramakrishna, “Characterization of neural stem cells on electrospun poly(L-lactic acid) nanofibrous scaffold.,” *Journal of biomaterials science. Polymer edition*, vol.

15, no. 12, pp. 1483–1497, 2004.

- [130] R. Casasola, N. L. Thomas, A. Trybala, and S. Georgiadou, “Electrospun poly lactic acid (PLA) fibres: Effect of different solvent systems on fibre morphology and diameter,” *Polymer*, vol. 55, no. 18, pp. 4728–4737, 2014.
- [131] R. Casasola, N. L. Thomas, and S. Georgiadou, “Electrospinning of poly(lactic acid): Theoretical approach for the solvent selection to produce defect-free nanofibers,” *Journal of Polymer Science Part B: Polymer Physics*, p. n/a-n/a, 2016.
- [132] J. H. Lee, T. G. Park, H. S. Park, D. S. Lee, Y. K. Lee, S. C. Yoon, and J. Do Nam, “Thermal and mechanical characteristics of poly(L-lactic acid) nanocomposite scaffold,” *Biomaterials*, vol. 24, no. 16, pp. 2773–2778, 2003.
- [133] F. H. Lin, Y. H. Lee, C. H. Jian, J. M. Wong, M. J. Shieh, and C. Y. Wang, “A study of purified montmorillonite intercalated with 5-fluorouracil as drug carrier,” *Biomaterials*, vol. 23, no. 9, pp. 1981–1987, 2002.
- [134] Z. K. N. Othman, Goran T. Vladisavljević, Noreen L. Thomas, “Fabrication of composite poly(D,L-lactide)/montmorillonite nanoparticles for controlled delivery of acetaminophen by solvent-displacement method using glass capillary microfluidics,” *Colloids and Surfaces B: Biointerfaces*, vol. 141, no. 2016, pp. 187–195, 2016.
- [135] S. I. Marras, K. P. Kladi, I. Tsvintzelis, I. Zuburtikudis, and C. Panayiotou, “Biodegradable polymer nanocomposites: The role of nanoclays on the thermomechanical characteristics and the electrospun fibrous structure,” *Acta Biomaterialia*, vol. 4, no. 3, pp. 756–765, 2008.
- [136] J. H. Park, H. W. Lee, D. K. Chae, W. Oh, J. D. Yun, Y. Deng, and J. H. Yeum, “Electrospinning and characterization of poly(vinyl alcohol)/chitosan oligosaccharide/clay nanocomposite nanofibers in aqueous solutions,” *Colloid and Polymer Science*, vol. 287, no. 2009, pp. 943–950, 2009.
- [137] K. Yoon and A. Kellarakis, “Nanoclay-directed structure and morphology in PVDF electrospun membranes,” *Journal of Nanomaterials*, vol. 2014, 2014.
- [138] Y. Wang, M. Li, J. Rong, G. Nie, J. Qiao, H. Wang, D. Wu, Z. Su, Z. Niu, and Y. Huang, “Enhanced orientation of PEO polymer chains induced by nanoclays in electrospun PEO/clay composite nanofibers,” *Colloid and Polymer Science*, vol. 291, no. 2013, pp. 1541–1546, 2013.
- [139] P. Badrinarayanan, F. K. Ko, C. Wang, B. a. Richard, and M. R. Kessler, “Investigation of the effect of clay nanoparticles on the thermal behavior of PLA using a heat flux rapid scanning rate calorimeter,” *Polymer Testing*, vol. 35, pp. 1–9, 2014.
- [140] S. I. N. Ayutthaya, S. Tanpichai, W. Sangkhun, and J. Wootthikanokkhan, “Effect of clay content on morphology and processability of electrospun keratin/poly (lactic acid) nanofiber,” *International Journal of Biological Macromolecules*, vol. 85, no. 2016, pp. 585–595, 2016.
- [141] Y. H. Lee, J. H. Lee, I. G. An, C. Kim, D. S. Lee, Y. K. Lee, and J. Do Nam, “Electrospun dual-porosity structure and biodegradation morphology of Montmorillonite reinforced PLLA nanocomposite scaffolds,” *Biomaterials*, vol. 26, no. 16, pp. 3165–3172, 2005.

- [142] K. T. Shalumon, K. H. Anulekha, S. V. Nair, S. V. Nair, K. P. Chennazhi, and R. Jayakumar, "Sodium alginate/poly(vinyl alcohol)/nano ZnO composite nanofibers for antibacterial wound dressings," *International Journal of Biological Macromolecules*, vol. 49, no. 3, pp. 247–254, 2011.
- [143] S. Anitha, B. Brabu, D. John Thiruvadigal, C. Gopalakrishnan, and T. S. Natarajan, "Optical, bactericidal and water repellent properties of electrospun nano-composite membranes of cellulose acetate and ZnO," *Carbohydrate Polymers*, vol. 97, no. 2, pp. 856–863, 2013.
- [144] R. Augustine, H. N. Malik, D. K. Singhal, A. Mukherjee, D. Malakar, N. Kalarikkal, and S. Thomas, "Electrospun polycaprolactone/ZnO nanocomposite membranes as biomaterials with antibacterial and cell adhesion properties," *Journal of Polymer Research*, vol. 21, no. 3, p. 347, 2014.
- [145] X. Ji, T. Wang, L. Guo, J. Xiao, Z. Li, L. Zhang, Y. Deng, and N. He, "Effect of Nanoscale-ZnO on the Mechanical Property and Biocompatibility of Electrospun Poly(L-lactide) Acid/Nanoscale-ZnO Mats," *J Biomed Nanotechnol*, vol. 9, no. 3, pp. 417–423, 2013.
- [146] H. Rodríguez-Tobías, G. Morales, A. Ledezma, J. Romero, and D. Grande, "Novel antibacterial electrospun mats based on poly(d,l-lactide) nanofibers and zinc oxide nanoparticles," *Journal of Materials Science*, vol. 49, no. 24, pp. 8373–8385, 2014.
- [147] N. Khan, "Applications of electrospun nanofibers in the biomedical field," *Studies by Undergraduate Researchers at Guelph*, vol. 5, no. 2, pp. 63–73, 2012.
- [148] D. Virovska, D. Paneva, N. Manolova, I. Rashkov, and D. Karashanova, "Electrospinning/electrospraying vs. electrospinning: A comparative study on the design of poly(l-lactide)/zinc oxide non-woven textile," *Applied Surface Science*, vol. 311, no. 2014, pp. 842–850, 2014.
- [149] M. Pluta, "Melt Compounding of Polylactide / Organoclay : Structure and Properties of Nanocomposites," *Physics*, vol. 44, no. 23, pp. 3392–3405, 2006.
- [150] K. Fukushima, C. Abbate, D. Tabuani, M. Gennari, and G. Camino, "Biodegradation of poly(lactic acid) and its nanocomposites," *Polymer Degradation and Stability*, vol. 94, no. 10, pp. 1646–1655, 2009.
- [151] N. Tenn, N. Follain, J. Soulestin, R. Crétois, S. Bourbigot, and S. Marais, "Effect of Nanoclay Hydration on Barrier Properties of PLA / Montmorillonite Based Nanocomposites," *Journal of physical chemistry C*, vol. 117, pp. 12117–12135, 2013.
- [152] A. R. McLaughlin and N. L. Thomas, "Preparation and thermal characterisation of poly(lactic acid) nanocomposites prepared from organoclays based on an amphoteric surfactant," *Polymer Degradation and Stability*, vol. 94, no. 5, pp. 868–872, 2009.
- [153] B. Tan and N. L. Thomas, "Tortuosity model to predict the combined effects of crystallinity and nano-sized clay mineral on the water vapour barrier properties of polylactic acid," *Applied Clay Science*, vol. 141, pp. 46–54, 2017.

- [154] N. Delpouve, G. Stoclet, A. Saiter, E. Dargent, and S. Marais, "Water barrier properties in biaxially drawn poly(lactic acid) films.," *The Journal of Physical Chemistry. B*, vol. 116, no. 15, pp. 4615–4625, 2012.
- [155] C.-C. Tsai, R.-J. Wu, H.-Y. Cheng, S.-C. Li, Y.-Y. Siao, D.-C. Kong, and G.-W. Jang, "Crystallinity and dimensional stability of biaxial oriented poly(lactic acid) films," *Polymer Degradation and Stability*, vol. 95, no. 8, pp. 1292–1298, Aug. 2010.
- [156] Y. Cai, Q. Li, Q. Wei, Y. Wu, L. Song, and Y. Hu, "Structures, thermal stability, and crystalline properties of polyamide6/organic-modified Fe-montmorillonite composite nanofibers by electrospinning," *Journal of Materials Science*, vol. 43, no. 18, pp. 6132–6138, 2008.
- [157] A. H. Touny, J. G. Lawrence, A. D. Jones, and S. B. Bhaduri, "Effect of electrospinning parameters on the characterization of PLA/HNT nanocomposite fibers," *Journal of Materials Research*, vol. 25, no. 5, pp. 857–865, 2011.
- [158] Q. Shi, C. Zhou, Y. Yue, W. Guo, Y. Wu, and Q. Wu, "Mechanical properties and in vitro degradation of electrospun bio-nanocomposite mats from PLA and cellulose nanocrystals.," *Carbohydrate polymers*, vol. 90, no. 1, pp. 301–8, Sep. 2012.